Accurate Recovery of the Dynamics and Masses of Triaxial Galaxies

Bianca Neureiter

München 2023

Accurate Recovery of the Dynamics and Masses of Triaxial Galaxies

Bianca Neureiter

Dissertation
an der Fakultät für Physik
der Ludwig–Maximilians–Universität
München

vorgelegt von
Bianca Neureiter
aus Salzburg

München, den 13. Juni 2023

Zusammenfassung

Um die Entstehungsgeschichte massereicher elliptischer Galaxien zu erforschen, können Galaxien bei hohen Rotverschiebungen untersucht werden, deren Entwicklungszustand dem eines noch jüngeren Universums entspricht. Alternativ kann man aber auch in lokalen, bereits entwickelten Galaxien nach dynamischen Relikten suchen, die Rückschlüsse auf den vorausgegangenen Entwicklungsprozess ziehen lassen. Während die erstgenannte Methodik mit einem Auflösungsverlust der Beobachtungsdaten aufgrund der großen Entfernung der Objekte einhergeht, verspricht die zweite Strategie hochaufgelöste photometrische und spektroskopische Daten. Um physikalische Erkenntnisse über die untersuchte Galaxie zu gewinnen, benötigt es neben hochaufgelösten Beobachtungsdaten außerdem ein präzises Modellierungsverfahren, welches in der Lage ist, Informationen über die intrinsische Massenverteilung und Orbitstruktur aus den Beobachtungen zu extrahieren. Da massereiche "Early-Type Galaxies" (ETGs) triaxiale Objekte sind, welche in einem zunächst unbekannten Blickwinkel beobachtet werden, ist die Extraktion von dreidimensionalen intrinsischen Informationen aus den projizierten zweidimensionalen Beobachtungsdaten ein komplexes Unterfangen. Aus diesem Grund haben frühere achsensymmetrische Modelle vereinfachende geometrische Annahmen benutzt, um die Komplexität der Thematik einzugrenzen. Achsensymmetrische Modelle können allerdings einen Ungenauigkeitsfaktor von ~2 in der Reproduktion des stellaren Massen-zu-Leuchtkraft Verhältnisses oder der Masse des Schwarzen Lochs aufweisen, wenn sie auf triaxiale Galaxien angewandt werden. Diese Unsicherheit ist zu groß, um offene wissenschaftliche Fragen zu klären. Beispiele für offene Fragen sind: Welche exakte Steigung weisen die Skalenrelationen von Schwarzen Löchern in massereichen ETGs auf? Welchen Ursprung hat deren Streuung? Ist die stellare ursprüngliche Massenfunktion ("stellar initial mass function", IMF) universell innerhalb verschiedener Galaxien oder nicht? Bisher wurde noch nie geklärt, mit welcher Genauigkeit die intrinsische Massenverteilung und Orbitstruktur von ETGs prinzipiell bestimmt werden kann – selbst wenn alle geometrischen Komplexitäten berücksichtigt werden.

Im Rahmen dieser Arbeit wurde daher eine ausführlich überprüfte und umfassend evaluierte dynamische Modellierungsroutine entwickelt – mit dem Ziel, die bestmöglich erreichbare Genauigkeit der Massen- und Orbitrekonstruktion von ETGs zu ergründen sowie zu erreichen. Hierfür wird ein neuer Schwarzschild-Modellierungscode namens `SMART` auf mehrere Projektionen einer realistischen und hochaufgelösten numerischen Simulation angewandt. Diese Simulation ahmt einen Verschmelzungsprozess von Galaxien nach und die daraus entwickelte triaxiale Galaxie weist ein zentrales Supermassereiches Schwarzes Loch im

Zentrum auf. Ich zeige, dass wir in der Lage sind, das stellare Massen-zu-Leuchtkraft Verhältnis, die Masse des Schwarzen Lochs sowie das Anisotropieprofil der simulierten ETG mit einer noch nie zuvor erreichten Genauigkeit von $5-10\%$ zu bestimmen. Damit gelingt es mir zu beweisen, dass projizierte kinematische Daten von triaxialen Galaxien prinzipiell nur geringe Entartungen enthalten. Die erreichte Präzision demonstriert außerdem die Stärke der Schwarzschild Modellierung im Allgemeinen und bietet eine Referenz für zukünftige Studien von ETGs.

Als erste Anwendung des neuen Codes auf echte Beobachtungsdaten modelliere ich die elliptische "core" Galaxie NGC 5419. Die Auswertung dieser Galaxie ist von besonderem Interesse, da sie zwei voneinander getrennte Kerne im Zentrum aufweist. Mithilfe von hochaufgelösten MUSE (Multi-Unit Spectroscopic Explorer) Beobachtungen des VLT (Very Large Telescope) der ESO (European Southern Observatory) und dem neuen Modellierungscode SMART zeige ich, dass NGC 5419 eine isotrope Orbitverteilung im Zentrum hat. Da eine solche untypisch für core Galaxien ist, deutet dies auf einen früheren Entwicklungszustand von NGC 5419 hin, welcher sich von dem von anderen beobachteten core Galaxien unterscheidet.

Abstract

In order to study the evolutionary path of massive elliptical galaxies, one can either study galaxies at high redshifts when the universe was younger or one can look for dynamic relics of their formation history by analysing evolved local galaxies. Whereas the first method is accompanied by a loss of resolution due to the great distance of the observed objects, the second strategy promises high precision of photometric and spectroscopic data. In addition to high-resolution observations, an accurate modeling procedure, which is able to extract information about the internal mass and orbit distribution out of the observational data, is needed. With this, valuable physical insights about the galaxy under study can be attained. Since massive early-type galaxies (ETGs) are three-dimensional triaxial objects that are observed at a-priori uknown viewing angles, the extraction of intrinsic information out of the projected two-dimensional observational data is a rather complex task. Because of this, previous axisymmetric modeling techniques used simplifying geometry assumptions in order to narrow down the entanglement of this issue. The recovery uncertainty of a factor of ~ 2 of the stellar mass-to-light ratio or black hole mass of axisymmetric models applied to triaxial galaxies, however, is not good enough to target certain scientific questions, e.g. about the origin of the scatter and exact slope of black hole scaling relations of ETGs or about the (non-)universality of the stellar initial mass function of galaxies. It is so far unknown which recovery accuracy of the intrinsic mass and orbit structure of ETGs can in principle be achieved, even when all geometry complexities are addressed.

In the course of this thesis, an extensively tested and evaluated dynamical modeling machinery was established in order to study and achieve the best possible recovery accuracy of the mass and orbit distribution of triaxial ETGs. By applying a new Schwarzschild modeling code called SMART to several projections of a realistic high-resolution N-body merger simulation including a supermassive black hole, I prove that state-of-the-art integral-field projected kinematic data contain only minor degeneracies which allows for a recovery of the stellar mass-to-light ratio, black hole mass and anisotropy profile with an unprecedented accuracy of $5 - 10\%$. The so achieved high recovery precision moreover demonstrates the strength of the Schwarzschild method in general and allows for reference calibration values for future studies of ETGs. As a first application of the new modeling machinery to real observational data, I analyse the elliptical core galaxy NGC 5419, which is a particular interesting object since it hosts two dinstinct nuclei in its center. I use high-resolution MUSE (Multi-Unit Spectroscopic Explorer) observations of ESO's VLT (European Southern Observatory; Very Large Telescope) and the new modeling code SMART in order to reveal an untypical central isotropic orbit distribution of NGC 5419 suggesting that this galaxy is observed at an earlier evolutionary phase than other core ETGs.

✳

"All of the rocky and metallic material we stand on, the iron in our blood, the calcium in our teeth, the carbon in our genes were produced billions of years ago in the interior of a red giant star."
— Carl Sagan, 'The Cosmic Connection: An Extraterrestrial Perspective'

Contents

List of Figures

Chapter 1

Introduction

1.1   Overview and outline

Looking up at the starry night sky has always been fascinating to mankind. While the mere sight of the night sky arouses awe and admiration in us, it also awakens an interest in understanding the big picture of the universe and its underlying physical processes.

If we either direct our eyes or even modern telescopes towards the sky, we can always only detect that part of the universe, which interacts with the electromagnetic field. This part, however, makes up only ~ 5% of the total matter. The majority of our universe is invisible. In order to obtain indirect conclusions about the dark fraction of our universe, we can draw on a multidisciplinary diversity of modern research and technologies, including high-resolution observations together with advanced computational methods.

This thesis deals with the most massive elliptical galaxies in the local universe. Evidence from observations and simulations suggests that these objects are the result of a two-phase formation process. After the Big Bang, small density fluctuations evolved into dark matter halos. Infalling gas caused star formation to occur in the potential well of these dark matter halos. Over time, dark matter halos and the very early formed galaxies residing therein experienced collisions due to the gravitational force acting between them, resulting in today's massive elliptical galaxies.

Since these galaxies are thus made up of stars that formed very early on, they show a red color. We call these galaxies "early-type galaxies" (ETGs). The formation history, including the merging processes of these objects, causes a diverse complexity of stellar orbits. Since gravity is a force that acts on large scales, the velocity distribution of the stars is anisotropic, resulting in the elliptical shape of early-type galaxies. Early-type galaxies at the high-mass end even have a triaxial shape, where the lengths of all three ellipsoidal principal axes are different.

We can use two different kinds of observational methods in order to study these objects. By using CCD chips, we can measure the photometry and with it the galaxy's distribution of the visible matter projected on the night sky. With the help of modern integral field spectrographs and the Doppler shift caused by the motion of the stars, we can measure

the projected velocity distribution summed over all stars along the line of sight.

In the case of triaxial early-type galaxies, it requires a series of computational methods in order to obtain three-dimensional information about the galaxy's intrinsic structure out of these two-dimensional projected measurements. The study of the three-dimensional structure and dynamical motion of the stars inside the galaxy is, however, necessary in order to determine the underlying potential and consequently the distribution of the visible and dark matter inside the observed object. A correct recovery of the intrinsic mass and dynamical composition of ETGs then allows to draw conclusions about the overall formation and evolution scenario of ETGs.

The main task of this thesis is the dynamical modeling of triaxial early-type galaxies at the high-mass end. For this purpose, a triaxial dynamical modeling framework called SMART has been established. The conceptual method behind SMART makes use of Schwarzschild's Orbit Superposition Technique, in which the overall galaxy's motion is described as the superposition of individual orbits. Within a dynamical model, the stellar orbits are evolved in an initially assumed gravitational potential. The dynamical model's stellar orbit configuration and mass parameters of the assumed potential, i.e. the black hole mass, dark matter distribution and stellar mass-to-light ratio, as well as observational viewing angles are then varied until the model matches with the observations. This provides the correct parameters of the galaxy under study.

The majority of Schwarzschild codes so far have used simplifying geometry assumptions, which – applied to triaxial galaxies – can result in a mass recovery uncertainty factor of ~ 2. The uncertainty factor of ~ 2 is however not good enough in order to target currently open research questions. Examples of open questions are: What is the exact correlation between black holes and the properties of their host galaxies? Is the stellar initial mass function, i.e. the initial distribution of stellar masses at birth, universal among different kinds of galaxies or not? If not, what exactly does the stellar initial mass function look like for early-type galaxies? Does it vary with the galaxy's radius?

The answer to all of these questions requires that the mass distribution of early-type galaxies can in principle be determined with high precision. However, it has so far never been quantified how much the recovery precision of triaxial early-type galaxies is in principle limited by degeneracies hidden in the observational data as well as dynamical modeling processes.

The main task of this thesis is therefore to determine and achieve the maximum possible recovery accuracy of the intrinsic structure and mass composition of massive early-type galaxies. Reaching this goal requires several steps: First – the development of an accurate triaxial dynamical modeling machinery – second – the verification of its accuracy by application on a realistic N-body merger simulation and – third – its application to precise observational data, which are evaluated with next-generation data analysis strategies.

Within the course of this thesis, three first-author papers were published. These three papers represent chapters 2 - 4 of this thesis.

In chapters 2 and 3, the new triaxial dynamical modeling code SMART is applied to realistic high-resolution simulation data of a triaxial galaxy. The study covered in these two papers reveals an unprecedented recovery accuracy of 5-10% of the dynamical structure and mass

distribution including the mass recovery of the central supermassive black hole of early-type galaxies by a triaxial dynamical modeling routine. This proved that the recovery accuracy by far exceeds the uncertainty factor of ~ 2 of current axisymmetric codes and it sets the basis for gaining new and more precise insights into the intrinsic properties and formation history of early-type galaxies. Moreover, it proves that projected kinematics in general only hold minor degeneracies, allowing an almost unique recovery.

In Chapter 4, `SMART` is applied to high-resolution observational data of the triaxial early-type galaxy NGC 5419. The application of `SMART` to NGC 5419 reveals a supermassive black hole mass measurement at the high-mass end in the order of $10^{10} M_{\odot}$, an early core formation state of this galaxy as well as a co-evolution of its kinematically misaligned core with the central black holes' kinematics.

The preceding introductory sections 1.2 - 1.10 provide explanations for the physical concepts and dynamical modeling processes as background knowledge for the subsequent papers. The above summarized evolutionary history, properties of early-type galaxies and observational methods will be described in more detail. The introduction starts with a short summary of the history of extragalactic astrophysics and the principle classification of galaxies. Moreover, the orbit families occurring in triaxial potentials will be presented and the observational indications for the triaxial shape of massive early-type galaxies will be explained. This chapter furthermore provides a summary of the current findings and knowledge about early-type galaxies as well as a detailed explanation of the Schwarzschild modeling procedure. The introduction concludes with the scientific motivation and the main findings of the subsequent papers.

1.2 Classification of elliptical galaxies

When Charles Messier (Messier, 1781) and Caroline and William Herschel (Herschel, 1786) started to map the night sky in the 18th century by cataloging "*nebulae*", it was not yet clear whether these objects were part of our own Milky Way or extragalactic *island universes* (as they were titled by the philosopher Immanuel Kant). While this was still subject of the *Great Debate* in 1921 (Shapley 1921; Curtis 1921), a few years later, Edwin Hubble was finally able to shine light on the nature of these *nebulae* by measuring the distances of Cepheids as standard candles (Leavitt, 1908) in the Andromeda and Triangulum galaxies (Hubble, 1925). Since their distances were much larger compared to the objects in our Milky Way, Hubble revealed that these *nebulae* were not part of our own home galaxy but extragalactic objects. With this, the era of extragalactic astronomy was settled and has remained an indispensable field of science ever since. It was also Edwin Hubble who, for the first time, proposed a classification of galaxies by using photographic plates. Figure 1.1 illustrates Hubble's classification scheme, also called 'tuning fork' diagram, by demonstrating Hubble Space Telescope (HST) images of local galaxies. According to their projected apparent morphology, Hubble (1926) distinguished between "*elliptical nebulae*" (E), which are shown on the left side, and "*the spirals*" (S) branching out on the right side of the
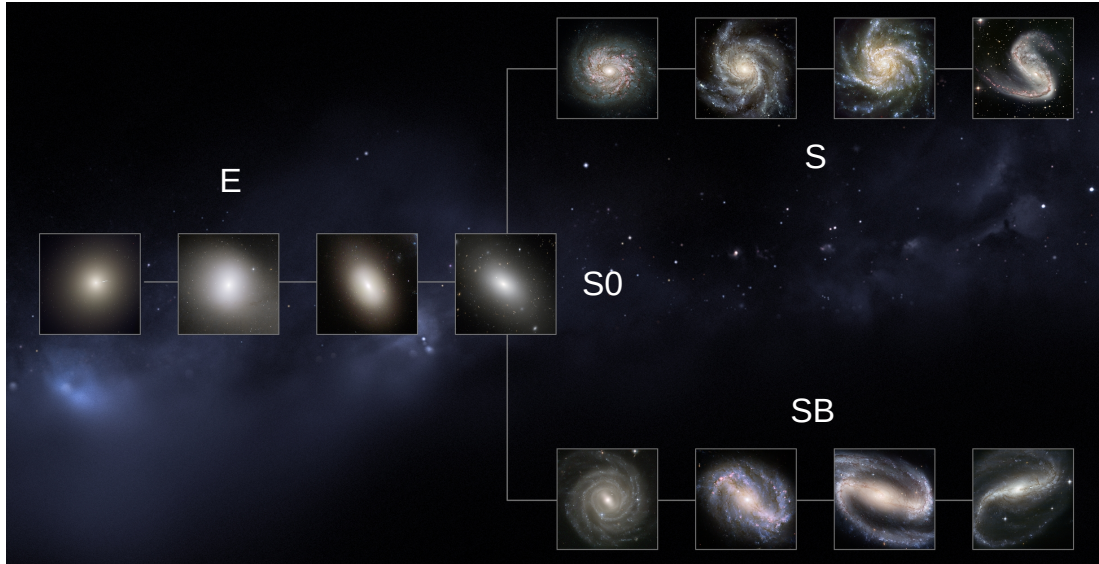
Figure 1.1: Hubble sequence. In Hubble's morphological classification scheme, galaxies get subdivided into elliptical (E; left), lenticular (S0; transition in the middle) and spiral galaxies (S; right). 'Normal spirals' (S) build the top branch and 'barred spirals' (SB) locate the bottom branch on the right side of Hubble's tuning fork diagram. In contradiction to the characteristic spiral arm features of spiral galaxies, ellipticals, which are the topic of this thesis, are smooth and featureless objects on the night sky (image credit: NASA, ESA, M. Kornmesser; edited).

tuning fork diagram. Lenticular galaxies (S0) are located in the transition in the middle. As one can see in Figure 1.1, elliptical galaxies appear as smooth, featureless and elliptical light distribution on the sky, hinting at an approximate dynamical equilibrium. Their name is based on the elliptical shape of their isophotes, which are the contour lines for equal surface brightness. Within the tuning fork diagram, the elliptical galaxies are subdivided with an increase in their flattening from left to right. In total, elliptical galaxies span a wide range of ellipticity $0 \leq \epsilon \lesssim 0.7$ with $\epsilon = 1 - b/a$ where a and b are the galaxy's projected semi-major and semi-minor axis, respectively.

In contradiction to the relaxed appearance of ellipticals, spiral galaxies show characteristic features resulting from their consistence of a disk, central bulge and spiral arms. In Hubble's classification scheme, the fractional size of the spiral arms to the central bulge component increases from left to right. The class of the 'normal spirals' (S) is located in the top branch of the tuning fork diagram and the 'barred spirals' (SB), which have a dominant bar in their centres, are shown in the bottom branch. Not pictured in Figure 1.1 are irregular galaxies, which show only weak or no regular structure at all.

Over time, Hubble's morphological classification got more and more refined based on increasingly advanced observational technologies and subsequent new findings not only about the galaxies' apparent morphologies but also about their related properties. de Vaucouleurs (1961) found that ellipticals differ from spirals also by their color. While the

Figure 1.2: Disky and boxy isophotes. Normal- and lower-luminosity elliptical galaxies typically show disky isophotal shapes ($a_4 > 0$; left panel), whereas the brightest and most massive elltipicals can have boxy deviations from perfect elliptical isophotes ($a_4 < 0$; right panel; image taken from Bender et al. (1988); edited).

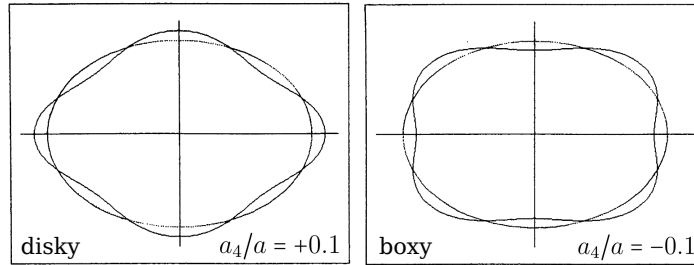younger stellar population in spirals and irregular galaxies, the so-called late-type galaxies (LTGs), typically let them appear bluer, lenticular and elliptical galaxies, the so-called early-type galaxies (ETGs), show redder colors, indicating an older stellar population. Dressler (1980) revealed that ETGs are predominantly found in dense environments such as galaxy groups and clusters, whereas LTGs occupy lower-density regions. In contrast to LTGs, ETGs are moreover characterized by their metal-rich stellar population, the quasi-absence of dust and gas prohibiting star formation activity (i.e. ETGs are 'quenched') and often by little to no rotation, which will be discussed further in section 1.7.

The invention of accurate CCD detectors and integral field spectrographs furthermore revealed a bimodality between less luminous and more luminous ETGs. When measuring the surface brightness (SB) of ETGs as two-dimensional projections on the night sky with the usage of CCD detectors, Bender et al. (1987) found that the isophotes of ETGs can show deviations from perfect ellipsoids, which can be described via a Fourier series. By analysing the Fourier coefficient a_4, elliptical galaxies get subdivided into normal and low-luminosity galaxies with disky-distorted isophotes (i.e. $a_4 > 0$) and giant ellipticals with boxy-distorted isophotes (i.e. $a_4 < 0$) (see Figure 1.2; Bender et al. 1987; Kormendy & Bender 1996).

Bender (1988a) and, later on, Kormendy & Bender (1996) showed that this dichotomy is also reflected in the large-scale rotation of ETGs. They find that the disky normal- and low-luminosity ETGs rotate rapidly while the boxy giant ellipticals are essentially non-rotating.

The so-found classification of early-type galaxies got confirmed by the study of the two-dimensional stellar kinematics of 48 representative elliptical and lenticular galaxies with the SAURON instrument (Bacon et al., 2001) at the William Herschel Telescope. Emsellem et al. (2007) and Cappellari et al. (2007) summarize the classification of early-type galaxies as 'fast rotators', which tend to have a relatively low luminosity of $M_B \gtrsim -20.5$, a flattened shape ($\epsilon \lesssim 0.7$) and well-aligned photometric and kinematic axes. The generally brighter ($M_B \lesssim -20.5$) 'slow rotators', on the other hand, tend to be fairly round ($\epsilon \lesssim 0.3$) with moderately triaxial shapes, they are more common among the most massive systems

and can show kinematic misalignments.

This kinematic classification into 'fast rotators' and 'slow rotators' essentially corresponds to the original classification by Kormendy & Bender based on the galaxies' isophotal shape, central structure and rotation (Lauer, 2012).

In the next section, a detailed explanation of how to extract information from photometric and spectroscopic observations will be provided, which includes more detailed insights into the bimodality of early-type galaxies.

1.3   Observations and bimodality of early-type galaxies

1.3.1   Surface brightness profiles

The measured surface brightness isophotes do not only provide a distinction between the beforehand mentioned boxy- and diskiness of ETGs, but, plotted against the radius, the isophotal SB profiles moreover indicate a difference between 'cuspy' and 'cored' ETGs.

Figure 1.3 shows the surface brightness profiles for a subsample of typical power-law galaxies with a steep central cusp (brown lines) and typical core ETGs (blue lines) with a shallow inner cusp interior to the 'core radius' (also called 'break radius'; taken from Lauer et al. 2007). The SB profiles in Figure 1.3 are plotted as a parametric form of a Nuker law (Lauer et al., 1995) fit. Lauer et al. (1995) define galaxies as core galaxies when their surface brightness profiles show a "break" from steep outer power laws to a shallower center, i.e. $SB(r) \propto r^{-\gamma}$ with $\gamma < 0.3$ at the HST resolution limit of $r \to 0.1$ arcsec.

As demonstrated in Figure 1.3, one can see a clear discrepancy, in particular in the central slopes, between the power-law and core galaxies.

The power-law galaxies belong to the fainter ETGs, whereas the most massive ellipticals appear as core galaxies. Their different photometric appearance in the above-mentioned boxy- and diskiness of the isophotes as well as their different central SB slopes, hint at a possible difference in the formation mechanisms of these galaxies. The formation mechanism for the most massive ETGs will be described in more detail in section 1.7.

While the Nuker law was designed to match the inner few ~ 3–10 arcsec of ETGs, the later introduced Sérsic profile (Sérsic, 1963) was developed to fit the entire profile out to larger radii:

$$\mathrm{SB}(r) = \mathrm{SB}_e \exp\left\{-b_n\left[\left(\frac{r}{r_e}\right)^{1/n} - 1\right]\right\}, \tag{1.1}$$

where SB_e is the measured surface brightness at the effective radius r_e, inside which half of the total light of the galaxy is contained. The Sérsic index n determines the curvature of the profile and b_n is a function of n, which is chosen so that half of the total luminosity is included within the elliptical isophote of r_e. With an increasing Sérsic component, the outer flattening of the profile becomes weaker, hinting at a more dominant halo. Empirically, the SB profiles showing $n > 2.5$ get assigned to ETGs and single Sérsic fits with $n < 2.5$ get
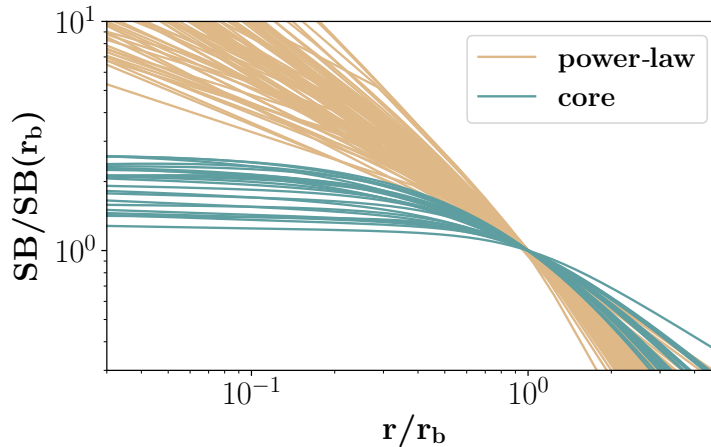
Figure 1.3: Power-law and core galaxies. When fitting Nuker law profiles to the surface brightness profiles of a sample of early-type galaxies from Lauer et al. (2007), one can see a clear difference between power-law ellipticals (colored brown), that show a steep central cusp and core ellipticals (colored blue) with a flattened center. The latter belong to the most massive ETGs, which are the subject of this thesis. To allow a better comparison, the here plotted radii and surface brightness profiles are normalized by their core radii r_b and corresponding $SB(r_b)$ values at this radius. The core radius is thereby defined as the transition point between the steep brightness profile and the shallower cusp in the center and also marks the point of maximum curvature of the profile in logarithmic coordinates. Power-law galaxies have more poorly defined breaking points than core galaxies, yet they generally show a modest decrease in slope as the center is approached (Lauer et al., 2007).

classified as SB profiles of LTGs (e.g. see Shen et al. 2003; Barden et al. 2005; Buitrago et al. 2013; Eales et al. 2015). In some cases, double or multi-component Sérsic functions provide a more suitable fit to the SB profiles of ETGs, especially in the case of the brightest cluster galaxies (BCGs) residing close to or at the centres of their host galaxy cluster (see e.g. Kluge et al. (2020) and references therein).

1.3.2 Kinematics and line-of-sight velocity distributions

Spectroscopic observations, e.g. in the form of two-dimensional data taken with an integral field spectrograph, provide information about the kinematics of a galaxy. Due to the motion of the stars in the galaxy and the resulting Doppler shift, the measured absorption line spectrum is broadened in comparison to the one of comparable standard stars at rest, which have the same metallicity and age as the observed galaxy's stellar population. Studying the broadening and exact shape of the absorption lines allows gaining insights into the galaxy's intrinsic stellar motion.

Similar to the surface brightness, the velocity distribution of the stars can only be measured in projected form and each measured absorption line consists of a superposition of
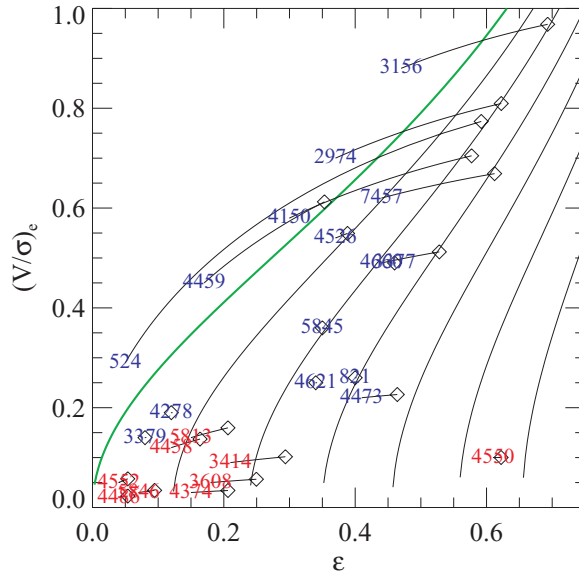
Figure 1.4: $(V/\sigma)_e - \epsilon$-diagram. The velocity dispersion dominated slow rotators (red labels) from a subsample of the SAURON survey clearly distinguish from the fast rotators (blue labels) in the $(V/\sigma)_e - \epsilon$-diagram (originally introduced by Illingworth (1977), Binney (1978) and Davies et al. (1983)). The slow rotators show lower $(V/\sigma)_e$-values at smaller ellipticities, i.e. rounder shapes. For the computation of $(V/\sigma)_e$ and ϵ, the individual galaxy's values at different measured bins were luminosity weighted and summed up out to one effective radius. The solid lines, which connect the galaxies' labels with the diamond symbols, show estimated error bars due to inclination uncertainties. The solid curves demonstrate model predictions for edge-on oblate galaxies with different anisotropies (image taken from Cappellari et al. 2007).

the Doppler-shifted absorption lines of all stars measured along the line of sight. Due to a statistical velocity distribution of the stars inside ETGs, the observed line-of-sight velocity distributions, the so-called LOSVDs, appear as Gaussian functions in a first approximation. The mean of the measured Gaussian LOSVD measures the galaxy's overall velocity while its width is determined by its velocity dispersion σ, which depends on the galaxy's mass and internal stellar motion. The most massive, slow rotating ellipticals are velocity dispersion dominated and typically show values of σ between 100 and 300 km/s (Cappellari et al. 2007; Emsellem et al. 2007; Saglia et al. 2016). Figure 1.4 shows the ratio between the luminosity-weighted velocity and velocity dispersion within one effective radius, plotted against the ellipticity for a sample of slow rotators (red labels) and fast rotators (blue labels) from the SAURON survey (de Zeeuw et al., 2002). Such $(V/\sigma)_e - \epsilon$-diagrams were already analysed early on by Illingworth (1977), Binney (1978) and Davies et al. (1983). One can clearly see that the slow-rotator ETGs are characterized by low $(V/\sigma)_e$-values and a fairly round shape, as already described in section 1.2. The fast rotators, on the other hand, show higher $(V/\sigma)_e$-values at a more flattened shape.

Figure 1.5: Mass-anisotropy degeneracy. As long as one cannot distinguish between radial or tangential orbit shapes, the velocity measurements of orbits along the line of sight of the observer (symbolised as eye) do not unambiguously provide information about the central mass M. The line-of-sight velocity of a radial (green) orbit $v_{\mathrm{LOSVD,1}}$ measured at the marked 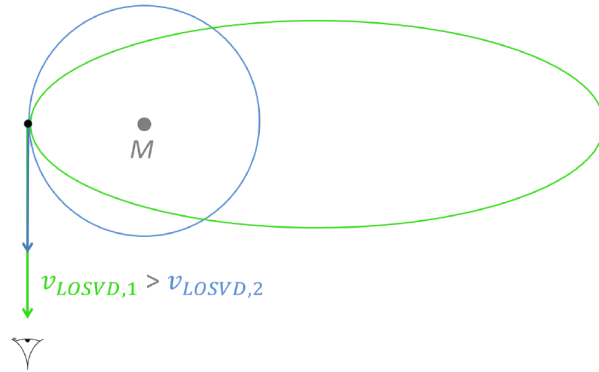point is larger than $v_{\mathrm{LOSVD,2}}$ of the circular orbit (blue). If the shape of the orbits get misinterpreted, the central mass gets over- or underestimated.

It was already briefly mentioned in the overview section and will be explained in more detail in the following section 1.4 that the gravity's property to act on long-range distances allows for an anisotropic orbit distribution. The $(V/\sigma) - \epsilon$-diagram only provides limited information about the galaxy's internal orbit distribution. When one wants to draw conclusions about the underlying mass distribution out of the measured LOSVDs, knowledge about the galaxy's stellar anisotropy, i.e. the ratio between radial and tangential orbits, is required. As long as there is no information about a galaxy's orbital anisotropy, the determination of its mass distribution is uncertain. This phenomenon is illustrated in Figure 1.5. An observer, symbolised as eye, can always only measure a star's velocity component along the line of sight and therefore the stellar orbital shape is initially unknown. (Even though the observed LOSVDs consist of the summed contribution of all stars along the line of sight, Figure 1.5 depicts the contribution of a single star to the observed LOSVD for an easier illustration and simplified description.) In principle, a star "1" populating a radial orbit (colored green), which orbits a central mass M and which is observed at the position marked in Figure 1.5, has a higher line-of-sight velocity $v_{\mathrm{LOSVD,1}}$ than a star "2" on a circular orbit (colored blue) at the same position rotating around the same central mass M, i.e. $v_{\mathrm{LOSVD,1}} > v_{\mathrm{LOSVD,2}}$. If the observed velocity $v_{\mathrm{LOSVD,1}}$ of the radial orbit gets misinterpreted as the one of a circular orbit, the central mass gets overestimated and vice versa. As long as there is no information about the radially or tangentially anisotropic orbit distribution, this so-called mass-anisotropy degeneracy cannot be solved (Binney & Mamon 1982; Dejonghe & Merritt 1992).

It was shown that, on closer inspection, the observed absorption lines differ from a perfect Gaussian profile and the specific deviations can help to disentangle this degeneracy (e.g. Gerhard 1993; Baes et al. 2005). The historically most common method for break-

ing the degeneracy between anisotropy and mass was the description of the deviations of
the absorption line from a perfect Gaussian profile by additional Gauss-Hermite functions
(Gerhard 1993; Bender et al. 1994):

$$f(y) = I_0 \exp\left(-\frac{y^2}{2}\right)\left(1 + h_3\mathscr{H}_3(y) + h_4\mathscr{H}_4(y)\right), \tag{1.2}$$

with I_0 being a normalization constant, $y = \frac{v - v_{fit}}{\sigma_{fit}}$ and

$$\mathscr{H}_3 = \left(2\sqrt{2}y^3 - 3\sqrt{2}\right)/\sqrt{6} \quad \text{and} \quad \mathscr{H}_4 = \left(4y^4 - 12y^2 + 3\right)/\sqrt{24}\,. \tag{1.3}$$

The third and fourth order Gauss-Hermite parameters h_3 and h_4 are the amplitudes of the
standard Hermite polynomials $\mathscr{H}_3$ and $\mathscr{H}_4$.
While further orders of deviations $h_5\mathscr{H}_5(y), h_6\mathscr{H}_6(y), h_7\mathscr{H}_7(y), \dots$ and in particular the
analysis and consideration of LOSVDs in a non-parametric way are able to reveal more and
more details of the intrinsic orbit distribution, we here focus on the illustrative description
of the third and fourth order Gauss-Hermite parameters h_3 and h_4.
Figure 1.6 shows the LOSVD shapes for absorption line profiles with non-zero h_3 and h_4.
The third order Gauss-Hermite parameter h_3 hints at a rotation signal of the galaxy as
a whole, which results in an asymmetric LOSVD shape with the prograde wings being
steeper than the retrograde wings (see Figure 1.6 (a) and (c); Bender et al. 1994). A
positive fourth order Gauss-Hermite parameter $h_4 > 0$ results in a peaked LOSVD pointing
to a radially anisotropic orbit distribution (see Figure 1.6 (b)) and a negative fourth order
Gauss-Hermite parameter $h_4 < 0$ results in a flat-topped LOSVD pointing to a tangentially
anisotropic orbit distribution (see Figure 1.6 (d)). Typical h_4 values for massive ETGs
lie within $|h_4| \lesssim 0.1$ (Veale et al., 2018). In addition to a possible velocity anisotropy
prevailing in the galaxy under study (e.g. Gerhard et al. 1998; Thomas et al. 2007b),
positive h_4-values can, in principle, also appear in isotropic systems if the mass profile
within the galaxy is not isothermal and consequent strong variations in the circular veloci-
ties are measured along the line of sight (Gerhard 1993; Baes et al. 2005; Veale et al. 2017).

The better the signal-to-noise ratio of the spectroscopic data, the more information
can be extracted from the measured LOSVDs and consequently more degeneracies hid-
den in the kinematic data can be disentangled. The progressively improving resolutions
of today's telescopes and some of the increasingly advanced kinematic extraction codes
(Bender 1990; Gebhardt et al. 2000; Cappellari 2017; Falcón-Barroso & Martig 2021) allow
to measure the full LOSVDs in a non-parametric way. In order to obtain accurate mass
distribution recoveries out of the LOSVD measurements, it requires a dynamical model,
which constructs a stellar orbit library whose modeled kinematics match the observations.
In order for a dynamical model to overcome the described degeneracies, which are hidden
in the kinematic data, it is useful to process as much information as possible from the
LOSVDs. In this respect, Schwarzschild's orbit superposition technique, which is used in
this thesis, advances other dynamical modeling techniques. This will be described in more
detail throughout this thesis. Before that, however, it will be clarified in which way the
discussed anisotropy is affecting the shape of ETGs.
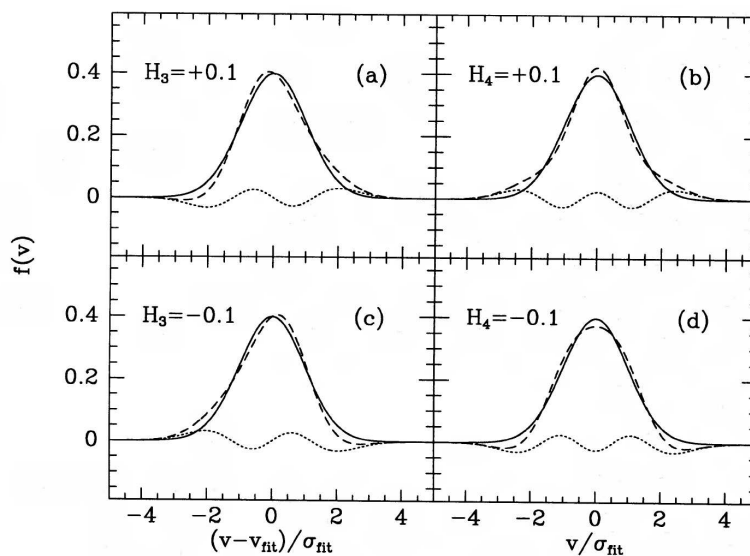
Figure 1.6: h_3 and h_4 Gauss Hermite parameters. A non-zero h_3 Gauss-Hermite parameter provides information about an intrinsic rotation of the observed galaxy. The steeper prograde wings result in an asymmetric LOSVD shape (see panels (a) and (b)). A nonzero h_4 Gauss-Hermite parameter hints at deviations from an isotropic orbit distribution. Radially anisotropic orbits result in a peaked LOSVD ($h_4 > 0$, see panel (b)) and tangentially anisotropic orbits cause a flat-topped LOSVD ($h_4 < 0$, see panel (d); image taken from Bender et al. 1994).

1.4   Relaxation time-scale and ellipticity

The observational findings described in the previous Section 1.3.2, namely that slow rotating early-type galaxies exhibit low v/σ-values (see Figure 1.4), raise a fundamental question: Why do ETGs in principle have an elliptical shape?

If an elliptical galaxy was comparable to a gas ball, the frequently colliding gaseous particles would quickly allocate along a Maxwellian distribution. In such a thermal distribution, the velocities of the stars would be isotropic and an elliptical deviation from a round shape could only be caused by rotational flattening. However, it can be shown (e.g. see Mo et al. 2010), that for an isotropic oblate rotator being flattened by the centrifugal force, the ratio between the galaxy's rotational velocity $v_{\rm rot}$ and velocity dispersion σ needs to satisfy the following relation:

$$\left(\frac{v_{\rm rot}}{\sigma}\right)_{\rm iso} \approx \sqrt{\frac{\epsilon}{1-\epsilon}}, \tag{1.4}$$

where ϵ is the galaxy's ellipticity. Since in slow-rotating ETGs $v_{\rm rot} << \sigma$, as demonstrated in Figure 1.4, the elliptical shape cannot be caused by rotational flattening. Following the tensor virial theorem[1], it can be shown (e.g. see Binney & Tremaine 2008, Mo et al. 2010) that an alternative explanation for a non-spherical shape and low rotation signal is an anisotropic stellar velocity distribution: If the stars in a galaxy move along a preferred direction and are equally distributed along pro- and retrograde orbits, the galaxy appears flattened while at the same time stays non-rotating. The condition for this is that stellar collisions happen so rarely that no thermalization of the stellar distribution takes place. The decisive difference between stars not getting thermalized and gaseous particles, like atoms or molecules, getting isotropically distributed in velocity space is the force that acts on them. While the interaction between gas particles happens on small timescales and only within short distances, the gravitational force acting between the stellar particles is long-range, resulting in a much slower relaxation process. The long-range characteristic of the gravitational force allows a single star moving through a galaxy to be gradually accelerated by the overall gravitational field of the galaxy, rather than experiencing deflection from individual pair-wise collisions. It can be shown with simple calculations (e.g. see Binney & Tremaine 2008) that the relaxation time $t_{\rm relax}$, which is defined as the time in which a star's velocity is changed by 100% by two-body encounters, is given as

$$t_{\rm relax} = t_{\rm cross}\frac{N}{\ln(N)}, \tag{1.5}$$

where N is the total number of stars in the whole galaxy and $t_{\rm cross} = \frac{R}{v}$ corresponds to the crossing time, after which a typical star with velocity v has crossed the galaxy with radius R once. For a typical galaxy with $t_{\rm cross} \sim 10^8$ yr and $N \sim 10^{12}$ (see e.g. Schneider 2006), the relaxation time exceeds by far the age of the universe of 13.8 Gyr. With this,

---

[1]The tensor virial theorem describes the balance between the kinetic energy $K = T + \frac{1}{2}\Pi$ consisting of the contributions T and Π from ordered and random motion, respectively, and the potential energy W in an equilibrium stellar system as $2K + W = 0$.

an ETG can be regarded as a collisionless system in which pair-wise collisions do not play any significant role in the dynamical evolution of the galaxy. This creates the basis for early-type galaxies to potentially exhibit anisotropic stellar velocity distributions, allowing for their elliptical shape to be independent of any constraints on their rotation speed.

1.5 Dynamical modeling

In the case of spiral galaxies, information about the mass distribution inside the galaxy can be obtained from the measured stellar kinematics in a straightforward way.
With the assumption of disk galaxies being intrinsically axisymmetric, the inclination of the disk, i.e. the angle between the plane of the disk and the line of sight, can be measured from the observed axis ratios of the disk. When taking the inclination into account and assuming that all stars in the disk of a spiral galaxy follow a circular motion, the balance between the gravitational and centrifugal force provides direct insight into the radial mass distribution $M(r)$ out of the observed velocity profile via

$$v_{\text{circ}}(r) = \sqrt{\frac{\text{G}M(r)}{r}}, \tag{1.6}$$

where G is the gravitational constant. In contrast to what the centrally concentrated distribution of the observed visible matter $M_{\text{visible}}(r)$ of a spiral galaxy would suggest, observed rotation curves of spirals typically do not decrease with radius in the outskirts of the galaxy but stay constant. With this, the distribution of the non-visible mass, i.e. the dark matter $M_{\text{dark}}(r)$ of the disk galaxy under study, can be inferred from the measured rotation curve $v_{\text{circ}}(r)$.
In the case of elliptical galaxies, the recovery of the visible and dark matter distribution from the observed line-of-sight velocity is a much more complicated task. First of all, the determination of the viewing angles, under which the elliptical galaxy is observed, is less straightforward, and second, the orbits of stars in ellipticals are much more complex and diverse than in spirals.
In order to reveal a three-dimensional galaxy's dynamical structure and mass composition, including the recovery of the stellar and dark matter distribution and the mass of the central black hole (BH), out of the two-dimensional photometric as well as spectroscopic observations, it requires a dynamical model. The concept of a dynamical model is based on the collisionless Boltzmann equation (CBE). The CBE implies that the distribution function $f\left(\overrightarrow{r}, \overrightarrow{v}, t\right)$, which is the most general and complete description of a stellar system, is constant over time, i.e.:

$$\frac{df(x_i, v_i, t)}{dt} = \frac{\partial f}{\partial t} + \frac{\partial f}{\partial x_i}\frac{\partial x_i}{\partial t} + \frac{\partial f}{\partial v_i}\frac{\partial v_i}{\partial t} = \frac{\partial f}{\partial t} + \left(\vec{\nabla}_r f\right) \cdot \vec{v} - \left(\vec{\nabla}_v f\right) \cdot \vec{\nabla}\Phi = 0. \tag{1.7}$$

We here use $\overrightarrow{r} = (x, y, z) = (x_i), i = 1...3$ for the space coordinates, $\overrightarrow{v} = (v_x, v_y, v_z) = (v_i), i = 1...3$ for the velocity and Φ for the gravitational potential. All relevant observables, i.e.

the LOSVDs $\mathcal{L}$ and surface brightness μ at time t and projected position (x_p, y_p) can be described as integrals of f:

$$\mathcal{L}(x_p, y_p, v_p, t) = \int f\left(\vec{r_p}, \vec{v_p}, t\right) dv_x dv_y dz,$$
$$\mu(x_p, y_p, t) = \int f\left(\vec{r_p}, \vec{v_p}, t\right) d^3 v_p dz, \tag{1.8}$$

with $\vec{r_p} = (x_p, y_p, z)$ and $\vec{v_p} = (v_x, v_y, v_p)$.

The gravitational potential Φ in equation 1.7 can be expressed via the Poisson's equation:

$$\Delta \Phi = 4\pi G \cdot \rho, \tag{1.9}$$

with G as graviational constant and ρ as the galaxy's total density distribution. In the case of elliptical galaxies ρ consists of the contributions from the stars ρ_*, dark matter ρ_{DM} and black hole ρ_{BH}:

$$\rho = \rho_* + \rho_{\mathrm{DM}} + \rho_{\mathrm{BH}}. \tag{1.10}$$

The stellar contribution to the density $\rho_* = \Upsilon \cdot \nu$ can be expressed as the stellar mass-to-light ratio $\Upsilon = M_*/L$ times the luminosity density $\nu = \int f(\vec{r}, \vec{v}, t) d^3 v$, which needs to be extracted by deprojecting the observed surface brightness. The density contribution from the black hole ρ_{BH} is concentrated to the galaxy's center and is determined by the black hole mass M_{BH}.

Dynamical models, which aim to reproduce the entire galaxy structure, make use of the Jeans theorem (e.g. Binney & Tremaine 2008). The Jeans theorem (Jeans, 1915) states that any steady-state solution of the CBE depends on the phase-space coordinates only through the integrals of motion $I(\vec{r}, \vec{v})$ of the potential, which are the constants along a stellar trajectory, i.e.:

$$\frac{d}{dt} I(\vec{r(t)}, \vec{v(t)}) = 0. \tag{1.11}$$

With the assumption that the galaxy under study is in a steady state, i.e. $\frac{\partial f}{\partial t} = 0$ (which then also applies to equation 1.7), the Jeans theorem consequently also holds for the distribution function f, i.e.:

$$f = f\left[I_1(\vec{r}, \vec{v}), \ldots, I_n(\vec{r}, \vec{v})\right], \tag{1.12}$$

$$\Rightarrow \frac{d}{dt} f(I_1, \ldots, I_n) = \sum_{j=1}^{n} \frac{df}{dI_j} \frac{dI_j}{dt} = 0, \tag{1.13}$$

where the number of the integrals of motion n depends on the given gravitational potential. (The specific number and characteristics of the integrals of motion in dependence on the underlying gravitational potential will be clarified in detail in section 1.6.1.) According to the Jeans theorem, the distribution function f is constant along the stellar orbits. Another result of the Jeans theorem is that the CBE could be solved by creating a function that depends only on the integrals of motion. However, in realistic gravitational potentials of

elliptical galaxies, not all integrals of motion are known in an analytic way (these will be introduced in section 1.6.1 as the non-classical integrals of motion).

There are several techniques that have so far been developed to recover the distribution function f from observations. These techniques include parametric methods, which are implemented as distribution-function-based or moment-based methods, as well as non-parametric methods, which are implemented as particle-based or orbit-based methods.

The *moment-based method* does not obtain the total distribution function of an observed system but concentrates on finding solutions of the Jeans equations as higher order velocity moments of the CBE, which best reproduce the observations such as the surface density and velocity dispersion (e.g. Binney & Mamon 1982; Binney et al. 1990; Magorrian & Binney 1994; Łokas 2002; Cappellari 2008). The Jeans modeling technique requires simplifying assumptions, such as spheroidal or axisymmetric geometry, in order to narrow down the number of unknowns and be able to solve the system of equations. Besides that, Jeans models can produce unphysical solutions because the underlying distribution function is not guaranteed to be strictly positive. Another disadvantage is the lack of processing constraints from higher-order moments of the LOSVDs or the full LOSVDs in a non-parametric form.

Within the framework of the *distribution-function-based method*, the observations are fitted with parameterized distribution functions (e.g. Dejonghe 1984, 1986; Bishop 1987; Gerhard 1991; Hunter & de Zeeuw 1992; Dehnen & Gerhard 1993; Magorrian 1995). The basic requirement for the distribution-function method, however, is the complete knowledge about all integrals of motion in the underlying potential, which again restricts the application to strict symmetry assumptions. Another disadvantage of the distribution-function-based method is that the solving for integral equations is more computationally expensive in comparison to the solving of differential equations in the Jeans models.

The *particle-based method* was introduced by Syer & Tremaine (1996) as made-to-measure (M2M) N-body method (e.g. Bissantz et al. 2004; de Lorenzi et al. 2007). Within the framework of an evolving gravitational potential, an N-body's particles' weights (i.e. the particles' masses) are slowly adapted as a function of time until the system matches the observations. This technique is, on the one hand, rather time expensive, but on the other hand, also flexible and unrestricted to any geometry.

The *orbit-based method* was founded by Schwarzschild (1979) and is called Schwarzschild's orbit superposition technique. The work of this thesis is based on this method, which will therefore be discussed in more detail in the next section.

1.5.1   Schwarzschild's orbit superposition technique

In Schwarzschild's orbit superposition technique, the galaxy's distribution function is approximated as the weighted superposition of a finite number of single orbit distribution functions, i.e.

$$f = \sum_{i=1}^{N_{\mathrm{orbit}}} w_i \cdot f_i, \tag{1.14}$$

where f_i is the normalized distribution function of orbit i, which shows a constant phase-density along the orbit and is zero everywhere else. w_i is the orbit's weight, i.e. the number of stars occupying orbit i, and N_{orbit} is the total number of orbits in the dynamical model. In Schwarzschild's orbit superposition technique, thousands of orbits get evolved in an assumed gravitational potential. The orbit library has to be chosen so that it representatively samples all orbit families, which can appear within the assumed gravitational potential. Since in the orbit-based method the integrals of motion are only implicitly entered via the orbital initial conditions, Schwarzschild's orbit superposition technique is particularly advantageous for systems where not all integrals of motion are known.

The orbital weights w_i have to be determined so that the LOSVDs of the model $\mathcal{L}_{\mathrm{mod}}$ match the observed LOSVDs $\mathcal{L}_{\mathrm{data}}$ in a least square sense (e.g. Richstone & Tremaine 1984), so that their deviation χ^2 is minimal:

$$\chi^2 = \sum_{j}^{N_{\mathrm{data}}} \left(\frac{\mathcal{L}_{\mathrm{data}}{}^j - \mathcal{L}_{\mathrm{mod}}{}^j}{\Delta \mathcal{L}_{\mathrm{data}}{}^j} \right)^2 \;\;, \tag{1.15}$$

where j is the notation for the N_{data} data bins. The observed surface brightness can serve as a boundary condition. The modeled LOSVD $\mathcal{L}_{\mathrm{mod}}$ consists of the weighted sum over the contributions $\mathcal{L}_{\mathrm{orb}}$ of all orbits i to the jth data bin, i.e.

$$\mathcal{L}_{\mathrm{mod}}{}^j \equiv \sum_{i=1}^{N_{\mathrm{orbit}}} w_i \mathcal{L}_{\mathrm{orb}}{}^{j,i}. \tag{1.16}$$

Besides the orbital weights, the a priori unknown viewing angles and quantities defining the galaxy's gravitational potential, i.e. the stellar mass-to-light ratio Υ, the black hole mass M_{BH} and dark matter distribution (cf. equations 1.9 and 1.10), are varied so long until a best-fit model in comparison to the observed kinematics can be found.

In this way, the galaxy's stellar orbit distribution, dynamical structure and mass distribution of all relevant contributions, i.e. the luminous and dark matter and also the mass of the central black hole, can be determined.

Schwarzschild's orbit superposition technique requires careful handling, e.g. when the set-up of the orbit library becomes increasingly complicated with an increase of the potential's phase-space structure, and, in general, it holds various challenges (see section 1.9.2). However, when implemented correctly, this technique provides tremendous power to precisely study a galaxy's internal composition, which will be demonstrated in the course of the thesis. As already briefly mentioned in section 1.3.2, one of the decisive advantages of the Schwarzschild modeling technique is that it allows for the processing of the LOSVDs in a non-parametric way.

In principle, Schwarzschild's orbit superposition technique requires a significant amount of computational time. One of the reasons for this is that the large orbit library has to be set up and newly evolved for every tested potential. Since the computational effort increases the more complicated the potential under study is, the majority of the Schwarzschild models developed so far restricted themselves to simplifying symmetry assumptions, such as sphericity or axisymmetry. However, as introduced in the previous sections, the brightest
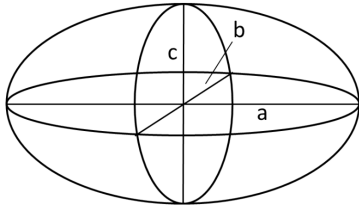
Figure 1.7: Triaxial ellipsoid. A triaxial ellipsoid shows three different principal axis lengths with $a > b > c$, where a is the semi-major, b the semi-intermediate and c the semi-minor axis length.

and most massive ETGs are neither spherical nor axisymmetric but triaxial objects, which will be discussed in the next section.

1.6 Triaxiality

An ellipsoidal object is called triaxial if the lengths of its principal axes are different, i.e. $a > b > c$, where a equals the semi-major axis, b is the semi-intermediate and c is the semi-minor axis of the galaxy (see Figure 1.7). The level of triaxiality can be described via the triaxiality parameter

$$T = \frac{1 - p^2}{1 - q^2},$$ (1.17)

where p and q describe the axis ratios of c and b to a:

$$q = \frac{c}{a}, p = \frac{b}{a}.$$ (1.18)

A galaxy is triaxial for $0 < T < 1$ and reaches a maximum of triaxiality if $T = 0.5$. In the case of axisymmetric galaxies, the number of different principal axis lengths decreases from three to two. An axisymmetric galaxy can either be oblate if $a = b > c$ and thus $T = 0$, or prolate if $a > b = c$ and thus $T = 1$.
By studying the average statistical distribution of the intrinsic shapes for a photometric data sample of 96,951 galaxies of the Sloan Digital Sky Survey (SDSS) Data Release 3, Vincent & Ryden (2005) report triaxiality parameters $T \in [0.4, 0.8]$ for massive elliptical galaxies with a de Vaucouleurs profile.

1.6.1 Orbits in triaxial potentials

A comprehensible overview of the possible orbit types prevailing in galactic potentials, such as a triaxial potential in massive ETGs, requires a preceding introduction of the integrals of motion, which uniquely define every stellar orbit. As mentioned in section 1.5, the integrals of motion are functions of phase-space coordinates that are conserved along the stellar trajectory. Their total number is determined by the shape of the potential and

restricts the dimensionality of the trajectory in phase-space.

Figure 1.8 gives an overview of possible stellar orbits and their corresponding integrals of motion in different potentials.

The stars in a Kepler potential move along closed and planar orbits. The exact shape of the individual trajectory is defined by five integrals of motion: the energy E, the angular momentum along all three directions L_x, L_y, L_z and the Runge-Lenz vector $\boldsymbol{S}$. Even though E and all components of the vectors $\boldsymbol{L}$ and $\boldsymbol{S}$ add up to seven conserved quantities, a Keplerian potential only conserves five independent integrals of motion, since these quantities depend on each other via two equations (e.g. see Goldstein et al. 2002).

The corresponding orbits are closed and planar (see Figure 1.8, left panel).

All orbits in spherical potentials are regular and are defined by four integrals of motion (E, L_x, L_y, L_z). They show a planar rosette shape (see Figure 1.8, second panel).

Orbits in axisymmetric potentials conserve at least two integrals of motion: the energy E and the angular momentum along either the short axis L_z of the galaxy or along the long axis L_x. The direction of the conserved angular momentum component determines whether a galaxy appears oblate (for L_z = const.) or prolate (for L_x = const.). If an orbit is regular, it conserves an additional non-classical integral of motion called I_3, which usually is not known analytically (e.g. Contopoulos 1963). Regular orbits appear as rosette-shaped orbits with an additional motion along the z-axis direction in oblate galaxies and along the x-axis direction in prolate ones (see Figure 1.8, third panel). There is no simple description for the non-classical integral of motion I_3, but two orbits (a) and (b) with $E_{(a)} = E_{(b)}$ and $L_{z,(a)} = L_{z,(b)}$ (in the case of an oblate galaxy) but $I_{3,(a)} \neq I_{3,(b)}$ show a different elongation along the z-axis.

In the case of a triaxial potential, there is only one classical integral of motion remaining – the energy E. Besides the energy E, regular orbits in triaxial potentials conserve two non-classical integrals of motion I_2 and I_3. As the right panel in Figure 1.8 shows, a perfect triaxial ellipsoid supports four types of regular orbits. The upper left panel pictures a box orbit that can go through the center and has no sense of rotation. This orbit type got its name from its box-like shape, which is constructed by the eight corners of the isopotential energy surface at which the orbit comes to rest for an instant. In contrast to the centrophilic box orbits, the other type of stable orbits in triaxial potentials are centrophobic and are so-called tube-orbits, which conserve a sense of rotation. As shown in Figure 1.8, triaxial potentials can exhibit short-axis tube orbits and outer and inner long-axis tube orbits. In addition to the regular orbits shown in Figure 1.8, realistic triaxial galactic potentials can also exhibit non-regular, chaotic orbits. These non-regular orbits only conserve E as single integral of motion.

Heiligman & Schwarzschild (1979) show that tube orbits around the intermediate axis are unstable in their numerical model with fixed axis ratios of 1:1.25:2. Also Binney & Tremaine (2008) demonstrate that tube orbits around the intermediate axis are unstable in a perfect triaxial potential.

As later described in section 1.7, the formation scenario of massive elliptical galaxies includes a mass assembly through mergers. Such merging events can cause deviations from a perfect ellipsoidal shape. As a consequence of a diverse merging history, increased com-

plexities such as radially changing axis ratios cannot be excluded. In addition to this, the existence of supermassive black holes (SMBHs) in real galaxies can cause a more spherical shape of the potential in the center resulting in a radial change of the integrals-of-motion space. In chapter 2, I will show that our new triaxial dynamical modeling code allows for orbits with a minor rotation signal (in the order of 10 km/s) around the y-axis, which appears to be stable for a limited time-span of at least 2 Gyrs within a realistic gravitational potential based on a triaxial merger remnant of an N-body merger simulation.

1.6.2   Observational hints for triaxiality

From an observational point of view, there are several indications that massive ETGs have triaxial shapes:

The position angles of the isophotes from the elliptical galaxy NGC 5831, as exemplarily demonstrated in Figure 1.9, radially change by $\sim 35°$ (Cappellari, 2002) from the inner isophotes to the outer ones. Such **isophotal twists** have already been observed early on (Bertola & Galletta 1979; Williams & Schwarzschild 1979) and recent studies using the photometric data from the HST Wide Field Camera 3 report that the majority of a sample of 35 high-mass ETGs show isophotal twists with center drifts of $\lesssim 10\%$ of the semi-major axis length for the isophotes (Goullaud et al., 2018). This observational phenomenon can either occur if the true principal axes of the observed galaxy intrinsically change their position angle with radius, or, more plausibly, if the axis ratios of a triaxial galaxy slowly change with radius and projection effects result in the observed isophotal twist (Binney, 1978).

Another hint for triaxiality is the presence of **minor-axis rotation**[2] (Schechter & Gunn, 1978) and **kinematic misalignment**. In principle, minor-axis rotation alone can appear in prolate galaxies, yet combined with kinematic twists and misalignment, it points to an intrinsic triaxial shape of the observed galaxy (Contopoulos 1956; Binney 1985), since rotation around two axes does not appear in axisymmetric potentials (as explained in the previous section 1.6.1).

Massive elliptical galaxies with isophote twists and depleted stellar cores (see section 1.3.1) are furthermore frequently reported to host **kinematically decoupled or distinct cores** (KDCs; Bender 1988b; Franx & Illingworth 1988; Emsellem et al. 2004; Hau & Forbes 2006; McDermid et al. 2006; Krajnović et al. 2011; Ene et al. 2018). An example for a KDC observed in the core elliptical NGC 4365 is shown in Figure 1.10. The initial standard model proposed for KDCs in ETGs involved their early formation through merging processes accompanied by dissipation (see e.g. Bender 1996; Davies et al. 2001).

---

[2]Minor-axis rotation means that a velocity gradient along the projected minor axis can be observed. Since the description of 'minor-axis' rotation might be misleading, it is also sometimes called long-axis or prolate rotation.

Kepler potential: spherical potential: axisymmetric potential: triaxial potential:

n Integrals of motion:

$n = 5$:
$E, L_x, L_y, L_z, \boldsymbol{S}$

$n = 4$:
E, L_x, L_y, L_z

$n = 3$:
E, L_z, I_3 (oblate)
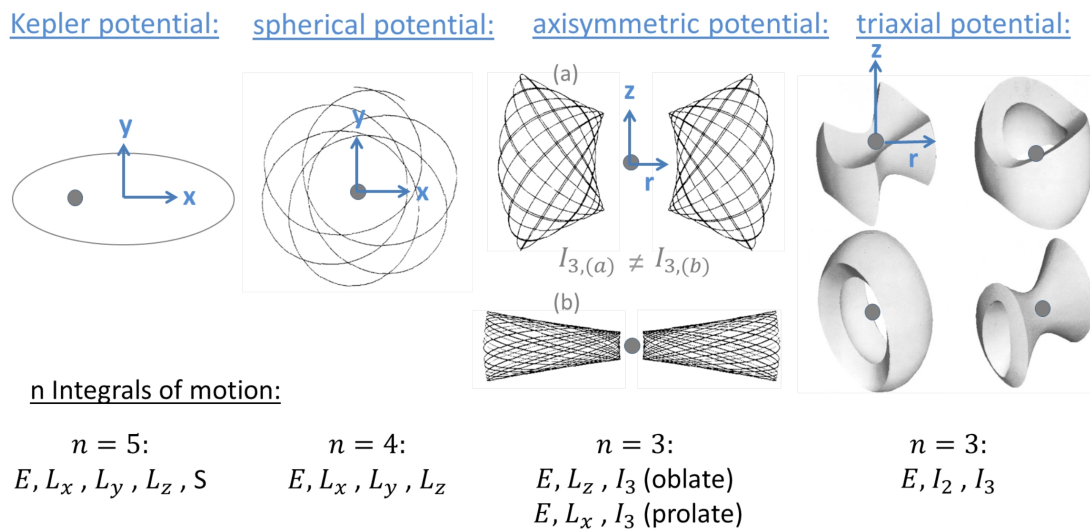E, L_x, I_3 (prolate)

$n = 3$:
E, I_2, I_3

Figure 1.8: Orbit types in different potentials. The stars in a Kepler potential move along planar and closed orbits (left panel), which are constrained by five integrals of motion $(E, L_x, L_y, L_z, \boldsymbol{S}$; these seven quantities depend on each other via two equations, resulting in five independent conserved constants). Here, the plane is arbitrarily chosen to match with the x-y-plane. The second panel shows the rosette-shaped planar orbits in a spherical potential having 4 constants (E, L_x, L_y, L_z) (image taken from Binney & Tremaine 2008; edited). Stars on regular orbits in axisymmetric potentials also move along rosette-shaped trajectories, yet with an additional perpendicular elongation along the z- (oblate systems) or x-axis (prolate systems) (third panel; image taken from Binney & Tremaine 2008; edited). The integrals of motion in an axisymmetric potential consist of the energy E and the angular momentum along one direction (either L_z for oblate or L_x for prolate systems). Regular orbits conserve an additional non-classical integral of motion I_3. Triaxial potentials show four main types of regular orbits, which are defined by the energy E and two non-classical integrals of motion I_2 and I_3. The right panel in this figure pictures box, z-tube, outer x- and inner x-tube orbits (from top left to bottom right; image taken from Statler 1987; edited). Axisymmetric and triaxial potentials can also host non-regular, chaotic orbits. In the case of chaotic orbits, the maximum possible number of conserved integrals of motion is not reached (chaotic orbits in axisymmetric potentials only conserve E and L_z (or L_x) and chaotic orbits in triaxial potentials only conserve E).
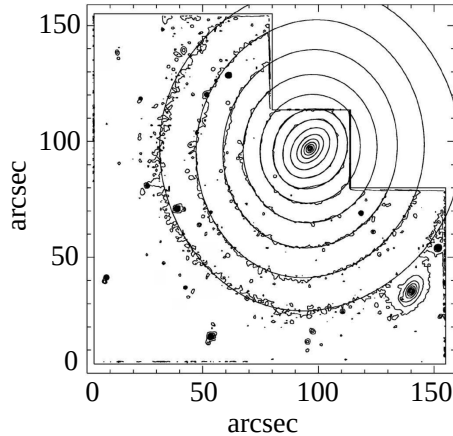
Figure 1.9: Isophotal twist in NGC 5831. From the inner isophotes to the outer isophotes, the elliptical galaxy NGC 5831 shows a position angle twist of ~ 35°. Such isophotal twists result from projection effects if the axis ratios of triaxial isodensity surfaces slowly change with radius. Isophotal twists are frequently observed in elliptical galaxies and can be seen as a tracer for triaxiality (image taken from Cappellari (2002); edited).

The age and metallicity of the stellar population inside the KDCs in many of the observed massive ETGs do not show any obvious difference in comparison to the surrounding stars (Davies et al. 2001; McDermid et al. 2006; Nedelchev et al. 2019; Kuntschner et al. 2010). Numerical ETG simulations revealed another explanation for the formation of kinematically counter-rotating cores, which can be caused as a result of merging events of similar mass progenitor galaxies, when the central supermassive black holes and the bound stellar nuclei experience orbital reversals during the infall (Rantala et al., 2019). In chapter 4, I will show that also complex KDCs as observed in the elliptical core galaxy NGC 5419 can be explained by a coherent flip of the rotation direction of stars on tube orbits at ~ 3 kpc distance from the galaxy center in combination with projection effects.

1.7   Formation scenario of ETGs

Besides the already discussed properties of the most massive ETGs, namely the boxiness of their isophotes, their slow rotation, high velocity dispersion, kinematic misalignments and triaxial shape, they stand out by a few other characteristic features which were already briefly mentioned in the previous sections and will be put into context here:
Bright ellipticals show high stellar population ages and high Mg/Fe ratios (the so-called α-enhancement). This points to a short star formation episode, which has taken place far back in time (e.g. Bower et al. 1992; Bender 1996, 1997; Thomas et al. 1999, 2005; Renzini 2006).
Moreover, Bender et al. (1987, 1989) revealed that boxy ellipticals are radio-loud and surrounded by gaseous X-ray halos, whereas disky ellipticals are not.
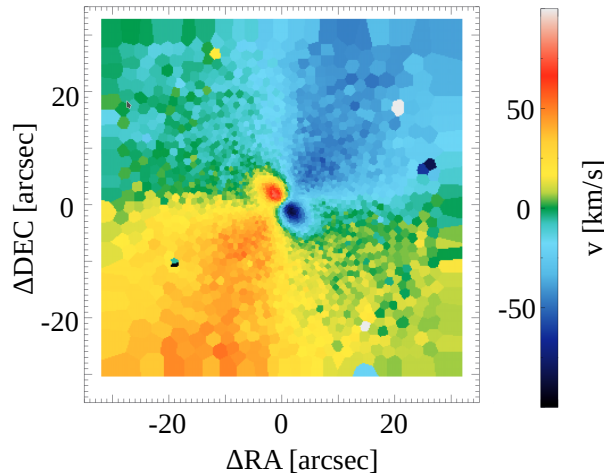
Figure 1.10: KDC in NGC 4365. In combination with isophotal twists and depleted stellar cores, triaxial galaxies frequently host kinematically decoupled cores (KDCs). The spectral observations of the early-type galaxy NGC 4365 with the Multi-Unit Spectroscopic Explorer (MUSE) at the Very Large Telescope (VLT) clearly show a kinematically distinct core (image taken from Nedelchev et al. (2019); edited).

And finally, Dressler (1980) discovered that there is a dependency between the environment and galaxy type, the so-called morphology-density relation. By studying the galaxy population in 55 rich clusters, Dressler (1980) found that the number of the massive ETGs – in contrast to spirals – increases with increasing density, i.e. the number of galaxies per unit volume. Accordingly, the majority of ETGs can predominantly be found in the densest regions in galaxy clusters.

These observed features combined form a consistent picture for the origin of the most massive ETGs. This picture describes a two-stage formation process, consisting of a rapid in-situ star-formation phase through infalling gas and an ex-situ mass accretion through gas-poor (dry) merging at $z \lesssim 2$ (e.g. Naab et al. 2009; Johansson et al. 2009, 2012; Oser et al. 2010; Moster et al. 2013; and see Naab & Ostriker 2017 for a review).

Our current understanding of galaxy formation and evolution (see e.g. Mo et al. 2010) begins with the Big Bang, after which small perturbations in the density field evolve with time via gravitational instability and form dark matter (DM) halos (see Figure 1.11). The primordial gas falls into these overdensities and loses energy via radiation. When the gas cloud inside the halo center becomes dense enough, it collapses into stars and forms stellar clusters. Since most of the gas is acquired by the largest dark matter halos, they quickly reach the critical mass of $M_{\text{crit}} = 10^{12} M_\odot$, at which further star formation is suppressed since further infalling gas becomes shock heated by the gravitational field (Rees & Ostriker 1977; Kereš et al. 2005; Dekel & Birnboim 2006; Cattaneo et al. 2006, 2008; Dekel & Birnboim 2008).

This can explain the old and α-enriched stellar population in ETGs at the high-mass end, whose progenitors are formed at this stage. The gas is supposed to keep its high
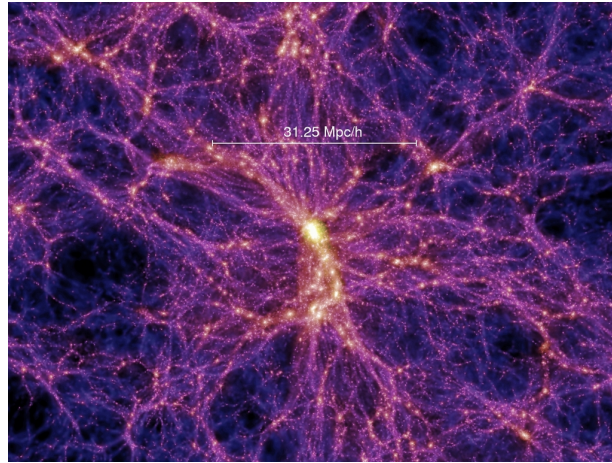
Figure 1.11: Hierarchical growth. According to the cold dark matter model, structure grows hierarchically initiated through gravitational instabilities from small primordial density fluctuations. Within the context of a growing dark matter halo, early-type galaxies have evolved through the successive mergers of progenitor galaxies. This image from the Millennium simulation (Springel, 2005) shows filaments within the cosmic web at redshift $z = 1.4$. The central high-density region represents a large dark matter halo which is seen as the birthplace of some of the earliest galaxies (image credits: https://www.mpa-garching.mpg.de).

temperature due to heating by additional accretion (Dekel & Birnboim 2006, 2008) and active galactic nuclei (AGN) feedback (Best, 2007) and can be observed as hot X-ray emitting gas in local massive and boxy ETGs (Bender et al. 1989). Such old ($z \gtrsim 2$) galaxies with evolved stellar populations and quenched star formation can be indeed found in observations, yet their size is a factor of 3–5 smaller compared to present-day ellipticals at similar masses (e.g. Daddi et al. 2005; Longhetti et al. 2007; Toft et al. 2007; Trujillo et al. 2007; van Dokkum et al. 2008; Saracco et al. 2009). When galaxy groups merge within the context of hierarchical growth to form massive clusters, dynamical friction will cause the most massive galaxies to sink to the center of the newly formed group. Due to their slow rotation and high mass, they will eventually merge and form a new and more massive remnant slow rotator. This picture corresponds to the high probability of massive ETGs to be found in the densest regions in galaxy clusters (Dressler, 1980). Moreover, such merging events are also able to explain the subsequent addition of stars at larger radii, explaining the strong size growth of ETGs since $z \sim 2$, especially when the mass ratio of the progenitor galaxies is minor, i.e. $M_1/M_2 \lesssim 1/3$ (so-called "minor-mergers"; Naab et al. 2009). The significant accretion of stars, which formed mainly in progenitors outside the main galaxy, can furthermore explain the high Sérsic indices of the SB profiles (see section 1.3.1; Hilz et al. 2013).

Besides, equal-mass merging events, so-called major mergers, serve as plausible formation scenario of the KDCs frequently observed in triaxial galaxies, as described in the previous

section 1.6.2 (Jesseit et al. 2007; Naab et al. 2007; Rantala et al. 2018). And finally, dry merger scenarios also provide an explanation for the formation of the stellar density core (as shown in section 1.3.1) in the most massive ETGs. The origin of the cores of ETGs has been related to the black hole core scouring process, where stars on radial orbits get close enough to the vicinity of a SMBH binary from a merger to experience a gravitational slingshot interaction and get kicked out from the center (Begelman et al. 1980; Hills & Fullerton 1980; Ebisuzaki et al. 1991; Milosavljević & Merritt 2001; Merritt 2006; Rantala et al. 2018; Nasim et al. 2021). The thereby constructed tangentially anisotropic central orbit distribution (see Figure 1.12) is reported to match between observations and numerical predictions (Thomas et al. 2014; Rantala et al. 2018; Mehrgan et al. 2019). By using high-resolution dissipationless N-body merger simulations (Rantala et al., 2018), Frigo et al. (2021) recently studied these processes in more detail and revealed that the core of ETGs forms in two phases during a dry merger scenario. First, the SMBHs of the progenitor galaxies rapidly sink to the center of the merger remnant due to dynamical friction, causing the surrounding stars to move to larger radii. This results in the 'missing stellar light' and the resulting flattened SB profile in the center. Afterwards, when the BHs formed a hard binary, stars on radial orbits, which get close enough to the center, experience gravitational slingshot interactions. This slowly changes the central orbit distribution from isotropic to tangential. The finding about the two distinct core formation phases, obtained by the analysis of simulations, has not been confirmed in observed galaxies so far.

As shown later in chapter 4, the elliptical galaxy NGC 5419 is a perfect candidate to study these processes based on real observational data, since this galaxy appears to be observed in the particularly interesting stage just between the two core formation phases. Indications for this galaxy to be in an earlier evolutionary state are its observed central double nucleus and depleted stellar core, yet still isotropic central orbit distribution, which is in contrast to the central tangential anisotropy typically observed in other core galaxies (as shown in Figure 1.12).

There are still unanswered questions and open research areas in the field of the formation history of ellipticals. For example, the previously described two-stage formation theory, consisting of in-situ star formation and ex-situ star accretion processes, suggests that the metallicity and stellar initial mass function, i.e. the initial distribution of stellar masses, radially changes within ETGs. Section 1.9.1 will explain in more detail how, in particular, the study of stellar initial mass function still presents open questions and current scientific challenges. This section will furthermore highlight the fact that accurate mass measurements and precise analyses of the most massive elliptical galaxies are yet to be conducted. For example, the found tangentially anisotropic orbit distribution has so far been only studied with axisymmetric models based on a limited sample of observed ETGs. The radial anisotropy profile of the most massive ETGs still needs to be analysed using triaxial models. The aim of this study is to establish the foundation for addressing such unresolved issues in this field.

In order to observationally confirm, detail, and expand the current picture of the formation scenario of elliptical galaxies, one must either study progenitor galaxies at high
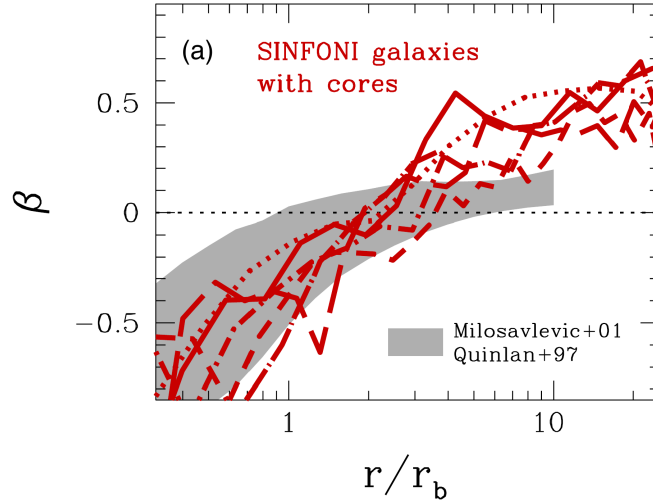
Figure 1.12: Central tangentially anisotropic orbit distribution in cored ETGs. The ratio of the radial and tangential component of a galaxy's orbit distribution can be described by the anisotropy parameter $\beta = 1 - \frac{\sigma_\theta^2 + \sigma_\phi^2}{2\sigma_r^2}$, which correlates the internal velocity dispersions in radial σ_r and tangential directions $\sigma_\theta, \sigma_\phi$ with each other. A tangentially biased orbit distribution results in negative β-values and an overpopulation of radial orbits results in positive β-values. The anisotropy parameter of a sample of core ETGs, which was observed with the integral field spectrograph SINFONI at the Very Large Telescope (VLT), is here plotted against the radius scaled by the galaxies' core radii r_b (red lines). As one can see, massive elliptical core galaxies characteristically show a tangentially biased central orbit distribution ($\beta < 0$). Within the evolutionary picture of ETGs that includes merging events, the central under-population of radial orbits can be explained by the BH scouring process, where stars on radial orbits get close enough to the BHs in order to experience slingshot interactions. The grey region shows the agreement with predictions from N-body simulations studying the core scouring process by equal-mass binary black holes (Quinlan & Hernquist 1997; Milosavljević & Merritt 2001; image taken from Thomas et al. (2014); edited).

redshifts, or analyse the characteristics of local remnants and search for relics hinting at their evolutionary path. In this respect, it turned out that the global properties of ETGs follow characteristic scaling relations, some of which are remarkably tight. Any established formation theory needs to be consistent with these scaling relations, which are the subject of the next section.

1.8   Properties and scaling relations of ETGs

1.8.1   Faber-Jackson relation

The first dynamical scaling relation for ETGs was discovered in the 70s by Faber & Jackson (1976), who found a correlation between the luminosity (in the B-band) L_B and central stellar velocity dispersion σ. This empirical Faber-Jackson relation is of the form

$$L_B \propto \sigma^n. \tag{1.19}$$

In its original definition, the slope n was determined as $n = 4$ but it has already been found early on that the slope for fainter ETGs is smaller and the slope for the brightest ETGs is slightly larger than this (e.g. Davies et al. 1983). Kormendy & Bender (2013) revised that the velocity dispersion of cored ellipticals increases much more slowly with the galaxy luminosity than for ellipticals without cores. Their found Faber-Jackson correlations (in the V-Band) are $L_V \propto \sigma^{3.74}$ for coreless galaxies and $L_V \propto \sigma^{8.33}$ for cored galaxies. Their observed relation is in agreement with what can be found in numerical simulations of dry major mergers as the dominant growth mode of ellipticals at the high-mass end.

The equivalent to the Faber-Jackson relation for spiral galaxies is the Tully-Fisher relation (Tully & Fisher, 1977), in which the velocity dispersion gets replaced by the galaxy's circular velocity.

1.8.2   Kormendy relation

Soon after the Faber-Jackson relation, another empirical relation between the mean surface brightness $< SB_e >$ within the effective radius r_e was found and reads

$$< SB_e >= a \log r_e + b, \tag{1.20}$$

with $a = 3.02$ and $b = 19.74$ for the B-band (Kormendy 1977; Hamabe & Kormendy 1987). The Kormendy relation states that larger ETGs have a fainter surface brightness at their effective radius than smaller ETGs.

1.8.3   The Fundamental Plane

Both laws, the Faber-Jackson and Kormendy relation, were later on discovered to be two projections of a plane in parameter space described by the properties of ETGs. According to this so-called Fundamental Plane (Djorgovski & Davis 1987; Dressler et al. 1987),

the three-dimensional parameter space consisting of the effective radius, central velocity dispersion and mean surface brightness at the effective radius is related as

$$\log r_e = \alpha \log \sigma + \beta < SB_e > +\gamma \qquad (1.21)$$

with $\alpha = 1.25$, $\beta = 0.32$ and $\gamma = -8.895$ for the B-band (Bender et al., 1998). The Fundamental Plane shows a tilt with respect to predictions from the virial theorem, which sets the gravitational mass M, velocity dispersion σ and the effective radius r_e in relation ($M \propto r_e \sigma^2$). A potential source for this tilt is the variation of the stellar mass-to-light ratio M_*/L with galaxy luminosity, caused by varying galaxy populations as well as structural non-homology (e.g. see Trujillo et al. 2004 and references therein).

1.8.4   Scaling relations between SMBHs and host galaxies

It is nowadays well known that massive black holes reside in the centers of ETGs. Within the last two decades, it turned out that also the BHs and their host galaxies hold fundamental relationships, hinting at a co-evolution between them. The black hole mass M_{BH} is proportional to the bulge luminosity L_{bulge} (Kormendy & Richstone 1995; Magorrian et al. 1998; Kormendy & Gebhardt 2001) as well as the galaxy's velocity dispersion σ outside the region influenced by the BH (Ferrarese & Merritt 2000; Gebhardt et al. 2000). Figure 1.13 shows the $M_{\mathrm{BH}} - \sigma$-relation for a sample of cored ETGs listed in Saglia et al. (2016) (black data-points) and the so far most massive measured BH in Holm 15A (red data-point; Mehrgan et al. 2019). The grey solid and dashed lines demonstrate the linear relation for cored ellipticals from Saglia et al. (2016) and McConnell & Ma (2013), which reads as

$$\log M_{\mathrm{BH}} = \alpha + \beta \log\left(\frac{\sigma}{200\mathrm{km/s}}\right), \qquad (1.22)$$

with $\alpha = 8.39$ and $\beta = 5.20$ (McConnell & Ma, 2013).

 Further insight into evolutionary processes linking the BHs and host galaxies was provided by the discovery of a tight correlation between M_{BH} and the 'missing stellar mass' inside the cores of massive ETGs (Kormendy & Bender, 2009). Figure 1.14 shows this correlation for all known ellipticals in the Virgo cluster plus non-members symbolised as open symbols from Kormendy et al. (2009).

 Moreover, dynamical models revealed that the sphere of influence r_{SOI} of black holes in core ellipticals almost exactly equals their core radius r_b (Thomas et al., 2016).

These findings support the core formation theory based on which the SMBHs are responsible for the construction of the depleted stellar density core (as already explained in section 1.7).

   The prerequisite for the black hole relations to allow for a correct study of the properties of BHs with respect to the evolution of their host galaxies is that the measurements of the relevant properties, in particular the black hole mass measurements, are bias-free. The
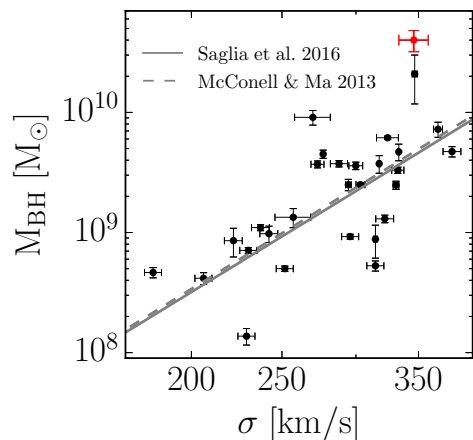
Figure 1.13: $M_{BH} - \sigma$-relation. The black hole masses M_{BH} of cored ETGs (black dots) are proportional to the galaxies' velocity dispersions σ. The red dot symbolises the most massive black hole found so far in Holm 15A. The grey lines correspond to the linear relations for cored ellipticals determined in Saglia et al. (2016) (solid line) and McConnell & Ma (2013) (dashed line). This image is taken from Mehrgan et al. (2019).
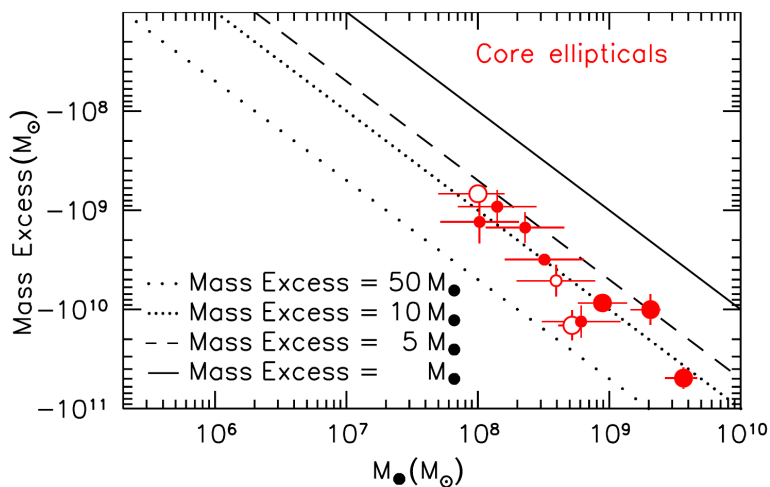
Figure 1.14: Correlation between stellar mass missing in cores and M_{BH}. The mass of the central missing light inside cores (here plotted as negative excess mass) tightly correlates with the black hole mass of ETGs, indicating that BHs and the formation of cores are closely related. The plotted sample consists of all known ellipticals in the Virgo cluster and additional non-members denoted by open symbols from Kormendy et al. (2009) (image is taken from Kormendy & Bender (2009); edited).

majority of the currently published black hole mass measurements are, however, based on dynamical models, which assume an axisymmetric shape as well as an edge-on inclination of the observed galaxy (see e.g. Gebhardt et al. 2003; Schulze & Gebhardt 2011; McConnell et al. 2011b,a, 2012; Rusli et al. 2011; Mehrgan et al. 2019). As it will be explained in more detail in the following section 1.9.1, these assumptions are – especially in the case of massive triaxial ETGs – invalid and can lead to non-negligible errors in the recovery of the black hole mass. The already mentioned fact that the Faber-Jackson relation 'saturates' for high-luminosity core ellipticals due to dissipationless mergers as their growth mode suggests a possible break in the $M_{\mathrm{BH}} - \sigma$-relation at the high-mass end. In order to accurately determine the exact slope of the $M_{\mathrm{BH}} - \sigma$-relation for the most massive ETGs, two requirements must be met. Firstly, a larger sample of black hole mass measurements at the high-mass end is necessary. Secondly, these BH mass measurements need to be based on precise *triaxial* modeling machineries, which are able to address all geometry complexities of the observed galaxy and which are able to recover the correct observational viewing angles.

Precise and bias-free black hole mass recoveries gained from accurate triaxial dynamical modeling machineries are moreover crucial in order to investigate whether the scatter in the black hole scaling relations, as e.g. visible in Figure 1.13, results from uncertainties in the black hole mass recoveries or if it is physical and hints to different formation mechanisms. The next section will list convincing arguments why in particular Schwarzschild models, which are able to deal with *triaxiality*, are necessary in this context in order to gain new scientific insights of massive ETGs.

1.9 Triaxial Schwarzschild modeling

1.9.1 The need for triaxial Schwarzschild models

Early implementations of Schwarzschild's orbit superposition technique were based on simplified assumptions of spherical symmetry (e.g. Richstone & Tremaine 1985; Rix et al. 1997). Since spherical assumptions do not hold for most galaxies, later implementations concentrated on axisymmetric potentials (e.g. van der Marel et al. 1998; Cretton et al. 1999; Gebhardt et al. 2000; Thomas et al. 2004; Valluri et al. 2004). When modeling ETGs at the high-mass end, however, also axisymmetric assumptions lead to biased results due to the triaxial nature of these objects. The application of axisymmetric models to a maximum triaxial galaxy showed that the stellar mass-to-light ratio can be biased up to 50% in extreme cases (Thomas et al., 2007a). Precise measurements of the stellar mass-to-light ratio, however, are crucial, in order to address scientific questions. In this context, a recently highly discussed issue has been the (non-)universality of the stellar initial mass function (IMF). The IMF describes the initial distribution of stellar masses inside a galaxy. To determine the IMF of our own Milky Way, one can directly count the stars. In the case of the Milky Way the IMF follows a Salpeter power law (Salpeter, 1955) ($dN(M) \propto M^{-x}dM$ with $x = 2.35$) for higher stellar masses ($M \gtrsim 0.5 M_{\odot}$) and shows a turnover to shallower

slopes at lower masses (Kroupa 2001; Chabrier 2003).

Since the individual stars in distant galaxies are not resolved, constraints on the IMF for galaxies beyond the Milky Way need to be measured indirectly. This can be done via different methods. One method is to fit stellar population synthesis (SSP) templates to absorption lines sensitive to the surface gravity of the stars (Spinrad, 1962). Another way is to determine a galaxy's stellar population by measuring its stellar mass-to-light ratio and comparing it to the ones from stellar population models. For this purpose, dynamical modeling can be used in order to determine the stellar mass-to-light ratio of the observed galaxy under study as a fit parameter. The stellar mass-to-light ratio can also be measured via gravitational lensing, where the distortion and magnification of the light from a background source give insight into the mass distribution of the foreground galaxy.

The IMF was for a long time believed to be universal among different kinds of galaxies. However, in recent years, studies utilizing the different mentioned methods repeatedly reported that the IMF depends on the galaxy mass or velocity dispersion and that the high-mass ETGs show the highest fraction of low-mass dwarf stars compared to the Milky Way like IMF (Treu et al. 2010; van Dokkum & Conroy 2010; Thomas et al. 2011; Cappellari et al. 2012; Spiniello et al. 2012; Conroy & van Dokkum 2012; Ferreras et al. 2013; La Barbera et al. 2013; Vazdekis et al. 2015; Smith et al. 2015; Lyubenova et al. 2016; Parikh et al. 2018). Such an IMF is called "bottom-heavy". Several measurements of the IMF furthermore point not only towards a non-universal IMF but also to a radially varying IMF within massive ETGs with a bottom-heavy IMF in the center and a Kroupa IMF at larger radii (Martín-Navarro et al. 2015; La Barbera et al. 2016; van Dokkum et al. 2017; Parikh et al. 2018; Domínguez Sánchez et al. 2019; Bernardi et al. 2019).

By comparing key absorption features of the stacked spectra of ETGs from the MaNGA (Mapping Nearby Galaxies at Apache Point Observatory) survey with stellar population models, Parikh et al. (2018) reveal a radially varying IMF where the radial IMF gradient within galaxies correlates with the stellar velocity dispersion. Their found local IMF-σ-relation is even steeper than the global relation with galaxy mass or velocity dispersion. The principal dependence of the radial IMF gradient with galaxy mass was independent of the used stellar population model, yet the absolute value of the IMF slope was model dependent.

Besides these not yet resolved uncertainties concerning the absolute value of the slope of the radial IMF gradient, there are other studies whose findings contradict the mentioned bottom-heavy nature and radial dependence of the IMF in massive ETGs. Alton et al. 2017, 2018 did not find any hints for radial IMF gradients in their sample of ETGs and Smith et al. (2015) and Collier et al. (2018) found a Kroupa IMF in nearby massive lensed ETGs.

In order to shine light on the mentioned remaining discrepancies and uncertainties concerning the IMF of ETGs, a detailed comparison between IMF constraints from independent methods, e.g. from SSP models and mass constraints from an accurately approved dynamical modeling machinery, is necessary. A study of the IMF with the help of dynamical models requires bias-free and accurate measurements of the M_*/L-ratio and an uncertainty of up to 50% due to wrong axisymmetry assumptions must be prevented by the implemen-

tation of precise triaxial routines.

A wrongly assumed mass-to-light ratio has further consequence in determining the mass of the central black hole. When modeling the mildly triaxial galaxy NGC 3379, van den Bosch & de Zeeuw (2010) find that the BH mass can be underestimated by 50% when using axisymmetric in comparison to triaxial models. Besides axisymmetric symmetry, another common simplification of dynamical models determining the black hole mass of ETGs was the already mentioned assumption of edge-on observations of galaxies (see e.g. Gebhardt et al. 2003; Schulze & Gebhardt 2011; McConnell et al. 2011b,a, 2012; Rusli et al. 2011; Mehrgan et al. 2019). Accurate triaxial dynamical modeling machineries, which aim for unbiased BH mass measurements due to correct geometry assumptions of the galaxy under study and which allow for a full recovery of the viewing angles, are therefore crucial in order to explore a possible revision of the exact slope of the BH scaling relations and to recover whether the scatter in BH scaling relations (see section 1.8.4 and Figure 1.13) could result from different BH growth mechanisms (Peng 2007; Hirschmann et al. 2010; Somerville & Davé 2015; Naab & Ostriker 2017).

1.9.2 Challenges in triaxial Schwarzschild models

The **triaxiality** of massive ETGs reduces the prevailing symmetry conditions and the fewer symmetry simplifications that can be adopted, the more complex and computationally expensive a dynamical model becomes. Since the uncertainty factor of ~ 2 for the stellar mass-to-light ratio and black hole mass recovery due to axisymmetric assumptions (as discussed in the previous section 1.9.1) is, however, not good enough to address scientific questions, like the IMF issue or exact measurements of BH scaling relations, the triaxial nature of ETGs *must* be targeted in a correct way.

Besides the triaxiality, the dynamical modeling of ETGs in general is associated with several challenging complexities, some of which are addressed in the following overview.

Dynamical models hold a variety of possible **degeneracies**, which are of different origin.

One potential source of uncertainties in dynamical models is the **degeneracy between the stellar and dark matter mass** distribution, where the latter one follows an **unknown dark matter halo shape**. E.g., when modeling galaxies from the Illustris (Vogelsberger et al., 2014) simulation with the triaxial Schwarzschild code from van den Bosch et al. (2008), Jin et al. (2019) find large stellar and dark matter mass uncertainties ranging from ~ 20 – 40%.

Another source of degeneracies is the fact that we can only ever observe the three-dimensional ETGs as a two-dimensional projection on the sky.

In order to construct a suitable density profile ν (see equation 1.10) as starting point for a dynamical model's luminous part of the assumed potential, a three-dimensional luminosity density has to be extracted from the two-dimensional surface brightness distribution. This issue, however, is not straightforward, since Rybicki (1987) proved that even in the axisymmetric limit, the **deprojection** of density distributions is not unique for all galaxies

observed at an inclination angle $i \neq 90°$, i.e. not seen edge-on. The reason for this is that several intrinsic densities result in an indistinguishable surface brightness when projected to the plane of the sky. In fact, the Fourier Slice Theorem holds a "cone of ignorance", inside which the Fourier transform of the surface brightness provides no information about the three-dimensional light distribution (Rybicki 1987; Gerhard & Binney 1996). For all axisymmetric galaxies observed at an inclination angle between $i \in [0°, 90°[$, the deprojection therefore becomes degenerate. This ambiguity becomes even more severe in the triaxial case. While parametric deprojection approaches generate fast and smooth solutions, non-parametric approaches provide a larger solution space of possible luminosity density distributions consistent with a given surface brightness. In this regard, de Nicola et al. (2020) developed a new triaxial semi-parametric deprojection code as an extended version based on the axisymmetric non-parametric deprojection routine by Magorrian (1999).

In addition to the two-dimensional projected surface brightness, the projected kinematic observations can also hold degeneracies, like the already mentioned well-known **mass-anisotropy degeneracy** (see section 1.3.2). The more information from the LOSVDs gets extracted, the better the mass-anisotropy degeneracy can get dissolved. Modern integral field-unit data and advanced kinematic LOSVD extraction techniques in principle allow for an extraction of the full LOSVDs in a non-parametric way (Bender 1990; Gebhardt et al. 2000; Mehrgan et al. 2019; Falcón-Barroso & Martig 2021). In order to overcome limitations of parametric methods (like the widely used Gauss-Hermite parameterisation), it therefore requires (i) precise enough kinematic observations, (ii) advanced LOSVD extraction codes and (iii) a dynamical modeling routine, which is able to process the full information contained in the LOSVDs.

Another challenge in the dynamical Schwarzschild modeling procedure is hidden in the **determination of the orbital weights** w_i as described in section 1.5.1. Since the number of integrated orbits N_{orbit} is usually much larger than the number of observational constraints N_{data}, the solving for w_i is ill-conditioned. Adding a **regularization** to the problem thereby can help to determine a unique orbit set w_i and to avoid overfitting. Finding a suitable regularization, which is chosen so that the data is well reproduced and simultaneously prevents the noise from being fitted, is not straightforward and a crucial part of the dynamical modeling procedure. The determination of w_i holds another degeneracy. When algorithmically picking out a single solution out of potentially many orbital sets w_i, which result in the same χ^2 (see equations 1.15 and 1.16), biased results cannot be excluded a priori. The relevant procedures implemented in Schwarzschild modeling techniques therefore require a general verification in order to guarantee that the parameters of interest are not severely affected by this.

Besides the determination of the orbital weights, the **construction of the orbit library** itself is one more tricky task within Schwarzschild's orbit superposition procedure. The main requirement of the orbit library is to representatively cover the phase space related to the given potential. The orbits' initial conditions therefore have to be sampled in such a way that the orbit library contains all orbital families, which can occur in the potential under study. Again, triaxial ETGs show a high complexity in this context. First, triaxial potentials host a variety of different orbit types (as shown in section 1.6.1), and second,

realistic triaxial potentials show a radially varying orbital structure, e.g. when the SMBH causes a more spherical shape of the potential in the center. A proper selection of initial conditions should allow for an automatic adaption to such radial changes.

While the best-fit model has been traditionally determined via a χ^2-minimization of the kinematic deviations (see equation 1.15), Lipka & Thomas (2021) and Thomas & Lipka (2022) convincingly demonstrated that the **determination of the best-fit model** is more challenging than previously expected. As described in section 1.5, the recovery of the intrinsic mass distribution and orbit structure, which represent the galaxy under study the best, requires the evaluation of several dynamical models with different parameters (i.e. the galaxy's viewing angles, the orbital weights, the stellar mass-to-light ratio, black hole mass and dark matter halo parameters). In this context, Lipka & Thomas (2021) and Thomas & Lipka (2022) showed that the intrinsic model flexibilities (i.e. the degrees of freedom) of their tested axisymmetric models with different parameters have a non-negligible impact on the comparison between their χ^2-values. The simplest description for this can be illustrated by the effect of the inclination on the model's flexibility. Dynamical models usually populate the stellar trajectories with a prograde as well as a retrograde version of the orbit. When a galaxy is seen edge-on, the model can distinguish between the orbits' velocity directions, which is not true in the case of a face-on observation. Consequently, the edge-on model shows increased flexibility, and with it a smaller χ^2-value, in comparison to the face-on model. Because of this, Thomas et al. (2007b) reported a surprisingly high amount of favored edge-on viewing angles, which were evaluated via a simple χ^2-minimization of their axisymmetric models of 17 ETGs. To avoid any bias and allow for a correct recovery of the inclination, Lipka & Thomas (2021) and Thomas & Lipka (2022) introduce a best-fit determination via a generalised information criterion $\mathrm{AIC_p} = \chi^2 + 2m_{\mathrm{eff}}$, which takes the model's degrees of freedom into account by computing the model's effective free parameters m_{eff}.

This list demonstrates some of the major challenges underlying the triaxial Schwarzschild modeling procedure. The complexity of the technique favors the occurrence of systematic uncertainties, which, however, need to be controlled in order to guarantee precise and accurate measurements. One way to address and rule out systematics is the extensive testing and application of the dynamical modeling machinery on highly precise simulated observations of a realistic galaxy. Besides that, even if all systematics can be excluded, it is so far unclear how much impact the degeneracies, which occur in this context, have on the uncertainty of the modeling results. While the resolution of today's telescopes allows for increasingly precise observational data, the question of which recovery accuracy dynamical models in principle can achieve has so far never been quantified. However, in order to answer scientific questions, e.g. about the (non-)universality of the IMF or the origin of the scatter and exact slope of BH scaling relations (see section 1.9.1), the knowledge about the generally achievable precision of dynamical models is required.

The dynamical Schwarzschild code SMART established in the course of this thesis is not only able to deal with the triaxial geometry of ETGs but it also handles the above-mentioned tricky challenges occurring in the context of Schwarzschild modeling with rigorous sensitiv-

ity. By application to several projections of an N-body merger simulation with a triaxial remnant galaxy including a SMBH, SMART's maximum possible recovery accuracy was extensively tested. Moreover, the application on the N-body simulation enabled to answer the question of how much the mentioned underlying degeneracies in principle affect the recovery accuracy of the intrinsic properties of triaxial ETGs. The crucial code implementations in SMART dealing with the above-listed challenges and the methodology for studying the underlying degeneracies and maximum possible recovery accuracy are summarized in section 1.10.3 below and will be extensively presented in chapters 2 and 3. However, before we focus on the aim and methodology of this thesis, the status quo of currently existing triaxial Schwarzschild codes from the literature are summarized in the following section.

1.9.3   Status quo of triaxial Schwarzschild models

At the time of this writing, only one existing triaxial Schwarzschild code, which is known from the literature, has been tested on triaxial simulation data and applied to real observations from triaxial ETGs. This code by van den Bosch et al. (2008) executes the deprojection as well as the computation for the potential and forces via the Multi Gaussian Expansion (MGE) method from Cappellari (2002). The sampling of the initial conditions in this code follows a recipe, which was originally generated for an application to triaxial separable potentials. Since such potentials show unnatural central cores, additional initial conditions resulting in a sufficient amount of box orbits have to be set up supplementarily. In order to reduce noise, the initial conditions of their so constructed orbits get dithered. After fitting the modeled Gauss Hermite moments from the LOSVDs to the observed ones, the best-fit model is determined via χ^2-minimization.

As already briefly stated in section 1.9.2, Jin et al. (2019) modeled different projections of nine triaxial early-type galaxies from the high-resolution Illustris simulation in order to evaluate the capability of this Schwarzschild code. Averaged over several mock data sets, they find a recovery uncertainty of the total enclosed mass within the effective radius of 15% with a maximum deviation of 36%. Depending on the choice of the DM halo shape, the stellar mass gets underestimated by $13-24\%$ and the dark matter mass overestimated by $18-38\%$. There was no recovery of black holes included in this study.

The importance of extensive testing and evaluation of dynamical modeling codes by application to appropriate mock data got re-emphasized when Quenneville et al. (2022) reported a bug in the code by van den Bosch et al. (2008), which was caused by incorrectly projected orbits.

1.10   This thesis

1.10.1   The aim of this thesis

The aim of this thesis is to establish a new dynamical modeling framework in which the best possible recovery accuracy of the intrinsic structure and mass composition of triaxial

early-type galaxies can be studied and achieved and furthermore to analyse the elliptical galaxy NGC 5419 with it. For this, I apply a new triaxial dynamical Schwarzschild modeling code called `SMART` to –first– several projections of a realistic, high-resolution N-body merger simulation with a triaxial remnant hosting a SMBH and –afterwards– the real observational data of the elliptical galaxy NGC 5419. Modeling a realistic simulated early-type galaxy with `SMART` does not only allow to debug, improve and refine the modeling routine `SMART`, but also to study the impact of degeneracies and the strength of the Schwarzschild method in general.

This study moreover allows us – for the first time – to analyse in detail how accurately the supermassive black hole mass of a triaxial galaxy can be recovered with triaxial dynamical modeling.

In principle, one can study the black hole mass recovery precision of a dynamical model by applying it to a realistic simulation for which the mass parameters are known, or one can compare the dynamical modeling results with black hole mass determinations from other measurement techniques.

Siopis et al. (2009), for example, compared their BH mass recovery of the spiral galaxy NGC 4528 from axisymmetric dynamical models to the BH mass determination from the kinematics of water masers and the mass determination of the BH in M 87 from axisymmetric models by Gebhardt & Thomas (2009) was recently verified through the very first image of a supermassive black hole from the Event Horizon Telescope (EHT; Event Horizon Telescope Collaboration et al. 2019). The Schwarzschild modeling code `FORSTAND` by (Vasiliev & Valluri, 2020), which is in principle able to deal with any geometry including triaxiality, has so far been tested by application to distribution-function-based axisymmetric disk models with and without bars (Vasiliev & Valluri, 2020), where the 3D shape was provided. However, no strong constraints on the SMBH mass could be reached.

By applying `SMART` to a realistic and high-resolution numerical merger simulation with a triaxial remnant hosting a SMBH throughout this thesis, we provide the first detailed study of black hole mass recoveries from an N-body simulation with triaxial Schwarzschild modeling.

Throughout this thesis, `SMART` has become an extensively tested and rigorously evaluated triaxial Schwarzschild code. This sets the basis to reliably study and interpret the modeling results of real observational data.

1.10.2   Scientific motivation

This thesis concentrates on the study of early-type galaxies at the high-mass end. Even though the intrinsic characteristics of ETGs – like their triaxial shape, diverse orbit structure and central SMBHs – make these galaxies particularly complex and difficult to model (cf. section 1.9.2), the recovery of their orbit and mass structure provides worthwhile insights. The facts that their IMF appears to show the highest deviation in comparison to the one of our home galaxy (see section 1.9.1) and that they host the most massive black holes found in the local universe, involve the potential to gain new insights, in particular into the understanding of galaxy formation and evolution. Some of the still open questions

are: What exactly does the stellar initial mass function of ETGs look like and does it vary with radius? What is the slope of BH scaling relations at the high-mass end? What is the origin of the non-negligible scatter in current BH scaling relations?

Unlike other studies, which focus on evaluating a global overview of the properties of a large sample of ETGs, the focus of this thesis concentrates on the study of individual objects with the highest possible precision.

So far, no study found in the literature addresses the question of how much the degeneracies – both hidden in the data and the dynamical modeling procedure of triaxial ETGs – limits the accuracy of measurement results, like the black hole mass, stellar mass-to-light ratio or anisotropy profile. When studying the statistical properties of large samples of galaxies, more focus is put on time-saving and computationally efficient methodologies than on the precision of the modeling machinery and observational data. In contrast to this, the motivation of this thesis is to exploit the full capacity of today's technologies in order to recover the properties of individual ETGs with the maximum achievable accuracy. By establishing a highly precise dynamical modeling code and combining it with high-resolution data and next-generation data analysis strategies, this thesis is able to set a state-of-the-art reference recovery accuracy of ETGs and it allows to evaluate the limits of the degeneracies involved therein.

The so accomplished new dynamical modeling machinery is then applied to high-resolution observational data of the deliberately chosen elliptical galaxy NGC 5419. This galaxy is particularly interesting to study, since observations hint at a central double nucleus. Dynamically modeling this galaxy is therefore motivated by promising new insights about an evolutionary state of NGC 5419 that appears to differ compared to ordinary ETGs.

1.10.3 The methodology

While computationally cheaper methods, like the Jeans modeling approach (see section 1.5), would be suitable for the analysis of a larger sample, the demand of this thesis requires the more time-consuming complexity of Schwarzschild's orbit superposition technique.

In order to be able to probe the maximum possible recovery accuracy of the most massive ETGs, the new triaxial dynamical modeling code `SMART` has implemented several unique and advanced features:

- `SMART` is able to process any 3D tabulated stellar density input, e.g. as provided by the semi-parametric triaxial deprojection code `SHAPE3D` by de Nicola et al. (2020).

- `SMART` computes the potential by expansion into spherical harmonics. This allows dealing with realistic non-parametric densities and halos.

- `SMART` launches thousands of orbits from a five-dimensional starting space to representatively sample all orbital shapes, in particular near-Keplerian orbits in galaxy centers. This allows an adaption to realistic changes in the gravitational potential

and the corresponding integrals-of-motion space, e.g. when the potential becomes
more spherical in the center due to the SMBH.

- `SMART` exploits the whole information from the full non-parametric LOSVDs. This
  provides more constraints on the dynamical model than using only the Gauss-Hermite
  moments (see section 1.3.2).

- `SMART` uses a generalised information criterion AIC_p (see section 1.9.2) to optimise
  the strength of regularization and to determine the best-fit model. This avoids biases
  when comparing different mass models with varying model flexibilities.

In order to verify that the newly developed modeling method is working bias-free and
to study the maximum accuracy which can be achieved when modeling two-dimensional
data of a triaxial galaxy, I applied `SMART` to the high-resolution numerical merger simula-
tion by Rantala et al. (2018). The simulation consists of a collisionless dark matter halo,
a collisionless stellar component and supermassive black holes, whose collisional interac-
tions with the stars are accurately computed via a regularised integration scheme (Rantala
et al., 2018). The simulation's triaxial remnant resembles the early-type galaxy NGC 1600
(Thomas et al. 2016). Its similarity to a real galaxy, its high resolution and the fact that
it precisely computes the dynamics close to the SMBH make this simulation most suitable
for this thesis.

To recover the intrinsic orbit and mass structure of NGC 5419, the beforehand ex-
tensively approved triaxial dynamical modeling code `SMART` is applied to high-resolution
Multi-Unit Spectroscopic Explorer (MUSE) spectral observations. The deprojection of
the surface brightness profile gained from HST observations is done by using the semi-
parametric triaxial deprojection code `SHAPE3D` (de Nicola et al., 2020). `SMART` processes
the full information contained in the LOSVDs, which are provided in a non-parametric
way by a novel spectral fitting code called WINGFIT (Thomas et al., in prep).

1.10.4 Outline and main findings

In chapter 2, I introduce the most important features of `SMART` in more detail and apply it
to several projections of the N-body merger simulation. This study focuses on the intrinsic
uncertainty of the dynamical modeling procedure alone, i.e. the true viewing angles and
the three-dimensional stellar luminosity profile are provided. This allows to discover the re-
covery precision of the intrinsic orbit structure and mass parameters from typical kinematic
data, independent of deprojection uncertainties. In this specific study, also the normalized
DM halo shape from the simulation is forwarded to `SMART`. I demonstrate that, given the
right deprojection and DM halo shape, `SMART` is able to reproduce the correct anisotropy
profile, black hole mass and stellar mass-to-light ratio of the tested ETG merger simulation
with an unprecedented precision of $5 - 10\%$. This strongly suggests that two-dimensional
projected kinematic data hold only minor degeneracies, provided that the deprojection is
known. I moreover show that the recovery of the macroscopic parameters of interest is not

notably affected by the degeneracy remaining in the reconstruction of the orbit distribution function, in particular, the determination of the orbital weights. This chapter is published as Neureiter et al. (2021).

To estimate the recovery accuracy and degeneracy uncertainties, which can be expected for a complete observational analysis, chapter 3 shows the application of SMART to the N-body simulation with the inclusion of a preceding deprojection of the simulated projected surface brightness as well as a fit of an unknown parameterised DM halo. For the deprojection, the semi-parametric triaxial code SHAPE3D by (de Nicola et al., 2020) is used. For this complete setup, I demonstrate that the triaxial N-body merger remnant's correct black hole mass, stellar mass-to-light ratio and total enclosed mass (inside the half-light radius) can again be reproduced with an unexpectedly high accuracy of $5-10\%$. This unprecedentedly high level of accuracy proves the powerful capacity of the Schwarzschild method in principle. It also highlights that the degeneracies, which are hidden in the dynamical modeling of two-dimensional kinematic data, have little impact on the reproduction of the dynamical structure and mass composition of a typical ETG, even if the deprojection is unknown a priori. This chapter is published as Neureiter et al. (2023a).

These preparatory investigations and recoveries from chapters 2 and 3 provide the basis for modeling real observational data with the newly developed modeling machinery. This is presented in chapter 4. Here, I apply the triaxial deprojection code SHAPE3D and Schwarzschild code SMART to Hubble Space Telescope (HST) photometric observations and high-signal MUSE spectral observations from the elliptical core galaxy NGC 5419. This ETG is particularly interesting because its observational data suggest the presence of a central double nucleus. When modeling NGC 5419, I recover an isotropic central orbit distribution, which is highly unusual for core ETGs. In this chapter, I provide a plausible explanation for the observational features of NGC 5419 by proposing that this galaxy is observed at an early stage of core formation. I moreover demonstrate that the galaxy's kinematically decoupled core can be explained by a rotation flip in tube orbits in combination with the projected overlay of tube orbits rotating around two different axes. This chapter is published as Neureiter et al. (2023b).

Chapter 2

SMART: A new implementation of Schwarzschild's Orbit Superposition technique for triaxial galaxies and its application to an N-body merger simulation

Bibliographic information

Author's contribution

For this publication, I evaluated all kinematic data and density information from the used N-body simulation, which are forwarded as input to the modeling routine SMART. I performed all dynamical models and evaluated the corresponding analyses relevant for this paper. As the first author, I have written the main parts and created all plots shown in this paper except for the uniqueness analysis, which was done by J. Thomas. J. Thomas furthermore contributed to this work with several input ideas for analyses, supportive discussions, supplementary text passages and text corrections. In the course of this study, I have repeatedly corrected, changed and optimized the triaxial modeling code SMART whose original version called SCHERPA was written by F. Finozzi based on the axisymmetric

progenitor code by J. Thomas. The parallelisation of the original Schwarzschild code was mainly done by A. Krukau. R. Saglia and R. Bender were responsible for initiating the idea for this paper and supported the work with valuable discussions as well as text corrections.

Copyright notice

SMART: a new implementation of Schwarzschild's Orbit Superposition technique for triaxial galaxies and its application to an *N*-body merger simulation

B. Neureiter [ID],[1]★ J. Thomas,[1,2] R. Saglia,[1,2] R. Bender,[1,2] F. Finozzi, A. Krukau,[3,4] T. Naab,[5] A. Rantala [ID][5] and M. Frigo [ID][5,6]

[1]*Max-Planck-Institut für Extraterrestriche Physik, Giessenbach-Str. 1, D-85748 Garching, Germany*
[2]*Universitäts-Sternwarte München, Scheinerstrasse 1, D-81679 München, Germany*
[3]*Leibniz-Rechenzentrum (LRZ), Boltzmannstrasse 1, D-85748 Garching, Germany*
[4]*Excellence Cluster Universe, Boltzmannstrasse 2r, D-85748 Garching, Germany*
[5]*Max-Planck-Institut für Astrophysik, Karl-Schwarzschild-Str. 1, D-85748 Garching, Germany*
[6]*Excellence Cluster ORIGINS, Boltzmannstrasse 2, D-85748 Garching, Germany*

ABSTRACT

We present SMART, a new 3D implementation of the Schwarzschild Method and its application to a triaxial *N*-body merger simulation. SMART fits full line-of-sight velocity distributions to determine the viewing angles, black hole, stellar and dark matter (DM) masses, and the stellar orbit distribution of galaxies. Our model uses a 5D orbital starting space to ensure a representative set of stellar trajectories adaptable to the integrals-of-motion space and it is designed to deal with non-parametric stellar and DM densities. SMART's efficiency is demonstrated by application to a realistic *N*-body merger simulation including supermassive black holes that we model from five different projections. When providing the true viewing angles, 3D stellar luminosity profile and normalized DM halo, we can (i) reproduce the intrinsic velocity moments and anisotropy profile with a precision of ~ 1 per cent and (ii) recover the black hole mass, stellar mass-to-light ratio and DM normalization to better than a few per cent accuracy. This precision is smaller than the currently discussed differences between initial-stellar-mass functions and scatter in black hole scaling relations. Further tests with toy models suggest that the recovery of the anisotropy in triaxial galaxies is almost unique when the potential is known and full LOSVDs are fitted. We show that orbit models even allow the reconstruction of full intrinsic velocity distributions, which contain more information than the classical anisotropy parameter. Surprisingly, the orbit library for the analysed *N*-body simulation's gravitational potential contains orbits with net rotation around the intermediate axis that is stable over some Gyrs.

Key words: methods: numerical – galaxies: elliptical and lenticular, cD – galaxies: evolution – galaxies: structure – galaxies: supermassive black holes – stars: kinematics and dynamics.

1 INTRODUCTION

Early-type galaxies (ETGs) have long been believed to emerge from collisions between other smaller progenitor galaxies (first proposed by Toomre & Toomre 1972), but nowadays it is clear that their formation history is more complex (e.g. Oser et al. 2010). Their structural and kinematic properties divide them into (1) fainter (absolute magnitude $M_B > -20.5$) and coreless fast rotators that are nearly axisymmetric and have discy-distorted isophotes and (2) brighter and more massive slow rotators with flat cores, which are moderately triaxial and have boxy-distorted isophotes (Faber et al. 1987; Bender 1988a; Bender et al. 1989; Kormendy & Bender 1996; Cappellari et al. 2007; Emsellem et al. 2007). For the formation of fainter elliptical galaxies, dissipational processes are believed to be important (e.g. Bender, Burstein & Faber 1992; Barnes & Hernquist

1996; Genzel et al. 2001; Tacconi et al. 2005; Cappellari et al. 2007; Hopkins, Cox & Hernquist 2008; Johansson, Naab & Burkert 2009), whereas the latest evolutionary phases in the formation of massive ellipticals are dominated by collisionless processes (e.g. Naab, Jesseit & Burkert 2006; Cappellari 2016; Naab & Ostriker 2017; Moster, Naab & White 2019).

In general, these merging events modify the potential structure and populate a rich diversity of stellar orbits (Röttgers, Naab & Oser 2014). The intrinsic shape and orbital structure of such galaxies are not directly observable. Instead, sophisticated dynamical models are needed to process kinematic and photometric observational data to extract all the information about the orbital structure and internal composition of the galaxy.

Dynamical models are based on the collisionless Boltzmann equation that governs the motion of stars in elliptical galaxies. Dynamical models that go beyond the recovery of velocity moments and aim at reconstructing the entire galaxy structure, additionally take advantage of the Jeans theorem (e.g. Binney & Tremaine

★ E-mail: bneu@mpe.mpg.de

2008). This implies that the distribution function, which is the most general description of a system of stars, is constant along individual trajectories in phase space. In this regard, Schwarzschild (1979) pioneered an orbit superposition technique, where the equations of motion are numerically integrated for a finite number of stellar trajectories embedded in an assumed gravitational potential with contributions from the stars and possibly dark components. The weighted superposition of the orbits is determined for which the surface brightness and projected velocity distributions of the model match the observed ones in a least squares sense (e.g. Richstone & Tremaine 1984). Besides the orbital weights, all unknown quantities like the central black hole mass and dark matter distribution are varied between different models. The model producing the best fit to the projected velocity distributions is then associated with the correct model parameters. Any galaxy in a steady state can be modelled by Schwarzschild's orbit superposition technique. In order to determine both, the mass and internal motions of the stars, and solve an underlying mass-anisotropy-entanglement, one needs to describe the deviation of the observed absorption lines from a Gaussian profile by additional Gauss–Hermite functions of at least third and fourth order (Gerhard 1993; van der Marel & Franx 1993; Bender, Saglia & Gerhard 1994), or, preferably if the signal-to-noise ratio permits, measure the line shape non-parametrically (e.g. Mehrgan et al. 2019).

Early applications of Schwarzschild's orbit superposition technique concentrated on spherical models (e.g. Richstone & Tremaine 1985; Rix et al. 1997). Since the simplified assumption of spherical symmetry is not true for most galaxies, later applications of Schwarzschild's orbit superposition technique assumed axisymmetry (e.g. van der Marel et al. 1998; Cretton et al. 1999; Gebhardt et al. 2000; Thomas et al. 2004; Valluri, Merritt & Emsellem 2004).

However, it is nowadays known that the most massive galaxies are neither spherical nor axisymmetric but triaxial objects. Observational indications are provided by isophotal twists in the surface brightness distribution, velocity anisotropy, minor axis rotation, kinematically decoupled cores, and the statistical distribution of the ellipticity of the isophotes (Illingworth 1977; Bertola & Galletta 1978, 1979; Schechter & Gunn 1978; Williams & Schwarzschild 1979; Bender 1988b; Franx & Illingworth 1988; Vincent & Ryden 2005). Schwarzschild (1979) proved the existence of self-consistent triaxial stellar systems in dynamical equilibrium with numerical orbit superposition models. Also, *N*-body simulations supported the idea of triaxial ellipsoidal stellar bulges and dark matter haloes (e.g. Aarseth & Binney 1978; Hohl & Zang 1979; Miller & Smith 1979; Barnes 1992; Jing & Suto 2002; Naab & Burkert 2003; Bailin & Steinmetz 2005).

High-mass galaxies are of particular interest in several astrophysical aspects, e.g. the stellar initial mass function (IMF) is discussed to vary among galaxies, with the largest excess stellar mass compared to the locally measured Kroupa (Kroupa 2001) or Chabrier (Chabrier 2003) IMF occurring in the most massive galaxies (e.g. Treu et al. 2010; van Dokkum & Conroy 2010; Thomas et al. 2011; Cappellari et al. 2012; Posacki et al. 2015; Smith, Lucey & Conroy 2015; Vazdekis et al. 2015; Parikh et al. 2018). Moreover, different growth models for supermassive black holes (SMBHs) predict different amounts of intrinsic scatter at the high-mass end of SMBH scaling relations (e.g. Peng 2007; Jahnke & Macciò 2011; Somerville & Davé 2015; Naab & Ostriker 2017). In order to address these questions, precision dynamical mass measurements of the stars and SMBHs are required and these are directly linked to triaxial modelling to avoid artificial scatter introduced by wrong symmetry assumptions. Thomas et al. (2007) showed that the stellar mass-to-light ratio (and, thus, indirect inferences about the IMF) can be biased by up to

50 per cent in extreme cases when using axisymmetric models for a maximally triaxial galaxy. Moreover, a wrongly assumed mass-to-light ratio influences the determination of the mass of the central black hole in the model. The work by van den Bosch & de Zeeuw (2010) suggests that the assumption of axisymmetry may bias black hole measurements in massive ellipticals. They find that the best-fitting black hole mass estimate doubles when modelling NGC 3379 with their triaxial code (van den Bosch et al. 2008) in comparison to axisymmetric models. Triaxial dynamical modelling routines are therefore required to recover unbiased stellar mass-to-light ratios and black hole masses with the best possible accuracy.

To understand the uncertainties and ambiguities of triaxial modelling one has to understand the following three essentially different effects:

1) The intrinsic uncertainty of the applied dynamical modelling algorithm, which can only be tested under circumstances where the solution is designed to be unique. This is one of the aspects covered in this paper.

2) The uncertainty in the reconstruction of orbital and mass parameters from typical observational data given the right deprojection, which is also addressed in this paper.

3) The uncertainty of the deprojection routine. This topic is covered in de Nicola et al. (2020).

All previously described effects need to be combined to evaluate the uncertainties in the whole modelling process. This will be investigated in a future paper.

So far, there exist two dynamical modelling codes using Schwarzschild's orbit superposition technique dealing with triaxiality by van den Bosch et al. (2008) and Vasiliev & Valluri (2019). Their estimated precision and efficiency will be later mentioned in the discussion. In this paper, we present our newly developed triaxial Schwarzschild code called SMART ('Structure and MAss Recovery of Triaxial galaxies') and test the code on a realistic high-resolution numerical merger simulation including SMBHs by Rantala et al. (2018).

This paper is structured as follows. We introduce SMART and describe its specific benefits in Section 2. We then discuss the most important aspects for choosing this particular simulation in Section 3. In this section, we furthermore explain all relevant steps to extract the data needed for modelling the simulation. In Section 4, we will show the results of these models. Section 5 deals with the quasi-uniqueness of the anisotropy recovery when fitting full line-of-sight velocity distributions (LOSVDs). This is followed by a short discussion about remaining sources of systematics and comparison to other triaxial modelling codes in Section 7. We summarize our results and conclusions in Section 8.

2 TRIAXIAL SCHWARZSCHILD CODE SMART

SMART ('Structure and MAss Recovery of Triaxial galaxies') is a fully 3D orbit superposition code based on the axisymmetric code of Thomas et al. (2004) and its original extension to three dimensions and non-axisymmetric densities by Finozzi (2018). It is written in FORTRAN 90/95 (Brainerd et al. 1996). SMART follows the classical Schwarzschild method consisting of the computation of the potential and forces for a given density, the setting up of an orbit library and the subsequent superposition of the orbits.

In the following sections, we will explain in more detail how SMART creates self-consistent density-, potential-, and orbit-configurations and how we weight the orbits in order to fit the input density and velocity structure. One main feature of our code is that
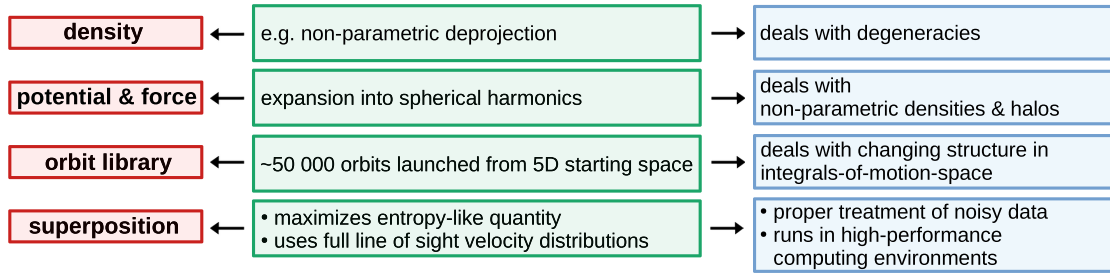
Figure 1. Our implemented triaxial Schwarzschild Modelling code SMART follows the classical Schwarzschild Modelling routine (red panels), but it is unique in calculating the potential by expansion into spherical harmonics, setting up an adaptive orbit library and computing the orbit superposition by maximizing an entropy-like quantity (green panels). This results in specific advantages (blue panels), e.g. that our code is able to deal with realistic changes in the gravitational potential, e.g. when the SMBH causes a more spherical potential in the centre. Our orbit library is adaptive and responds to changes in the integrals of motion. SMART can process density output from any deprojection routine, e.g. a non-parametric deprojection dealing with degeneracies.

it uses a 5D starting space for the orbit library to adapt to potentials with a radially varying structure of the integrals-of-motion space. Fig. 1 gives a schematic overview of the code's main modules and the benefits of their specific implementation.

2.1 Coordinate systems and binning

We use two different coordinate systems to describe the intrinsic and projected properties of a galaxy. To transform between the intrinsic coordinates (x, y, z), adapted to the symmetry of the object, and the coordinates (x', y', z') adapted to the sky projection, two matrices P and R are used:

$$\begin{pmatrix} x' \\ y' \\ z' \end{pmatrix} = R \cdot P \cdot \begin{pmatrix} x \\ y \\ z \end{pmatrix}, \tag{1}$$

with

$$R = \begin{pmatrix} \sin\psi & -\cos\psi & 0 \\ \cos\psi & \sin\psi & 0 \\ 0 & 0 & 1 \end{pmatrix} \tag{2}$$

and

$$P = \begin{pmatrix} -\sin\varphi & \cos\varphi & 0 \\ -\cos\vartheta\cos\varphi & -\cos\vartheta\sin\varphi & \sin\vartheta \\ \sin\vartheta\cos\varphi & \sin\vartheta\sin\varphi & \cos\vartheta \end{pmatrix}. \tag{3}$$

P and its corresponding viewing angles ϑ and φ project to the plane of the sky with z' being the line of sight. R and its corresponding rotation angle ψ rotate the coordinates x' and y' in the plane of the sky along z'. If not stated otherwise, the intrinsic long axis is hereafter assumed to coincide with x, the intrinsic intermediate axis with y and the intrinsic short axis with z.

SMART works with a cell structure based on spherical coordinates. Intrinsic properties like the stellar or dark matter distribution or individual orbital properties are integrated over small cells in configuration and/or velocity space. We use a linear sampling for the longitude $\theta \in [-90°, 90°]$ and the azimuth $\phi \in [0°, 360°]$. Radial bins are spaced in even intervals of the radial binning index

$$i_r = \frac{1}{a}\log\left(c + \frac{a}{b}r\right). \tag{4}$$

The constant c allows to adapt the central binning scheme from logarithmic ($c = 0$) to linear ($c = 1$). The constants a and b are determined once the radial extent of the library $r_{min} \leq r \leq r_{max}$ and

the number of radial bins N_r are set and they are chosen so that the minimum radius r_{min} lies within the first radial bin and the maximum radius r_{max} in the last one (see also Siopis et al. 2009).

Similar to the spatial properties, the LOSVDs are integrated over small cells in phase space given by the spatial pattern of the observations (e.g. Voronoi bins; Cappellari & Copin 2003) and the velocity resolution of the LOSVD data. Like its axisymmetric predecessor (Thomas et al. 2004), the code uses the entire information contained in the full LOSVDs. See Sections 3.1.3 and 3.1.4 for more details.

2.2 Density and potential

The total gravitational potential

$$\Phi = \Phi_* + \Phi_{DM} + \Phi_{SMBH} \tag{5}$$

is composed as the sum of a Keplerian contribution from a supermassive black hole (Φ_{SMBH}) and the contributions from the stars (Φ_*) and dark matter (Φ_{DM}). SMART allows to use non-parametric densities for both the stars and the dark matter. The stellar density is generally assumed to be provided in 3D tabulated form (as for example returned from a non-parametric deprojection, e.g. de Nicola et al. 2020). The same holds for the dark matter halo. However, the code can also run with quasi-parametric deprojections (e.g. Multi Gaussian Expansion or MGE models, Monnet, Bacon & Emsellem 1992; Emsellem, Monnet & Bacon 1994; Cappellari 2002). It can also run with parametric dark matter haloes (e.g. NFW profiles; Navarro, Frenk & White 1996).

The solution to the Poisson equation is obtained with the help of an expansion in spherical harmonics (Binney & Tremaine 2008). For this, the stellar and dark matter density are individually interpolated by first performing a bi-linear interpolation among the elevation and azimuthal angle bins and afterwards a linear interpolation among the logarithm of the radial bins. For integrating these interpolated densities we use a 10-point Gaussian quadrature algorithm from Press et al. (1996). The advantage of calculating the potential by expansion into spherical harmonics in comparison to other techniques, e.g. by using the MGE method, is its ability to deal with non-parametric densities and haloes.

2.3 Orbit library

Every orbit in a gravitational potential is uniquely defined by its integrals of motion (e.g. Binney & Tremaine 2008). The number of (isolating) integrals of motion depends on the given potential.

Furthermore, every integral of motion reduces the dimensionality of the trajectories of the stars in the galaxy. Regular potentials admit in general three integrals of motion, one of which being the energy E. In the axisymmetric case, another classical integral is known explicitly: the z-component of the angular momentum, L_z. The third integral, I_3, is usually not known explicitly. In the general triaxial case, only the energy is given explicitly. Near the central SMBH, however, the potential becomes more and more Keplerian and the number of isolating integrals of motion in a Keplerian potential is five. An example for a system in an almost Keplerian potential that is described by a five-integral distribution function is the asymmetric disc in the centre of M31 (Bender et al. 2005; Brown & Magorrian 2013). Since our code is not restricted to axisymmetric or triaxial symmetries, we aim for a 5D starting space for the stellar orbits, which we gain by systematically sampling E, L_z, v_r, r, and ϕ. The details of the initial conditions sampling technique are described in Section C.

In total, SMART sets up and integrates ~50 000 orbits for 100 surfaces of section (SOS) crossings, i.e. for 100 crossings of the equatorial plane in upwards direction (for a more detailed description of SOS, see Appendix C). This number of orbits was intentionally chosen to be higher than in the axisymmetric predecessor code of Thomas et al. (2004) to address all necessary complexities given by, e.g. a radially changing structure in the integrals-of-motion space. Moreover, this amount of orbits proves to be sufficient to directly recover the (phase-space) density without any dithering of orbits in the starting space.

If the potential at hand is, e.g. axisymmetric, then all orbits conserve L_z and precess around the rotation axis. In this case, the orbits will fill the ϕ dimension automatically. Likewise, orbits will be represented by invariant curves in the (r, v_θ)-plane, due to the conservation of I_3. Hence, when sequentially sampling the orbital launch conditions, the dimension of the submanifold containing all the orbital initial conditions that are not yet represented shrinks automatically, according to the number of integrals of motion provided by the gravitational potential under study.

Since, in general, triaxial potentials have three integrals of motion, a 2D starting space at a given energy (de Zeeuw 1985; Schwarzschild 1993) would provide a sufficient orbit sampling: One could sample initial conditions from the (x,z)-plane producing mainly tube orbits and compensate this with launching additional box orbits from the equipotential surfaces (van den Bosch et al. 2008). However, it is not clear whether the distribution function of realistic triaxial galaxies requires a 5D starting space near the SMBH in the centre. With our choice of a 5D starting space, we guarantee that our set of orbits adapts to the actual complexity of the integrals-of-motion space. In a realistic triaxial galaxy, like in the studied simulation, it changes from a more spherical centre (requiring at least four integrals of motion) into nearly prolate outskirts. Furthermore, it allows us to model systems like eccentric discs with distribution functions that obviously depend on more than three integrals of motion. In Fig. C1, we show that our implemented orbit sampling and integration routine (cf. Section 2.3.1) yields a homogeneous and dense coverage of phase space.

2.3.1 Orbit integration and classification

SMART integrates the orbital equations of motions $\frac{d\vec{v}_i}{dt} = -\vec{\nabla}\phi(\vec{x}_i)$, where i denotes the orbit index, in Cartesian coordinates by means of the Cash–Karp algorithm (Cash & Karp 1990). The fifth-order Runge–Kutta method is implemented by using an adaptive integra-tion step-size (see Press et al. 1996). The default integration time of the individual orbits corresponds to 100 SOS crossings.

At each integrated time-step, the contribution of orbit i to the luminosity, internal velocity moments, and projected LOSVDs is calculated as the fraction of time the orbit spends in the corresponding bins. Projected quantities are convolved with the relevant PSF (point spread function) in every time-step and before binning. The PSF can either be provided as a parametrized 2D Gaussian or in terms of a PSF image. The convolution is performed via Monte Carlo method by randomly perturbing the coordinates $x'(t)$, $y'(t)$ (cf. Section 2.1) in dependence of the respective PSF.

Modelling a galaxy with SMART does not require an exact orbit classification analysis. However, we built in an approximate classification method. For this, SMART checks the sign conservation of the angular momentum in x-, y-, and z-direction for every SOS-crossing event. If the sign of L_x is conserved for the whole integration time and if this is not true for L_y and L_z, the orbit gets classified as x-tube. The same applies to the other directions (cf. Barnes 1992). If the 100 SOS crossings do not hold an angular momentum sign conservation along any direction, the orbit gets classified as box/chaotic orbit. If the sign conservation is true for every direction or if the orbit shows no radial and azimuthal change during the integration time, the orbit is classified as spherical/Kepler orbit.

2.4 Orbit superposition

The orbital weights w_i, which are decisive for the consistency between the observed and modelled luminosity as well as for the projected velocity profiles, are iteratively changed until the difference χ^2 between the observed LOSVDs $\mathcal{L}_{\text{data}}$ and modelled LOSVDs $\mathcal{L}_{\text{mod}}$ is minimal:

$$\chi^2 = \sum_{j'}^{N_{\text{losvd}}} \sum_{k}^{N_{\text{vlos}}} \left(\frac{\mathcal{L}_{\text{data}}{}^{j'k} - \mathcal{L}_{\text{mod}}{}^{j'k}}{\Delta\mathcal{L}_{\text{data}}{}^{j'k}} \right)^2 . \tag{6}$$

Here, j' describes the spatial bin index of the N_{losvd} data cells and k describes the velocity bin index of the N_{vlos} velocity bins. $\Delta\mathcal{L}_{\text{data}}{}^{j'k}$ is the error of the data in the specific bin. An advantage of SMART is that it uses the full information contained in the LOSVDs and not only the Gauss-Hermite parameters alone (cf. e.g. Mehrgan et al. 2019 for a discussion of the benefits of using non-parametric LOSVDs in measuring galaxy masses). The luminosity density serves as a boundary condition for the choice of the orbital weights.

The problem of solving for the weights w_i is usually underdeter-mined because the number of orbits is much larger than the number of data points. We therefore regularize our models by maximizing an entropy-like quantity

$$\hat{S} \equiv S - \alpha\,\chi^2, \tag{7}$$

where

$$S = -\sum_i w_i \ln\left(\frac{w_i}{\omega_i} \right). \tag{8}$$

In the absence of any other constraints, the entropy maximization yields $w_i \propto \omega_i$ (cf. Section 5). Thus, the ω_i are bias factors for the orbital weights w_i and can be used to smooth the orbit model. Moreover, they can be used to construct orbit models with specific properties, e.g. orbit models dominated by certain families of orbits (cf. Section 5 for examples).

The particular form of the entropy in equation (8) guarantees the positivity of the orbital weights. The maximum-entropy technique is

flexible, however. Other choices for the entropy allow for negative weights as well (Richstone & Tremaine (1988)).

Technically, for each regularization value α, SMART maximizes $\hat{S}$ by computing the relevant Lagrange multipliers. The iterative adjustment of the w_i's is performed by using Newton's method. The implemented method is based on Richstone & Tremaine (1988). A detailed description of the algorithm as well as tests demonstrating the high accuracy performance of SMART can be found in Appendix D.

As we will describe in full detail in Section 5, the entropy term in equation (7) makes the solution of the orbital weights unique. While this might be advantageous from an algorithmic point of view it comes in principle with the danger of a potential bias. As we will show, by varying the orbital bias factors ω_i the maximum-entropy technique allows in principle to reconstruct any of the potentially degenerate solutions for the orbital weights (cf. Section 5). However, the results of the following sections imply that when fitting all the information contained in the full LOSVDs, the remaining degeneracies in the weight reconstruction have only little impact on the 'macroscopic' galaxy parameters of interest, like the anisotropy for example.

One natural choice for the orbital bias factors is $\omega_i = V_i$, where V_i is the phase-space volume represented by orbit i (cf. e.g. Richstone & Tremaine 1988; Thomas et al. 2004). With this choice,

$$S = -\sum_i w_i \ln \left(\frac{w_i}{V_i} \right) = -\int f \ln(f) \mathrm{d}^3 r \mathrm{d}^3 v \qquad (9)$$

equals the Boltzmann entropy. Since the Boltzmann entropy increases during dissipationless evolutionary processes due to phase mixing and violent relaxation, galaxy models with large Boltzmann entropy are more likely than those with a small one (Richstone & Tremaine 1988; Thomas et al. 2007). However, in collisionless self-gravitating systems, every entropy-like functional is assumed to increase in phase space, such as the generalized H-function (Tremaine, Henon & Lynden-Bell 1986), the entropy of the ideal gas (White & Narayan 1987) or the Tsallis entropy (Tsallis 1988). The choice of ω_i is thus arbitrary to some degree. This and the fact that in case of a triaxial potential it is computationally expensive to calculate the correct phase-space volume V_i for every orbit motivated us to set

$$\omega_i = \mathrm{const.} = 1. \qquad (10)$$

This functional form was also tested by de Lorenzi et al. (2007) in a slightly different context of a made-to-measure (M2M; Syer & Tremaine 1996; Bissantz, Debattista & Gerhard 2004) algorithm for N-body particle models. Compared to the Boltzmann entropy, ω_i = const. leads to relative preference of orbits with actually small V_i, while orbits with large V_i are relatively suppressed. With this choice of constant orbital bias factors ω_i, the entropy equation (cf. equation 8) resembles the Shannon entropy and yields the least 'informed' set of orbital weights.

2.5 Mass optimization with SMART

SMART is conceived to determine the viewing angles and the mass components, like the dark matter halo, the stellar mass-to-light ratio and black hole mass by looking for the model with the smallest χ^2. To deal with this multidimensional parameter space, SMART uses NOMAD (Nonlinear Optimization by Mesh Adaptive Direct search), a software optimized for time-consuming constrained black-box optimizations (Audet & Dennis 2006; Le Digabel 2011). NOMAD is able to optimize a noisy function with unknown derivatives to

converge to the best-fitting model by using a direct-search scheme. SMART runs on multiple computer cores. The orbit processing (including the setup of the initial conditions, orbit integration, orbit classification, and computation of the internal and projected velocity distributions) as well as the relevant linear algebra operations applied for their superposition are parallelized.

3 THE *N*-BODY SIMULATION

In order to test SMART on a realistic mock galaxy, we use a high-resolution collisionless numerical merger simulation by Rantala et al. (2018). The simulation is a single generation binary galaxy merger of two equal-mass elliptical galaxies with an effective radius of 7 kpc hosting an SMBH of 8.5×10^9 M$_\odot$ each and corresponds to the so-called γ-1.5-BH-6 simulation in Rantala et al. (2018). The two initial galaxies are set up by using a spherically symmetric Dehnen density-potential (Dehnen 1993) with an initial inner stellar density slope of $\rho \propto r^{-3/2}$ for both progenitor galaxies. The merger results in a remnant triaxial galaxy with a SMBH of 1.7×10^{10}M$_\odot$ with a sphere of influence[1] of $r_{\mathrm{SOI}} \sim 1$ kpc and an effective radius of $r_e \sim 14$ kpc. With that, the remnant resembles NGC 1600, a galaxy showing a very large core with a tangentially biased central stellar orbit distribution (Thomas et al. 2016). The simulation is based on the hybrid tree-N-body code KETJU (Rantala et al. 2017; Karl et al. 2015) which is able to accurately compute the dynamics close to the black hole due to the algorithmic chain regularization method AR-CHAIN (Mikkola & Merritt 2006, 2008). The computation of the global galactic dynamics is based on the tree code GADGET-3 (Springel 2005).

We analyse a snapshot of the simulation $\sim$1.4 Gyr after the galaxy centres have merged, such that the remnant can be assumed to be in a steady state. At this stage, the actual distance of the two merging black holes in the simulation is 5 pc. The merger remnant shows a radially varying triaxiality parameter, being more oblate at smaller radii and increasingly more round in the centre with a maximum of triaxiality, i.e. $T = 0.5$, at about 3 kpc and more prolate outskirts. The simulation contains 8.3×10^6 stellar particles with masses of 10^5M$_\odot$ each, leading to a total stellar mass of 8.3×10^{11}M$_\odot$. The mass ratio of one SMBH and one stellar particle is $M_{\mathrm{BH}}/M_* = 8.5 \times 10^4$ and therefore sufficiently large to investigate a realistic interaction of the SMBH binary with the stars (Mikkola & Valtonen 1992). The number of dark matter particles is 2×10^7 with masses of 7.5×10^6M$_\odot$ each, leading to a total dark matter mass of 1.5×10^{14}M$_\odot$.

The simulation is particularly suitable to test SMART because of its (1) very high resolution (including properly resolved black hole dynamics); (2) realistic orbital structure and shape; (3) realistic mass composition (black hole, stars, and dark matter) with a realistic stellar density core (e.g. Thomas et al. 2009; Rantala et al. 2019). Finally, the number of stellar particles is large enough to measure fully resolved LOSVDs from the central sphere of influence of the black holes out to dark-matter-dominated regions.

3.1 Processing the simulation data

3.1.1 Orientation of the simulation

We aim at orienting our intrinsic coordinate system as closely as possible to the intrinsic symmetry axes of the merger remnant.

---

[1]We here use the definition of the sphere of influence as the radius within which the total stellar mass equals the black hole mass, i.e. $M_*(r_{\mathrm{SOI}}) = M_{\mathrm{BH}}$.

However, the stellar and dark matter principal axes of the simulated remnant are not aligned. Hence, the orientation of the main axes depends on the radius and on the mass component for which the reduced inertia tensor (see e.g. Bailin & Steinmetz 2005) is calculated. Such a shift between the stellar and dark matter halo axes is not unexpected for collisionless merger simulations (see e.g. Novak et al. 2006). We decided to centre the remnant on the stars and black holes and afterwards orientate it by using the reduced inertia tensor for stars and dark matter within 30 kpc. With this, the stellar elliptical isophotes for the three different projections are well aligned with the projected principal axes within the field of view of 15 kpc × 15 kpc. There is a negligible residual misalignment which is strongest for the major axis projection but nowhere larger than ∼5° (see Figs 3 and A1).

3.1.2 Density

Due to the good alignment and taking advantage of the nearly triaxial intrinsic symmetry of the merger remnant, we increase the resolution of the simulation for computing the density by a factor of 8 by folding all stellar and dark matter particles into one octant. The stars are then binned into concentric radial shells with 1000 stars in each shell and the dark matter particles are binned into radial shells with 5000 dark matter particles each. The single shells are subdivided into angular bins such that the elevation angle $\theta \in [0°, 90°]$ increases in constant $\sin(\theta)$-steps of 0.1 and that the azimuthal angle $\phi \in [0°, 90°]$ increases in constant ϕ-steps of 10°.

Within $r < 0.28$ kpc for the stellar and $r < 10$ kpc for the dark matter particles, the resolution is too low to extract a smooth density. Here, we extrapolate the logarithmic densities from the outer parts by a first-order polynomial fit in the logarithm of the radius. For the stellar densities, we use the slope and vertical intercept averaged over all angular bins. The dark matter density is extrapolated by using the slopes and vertical intercept values of the individual angular bins. We ensure that the total enclosed mass is well covered by the extrapolated density. To smooth the radial density profiles, SCIPY's Gaussian_filter()-function (Virtanen et al. 2019) is used.

3.1.3 Spatial binning

For spatially binning the kinematic input data, we use the Voronoi tessellation method of Cappellari & Copin (2003). For each tested projection (see Section 3.2), we construct a separate set of Voronoi bins. To end up with a roughly constant number of stellar simulation particles N_* in each bin, we define the signal-to-noise ratio as

$$\frac{\text{signal}}{\text{noise}} = \sqrt{\text{signal}} = \sqrt{N_*} = \begin{cases} 70 \text{ for } r < r_{\text{SOI}}, \\ 150 \text{ for } r_{\text{SOI}} < r < 15 \text{ kpc}. \end{cases} \quad (11)$$

When calculating the average over the five different projections, this results in a total number of $N_{\text{losvd}} = N_{\text{voronoi}} = 227$ Voronoi bins within the whole field of view and 54 Voronoi bins within r_{SOI}.

This resolution is chosen to conform with realistic observational data and does not exceed high-resolution wide-field spectral observations by, e.g. MUSE (cf. Mehrgan et al. 2019) but still proves to be sufficiently high for this analysis.

3.1.4 Kinematic data and velocity binning

For each spatial bin, we calculate the LOSVDs for $N_{\text{vlos}} = 45$ equally-sized velocity bins with $v_{\text{min}}^{\text{max}} = \pm 1600$ km s^{-1}, which is chosen so

that it covers about 10 times the velocity dispersion. This results in a velocity resolution of $\Delta v_{\text{vlos}} = 71.11$ km s^{-1}.

It is not trivial which 'error' for the kinematic input data of the simulation should be used since we do not have an error in the simulation in the sense that repeated measurements give the same results. However, the χ^2-minimization formally requires information about an 'error'. We tested several assumed 'error-bars', such as

(i) the difference between two kinematic data sets, each determined by using half of the simulation particles,
(ii) the Poisson noise, and
(iii) a constant absolute error for each LOSVD as 10 per cent of the maximum per LOSVD.

In order to prevent an underestimation of the relative error for the major axis projection holding more particles along the line of sight than the other projections, the constant absolute error proves to be the most suitable method and is used in the present analysis. The choice of setting the error value to 10 per cent of the maximum value of each LOSVD corresponds to a velocity uncertainty of $\Delta v = 13$ km s^{-1}, dispersion error of $\Delta \sigma = 13$ km s^{-1} (or 5 per cent relative error) and $\Delta h_n = 0.03$ for the higher order Gauss–Hermite moments. This is a reasonable choice both in terms of real observational errors and of the scatter in the kinematic maps of the merger simulation (see Figs 3 and B1).

3.2 Applying SMART to the simulation

For the purpose of testing our code, SMART is provided with the correct viewing angles and with the 3D normalized stellar (i.e. luminosity) density ρ_* from the simulation as well as with the normalized 3D dark matter density ρ_{DM}. The DM scaling parameter s_{DM} is to be determined by SMART. We skipped any surface brightness deprojection, since degeneracies in the deprojection (see e.g. de Nicola et al. 2020) would only hamper a correct evaluation of our code. We parametrize the density as

$$\rho = M_{\text{BH}} \times \delta(r) + \Upsilon \cdot \rho_* + s_{\text{DM}} \cdot \rho_{\text{DM}}, \quad (12)$$

where our fit parameters are the black hole mass M_{BH}, stellar mass-to-light ratio Υ, and the multiplication factor s_{DM} defining the magnitude of the dark matter density profile favoured by SMART. We determine these parameters by finding the minimum in χ^2.

We model and analyse five different projections with (1) $\vartheta = 90°$, $\varphi = 0°$, i.e. the major axis projection, (2) $\vartheta = 90°$, $\varphi = 90°$, i.e. the intermediate axis projection, (3) $\vartheta = 0°$, $\varphi = 90°$, i.e. the minor axis projection, (4) $\vartheta = 90°$, $\varphi = 10°$, i.e. a projection 10° off the major axis in azimuthal direction, and (5) $\vartheta = 90°$, $\varphi = 45°$, i.e. a projection in between the major and intermediate axis projection. Without loss of generality, ψ was set to 90° for all three viewing directions, i.e. R (see equation 2) equals the unit matrix.

The field of view is chosen to be 15 kpc × 15 kpc. The minimum sampled starting radius is set to $r_{\text{min}} = 0.05$ kpc and the maximum sampled starting radius is set to $r_{\text{max}} = 80$ kpc. We find optimal results for a central binning with $c = 0.5$ in equation (4) because this guarantees that in case of the simulated merger remnant the difference of the circular velocity within one radial bin equals the model's velocity resolution $\Delta v_{\text{vlos}} = 71.11$ km s^{-1} at a radius of $r = 0.16$ kpc $= 0.16 \cdot r_{\text{SOI}}$. For $c = 1$, this would be only reached at $r = 0.38$ kpc $= 0.38 \cdot r_{\text{SOI}}$, resulting in a deteriorated black hole mass recovery by ∼ 10 per cent.

For each tested projection, we model two halves of the LOS kinematic data. After correct projection on to the plane of the sky (see Section 2.1), we separately model the half of the kinematic data with

positive x'-coordinates (hereafter called 'right half' of the galaxy) and the half of the kinematic data with negative x'-coordinates (hereafter called 'left half' of the galaxy).

4 RESULTS

4.1 Choice of regularization

When applying the code to realistic noisy measurements, regularization becomes important to prevent the orbital weights to fit the noise in the data. The optimal regularization parameter α for a specific observational data set can be determined by running Monte Carlo simulations on kinematic mock data (Thomas et al. 2005) and is given as the one providing the minimum deviation of the intrinsic properties (like the distribution function, or velocity moments, or mass parameters) in comparison to the default model. When fitting noiseless ideal data, one would expect best results for $\chi^2 \rightarrow 0$, or $\alpha \rightarrow \infty$ (neglecting recovery degeneracies and assuming an 'error' can be defined). Even in that case, however, due to residual systematics (like finite resolution of the orbit library etc.) and due to the intrinsic noise in the N-body simulation, we still expect that the best result may not necessarily be achieved asymptotically for very large α, but already for some finite value of the regularization parameter. To take this into account, we split the code test into two phases: (1) We fit the orbit model with the correct mass parameters and determine that value of α for which the internal structure of the simulation is best recovered. Specifically, we use the second-order velocity moments for this comparison. (2) We then also vary the mass parameters and test how well they can be recovered. Our benchmark is the optimized α from the comparison of the moments, but we will discuss the results for all α to demonstrate their robustness.

For determining the deviation between the model's velocity dispersions σ_r, σ_θ, and σ_ϕ and the real ones from the simulation, we define

$$\mathrm{rms}_\sigma = \frac{1}{3} \sum_i \mathrm{rms}_{\sigma_i} = \frac{1}{3} \sum_i \sqrt{\frac{1}{N_{\mathrm{data}}} \sum_{j=1}^{N_{\mathrm{data}}} \left(\frac{\sigma_{i,\mathrm{data}} - \sigma_{i,\mathrm{mod}}}{\sigma_{i,\mathrm{data}}} \right)^2},$$
(13)

where the index i denotes the three coordinates r, θ, ϕ.

These rms_σ profiles of the five tested projections and their respective modelled halves in dependence of the regularization parameter α are plotted as thick lines in the top row of Fig. 2. The x-axis ticks, thereby mark all α-values that were tested in this analysis.

The second row in Fig. 2 shows the quality of the fit as χ^2/N_{data} profile (for definition of χ^2 see formula 6) again plotted against the regularization parameter. χ^2 as deviation from the kinematic input data with the modelled fit is here normalized over the number of input data N_{data}, which is composed of the number of Voronoi bins N_{voronoi} times the number of kinematic bins N_{vlos}. As expected, the fit to the data is poor when α is low (high χ^2/N_{data}). In this regime, it is the entropy term which is essentially maximized and the data (via $\alpha \cdot \chi^2$, cf. equation 7) have little influence on the fit. With this, the anisotropy strongly depends on the ω_i and, in our case, happens to be a poor representation of the internal moments of the merger (high *rms* values, see Fig. 2, first row). With increasing α, both the fit quality and the agreement with the merger structure improve. However, at very high α-values further improvements of the fit do not make the internal moments better since we are dominated by the noise of the N-body simulation. The most suitable choices of regularization can be read off from the minima $\min(\mathrm{rms}_\sigma)$ of the rms_σ profiles and are marked as thick vertical lines in Fig. 2. Their average value is

$\alpha(\min(\mathrm{rms}_\sigma)) = 0.41$. This value, however, depends on the specific implemented set-up of SMART as well as of the input data. Evaluated at the individual most suitable regularization values and afterwards averaged over all 10 models (5 projections and two halves each), we get a minimum value of only $\min(\mathrm{rms}_\sigma) = 0.008$. This extremely good agreement demonstrates that our orbit sampling represents the phase space very well.

We also test the influence of rotation on the comparison. Due to the overall small angular momentum and thus small absolute velocity amplitude however, the relative errors in v are sometimes large. The absolute error of the first-order velocity moments, averaged over all angular and radial bins, is only $\Delta v = 3.9 \, \mathrm{km \, s^{-1}}$, but the maximum velocity over these bins is likewise only $23.4 \, \mathrm{km \, s^{-1}}$. We therefore here define $\mathrm{rms}_{v,\sigma}$ as normalized deviation between the first internal moments and the velocity dispersions together as

$$\mathrm{rms}_{v,\sigma} = \frac{1}{3} \sum_i \mathrm{rms}_{v_i,\sigma_i} = \frac{1}{3} \sum_i \sqrt{\frac{1}{2N_{\mathrm{data}}} \sum_{j=1}^{N_{\mathrm{data}}} \left(\Delta_{v_i}^2 + \Delta_{\sigma_i}^2 \right)},$$

with $\Delta_{v_i} = \dfrac{v_{i,\mathrm{data}} - v_{i,\mathrm{mod}}}{\sqrt{v_{i,\mathrm{data}}^2 + \sigma_{i,\mathrm{data}}^2}}$ and $\Delta_{\sigma_i} = \dfrac{\sigma_{i,\mathrm{data}} - \sigma_{i,\mathrm{mod}}}{\sqrt{v_{i,\mathrm{data}}^2 + \sigma_{i,\mathrm{data}}^2}}$, (14)

where the index i again denotes the three coordinates r, θ, ϕ.

The $\mathrm{rms}_{v,\sigma}$ profiles are plotted against the regularization parameter as thin lines in the top row of Fig. 2. As expected, their minima appear at regularization values similar to the ones of the rms_σ profiles. They are marked as thin vertical lines and their average value is $\alpha(\min(\mathrm{rms}_{v,\sigma})) = 0.012$. Again, this value depends on the specific set-up. Evaluated at the individual $\alpha(\min(\mathrm{rms}_{v,\sigma}))$-values and afterwards averaged over the five different projections and their respective modelled halves we gain a value of only $\min(\mathrm{rms}_{v,\sigma}) = 0.012$.

All values in the vicinity of $\alpha(\min(\mathrm{rms}_\sigma))$ and $\alpha(\min(\mathrm{rms}_{v,\sigma}))$ are good regularization choices. Within this regularization region, SMART is able to well fit the kinematic input data for each tested projection (see Figs 3 and B1). Averaged over the five different projections and their respective modelled halves we receive mean values and deviations of $\bar{v} = (0.11 \pm 2.09) \, \mathrm{km \, s^{-1}}$, $\bar{\sigma} = (309.75 \pm 2.54) \, \mathrm{km \, s^{-1}}$, $\bar{h_3} = 0.00 \pm 0.01$ and $\bar{h_4} = 0.01 \pm 0.01$, again evaluated at $\alpha(\min(\mathrm{rms}_\sigma))$. The χ^2-maps in Figs 3 and B1 show that the models for each projection are able to fit the kinematic input data homogeneously well over the field of view with slightly larger deviations in the centre. If not specifically annotated, the results shown in the further analysis are evaluated at $\alpha(\min(\mathrm{rms}_\sigma))$. However, the quality of the models does not strongly depend on the exact regularization value because a broader range of regularization values around these determined α-values is sufficiently appropriate and results in equally good mass parameter reproductions within the overall scatter (see also third and fourth lines in Fig. 2 that will be explained in Section 4.3).

4.2 Reproduction of internal moments and orbit structure

The previously shown small rms_σ and $\mathrm{rms}_{v,\sigma}$ values already demonstrate the very good recovery of the internal moments by the model when providing the correct mass parameters and viewing angles. The high level of agreement between model and simulation is further illustrated in Fig. 4. The anisotropy parameter $\beta = 1 - \frac{\sigma_\theta^2 + \sigma_\phi^2}{2\sigma_r^2}$ of the model matches the profile of the simulated one (see Fig. 4, middle panel). The model is also able to reproduce the negative β within the core radius r_b, which equals the black hole sphere of influence
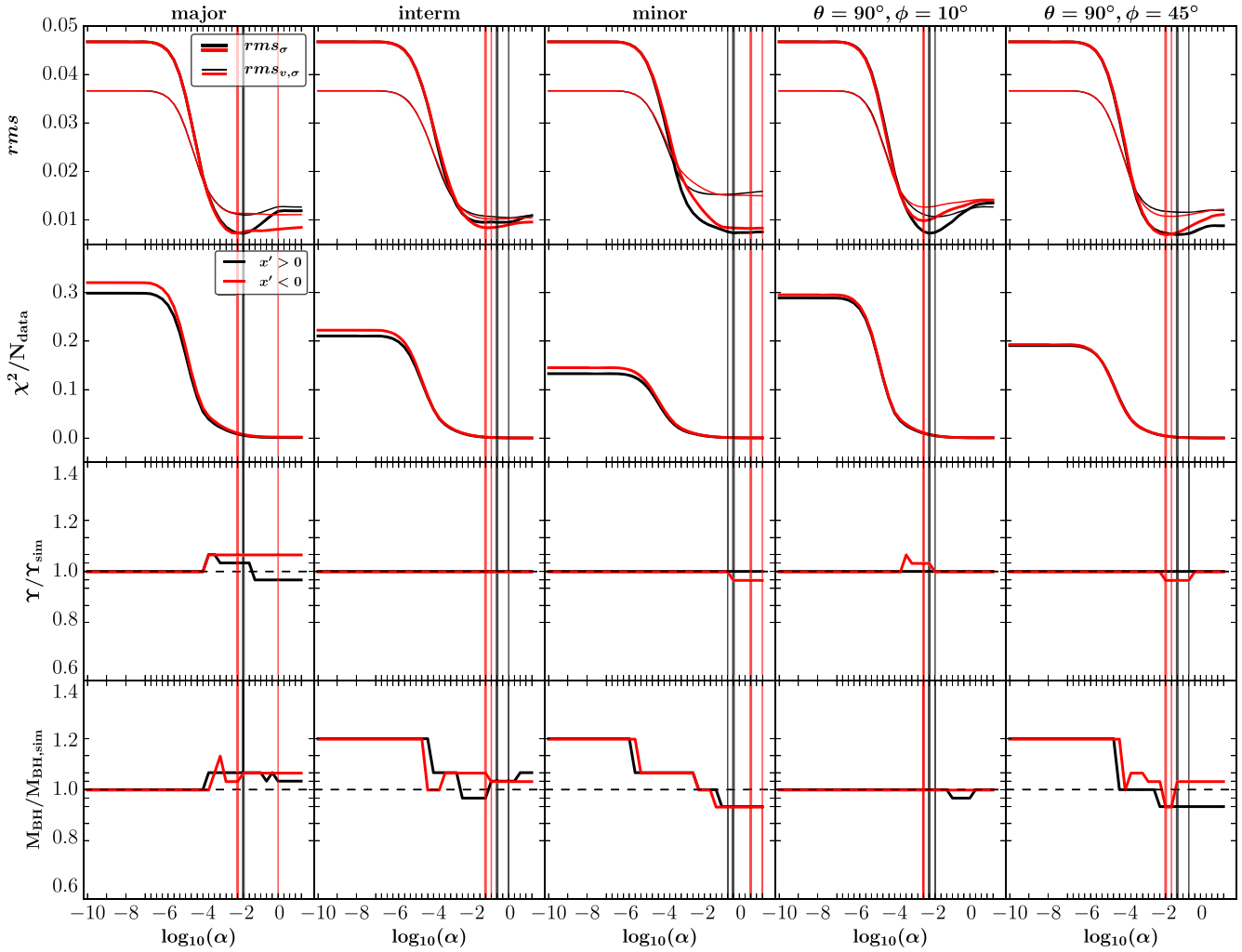
Figure 2. Choice of regularization and 1D mass recovery results for the five different projections (different columns). The first row shows the rms_σ- (thick line) and $rms_{v,\sigma}$-profile (thin line) for the modelled right half of the galaxy (black) and left half of the galaxy (red) with the correct black hole mass, stellar mass-to-light ratio and dark matter scale factor as input. All values are plotted against the increasing regularization value α in logarithmic units. The x-axis-ticks thereby symbolize the tested α-values. The minima $\min(rms_\sigma)$ (thick line) and $\min(rms_{v,\sigma})$ (thin line) are marked as vertical lines and suggest suitable regularization values. The thin black vertical line in the major axis panel thereby overlaps with the thick black vertical line and the thin red vertical line in the $\vartheta = 90°, \varphi = 10°$ panel overlaps with the thick red vertical line. The second row shows the corresponding χ^2/N_{data} values. The third and fourth rows show the 1D mass recovery results for the stellar mass-to-light ratio Υ/Υ_{sim} and black hole mass $M_{BH}/M_{BH,sim}$ normalized over the correct values of the simulation. The y-axis-ticks for the third and fourth row symbolize the concrete masses that were tested and used as input values for the models. The black dotted line marks unity which is achieved when the model correctly recovers the mass. The stellar mass-to-light ratio and black hole mass were recovered with an accuracy better than 5 per cent. Such an intrinsic precision under similar conditions has not yet been demonstrated with other Schwarzschild modelling codes.

(Thomas et al. 2016), reflecting the tangential orbit distribution due to black hole 'core scouring': Within the sphere of influence ETGs at the high-mass end exhibit central regions that are fainter than an extrapolation of a Sérsic function (Sérsic 1963) as fit to the outer surface brightness profile would suggest. The commonly accepted theory for the formation of these 'cores' is a gravitational slingshot process of stars on radial orbits caused by SMBH binaries that were arised by galaxy mergers (e.g. Begelman, Blandford & Rees 1980; Hills & Fullerton 1980; Ebisuzaki, Makino & Okumura 1991; Milosavljević & Merritt 2001; Merritt 2006; Rantala et al. 2018).

The classification of the integrated orbits is also plotted in Fig. 4 (bottom panel). Orbits in the immediate vicinity of the black hole are spherical and Keplerian orbits as expected due to the SMBH. Z-tubes are the pre-dominant orbits within $0.3\,\text{kpc} < r < 3\,\text{kpc}$ causing the more oblate shape of the galaxy in this range. For $r > 3\,\text{kpc}$,

the majority of orbits are classified as x-tubes corresponding to the prolate shape in the outskirts of the simulation as described in Section 3. Our orbit classification analysis well matches the one by Frigo et al. (in preparation), which is done via an orbit frequency analysis of the simulation.

4.3 Mass recovery

So far, we have provided SMART with the correct mass parameters of the stellar mass-to-light ratio Υ_{sim}, black hole mass $M_{BH,sim}$, and dark matter multiplication factor $s_{DM,sim}$ of the simulation. Even though SMART can be provided with any type of dark matter profile, we here transfer the dark matter density profile shape of the simulation and concentrate on finding the correct mass multiplication scale factor s_{DM} of this pre-determined halo shape (cf. equation 12).
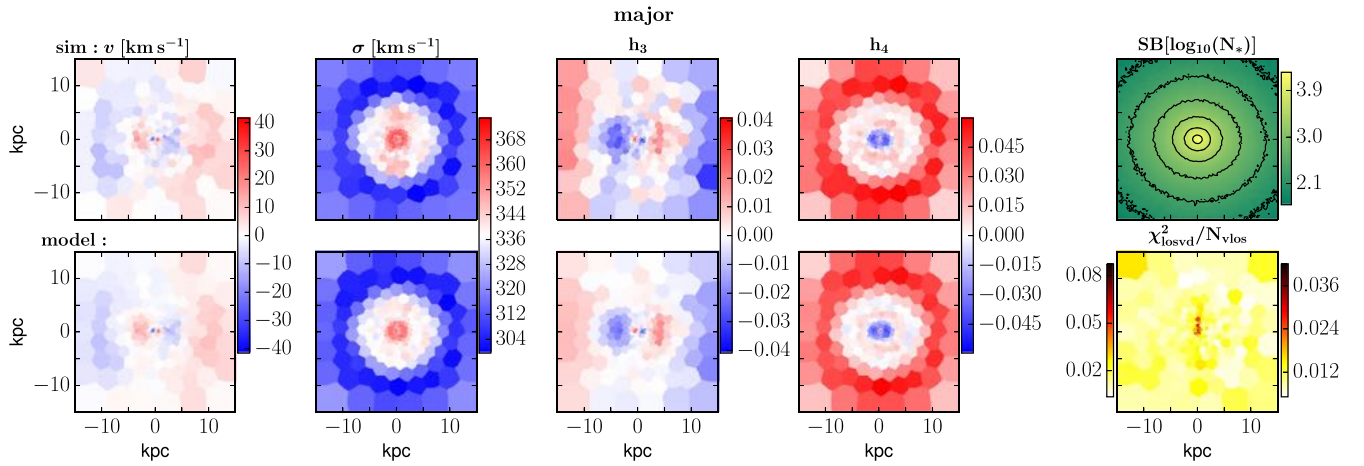
Figure 3. Velocity maps of the simulation (top row) and of the model (bottom row) for the major axis projection, i.e. the projection with the line of sight being parallel to the major axis of the simulation based on the simulation's orientation described in Section 3.1.1 (for the other projections see Fig. B1). The different panels show the velocity in $\mathrm{km\,s^{-1}}$ (first column), velocity dispersion in $\mathrm{km\,s^{-1}}$ (second column), the h_3-parameter (third column), and h_4-parameter (fourth column) plotted over the whole field of view. The fifth panel in the top row shows the corresponding surface brightness map from the simulation in units of logarithmic numbers of stellar particles N_*. The contour lines correspond to isodensity surfaces. The fifth panel in the bottom row shows $\chi^2_{\mathrm{losvd}}/N_{\mathrm{vlos}}$ as deviation from the kinematic input data with the modelled fit. We show the result for the model with the correct stellar mass-to-light ratio, black hole mass and dark matter scale factor as input parameters evaluated at the most suitable regularization parameter of $\alpha(\min(\mathrm{rms}_\sigma))$. The maps in the second row consist of the results of the modelled left and right half of the galaxy. Therefore, the χ^2-maps show two colourbars for the two different halves.
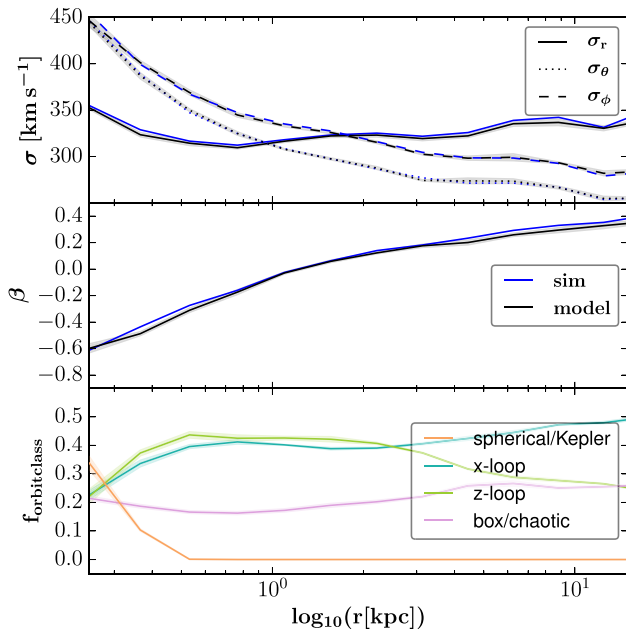
Figure 4. Reproduction of the internal properties within $r \in [0.25\,\mathrm{kpc}, 15\,\mathrm{kpc}]$. Top panel: The internal velocity dispersions in radial direction σ_r (solid line), elevation direction σ_θ (dotted line), and azimuthal direction σ_ϕ (dashed line) from the model (black lines) averaged over the five different projections accurately follow the real ones from the simulation (blue lines) out to 15 kpc as field of view. The grey shaded lines mark the deviations between the different projections. Middle panel: Also, the anisotropy parameter β is well reproduced and represents the tangentially anisotropic orbit distribution ($\beta < 0$) within the core radius $r_b = r_{\mathrm{SOI}} \sim 1\,\mathrm{kpc}$ as well as the radially anisotropic orbit distribution ($\beta > 0$) outside r_b. Bottom panel: Radial distribution of the orbit fractions $f_{\mathrm{orbitclass}}$ classified by SMART.

The following sections will show the 1D mass reproduction results of individually determining the favoured stellar mass-to-light ratio Υ or black hole mass M_{BH} (Section 4.3.1) as well as the 2D mass recovery results of simultaneously determining the favoured Υ and M_{BH} (Section 4.3.2) or Υ and s_{DM} (Section 4.3.3). We skip any 3D mass parameter recovery, since this would not provide more information than the combined 2D recoveries in the context of testing the orbit library.

### 4.3.1 1D mass recovery of Υ and M_{BH}

Fig. 2 shows the 1D mass recovery results of Υ (third row) and M_{BH} (fourth row) for the five different projections and their respective modelled halves. For testing the recovery of the black hole mass, we provide the model with the correct Υ_{sim} and $s_{\mathrm{DM,sim}}$ values and run nine models with different black hole masses within $M_{\mathrm{BH}} \in [0.79 M_{\mathrm{BH,sim}}, 1.21 M_{\mathrm{BH,sim}}]$ including the correct one. The tested mass grid has a smaller grid size close to $M_{\mathrm{BH}}/M_{\mathrm{BH,sim}} = 1$ and the exact tested values can be read off from the ordinate ticks in Fig. 2.

For testing the 1D mass recovery of the stellar mass-to-light ratio, we provide $M_{\mathrm{BH,sim}}$ and $s_{\mathrm{DM,sim}}$ and test the same $\Upsilon/\Upsilon_{\mathrm{sim}}$ values as for the black hole mass analysis.

Fig. 2 shows the favoured mass parameters, i.e. the mass parameters where χ^2/N_{data} is smallest, as a function of α. As one can see, for our fiducial choice of α (i.e. $\alpha = \alpha(\min(\mathrm{rms}_\sigma))$ as the best recovery of the velocity dispersions), the *average* mass recovery performs excellently, with $\Delta M_{\mathrm{BH}} = 5$ per cent and $\Delta \Upsilon = 2$ per cent. In fact, above $\log \alpha \gtrsim -3$, the results are very robust with little dependency on α. Within the overall minor scatter, all models, independent from the chosen half of the galaxy or projection, show equally good fits and reproductions of the internal moments and mass parameters.

4.3.2 2D mass recovery of Υ and M_{BH}

For simultaneously recovering Υ and M_{BH} by SMART, we sample a 2D grid of input masses for 49 models per projection with Υ
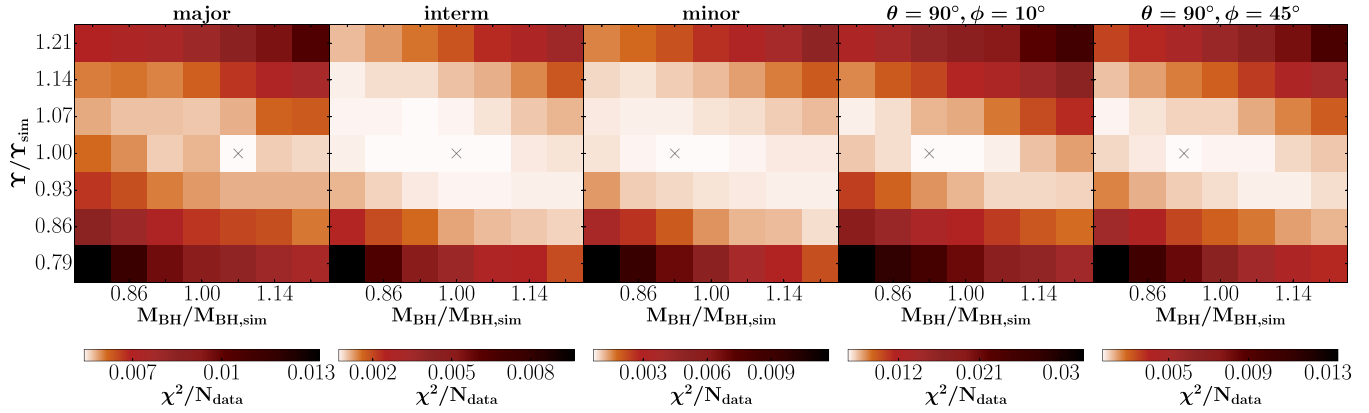
Figure 5. 2D mass recovery results of Υ and M_{BH} for the positive halves of the five different projections. For each projection, we evaluate 49 models with different Υ and M_{BH} input masses, covering a 2D grid with a step size of 7 per cent around the correct mass parameter. Each plot contains the χ^2/N_{data} colourbar for the individual projection. The favoured models are marked with a grey cross. The model always finds the correct stellar mass-to-light ratio and the black hole mass with a minor averaged deviation of 6 per cent.
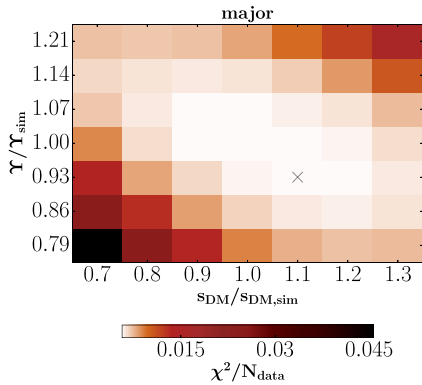
Figure 6. 2D mass recovery results of Υ and s_{DM} for the positive half of the major axis projection. s_{DM} thereby is the mass multiplication scale factor of the pre-determined halo shape of the simulation. We evaluate 49 models with different Υ and s_{DM} input masses, covering a 2D grid with a step size of 7 per cent for the stellar mass-to-light ratio and 10 per cent for the dark matter scaling multiplication factor. The favoured model is marked with a grey cross. The model slightly overestimates the dark matter halo scale factor by 10 per cent and slightly underestimates the stellar mass-to-light ratio by 7 per cent.

4.3.3 2D mass recovery of Υ and s_{DM}

For recovering Υ and s_{DM}, we sample a 2D grid of input masses for 49 models along the major axis projection with $\Upsilon \in [0.79\Upsilon_{sim}, 1.21\Upsilon_{sim}]$ and $s_{DM} \in [0.7s_{DM,sim}, 1.3s_{DM,sim}]$. We here model the right half of the major axis projection. The result is shown in Fig. 6. Evaluated at $\alpha(\min(\mathrm{rms}_\sigma))$, the dark matter scale factor is slightly overestimated by 10 per cent and the stellar mass-to-light ratio is
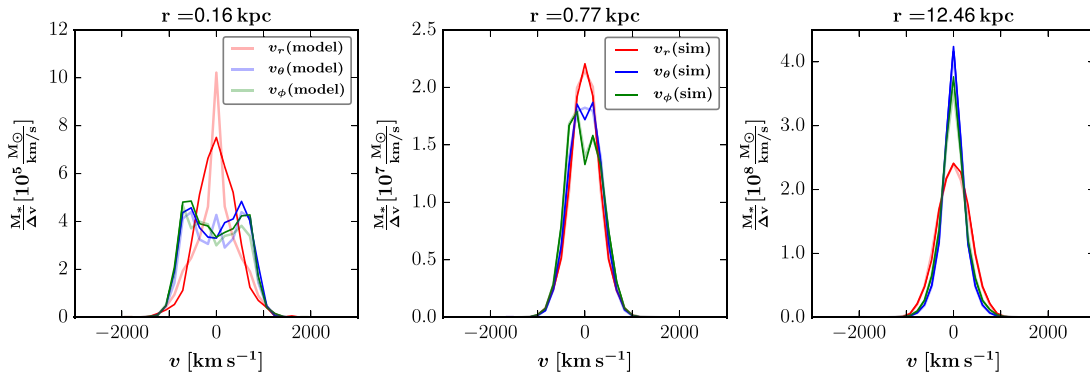
slightly underestimated by 7 per cent, confirming the accurate mass reconstruction from the previous tests.

In conclusion, these mass recovery results demonstrate that our orbit sampling and superposition algorithms allow for a very accurate reconstruction of the mass composition and orbital structure of triaxial systems with known density shapes.

4.4 Beyond second-order velocity moments

So far, we have focused on the reproduction of the first- and second-order internal velocity moments. The previous sections have shown that the full shape of the LOSVDs contains enough information to accurately reconstruct the mass and the anisotropy structure of the orbit distribution. In Fig. 7, we show the full mass-weighted stellar velocity distributions per velocity bin against the velocity in km s^{-1} in radial, longitudinal, and azimuthal direction when integrating over the other velocity components and respective spatial bins of the model. We find that the central azimuthal and longitudinal velocity distributions within $r < r_{SOI}$ have two maxima that become more pronounced closer to the centre (see Fig. 7). This likely reflects the strong tangential anisotropy produced during the formation of the core and is probably linked to the negative h_4 parameter at the centre of the merger remnant (see Figs 3 and B1), which will be investigated in more detail in a separate paper. The whole internal velocity distributions contain more information about the formation process than the velocity moments alone can do. So, we extended SMART to calculate the internal velocity distributions for 31 velocity bins within the positive and negative escape velocity, i.e. $v_{min}^{max} = \pm v_{esc}(r, \theta, \phi)$, evaluated at each radial and angular bin of the SMART-specific grid (see Section 2.1). The internal velocity distributions averaged within spherical shells reproduce the ones from the simulation sufficiently well, with a deviation of $rms = 0.07$ averaged over all velocity bins with $v < 1000$ km s^{-1} and radial bins within $r \in [0.25 \text{ kpc}, 15 \text{ kpc}]$ (see Fig. 7). Including the outer wings of the internal velocity distributions with $v > 1000$ km s^{-1}, the rms increases, however, the number of simulation particles in these bins is very small. We will apply this ability of SMART to model the whole internal velocity distribution in future studies of real observational data.

We checked the behaviour of the rms profile in dependence of the regularization as deviation of the whole internal velocity distributions and compared it with the rms_σ and $\mathrm{rms}_{v,\sigma}$ profiles. It thereby showed

$\in [0.79\Upsilon_{sim}, 1.21\Upsilon_{sim}]$ and $M_{BH} \in [0.79M_{BH,sim}, 1.21M_{BH,sim}]$. We again model all five different projections but fit only the right half of the galaxy since the 1D mass recovery showed no significant difference between the respective halves of each projection. The results are plotted in Fig. 5. Evaluated at the regularization value $\alpha(\min(\mathrm{rms}_\sigma))$ the stellar mass-to-light ratio is in every case correctly recovered and the black hole mass is reproduced with an accuracy of 6 per cent averaged over the different projections.

Figure 7. Internal velocity distributions in radial (red), elevation (blue), and azimuthal (green) direction when integrating over the respective spatial bin of the model and the other velocity components for three different radii of $r = 0.16$ kpc (left-hand panel), $r = 0.77$ kpc (middle panel), and $r = 12.46$ kpc (right-hand panel). The internal velocity distributions are calculated for 31 velocity bins within the positive and negative escape velocity evaluated at each radial and angular bin of the SMART-specific grid. We here show the mass-weighted stellar internal velocity distributions per velocity bin averaged within spherical shells. The non-shaded lines correspond to the simulation data and the shaded lines show the modelled results. In closer vicinity of the black hole, the elevation and azimuthal distribution show two maxima corresponding to the tangentially anisotropic orbit distribution. SMART is able to reproduce the internal velocity distributions in general and is also able to follow this specific behaviour in the central bins.

the same form and its minimum appeared in the same regularization region and therefore does not provide additional information when determining the most suitable regularization value.

4.5 Robustness and uniqueness checks

In order to test the robustness of the results against modifications of our fiducial set-up and in order to test the uniqueness of the results, we make the following checks and considerations:

4.5.1 PSF convolution and noise

While Valluri et al. (2004) describe that three-integral, axisymmetric, orbit-based modelling algorithms in general show a flat-bottomed χ^2 distribution, being unable to determine the black hole mass to better than a factor of ~ 3.3, Magorrian (2006) demonstrates that this is only true for noiseless data. According to this, our model should not be able to precisely determine the correct black hole mass of the simulation due to the lack of an 'error'. However, the previous results have already shown that SMART achieves a well-defined black hole mass due to a well-defined minimum in the χ^2-profile, which was probably supported by the intrinsic noise of the $N-$body simulation. Nevertheless, we check whether the minimum in the χ^2-curve changes when simulating an 'error' in the kinematic input data. For this, we model the positive half of the intermediate axis projection by adding Gaussian noise to the simulation chosen so that the velocity dispersion of the noisy kinematic simulation data results in an observationally realistic error of ~ 3 per cent ($\bar{v} = (0.14 \pm 7.64)\,\mathrm{km\,s^{-1}}$, $\bar{\sigma} = (288.86 \pm 7.80)\,\mathrm{km\,s^{-1}}$, $\bar{h}_3 = 0.00 \pm 0.02$, $\bar{h}_4 = 0.02 \pm 0.02$). To achieve even more realistic conditions we furthermore smooth the data by simulating a psf convolution with a FWHM of 2.43 arcsec which corresponds to 0.24 kpc, i.e. about a fourth of the sphere of influence, when assuming the galaxy to be at a distance of 20 Mpc. The so constructed velocity maps can be seen in Fig. B2. We provide SMART with the information about the used FWHM-value for the 2D psf convolution and test the same Υ and M_{BH} input masses as in Section 4.3. The corresponding results for the 1D mass recoveries when modelling this modified input data are plotted as turquoise lines in Fig. 8, and do not differ decisively from the ones
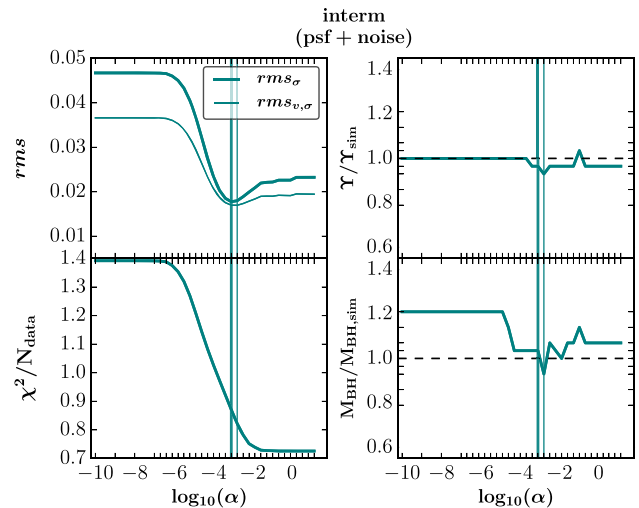
Figure 8. Choice of regularization and 1D mass recovery results for the positive half of a psf convolved noisy version of the intermediate axis projection. The rms and χ^2/N_{data} profiles show the same shape and suitable regularization region than for the noiseless and non-psf-convolved case. Also, the Υ- and M_{BH} reproduction shows no remarkable change within the overall scatter.

without psf convolution and noise. The stellar mass-to-light ratio is slightly underestimated by $\Delta\Upsilon(\alpha(\min(\mathrm{rms}_\sigma))) = 3.5$ per cent or $\Delta\Upsilon(\alpha(\min(\mathrm{rms}_{v,\sigma}))) = 7$ per cent and the black hole mass is overestimated by $\Delta M_{\mathrm{BH}}(\alpha(\min(\mathrm{rms}_\sigma))) = 3.5$ per cent or underestimated by $\Delta M_{\mathrm{BH}}(\alpha(\min(\mathrm{rms}_{v,\sigma}))) = 7$ per cent. The rms_σ, $\mathrm{rms}_{v,\sigma}$, and χ^2/N_{data} profiles are of course shifted upwards but follow the same form than the ones without noise and psf convolution (cf. Fig. 2). Fig. 9 shows the 2D mass recovery result of Υ and M_{BH} for this model. The stellar mass-to-light ratio is again correctly reproduced and the black hole mass is underestimated by only 7 per cent. With this, SMART is able to model the noisy and psf convolved kinematics as well as the default kinematics without any 'error' equally well within the overall scatter.
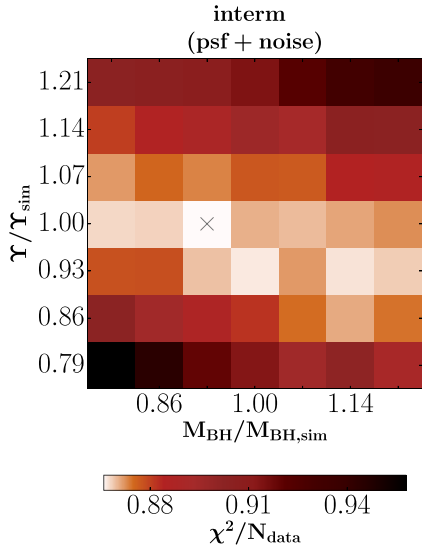
Figure 9. 2D mass recovery results of Υ and M_{BH} for the positive half of a psf convolved noisy version of the intermediate axis projection. We again evaluate 49 models with different Υ and M_{BH} input masses, covering a 2D grid with a step size of 7 per cent around the correct parameters. The favoured model is marked with a grey cross. The model finds the correct stellar mass-to-light ratio and slightly underestimates the black hole mass by 7 per cent. Within the overall scatter this resembles the results of the models without noise and psf convolution.

4.5.2 Changing the orbital bias factors ω_i

As discussed in Section 2.4, the orbital bias factors ω_i of equation (8) can be used to control the orbital weights w_i. In the absence of other constraints $w_i \sim \omega_i$. Our choice of $\omega_i = 1$ is somewhat arbitrary. In fact, it biases the w_is strongly away from the true solution. Thus, we want to test whether this affects our fits. Specifically, we test the opposite extreme. We remodel the positive half of the major axis, abbreviated below as X^+, by setting $\omega_i = w_i(X^+)$, where $w_i(X^+)$ are the orbital weights of the best-fitting model for X^+. We also remodel X^+ by setting the bias factors $\omega_i = w_i(X^-)$ to the orbital weights of the best-fitting model for the negative half of the major axis X^-. Fig. 10 shows the results for these completely independent model fits. As expected, the *rms* and χ^2/N_{data} profiles start with smaller values, since at $\alpha = 0$, the ω_is bias the orbital weights the strongest. As motivated above, in the specific case here, the weights are biased towards a previous fit, which explains the better initial χ^2 and *rms*. However, at our fiducial α range, the reproduction of the internal moments and the quality of the fit is the same as for the case with identical ω_is. As a consequence, this implies that the simplifying assumption of constant ω_i does not change the modelling results significantly.

4.5.3 Degeneracy

When redoing the just described analysis (Section 4.5.2) but using the orbital bias factors of the right half of the *intermediate* axis projection $\omega_i(Y^+)$ (brown line in Fig. 11) as initial values for remodelling X^+ we gain a minor improvement in the reconstruction of the internal moments since the rms_σ and $rms_{v,\sigma}$ values are a bit smaller compared to the default model (black line), though the mass recovery shows equal results. The fact that, for the same quality of fit (i.e. same χ^2), the *rms* of the internal moments is smaller for the model with ω_i assumed to be equal to orbital weights from another modelled
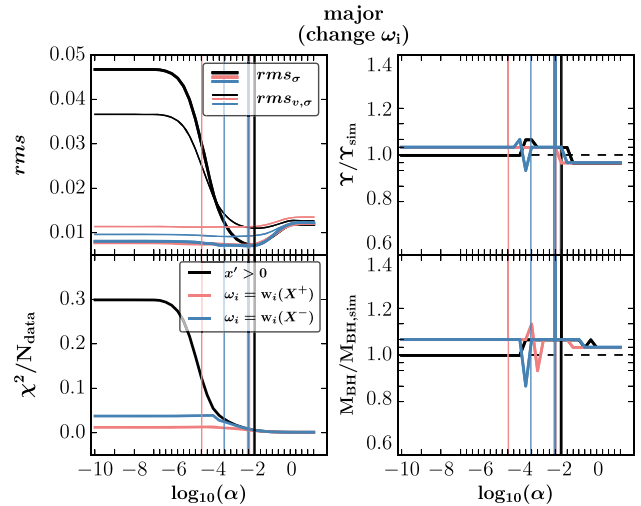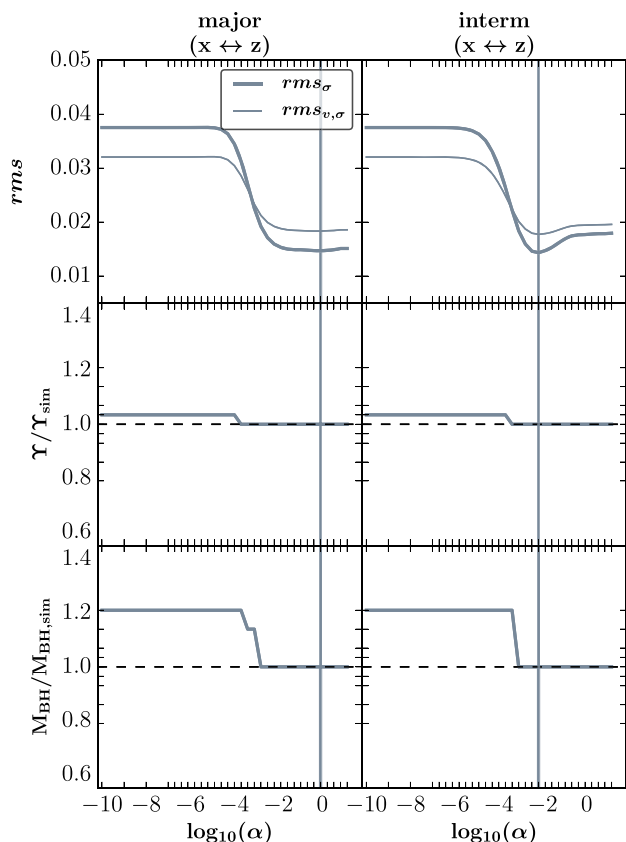

Figure 10. Choice of regularization and 1D mass recovery results for the positive half of the major axis projection when using the default constant orbital bias factors $\omega_i = $ const. (black line), when using the best-fitting orbital weights $w_i(X^+)$ of the positive half of the major axis as orbital bias factors, i.e. $\omega_i = w_i(X^+)$ (pink line), and when using $w_i(X^-)$ of the negative half of the major axis as orbital bias factors, i.e. $\omega_i = w_i(X^-)$ (blue line). The modified orbital bias factors do not improve the results, indicating that the choice of $\omega_i = $ const. is sufficient.
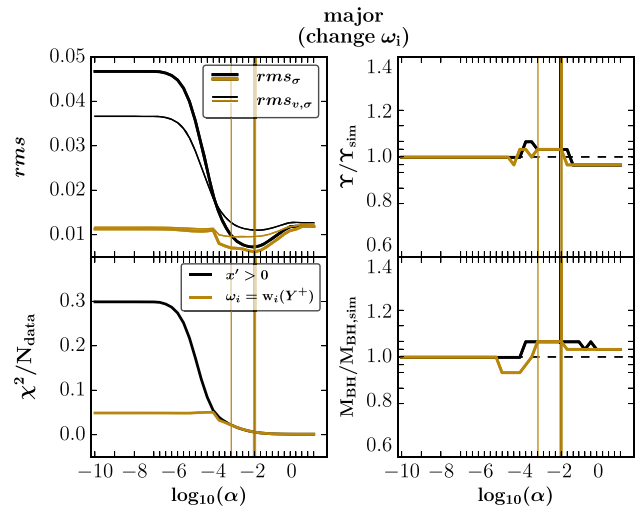
Figure 11. Choice of regularization and 1D mass recovery results for the positive half of the major axis projection when using the default constant initial orbital bias factors $\omega_i = $ const. (black line) and when using the best-fitting orbital weights $w_i(Y^+)$ of the positive half of the intermediate axis as orbital bias factors, i.e. $\omega_i = w_i(Y^+)$ (brown line). The additional information from the second projection axis appears to reduce the degeneracy leading to a minor improvement in the internal moments reproduction as seen in the lower rms_σ and $rms_{v,\sigma}$ values.

projection direction (in this case from the intermediate axis projection Y) suggests that these ω_i contain some information in addition to the kinematics of the given projection (in this case the major axis projection X). The fact that information from another line of sight can improve the model is not surprising. In fact, it shows that some of the already very small residual *rms* in the internal velocity moments is due to remaining degeneracies in the recovery of the

Figure 12. Choice of regularization and 1D mass recovery results for the positive half of the major axis projection (left column) and positive half of the intermediate axis projection (right column) when changing the *x*- and *z*-coordinates in the simulation so that the orbit sampling in SMART changes from a sampling of v_ϕ to v_θ. Whereas the mass recovery gets slightly improved, the rms$_\sigma$ and rms$_{v,\sigma}$ profiles show slightly deteriorated values. Overall, both techniques basically lead to the same results.

orbital weights. These degeneracies seem to be surprisingly small. However, our results imply that as long as the deprojected light profile and normalized DM halo are known and the orbit sampling is dense, masses and anisotropies can be recovered with very high accuracy, independent of the viewing angle.

4.5.4 Change in orbit sampling technique

Even though our results already prove the efficient ability of our orbit library to completely reproduce all necessary orbits in a triaxial potential, we want to check the robustness of our orbit sampling method (cf. Appendix C). We therefore change the angular momentum sampling direction from the minor axis to the major axis. This corresponds to a change of v_ϕ to v_θ samplings. The basic idea is that a more homogeneous angular momentum sampling along the major axis instead of the minor axis might improve the mass recovery. Thus, we change the major and minor axis coordinates within the simulation and rerun the models for the new major- (left column in Fig. 12) and intermediate-axis-kinematics (right column in Fig. 12). With this, the angular momentum orbit sampling is proceeded along the major axis of the simulated remnant. The results are shown in Fig. 12. One can see that both orbit libraries produce the same results. In fact, the modified orbit sampling procedure reveals a slightly better mass recovery but slightly worse internal moments reproduction

(higher rms$_\sigma$ and rms$_{v,\sigma}$ values) for equally good kinematic fits. Nevertheless, regardless of the chosen angular momentum sampling axis our orbit sampling technique (cf. Appendix C) of creating initial conditions, which belong to certain energy shells and angular momentum sequences, has proven to be a highly efficient technique. It produces a general and complete set of orbits for triaxial potentials being able to deal with changing structure in the integrals-of-motion space since it manages to reproduce all relevant properties and to radially adapt itself to the more spherical centre as well as the more prolate outskirts of the simulated galaxy.

4.5.5 Summary of robustness and uniqueness checks

In conclusion, these checks prove that SMART is robust against minor internal modifications as well as input data changes. SMART has proved its ability to handle with noisy and psf convolved data. Furthermore, we have shown that constant orbital bias factors are a good approximation. Even though it is impossible to get observations from two viewing points, we have demonstrated that this would allow to reduce the minor degeneracies allowed by the kinematic data even further. We have verified this by using the orbital bias factors from a second projection direction. Moreover, the results are not affected by changing the orbit sampling technique from setting up L_z sequences to setting up L_x sequences. This shows that, as expected, the choice of sampling axis is not decisive and that the orbit sampling routine is universal.

5 THE QUASI-UNIQUENESS OF THE ANISOTROPY RECONSTRUCTION WHEN FITTING FULL LOSVDS

The results of the previous section have shown that the anisotropy of the *N*-body merger remnant can be reconstructed with very high accuracy from the Schwarzschild models that we fitted to the full LOSVDs. This not only demonstrates the high accuracy of our orbit superposition model, but it also implies that when models can exploit the full information contained in the entire LOSVDs, the remaining degeneracy in the recovery of the distribution function cannot affect the anisotropy or mass recovery significantly. In this section, we want to use the maximum entropy technique to explore this in more depth.

5.1 The Maximum Entropy Technique and the Mathematical Structure of the Solution Space

As already described in Section 2.4, we solve for the orbital weights w_i by using a maximum entropy technique (cf. equations 7 and 8). The χ^2 term in equation (7) contains the kinematical constraints and is the deviation between observed LOSVDs $\mathcal{L}_{\mathrm{data}}$ and the model prediction $\mathcal{L}_{\mathrm{mod}}$, i.e. the weighted sum over the contributions of all orbits to LOSVD j' and line-of-sight velocity bin k,

$$\mathcal{L}_{\mathrm{mod}}^{j',k} \equiv \sum_{i=1}^{N_{\mathrm{orbit}}} w_i \, \mathcal{L}_{\mathrm{orb}}^{j',k,i}. \qquad (15)$$

It is convenient to think of the observed $\vec{\mathcal{L}}_{\mathrm{data}}$ and the model predictions $\vec{\mathcal{L}}_{\mathrm{mod}}$ as vectors with $N_{\mathrm{data}} = N_{\mathrm{losvd}} \times N_{\mathrm{vlos}}$ elements. Then,

$$\vec{\mathcal{L}}_{\mathrm{mod}} = \mathcal{L}_{\mathrm{orb}} \cdot \vec{w}, \qquad (16)$$

where $\mathcal{L}_{\mathrm{orb}}$ is a matrix with N_{data} rows and N_{orbit} columns.

In addition to the kinematical observations $\vec{\mathcal{L}}_{\mathrm{data}}$, the orbital weights $\vec{w}$ are subject to photometric constraints. In analogy to

equation (16):

$$\vec{p}_{mod} = P_{orb} \cdot \vec{w}, \tag{17}$$

where $\vec{p}_{mod}$ is a vector with the model predictions for the 3D luminosity density at spatial position j_3 in the galaxy ($j_3 = 1, \ldots, N_{phot}$). To guarantee the self-consistency of our model, the respective observed $\vec{p}_{data}$ are not included via a χ^2 term. Instead, we treat them as boundary conditions for the fit:

$$\vec{p}_{data} \overset{!}{=} \vec{p}_{mod}. \tag{18}$$

Hence, we seek for the maximum of equation (7) subject to the linear equality constraints

$$\vec{p}_{data} - P_{orb} \cdot \vec{w} = 0. \tag{19}$$

For convenience, we normalize the $\vec{p}_{data}$ such that $\sum \vec{p}_{data} = 1$. Since we are only interested in positive orbital weights (see below), the orbital weights obey $0 \leq w_i \leq 1$ and we can restrict the maximization to the respective N_{orbit}-dimensional convex quader.

To show that equation (7) has a unique global maximum that can be controlled through the bias factors ω_i it is convenient to consider the equivalent minimization problem for $f \equiv -\hat{S}$, given by multiplying equation (7) with -1.

Let us first consider equation (7) without the entropy term S. The χ^2 term can be written as

$$\chi^2 = -\vec{\mathcal{L}}_{data}^T C_v \vec{\mathcal{L}}_{data} + 2\vec{\mathcal{L}}_{data}^T C_v \mathcal{L}_{orb} \vec{w} - \vec{w}^T \mathcal{L}_{orb}^T C_v \mathcal{L}_{orb} \vec{w}, \tag{20}$$

where C_v is the covariance matrix of the observed LOSVDs and is positive definite. The Hesse matrix of χ^2 reads

$$\nabla^2 \chi^2 = 2\mathcal{L}_{orb}^T C_v \mathcal{L}_{orb}. \tag{21}$$

Because $\mathcal{L}_{orb}$ is positive by construction, the symmetric matrix $\nabla^2 \chi^2$ is at least positive semidefinite and χ^2 is convex.

The minimization of χ^2 alone, subject to the linear equality constraints equation (19), is therefore a convex optimization problem with affine equality constraints in standard form. As such, it only has a global minimum (e.g. Boyd & Vandenberghe 2004). In general, we cannot assume that χ^2 is *strictly* convex (i.e. that $\nabla^2 \chi^2$ is positive definite). The set of orbital weights that solve $\chi^2(\boldsymbol{w}) = \chi^2_{min}$ may therefore be non-unique. This is not surprising given that the linear equation

$$\vec{\nabla} \chi^2 = 2\vec{w}^T \mathcal{L}_{orb}^T C_v \mathcal{L}_{orb} + 2\vec{\mathcal{L}}_{data}^T C_v \mathcal{L}_{orb} \equiv 0 \tag{22}$$

will in general be underconstrained if $N_{orbit} > N_{data}$. As already mentioned above, the reconstruction of the distribution function is not unique even if the deprojected density and the potential are known. We give an example in Appendix D.

Because the Hesse matrix of $-S$ is diagonal with the ith element equal to $1/w_i$, the entropy $-S$ is *strictly* convex. In contrast to the case of χ^2, the set of orbital weights that minimize $-S$ (or, equivalently, that maximise S) is *unique*. For the entropy alone this is easy to see since

$$\nabla S = -\log \frac{w_i}{\omega_i} - 1 \equiv 0 \tag{23}$$

can be solved analytically: $w_i = \exp(-1) \cdot \omega_i$. The constraints from equation (19) will shift the solution, but the strict convexity still guarantees it to remain unique (e.g. Boyd & Vandenberghe 2004).

For general $\alpha > 0$, the Hesse matrix of f is the sum $\nabla^2(-S) + \alpha\nabla^2\chi^2$ and f is always strictly convex. Equation (7) subject to the constraints (19) hence always has a unique solution.

As already mentioned above, from an algorithmic point of view, it is advantageous to have a unique solution. From the physical point of

view this is not desirable because any algorithm that picks up only one of the potentially many solutions that minimize χ^2 in equation (6) may lead to a *bias*. However, suppose $\vec{s}_1$ and $\vec{s}_2$ are two solutions which lead to the same χ^2_{min}. By setting $\omega_i = s_{1,i} \cdot \exp(1)$ we can make $\vec{s}_1$ the global solution of equation (7). Likewise, by setting $\omega_i = s_{2,i} \cdot \exp(1)$ we can make $\vec{s}_2$ the global solution of equation (7). This shows that the maximum-entropy formulation of the problem allows in principle the reconstruction of the entire solution space (via variation of the ω_i).

5.2 Testing the uniqueness of the anisotropy recovery

The previous section has shown that the recovery of the distribution function (or, equivalently, of the orbital weights) is in general not unique, even when the deprojection and the potential are known. The maximum entropy technique recovers one of the many possible solutions, which is unique for every given set of ω_i. Variation of the ω_i allows to sample the full solution space. On the other hand, the fits of the N-body merger remnant have shown that the anisotropy recovery is very accurate and stable even to variations of the ω_i. Moreover, in Appendix D we explicitly construct two different phase-space distribution functions that fit a given set of kinematics equally well. Even though they have different orbital weights, they reveal very similar anisotropies in the second-order velocity moments. This suggests that while the recovery of the full distribution function is non-unique, the anisotropy of the second-order moments is actually very well constrained by the information contained in the full LOSVDs.

To investigate this further, we create kinematic data of several toy models with different intrinsic properties: with randomized orbit weights (called RANDOM in the following), with an overpopulation of box/chaotic orbits (called BOX), with an overpopulation of z-tubes (called ZTUBE), with an overpopulation of only the prograde z-tubes (called ZROT) and with an overpopulation of x-tubes (called XTUBE). We then fit the mock kinematic data of these toy models under different choices for the ω_i, trying to push the fitted orbit model towards extreme shapes. The goal is to test how accurate and stable the recovery of the internal velocity anisotropy is, when we fit the entire information contained in the LOSVDs.

The toy models are constructed as maximum-entropy models [i.e. through maximization of equation (7) with $\alpha = 0$; cf. Thomas et al. 2007]. For the BOX model, we increase the ω_i of all box orbits by a factor of 1000, for the XTUBE and ZTUBE models we increase the ω_i of the respective tube orbits by the same amount. For the ZROT toy model we increase the ω_i only for prograde z-tubes and for the RANDOM model we use randomized ω_i (cf. Appendix D). The weights are then still forced to satisfy the density constraints of the N-body simulation. For each toy model, we create kinematic mock data for four different projections (major-, intermediate-, minor-axis projections and the $\theta = 45°$, $\phi = 45°$ projection). We then model every projection of all toy models (in total 20 different input data) and test four different methods for the fits: We use (i) our default constant orbital bias factors, i.e. $\omega_i = 1$ corresponding to the Shannon-entropy (abbreviated as 'shannon' in Fig. 13), (ii) increased orbital bias factors by a factor of 10 for the box/chaotic orbits (box10), (iii) increased orbital bias factors by a factor of 10 for the z-tubes (ztube10), and (iv) increased orbital bias factors by a factor of 10 for the x-tubes (x-tube10).

Fig. 13 shows the resulting anisotropy profiles (when averaging over shells) for these models. The different rows correspond to the different input toy models and the different columns show the individual projection directions. The dotted data points symbolize the
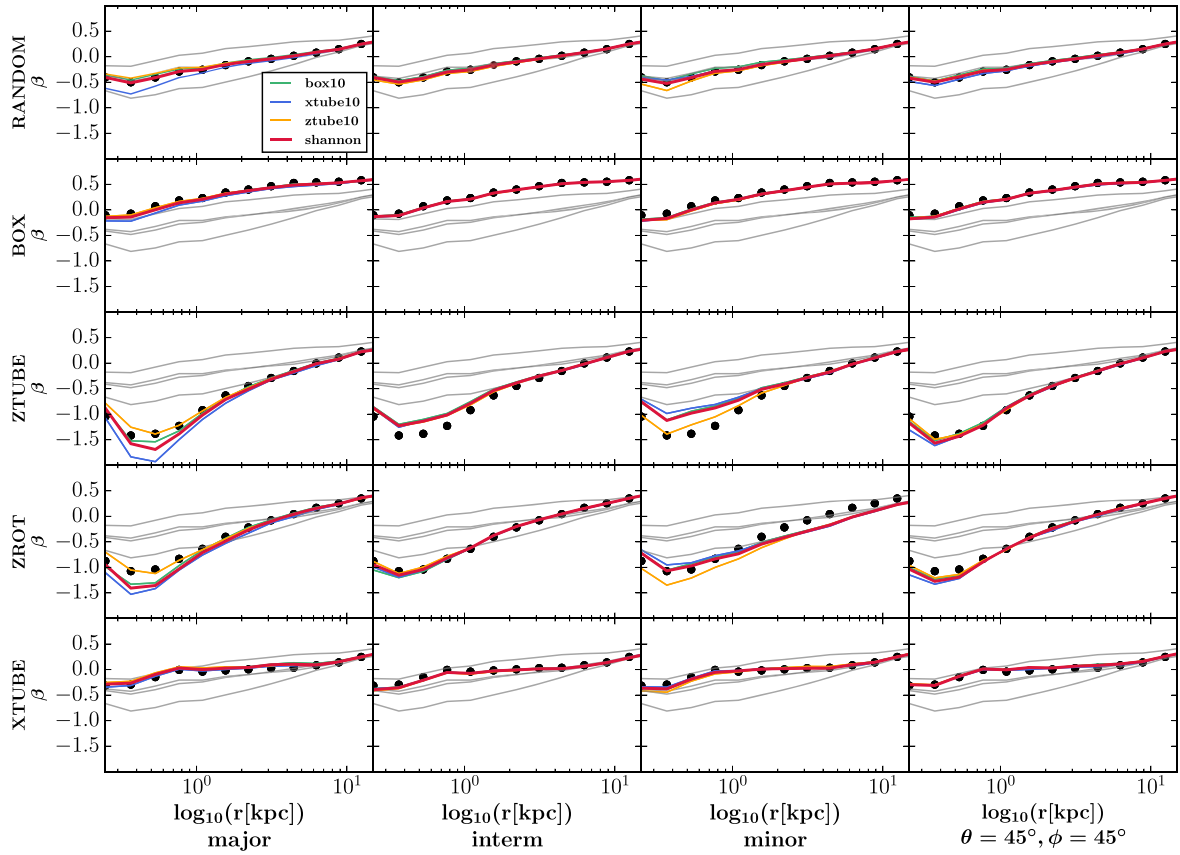
Figure 13. Recovery of the anisotropy profiles of different input toy models by SMART fits with different entropy functions. The input models (black dots) are constructed to have specific orbit classes overrated, resulting in different anisotropy profiles (the overrated orbit type is labelled on the *y*-axis of each individual row, details in the text). All the five toy models can be well recovered. This is independent of the choice of the projection axis (different columns; from left to right major, intermediate, minor and a diagonal axis) and from the assumed entropy function in the fit (coloured lines). For example, the anisotropy profile of the toy model with an overpopulation of box/chaotic orbits (called BOX; second row) is well reproduced by models maximizing the Shannon-entropy (red lines, labelled shannon) but also with other entropy functions that use a 10 times higher bias factor for box-orbits (green, labelled box10), for *x*-tubes (blue, xtube10) or for *z*-tubes (orange, ztube10). The grey lines correspond to the anisotropies implied by maximizing these four different entropy functions without fitting the kinematic data. They symbolize the variety of anisotropy profiles that are in principle possible for different choices of ω_i. After fitting the kinematic data, the average deviation (averaged over all radii and toy models fitted with different entropy techniques) between recovered and input anisotropy is very small, $|\Delta\beta| = 0.05$.

anisotropy profiles of the input toy models (which are of course the same for the different projections). The coloured lines (green, blue, orange, red) show the recovered anisotropies of SMART fits using entropy functions with enhanced bias factors for specific orbit types as described under (i)–(iv) above. The grey lines, for comparison, show the anisotropies that result when we maximize the above entropy functions (i)–(iv) without fitting the mock LOSVDs of the toy models. The grey lines therefore illustrate the variety of different anisotropy profiles that can be constructed by varying the orbital bias factors ω_i. They also indicate the range of different anisotropy profiles that are consistent with the given density distribution.

As one can see, even though the entropy functions tend to push the fits into extreme directions, the range of anisotropy profiles recovered after the fit to the LOVSDs is very narrow. When averaging over all radii and toy models fitted with different entropies, the mean deviation to the input models (dots) is $|\Delta\beta| = 0.05$. The average spread in beta inside the sphere of influence is slightly larger $|\Delta\beta(r < r_{SOI})| = 0.09$ than $|\Delta\beta(r_{SOI} < r < r_{FOV})| = 0.03$ outside r_{SOI}. One possible explanation for this might be the increase of degrees of freedom of spherical orbits near the centre. In addition, because β involves the ratio of the intrinsic dispersions, the same fractional error in the intrinsic dispersions results in a four times larger $|\Delta\beta|$

when the anisotropy is as tangential as $\beta = -1.5$ compared to the isotropic case. Overall, the Shannon entropy (red line) is able to recover the beta anisotropy best. This is our default entropy used in SMART.

These results together with Section 4 strongly suggest that the information contained in the full LOSVDs constrains the anisotropy in the second-order velocity moments very well. In turn, this is the reason why our models can reproduce the mass of the black hole and of the stars in the *N*-body simulation very well.

At larger radii, solely the reconstruction of the intrinsic anisotropy of the toy model with enhanced prograde *z*-tubes (i.e. ZROT) turns out to be difficult when viewed along the minor axis. This, however, is expected, since any rotation around the minor-axis cannot be observed and, thus, not be reconstructed from this viewing direction. Since we use equal ω_i for prograde and retrograde orbits in our *fitted* models, these models do not have intrinsic rotation in the *z*-tubes for this projection. Consequently, the tangential velocity *dispersion* is larger than in the toy model and the fitted β becomes too negative. We checked that if we use the true second-order velocity moment rather than the velocity dispersion in the tangential direction, then the differences between the outer profiles of the ZROT model and the fits along the minor axis disappear.
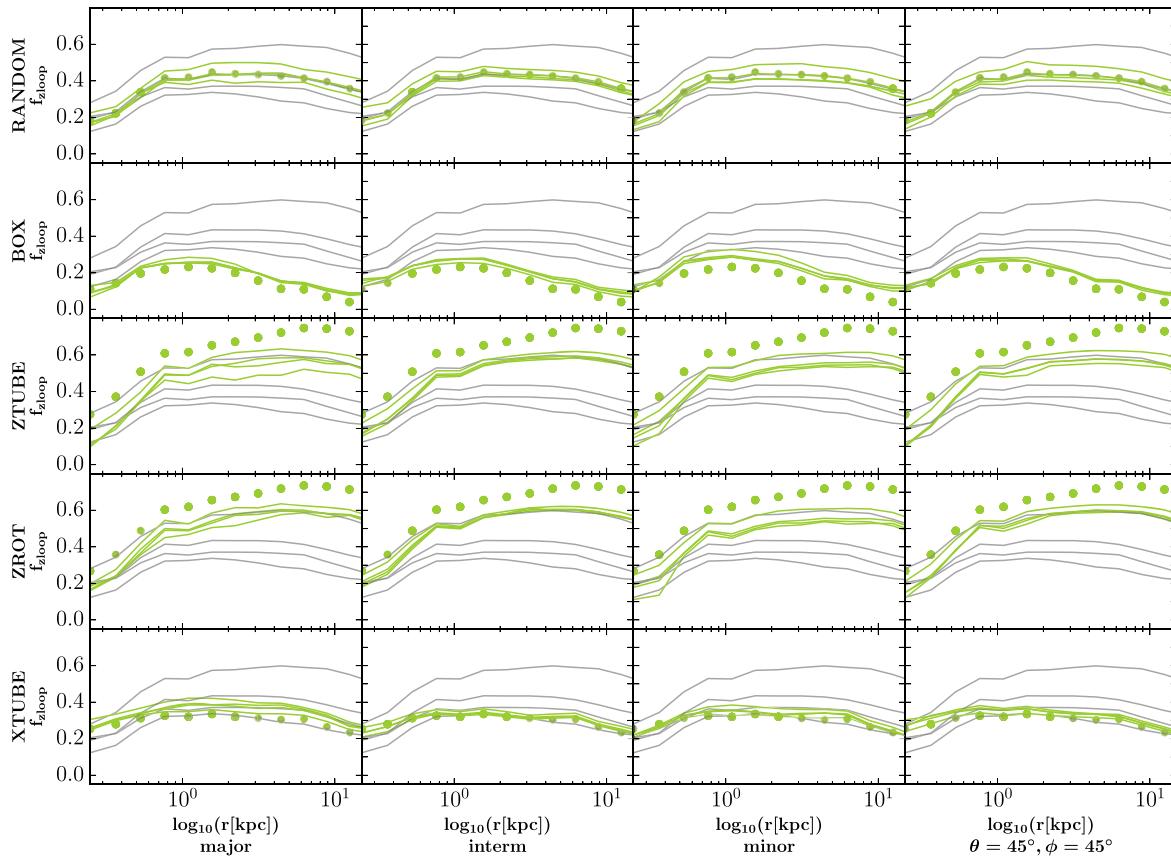
Figure 14. Recovery of the *z*-loop orbit fractions of different input toy models by models with different entropy methods. We here show the same analysis as in Fig. 13 but now for the reconstruction of the fraction of orbits classified as *z*-tubes. The colour coding is adapted to Figs 4 and C1. Independent of the tested projection, the *z*-loop fractions of the individual input toy models are well recovered by the models using different entropy methods. The same is true for the other orbit class fractions (see Figs E1- E3).

For dynamical models which aim for a full phase-space reconstruction (like Schwarzschild models) and which use the full information encoded in the LOSVDs (see also Vasiliev & Valluri 2019) the anisotropy should be recoverable with a typical error of $|\Delta\beta| \approx 0.05$. We solely found larger anisotropy discrepancies (up to $|\Delta\beta| = 0.5$) in extremely tangentially biased regions inside the sphere of influence.

As an example of the corresponding accordance of the reconstructed orbit fractions, Fig. 14 shows the case of *z*-tubes. The intended overpopulation of the *z*-tubes in the ZTUBE toy model (third row) and the ZROT toy model (fourth row) can be clearly seen in comparison to the other toy models. Independent of the chosen line of sight and entropy method (i.e. the bias factors ω_i), the fraction of *z*-tubes is qualitatively recovered and follows the enhancement tendencies. The orbit fractions however are less well determined than the anisotropy by the data and show a stronger dependence on the entropy. The same is true for the *x*-tubes, box/chaotic, and spherical/Kepler orbits shown in Figs E1–E3.

6 INTERMEDIATE AXIS ROTATION

One of the first investigations to check whether tube orbits with net rotation around the intermediate axis are stable in a triaxial ellipsoid was done by Heiligman & Schwarzschild (1979), who studied a triaxial model with fixed axis ratios of 1:1.25:2 by numerical methods and stated that '*Y*-tube orbits nearly certainly do not exist in the

adopted model'. Also Binney & Tremaine (2008, p. 263) assert that 'tube orbits around the intermediate axis are unstable' in a triaxial potential. Adams et al. (2007) analysed the orbit instability of orbits in a triaxial cusp potential, which are initially confined to one of the three principal axes, under a perturbation along the perpendicular direction. They found that orbits around any of the principal axes are unstable to perpendicular motions. However, according to previous results, they again state that orbits around the intermediate axis are more likely to be unstable. This instability is strongest for original box orbits lying in the *x*–*z* plane when the axial ratio of these two axes in the original plane is largest.

Our orbit classification routine in SMART finds no *y*-tubes in the sense that there is no sign conservation of the angular momentum along the intermediate axis over our default integration period of 100 SOS-crossings, agreeing with the aforementioned works done by other groups. However, some of the orbits integrated for the *N*-body models do show *y*-rotation for a limited time-span. When providing SMART with artificial projected input LOSVDs that mimic a net rotation along the intermediate axis, the model is able to produce a *y*-rotation signal of the order of $10 \, \mathrm{km \, s^{-1}}$ in the fit. A rotation of this magnitude is small but in principle detectable with today's telescopes' resolution. Fig. 15 shows the SMART fit to the major-axis projection of the simulation (cf. Fig. 3) when assuming the viewing angles of the minor-axis projection. With this, we simulate a hypothetical rotation along the intermediate axis. The top row shows the velocity- and h_3-map when stopping the orbit integration after 2
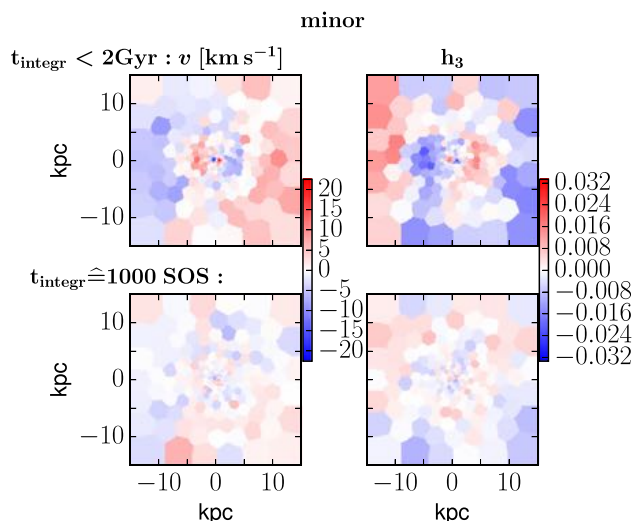
Figure 15. Fitting mock kinematic input data containing intermediate axis rotation. When modelling artificial LOSVDs showing a net rotation along the intermediate axis, SMART is able to reproduce a *y*-rotation signal when integrating the orbits for a limited integration time of 2 Gyr (first row). The *y*-rotation becomes visible in the *v* (left-hand panel) and h_3 (right-hand panel) maps. When integrating for 1000 SOS-crossings (second row), the *y*-rotation signal cannot be fitted by the model any more.

Gyr if this is shorter than the time needed for 100 SOS-crossings. Indeed, the model reproduces a *y*-rotation signal. The amplitude of this residual *y*-rotation becomes smaller and smaller when the orbital integration time is increased, and vanishes when all orbits are integrated for 1000 SOS-crossings (bottom row).

This analysis indicates that the model's triaxial potential, which is constructed based on the 3D density from the realistic *N*-body merger simulation – contrary to expectations – contains orbits with *y*-rotation for a physically relevant time span. What remains unclear at this moment is whether such a *y*-rotation indeed appears in real elliptical galaxies. If so, then the connection between kinematic misalignments and photometric twists is less constrained than often assumed when only rotation around the intrinsic long and short axes is considered.

7 DISCUSSION

7.1 Remaining sources of systematics

All relevant properties of the simulated merger remnant galaxy were proven to be recovered with a convincing precision and the deviations we found are almost negligible. The remaining deviations (in the $\sim 5 - 10$ per cent level) can be either originated by SMART or the simulation. One remaining contribution to the scatter in the final mass recovery certainly comes from the finite binning resolution of the simulation data and of the SMART models (see Sections 2 and 3). Especially, the need of extrapolating the density towards the centre due to limited resolution of the simulation holds uncertainties.

One more inaccuracy is potentially induced by the softening length in the simulation used to avoid unrealistic two-body encounters between massive particles. Force calculations for radii smaller than the softening length are consequently modified by the softening. In the close vicinity of the black hole, the stellar particles in the simulation are modelled using a non-softened algorithmic chain regularization technique (ARCHAIN; Mikkola & Merritt 2006, 2008) including post-Newtonian corrections (e.g. Will 2006). The

particles outside this chain radius are treated by using softened gravitational force calculations based on the GADGET-3 (Springel 2005) leapfrog integrator. The chain radius r_{chain} is chosen to be at least 2.8 times larger than the GADGET-3 softening length ϵ ($r_{\text{chain}} > 2.8\epsilon$) to ensure that the particles within the chain remain non-softened. The softening length in the simulation for the stellar particles is $\epsilon_* = 3.5$ pc and the softening length for the dark matter particles is $\epsilon_{\text{DM}} = 100$ pc. The mass recovery of the global stellar mass-to-light ratio and dark matter scale factor will be unaffected by these relatively small values. However, there might be a remaining influence on the black hole mass recovery within r_{SOI}. Nevertheless, this effect is expected to be small.

7.2 Comparison to other triaxial Schwarzschild models

We found two other dynamical modelling codes in the literature using Schwarzschild's orbit superposition technique dealing with triaxiality by van den Bosch et al. (2008) and Vasiliev & Valluri (2019). The code FORSTAND by Vasiliev & Valluri (2019) is applicable to galaxies of all morphological types. When assuming that the deprojection and dark matter halo is known and provided to the code, the models of noise-free axisymmetric disc mock data sets taken from *N*-body simulations showed very weak constraints on M_{BH}: any value between zero and 5–10 times the true black hole mass was equally consistent with the data. Read from fig. 2 in their paper, the stellar mass-to-light ratio showed a variation of around 20 per cent.

Jin et al. (2019) tested the triaxial Schwarzschild code by van den Bosch et al. (2008) by applying it to nine triaxial galaxies from the large-scale, high-resolution Illustris-1 simulation (Vogelsberger et al. 2014), which provides a stellar and dark matter resolution of $\sim 10^6 M_\odot$. When fixing the black hole mass and allowing the model to deproject the mock data set, the stellar mass within an average effective radius is underestimated by ~ 24 per cent and the dark matter is overestimated by ~ 38 per cent. Their averaged model results obtained from mock data with different viewing angles tend to be too radial in the outer regions with better anisotropy matches in the inner region.

Of course, these results cannot be used for direct comparison due to a widely varying resolution and in case of the analysis by Jin et al. (2019) the deprojection probably causes the major deviation. However, SMART for sure is able to add further progress in modelling triaxial galaxies and convinces with its proved precision.

8 SUMMARY AND CONCLUSION

We have developed a new triaxial dynamical Schwarzschild code called SMART and tested its efficiency and reliability by applying it to an *N*-body merger simulation including SMBHs. The simulation was deliberately selected due to its high accuracy, reasonable formation process, realistic internal structure and ability to precisely calculate the dynamics close to the central black hole. This ensured the possibility to check whether SMART is able to recover all relevant properties including the mass of an SMBH of a realistic triaxial galaxy when providing the deprojected light profile and normalized DM halo.

SMART is assembled with the feature to compute the potential and force by expansion into spherical harmonics, allowing to deal with non-parametric densities and haloes. Its orbit library contains 50000 integrated orbits that are set up by creating random initial radial and velocity values within given energy shells and angular momentum sequences and by filling the surfaces of section. This ensures the ability to adapt itself to a radially changing number of integrals

of motion. The orbit superposition is executed by maximizing an entropy-like quantity and by using the full LOSVDs instead of only Gauss–Hermite parameters alone.

These benefits enable SMART to reconstruct all relevant properties and features of the merger remnant with an excellent precision. We will now recap the requirements that were set on SMART and proved to be fulfilled in this analysis:

(i) SMART is able to reproduce the anisotropy profile and internal velocity dispersions with an rms_σ of only 1.2 per cent.

(ii) SMART reproduces the stellar mass-to-light ratio; black hole mass; and mass scale factor of the dark matter density profile with a precision on the 5–10 per cent level. To our knowledge, this is the first time that the intrinsic precision at given de-projected light profile has been quantified to be so high. This sets the basis for further investigations of the whole modelling procedure.

(iii) SMART well fits the LOSVDs with mean values and deviations of only $\bar{v} = (0.11 \pm 2.09)\,\mathrm{km\,s^{-1}}$, $\bar{\sigma} = (309.75 \pm 2.54)\,\mathrm{km\,s^{-1}}$, $\bar{h_3} = 0.00 \pm 0.01$ and $\bar{h_4} = 0.01 \pm 0.01$.

For the determination of these accuracy values, the simulation is modelled from up to five different projections. The mass recovery precision can be achieved for noiseless as well as noisy and psf convolved kinematic input data.

We extensively discuss that the maximum-entropy technique provides an elegant technique to study the range of possible orbit distributions consistent with a given set of data. Our tests with the N-body data and with additional toy models strongly suggest that when the full information contained in the entire LOSVDs is used to constrain the model, then the remaining degeneracies in the recovery of the exact phase-space distribution function do not affect 'macroscopic' properties of the galaxy models, like the anisotropy in the second-order velocity moments. This is the basis for the very good reconstruction of the orbital structure and mass of the black hole and stars with SMART.

It was shown that the orbit library is robust against axis changes and generates a complete set of well superpositioned orbits necessary to model a triaxial galaxy with all corresponding internal structures.

Also the accurate mass parameter recovery accomplished by SMART suggests only minor degeneracies contained in the projected kinematic data, provided that the deprojection is known. We showed that these remaining minor degeneracies could in principle be narrowed even more if information about the orbital bias factors from a second projection direction were provided.

When analysing the elevation and azimuthal internal velocity distributions of the simulation we find that the central radial bins show two maxima. This corresponds to the negative h_4-parameter in the centre and the strong tangential anisotropy produced during the core formation. SMART is able to reconstruct this phenomenon with an accuracy of ~ 7 per cent.

One more discovery of scientific interest is intermediate axis rotation which is produced by orbits contained in the model's orbit library representing the simulation's triaxial potential. Independent of the question whether such intermediate axis rotation really appears in the real universe, it was shown that our model contains orbits with y-rotation whose stability was empirically found to be maintained up to at least 2 Gyr.

ACKNOWLEDGEMENTS

DATA AVAILABILITY STATEMENT

The data underlying this article will be shared on reasonable request to the corresponding author.

REFERENCES

Aarseth S. J., Binney J., 1978, MNRAS, 185, 227
Adams F. C., Bloch A. M., Butler S. C., Druce J. M., Ketchum J. A., 2007, ApJ, 670, 1027
Anderson E. et al., 1999, LAPACK Users' Guide, 3rd edn., Society for Industrial and Applied Mathematics, Philadelphia, PA
Audet C., Dennis J., Jr, 2006, SIAM J. Optim., 17, 188
Bailin J., Steinmetz M., 2005, ApJ, 627, 647
Barnes J. E., 1992, ApJ, 393, 484
Barnes J. E., Hernquist L., 1996, ApJ, 471, 115
Begelman M. C., Blandford R. D., Rees M. J., 1980, Nature, 287, 307
Bender R. et al., 2005, ApJ, 631, 280
Bender R., 1988a, A&A, 193, L7
Bender R., 1988b, A&A, 202, L5
Bender R., Moellenhoff C., 1987, A&A, 177, 71
Bender R., Surma P., Doebereiner S., Moellenhoff C., Madejsky R., 1989, A&A, 217, 35
Bender R., Burstein D., Faber S. M., 1992, ApJ, 399, 462
Bender R., Saglia R. P., Gerhard O. E., 1994, MNRAS, 269, 785
Bertola F., Galletta G., 1978, ApJ, 226, L115
Bertola F., Galletta G., 1979, A&A, 77, 363
Binney J., Tremaine S., 2008, Galactic Dynamics. 2nd edn., Princeton Univ. Press, Princeton, NJ
Bissantz N., Debattista V. P., Gerhard O., 2004, ApJ, 601, L155
Boyd S., Vandenberghe L., 2004, Convex Optimization. Cambridge Univ. Press, Cambridge
Brainerd W. S., Goldberg C. H., Adams J. C., Garcia A., McKay S., Christian W., 1996, Comput. Phys., 10, 135
Brown C. K., Magorrian J., 2013, MNRAS, 431, 80
Cappellari M. et al., 2007, MNRAS, 379, 418
Cappellari M. et al., 2012, Nature, 484, 485
Cappellari M., 2002, MNRAS, 333, 400
Cappellari M., 2016, ARA&A, 54, 597
Cappellari M., Copin Y., 2003, MNRAS, 342, 345
Cash J., Karp A., 1990, ACM Trans. Math. Softw., 16, 201
Chabrier G., 2003, PASP, 115, 763
Cretton N., de Zeeuw P. T., van der Marel R. P., Rix H.-W., 1999, ApJS, 124, 383
de Lorenzi F., Debattista V. P., Gerhard O., Sambhus N., 2007, MNRAS, 376, 71
de Nicola S., Saglia R. P., Thomas J., Dehnen W., Bender R., 2020, MNRAS, 496, 3076
de Zeeuw T., 1985, MNRAS, 216, 273
Dehnen W., 1993, MNRAS, 265, 250
Ebisuzaki T., Makino J., Okumura S. K., 1991, Nature, 354, 212
Emsellem E. et al., 2007, MNRAS, 379, 401
Emsellem E., Monnet G., Bacon R., 1994, A&A, 285, 723
Faber S. M., Dressler A., Davies R. L., Burstein D., Lynden Bell D., Terlevich R., Wegner G., 1987, in Faber S. M., ed., Nearly Normal Galaxies. From the Planck Time to the Present, p. 175
Finozzi F., 2018, Triaxial Models of Massive Elliptical Galaxies, PhD thesis. Ludwig-Maximilians-University, Munich
Franx M., Illingworth G. D., 1988, ApJ, 327, L55
Gebhardt K. et al., 2000, AJ, 119, 1157
Genzel R., Tacconi L. J., Rigopoulou D., Lutz D., Tecza M., 2001, ApJ, 563, 527
Gerhard O. E., 1993, MNRAS, 265, 213
Heiligman G., Schwarzschild M., 1979, ApJ, 233, 872
Henon M., Heiles C., 1964, AJ, 69, 73

Hills J. G., Fullerton L. W., 1980, AJ, 85, 1281
Hohl F., Zang T. A., 1979, AJ, 84, 585
Hopkins P. F., Cox T. J., Hernquist L., 2008, ApJ, 689, 17
Illingworth G., 1977, ApJ, 218, L43
Jahnke K., Macciò A. V., 2011, ApJ, 734, 92
Jin Y., Zhu L., Long R. J., Mao S., Xu D., Li H., van de Ven G., 2019, MNRAS, 486, 4753
Jing Y. P., Suto Y., 2002, ApJ, 574, 538
Johansson P. H., Naab T., Burkert A., 2009, ApJ, 690, 802
Karl S. J., Aarseth S. J., Naab T., Haehnelt M. G., Spurzem R., 2015, MNRAS, 452, 2337
Kormendy J., Bender R., 1996, ApJ, 464, L119
Kroupa P., 2001, MNRAS, 322, 231
Le Digabel S., 2011, ACM Trans. Math. Softw., 37, 1
Magorrian J., 2006, MNRAS, 373, 425
Mehrgan K., Thomas J., Saglia R., Mazzalay X., Erwin P., Bender R., Kluge M., Fabricius J., 2019, ApJ, 887, 195
Merritt D., 2006, ApJ, 648, 976
Mikkola S., Merritt D., 2006, MNRAS, 372, 219
Mikkola S., Merritt D., 2008, AJ, 135, 2398
Mikkola S., Valtonen M. J., 1992, MNRAS, 259, 115
Miller R. H., Smith B. F., 1979, ApJ, 227, 407
Milosavljević M., Merritt D., 2001, ApJ, 563, 34
Monnet G., Bacon R., Emsellem E., 1992, A&A, 253, 366
Moster B. P., Naab T., White S. D. M., 2019, preprint (arXiv:1910.09552)
Naab T., Burkert A., 2003, ApJ, 597, 893
Naab T., Ostriker J. P., 2017, ARA&A, 55, 59
Naab T., Jesseit R., Burkert A., 2006, MNRAS, 372, 839
Navarro J. F., Frenk C. S., White S. D. M., 1996, Astrophys. J., 462, 563
Novak G. S., Cox T. J., Primack J. R., Jonsson P., Dekel A., 2006, ApJ, 646, L9
Oser L., Ostriker J. P., Naab T., Johansson P. H., Burkert A., 2010, ApJ, 725, 2312
Parikh T. et al., 2018, MNRAS, 477, 3954
Peng C. Y., 2007, ApJ, 671, 1098
Posacki S., Cappellari M., Treu T., Pellegrini S., Ciotti L., 2015, MNRAS, 446, 493
Press W., Vetterling W., Metcalf M., Flannery B., Teukolsky S., 1996, Cambridge University Press, Cambridge
Rantala A., Pihajoki P., Johansson P. H., Naab T., Lahén N., Sawala T., 2017, ApJ, 840, 53
Rantala A., Johansson P. H., Naab T., Thomas J., Frigo M., 2018, ApJ, 864, 113
Rantala A., Johansson P. H., Naab T., Thomas J., Frigo M., 2019, ApJ, 872, L17
Richstone D. O., 1982, ApJ, 252, 496
Richstone D. O., Tremaine S., 1984, ApJ, 286, 27
Richstone D. O., Tremaine S., 1985, ApJ, 296, 370
Richstone D. O., Tremaine S., 1988, ApJ, 327, 82
Rix H.-W., de Zeeuw P. T., Cretton N., van der Marel R. P., Carollo C. M., 1997, ApJ, 488, 702
Röttgers B., Naab T., Oser L., 2014, MNRAS, 445, 1065
Schechter P. L., Gunn J. E., 1978, AJ, 83, 1360
Schwarzschild M., 1979, ApJ, 232, 236
Schwarzschild M., 1993, ApJ, 409, 563
Sérsic J. L., 1963, Boletin de la Asociacion Argentina de Astronomia La Plata Argentina, 6, 99
Siopis C. et al., 2009, ApJ, 693, 946
Smith R. J., Lucey J. R., Conroy C., 2015, MNRAS, 449, 3441
Somerville R. S., Davé R., 2015, ARA&A, 53, 51
Springel V., 2005, MNRAS, 364, 1105
Syer D., Tremaine S., 1996, MNRAS, 282, 223
Tacconi L. J. et al., 2005, Messenger, 122, 28
Thomas J. et al., 2009, MNRAS, 393, 641
Thomas J. et al., 2011, MNRAS, 415, 545
Thomas J., Saglia R. P., Bender R., Thomas D., Gebhardt K., Magorrian J., Richstone D., 2004, MNRAS, 353, 391
Thomas J., Saglia R. P., Bender R., Thomas D., Gebhardt K., Magorrian J., Corsini E. M., Wegner G., 2005, MNRAS, 360, 1355

Thomas J., Jesseit R., Naab T., Saglia R. P., Burkert A., Bender R., 2007, MNRAS, 381, 1672
Thomas J., Ma C.-P., McConnell N. J., Greene J. E., Blakeslee J. P., Janish R., 2016, Nature, 532, 340
Toomre A., Toomre J., 1972, ApJ, 178, 623
Tremaine S., Henon M., Lynden-Bell D., 1986, MNRAS, 219, 285
Treu T., Auger M. W., Koopmans L. V. E., Gavazzi R., Marshall P. J., Bolton A. S., 2010, ApJ, 709, 1195
Tsallis C., 1988, J. Stat. Phys., 52, 479
Valluri M., Merritt D., Emsellem E., 2004, ApJ, 602, 66
van den Bosch R. C. E., de Zeeuw P. T., 2010, MNRAS, 401, 1770
van den Bosch R. C. E., van de Ven G., Verolme E. K., Cappellari M., de Zeeuw P. T., 2008, MNRAS, 385, 647
van der Marel R. P., Franx M., 1993, ApJ, 407, 525
van der Marel R. P., Cretton N., de Zeeuw P. T., Rix H.-W., 1998, ApJ, 493, 613
van Dokkum P. G., Conroy C., 2010, Nature, 468, 940
Vasiliev E., Valluri M., 2019, A New Implementation of the Schwarzschild Method for Constructing Observationally Driven Dynamical Models of Galaxies of All Morphological Types, Vol. 889, preprint (arXiv:1912.04288) .
Vazdekis A. et al., 2015, MNRAS, 449, 1177
Vincent R. A., Ryden B. S., 2005, ApJ, 623, 137
Virtanen P. et al., 2019, SciPy 1.0: fundamental algorithms for scientific computing in Python, 17, Springer Science and Business Media LLC, preprint (arXiv:1907.10121)
Vogelsberger M. et al., 2014, Nature, 509, 177
White S. D. M., Narayan R., 1987, MNRAS, 229, 103
Will C. M., 2006, Living Rev. Rel., 9, 3
Williams T. B., Schwarzschild M., 1979, ApJS, 41, 209

APPENDIX A: SURFACE BRIGHTNESS, ELLIPTICITY, AND POSITION ANGLE PROFILE

When fitting elliptical isophotes (Bender & Moellenhoff 1987) to the surface brightness maps for the principal axis directions of the
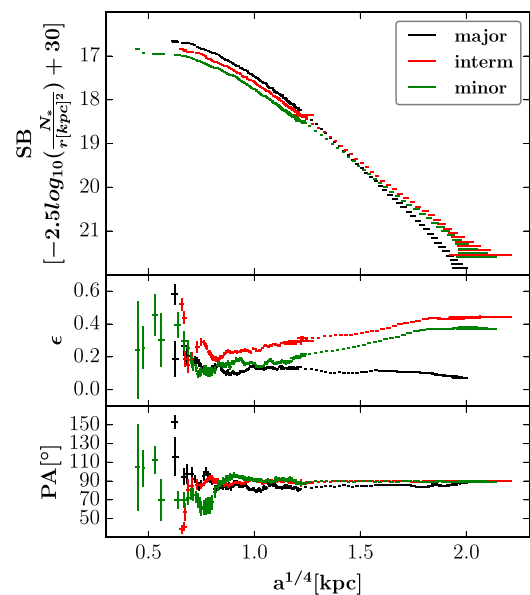

Figure A1. Surface brightness (first row), ellipticity (second row), and position angle profile (third row) for the major- (black), intermediate- (red), and minor-axis (green) projections of the simulation plotted against the semimajor axis *a* of the elliptical isophotes. The simulation demonstrates to be generic triaxial.

simulation in units of stellar simulation particles one can see that all three projections differ in their surface brightness (SB) and ellipticity profile ($\epsilon = 1 - b/a$ with a being the semimajor and b being the semiminor axis of the elliptical isophotes). The position angle (PA) profile shows some isophotal twists. Overall, the simulation appears to show typical triaxial behaviour (see Fig. A1).

APPENDIX B: VELOCITY, SURFACE BRIGHTNESS, AND χ^2 MAPS

Figs B1 and B2 show the velocity maps of the kinematic input data and their fits by SMART for four different projection axes and an additional psf convolved version of the intermediate axis. The plots
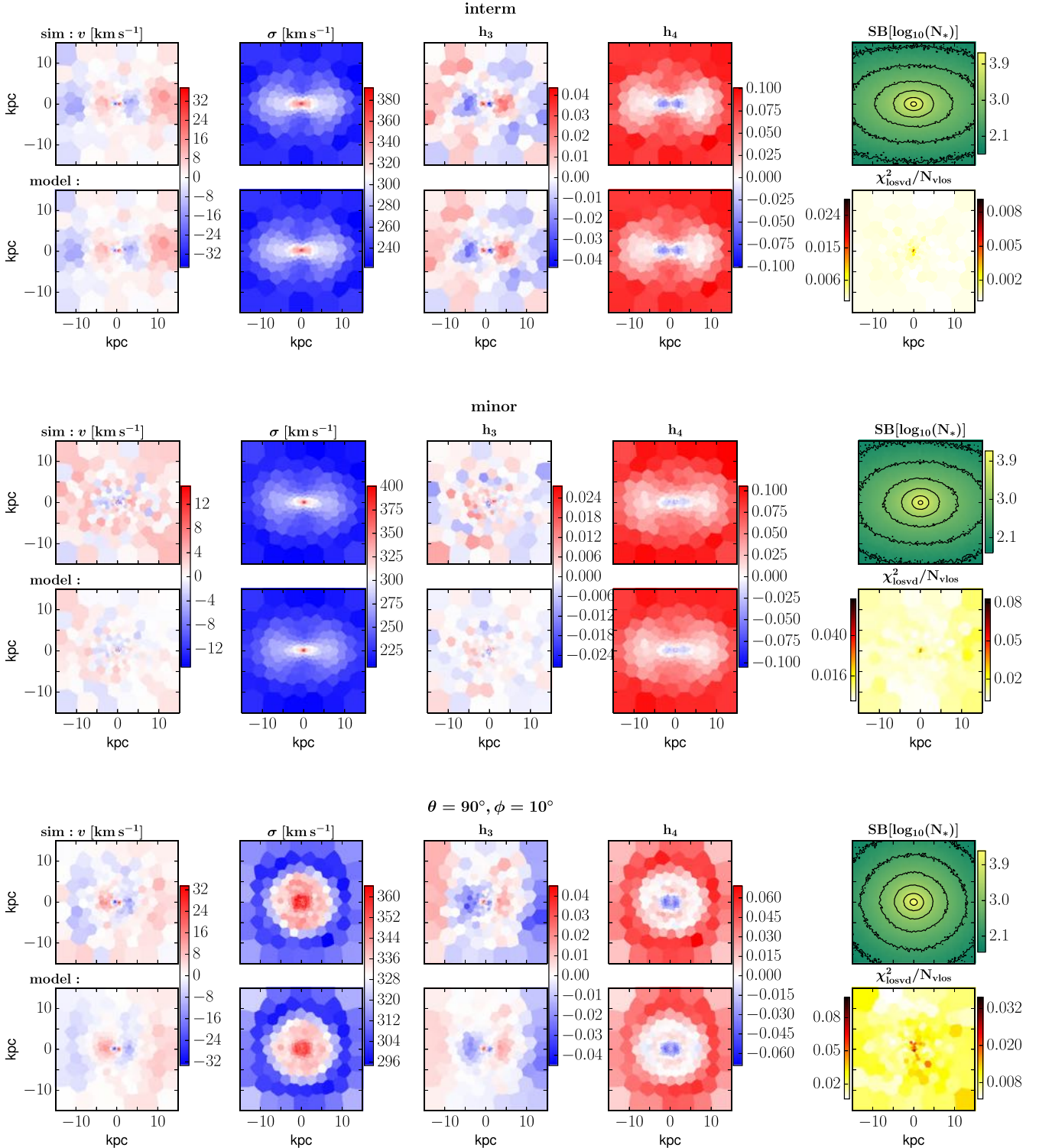
Figure B1. Velocity and surface brightness maps of the simulation (top row) as well as velocity maps of the model and χ^2 map as deviation from the kinematic input data with the modelled fit (bottom row) for different projections. The individual projection axis can be read from the title (for the major axis projection and a more detailed caption description see Fig. 3).
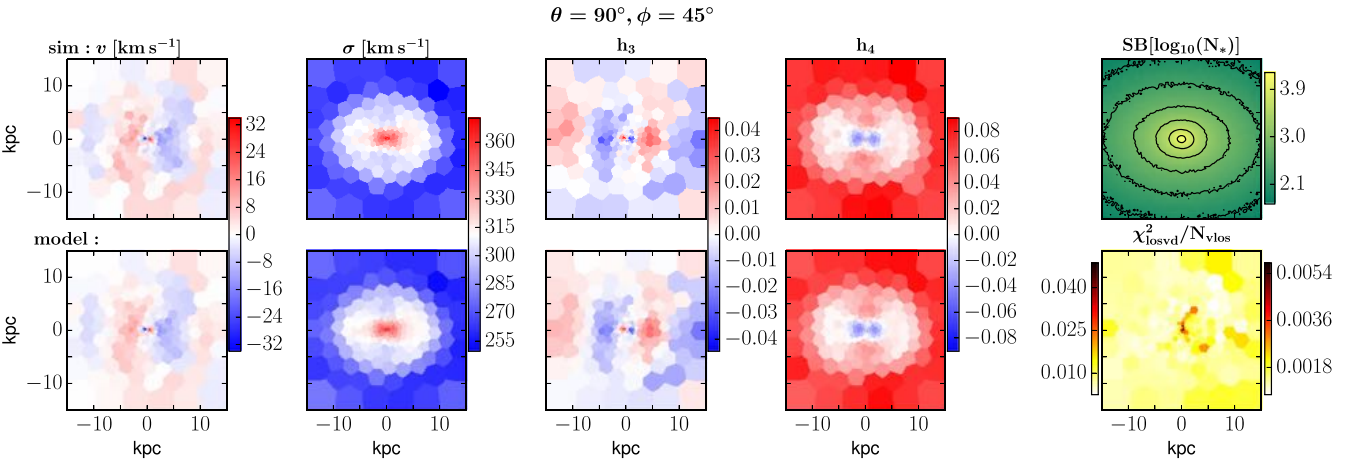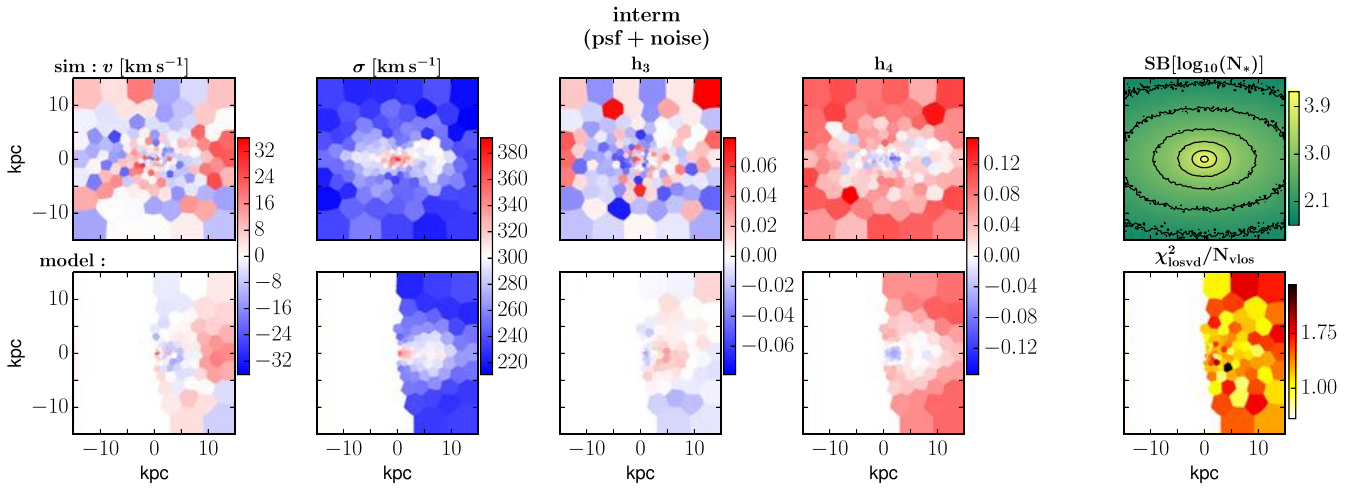
$\theta = 90°, \phi = 45°$

Figure B1 *– continued*

interm
(psf + noise)

Figure B2. Velocity and surface brightness maps of the simulation (top row) as well as velocity maps of the model and χ^2-map as deviation from the kinematic input data with the modelled fit (bottom row) for the noisy and psf convolved intermediate axis projection (for a more detailed description, see caption in Fig. 3 and Section 4.5.1).

also contain surface brightness maps in form of stellar simulation particles and χ^2-maps as deviation between the simulation data and modelled fit. As already described in Section 4.1 one can see that SMART manages to fit the kinematic input data independent of the chosen projection.

## APPENDIX C: ORBITAL REPRESENTATION OF THE PHASE SPACE

For generating our orbital initial conditions we set up energy shells by calculating the maximum allowed potential energy for N_E radii between the minimum allowed pericenter chosen to be $r_{peri,min} = r_{min}$ and the maximum allowed apocenter of $r_{apo,max} = r_{max}$. The radial bins are sampled by using formula 4. Each energy shell $i_E \in [1, N_E]$ is then subdivided in $i_E(L_z)$ sequences. We empirically find $i_E(L_z) = i_E^2$ as appropriate choice for the number of sequences per energy shell. The orbits for a specific sequence share the same initial z-component of the angular momentum L_{z,i_E}. These L_{z,i_E} sequences are logarithmically sampled between the minimum and maximum

allowed L_z-value in dependence of the radius $r(i_E)$ of the specific bin.

The final orbital initial spatial conditions (r_i, θ_i, ϕ_i) are then given

(i) by randomly sampling azimuthal angles $\phi_i \in [0, 2\pi]$,

(ii) by setting the elevation angles $\theta_i = 0$ because every orbit crosses the equatorial plane, and

(iii) by randomly sampling possible radial values r_i between the minimum and maximum allowed apsis, i.e. $r_i \in \left[r_{peri}(L_{z,i_E}), r_{apo}(L_{z,i_E}) \right]$.

While sampling the energy as an integral of motion is straightforward, the sampling of L_z is an arbitrary way to qualify the azimuthal velocity v_ϕ as the parameter we actually want to sample. In analogy, one could also sample the elevation velocity v_θ in terms of the x-component of the angular momentum L_x, which is discussed in more detail in Section 4.5.4. The computation of $r_{peri}(L_{z,i_E})$ and $r_{apo}(L_{z,i_E})$ is thereby done under the wrong assumption that L_{z,i_E} was conserved. Strictly speaking, this is only true for an axisymmetric potential as limiting case. However, our tests above show that this does not bias the results obtained with our orbit library. The remaining
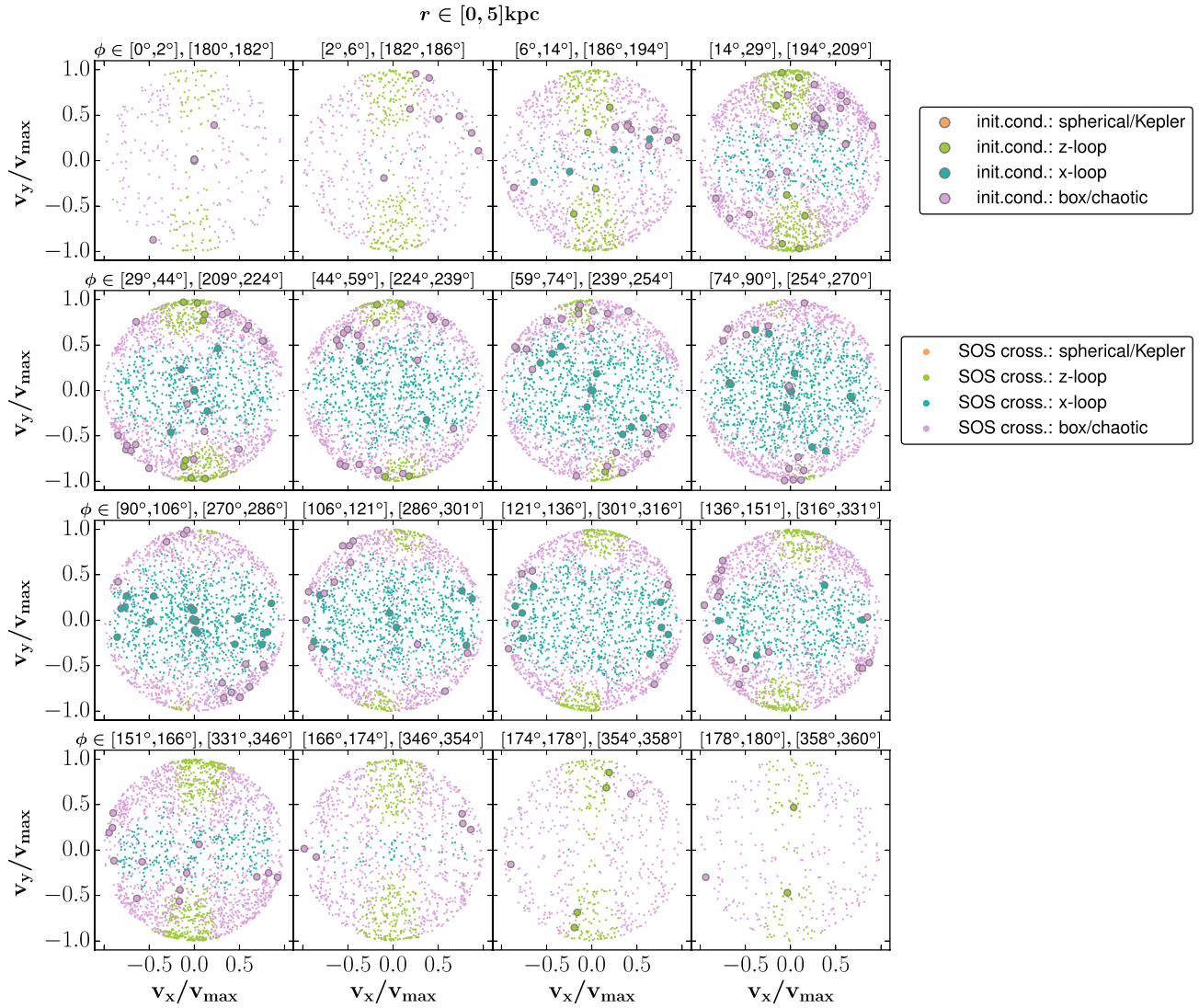
Figure C1. Orbital Phase-space coverage in the $x - y$ plane. We here plot the normalized velocity components v_x, v_y of all orbits in a single energy shell. This includes the orbital starting points (thick dots) as well as SOS-crossings during the time evolution of the orbits (thin dots). To consider all five dimensions of our starting space we distinguish between several radial and azimuthal annulus sectors of the plane (the chosen radial and azimuthal intervals are labelled above the individual panels). The orbit library produces a representative coverage of the phase space because the orbital imprints homogeneously fill the area enclosed by the unit circle.

initial velocity conditions $(v_{r,i}, v_{\theta,i}, v_{\phi,i})$ can then be subsequently computed as

(i) $v_{\phi,i} = \frac{L_{z,i_E}}{r_i}$,

(ii) $v_{r,i} \in [0, v_{r,\max}]$ with $v_{r,\max} = \sqrt{2(E - \Phi(r_i, \theta_i = 0, \phi_i)) - v_{\phi,i}^2}$, where E is the total energy and Φ the potential and

(iii) $v_{\theta,i} = \sqrt{2(E - \Phi(r_i, \theta_i = 0, \phi_i)) - v_{\phi,i}^2 - v_{r,i}^2}$.

More initial conditions are generated by filling the surfaces of section (SOS; Henon & Heiles 1964; Richstone 1982). The surface of section, also called Poincaré section, consists of the r_i- and $v_{r,i}$-values of the orbits crossing the equatorial plane, i.e. $\theta_i = 0$, in upwards direction. The topology of the SOS depends on the integrals of motion. The orbit library representatively fills the phase-space if the SOS is properly filled. For this, we randomly generate azimuthal

angles ϕ_i which get divided in N_{sector} azimuthal sectors. For each azimuthal sector, we then sample $(r_i, v_{r,i})$-tuples that are chosen so that their distance to the nearest imprint-tuple is maximized. The remaining initial conditions $v_{\phi,i}$ and $v_{\theta,i}$ are generated as before. To create a homogeneous distribution of pro- and retrograde orbits, the orbits contained in the library which are later on classified as regular orbits (see Section 2.3.1) get duplicated by changing the sign of their direction of rotation.

For an illustration of our 5D starting space of the stellar orbits in Fig. C1, we show a series of 2D plots with velocity spheres on annulus sectors (chosen radial and azimuthal sections) in the equatorial plane (i.e. $\theta = 0$). Since the magnitude of the velocity vector $\sqrt{v_x^2 + v_y^2 + v_z^2}$ is determined by the energy E, it is sufficient to plot v_x, v_y-imprints for a certain energy shell (the remaining v_z-component is then given as velocity shell in dependence of the value of E). We show both, the velocity components v_x, v_y of the
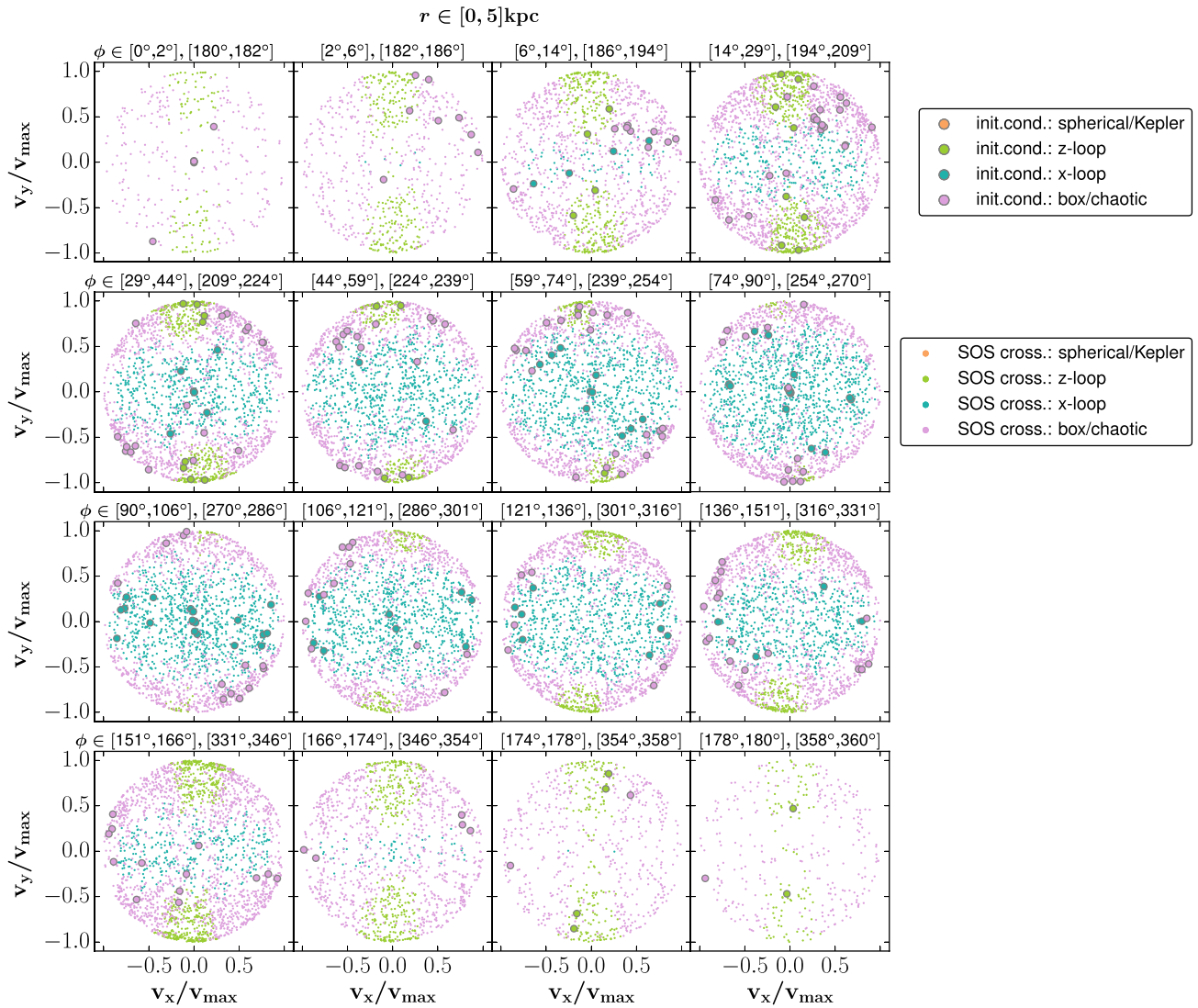
Figure C1 *– continued*

orbital initial starting point (marked as thick dots) as well as the orbital imprints for every crossing event in the subsequent time evolution (thin dots). The velocity components are normalized by $v_{max}(r, \theta, \phi) = \sqrt{2(E - \Phi(r, \theta, \phi))}$, with Φ being the gravitational potential. The different colours correspond to the different orbit types. Fig. C1 shows that the orbits of our orbit library homogeneously represent the accessible phase space. A sufficient coverage of the phase space is crucial for a reliable model. In addition, one can see that the actual starting points of the orbits can be chosen in very different ways. Our random choice is only one possibility that leads to an appropriate phase-space representation. Most of the space gets automatically filled by the orbital imprints over time.
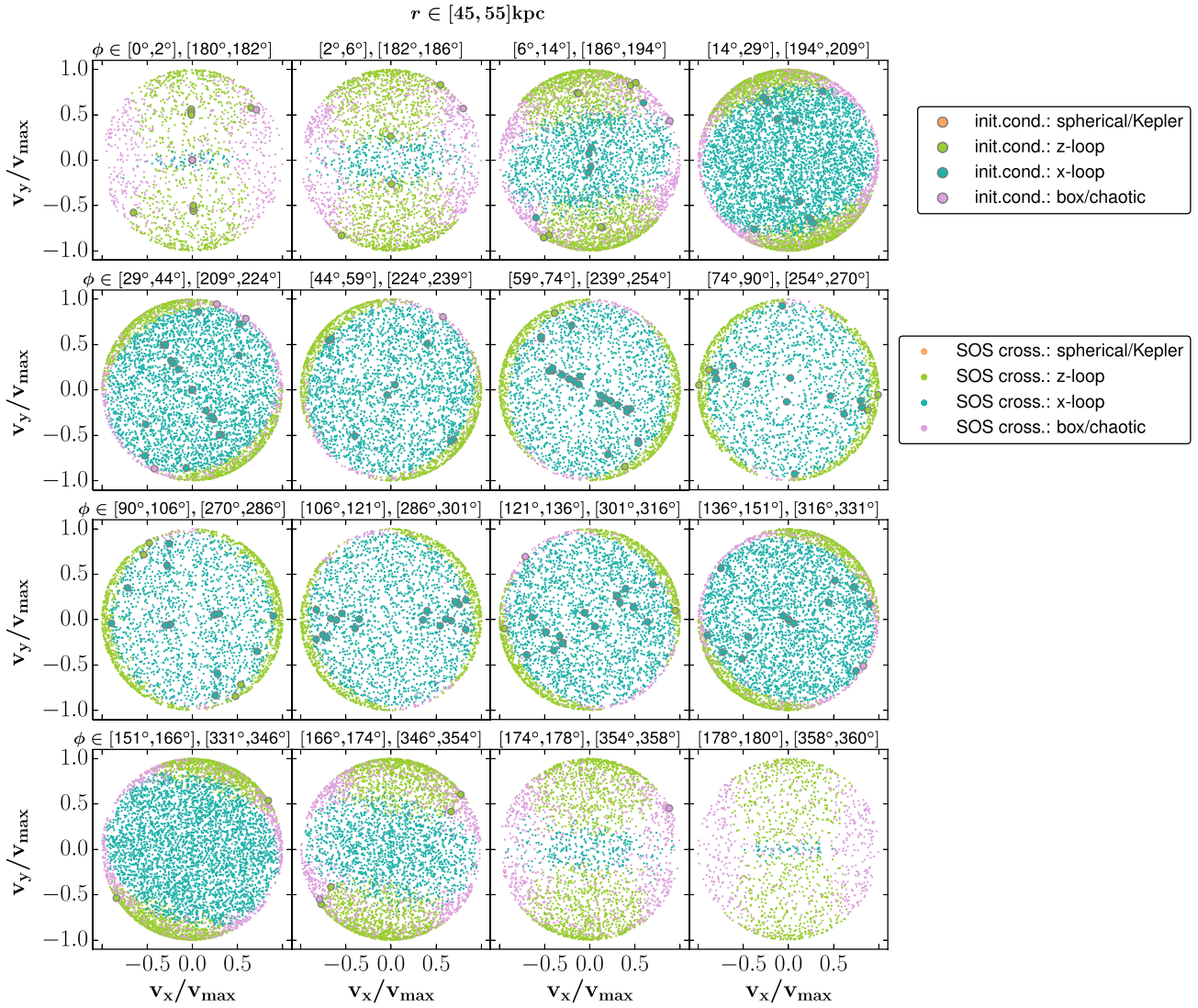
$r \in [45, 55]\,\mathrm{kpc}$

Figure C1 *– continued*

APPENDIX D: OPTIMIZATION ALGORITHM AND TEST

To find the unique set of orbital weights that maximizes $\hat{S}$ our code conceptionally seeks for a solution

$$\nabla_w \hat{S} = 0, \tag{D1}$$

subject to the constraints (19).

Technically, we follow Richstone & Tremaine (1988) and treat the orbital weights $\boldsymbol{w}$ and the kinematical model predictions

$$\vec{y} \equiv \vec{\mathcal{L}}_{\mathrm{data}} - \vec{\mathcal{L}}_{\mathrm{mod}} \tag{D2}$$

as independent variables. The actual dependence $\vec{y} = \vec{y}(\vec{w})$ (equation 16) is added to the constraints.

Thus, let

$$\vec{x} \equiv \begin{pmatrix} \vec{w} \\ \vec{y} \end{pmatrix} \tag{D3}$$

be the $N_{\mathrm{orbit}} + N_{\mathrm{data}}$ new variables, then the model solves

$$\nabla_x \hat{S} - \mathbf{C}^{\mathrm{T}} \cdot \lambda = 0 \tag{D4}$$

for the x_i and for $N_{\mathrm{data}} + N_{\mathrm{phot}}$ Lagrange multipliers λ_j (combined in the vector $\vec{\lambda}$). The matrix

$$\mathbf{C} \equiv \begin{pmatrix} \mathrm{P}_{\mathrm{orb}} & 0 \\ \mathcal{L}_{\mathrm{orb}} & 1 \end{pmatrix} \tag{D5}$$

contains the constraint equations

$$\begin{pmatrix} \vec{p}_{\mathrm{data}} \\ \vec{\mathcal{L}}_{\mathrm{data}} \end{pmatrix} = \mathbf{C} \cdot \vec{x}. \tag{D6}$$

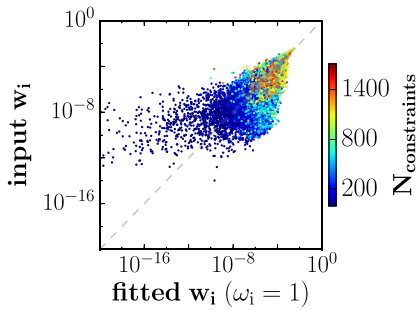Equation (D4) is non-linear and solved with a Newton method:

$$\vec{x}^{(n+1)} = \vec{x}^{(n)} - \left(\frac{\mathrm{dg}}{\mathrm{dx}}\right)^{-1} \vec{g}, \tag{D7}$$

or,

$$\vec{\Delta} \boldsymbol{x}^{(n)} = - \left(\frac{\mathrm{dg}}{\mathrm{dx}}\right)^{-1} \vec{g}, \tag{D8}$$

where

$$g \equiv \nabla_x \hat{S} - \mathbf{C}^{\mathrm{T}} \cdot \lambda. \tag{D9}$$

Figure D1. Recovery of the orbital weights of the RANDOM test model described in Section D. Each dot represents one orbit with the colour indicating the number of LOSVD data points $N_{\text{constraints}}$ that the orbit contributes to. For the recovery of the weights we fitted the kinematics of the RANDOM model using our fiducial constant bias factors $\omega_i = \text{const.}$ (Shannon entropy). Due to the degeneracy in the χ^2 minimization, the recovered orbital weights differ from the original weights. Larger differences are observed for orbits which are less constrained by data (blue points).

At each iteration, the Lagrange multipliers are updated via (D6),

$$\begin{pmatrix} \Delta \vec{\boldsymbol{p}}_{\text{data}} \\ \Delta \vec{\boldsymbol{\mathcal{L}}}_{\text{data}} \end{pmatrix} = \mathrm{C} \cdot \Delta \vec{x}, \tag{D10}$$

which leads to

$$\mathrm{A} \cdot \vec{\lambda} = \begin{pmatrix} \Delta \vec{\boldsymbol{p}}_{\text{data}} \\ \Delta \vec{\boldsymbol{\mathcal{L}}}_{\text{data}} \end{pmatrix} + \mathrm{C} \cdot \left(\frac{\mathrm{dg}}{\mathrm{dx}} \right)^{-1} \cdot \nabla_x \hat{S}, \tag{D11}$$

$$\mathrm{A} \equiv \mathrm{C} \left(\frac{\mathrm{dg}}{\mathrm{dx}} \right)^{-1} \mathrm{C}^{\mathrm{T}}. \tag{D12}$$

The Jacobian $\frac{\mathrm{dg}}{\mathrm{dx}}$ is diagonal and its inverse is easy to compute. The only matrix that needs to be inverted numerically is A and its dimension is $N_{\text{data}} + N_{\text{phot}} < N_{\text{orbit}}$.

Modulo the scaling by $(\frac{\mathrm{dg}}{\mathrm{dx}})^{-1}$, A reads

$$\mathrm{A} = \begin{pmatrix} \mathrm{P}_{\text{orb}} \mathrm{P}_{\text{orb}}^{\mathrm{T}} & \mathrm{P}_{\text{orb}} \mathcal{L}_{\text{orb}}^{\mathrm{T}} \\ \mathcal{L}_{\text{orb}} \mathrm{P}_{\text{orb}}^{\mathrm{T}} & \mathcal{L}_{\text{orb}} \mathcal{L}_{\text{orb}}^{\mathrm{T}} + 1 \end{pmatrix}. \tag{D13}$$

The required linear algebra operations are implemented through the LAPACK library (Anderson et al. 1999).

In practice, to find the best-fitting orbit model, we start with a very small value α_0 and then iteratively increase α until χ^2 does not change anymore. Everytime we change $\alpha \rightarrow \alpha + \mathrm{d}\alpha$ the unique solution to equation (7) will shift slightly from $\vec{w}$ to $\vec{w} + \mathrm{d}\vec{w}$ in the space of the orbital weights. Because $f \equiv -\hat{S}$ is differentiable with respect to α we can keep the new solution $\vec{w} + \mathrm{d}\vec{w}$ in an arbitrarily small neighbourhood around $\vec{w}$ by limiting $\mathrm{d}\alpha$ accordingly. For strictly convex f, the Newton method converges locally (and the convergence is quadratic). This means that once we have found a solution for some value of α, the convergence of the Newton steps for neighbouring $\alpha + \Delta \alpha$ is guaranteed (and fast) if we use the solution at α as starting point for the search at $\alpha + \Delta \alpha$: it is only a question of limiting $\Delta \alpha$, if necessary. In this way, we can iteratively solve for any value of α starting from α_0. In practice, we increase α by a factor of 2 in each iteration. Intermediate steps with a smaller α increment are inserted in case an iteration has not converged (which almost never happens).

At the initial α_0 we start from a homogeneous distribution of orbital weights. Methods with guaranteed convergence even from starting points outside of the constraint conditions have been developed. We do not use such methods, because in practice we always find the solution of equation (D4) even from an initially homogeneous
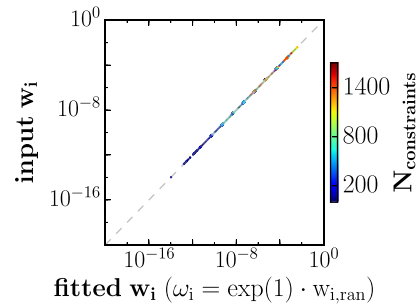
Figure D2. Same as Fig. D1, but here we fitted the RANDOM model using $\omega_i = \exp(1) \cdot w_{i,\text{ran}}$. With these bias factors the unique maximum of equation (7) should occur at the original weights $w_{i,\text{ran}}$ of the RANDOM model. And indeed, even though we start the fit with an initial guess where all the weights are equal, the true solution is reproduced with very high precision. This demonstrates the robustness and high accuracy of our optimization algorithm. The two different fits presented here and in Fig. D1 illustrate how the maximum entropy technique with variable ω_i can be used to sample different solutions that minimize the χ^2.
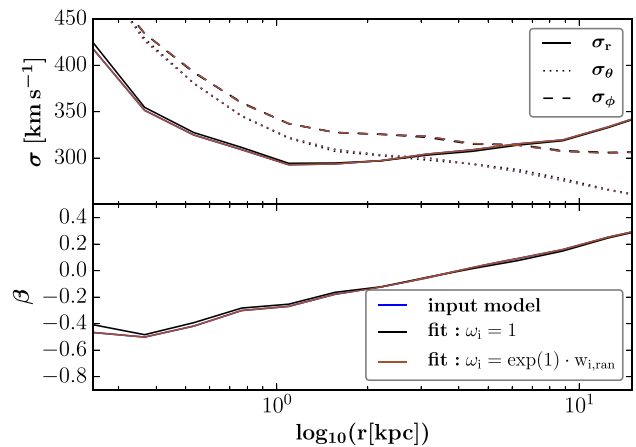
Figure D3. Internal velocity structure of the two fits presented in Fig. D1 (black lines) and D2 (red lines). Despite the different orbital weight distributions, the anisotropy in the second-order velocity moments is almost equally well recovered in both cases. This provides evidence that when using the full information contained in the entire LOSVDs, the remaining degeneracies in the recovery of the distribution function of triaxial galaxies (i.e. the differences in the detailed population of the various orbits) have only little impact on the 'macroscopic' internal galaxy properties like the anisotropy β. This, in turn, is crucial for a precise mass reconstruction.

distribution of orbital weights. Since the solution is global and unique for each α, convergence at any step of the α sequence can be tested based on equation (D4) itself.

To test our implementation, we reconstruct the kinematical data of a toy model with randomized orbital weights. The toy model is constructed as a maximum-entropy model [i.e. through maximization of $\hat{S}$ in equation (7) with $\alpha = 0$]. The bias factors ω_i for the orbital weights are set to $\omega_i = 10^{r_i}$, where $r_i \in [0, 3]$ are random numbers. After maximization of $\hat{S}$ subject to the density constraints, the resulting orbital weights w_i satisfy the density constraints of the N-body simulation. Due to these density constraints, the w_i are not directly proportional to the random ω_i, yet they are still very strongly affected by them and thus we call this toy model with randomised orbital weights RANDOM in the following. We adapt

$r_{\mathrm{peri,min}} = r_{\mathrm{min}} = 0.05\,\mathrm{kpc}$ and $r_{\mathrm{apo,max}} = r_{\mathrm{max}} = 21\,\mathrm{kpc}$. If an orbit conserves the sign of at least one angular-momentum component, then this orbit has a duplicate companion orbit with opposite direction of rotation in the library (this concerns tube orbits and spherical orbits; see also Section C). Let i^+ and i^- denote the orbital indices of such a pair of orbits, where i^+ refers to the orbit with initial velocity components $v_r, v_\theta, v_\phi > 0$. To increase the degree of difficulty for reconstructing the RANDOM model, we modify the weights of orbits in such a pair:

$$w_{i^+,\mathrm{ran}} = (1 - c_w) \cdot (w_{i^+} + w_{i^-}),$$

$$w_{i^-,\mathrm{ran}} = c_w \cdot (w_{i^+} + w_{i^-}). \qquad (D14)$$

By using $c_w = 10^{-3}$, equation (D14) leads to increased weights $w_{i^+,\mathrm{ran}}$ and almost eliminated weights $w_{i^-,\mathrm{ran}}$, corresponding to an internal rotation of the model (see also Thomas et al. 2007). We then modelled the LOSVDs of the major axis projection of this RANDOM toy model with SMART in order to test our solver algorithm for the orbital weights.

Because the χ^2 minimization is non-unique (cf. Section 5), the solution of equation (7) will in general not occur at the true weights $w_{i\cdot\mathrm{ran}}$ of the RANDOM model. We therefore tried two different configurations: (i) we used the default orbital bias factors $\omega_i = 1$ (Shannon entropy) and (ii) we set $\omega_i = \exp(1) \cdot w_{i,\mathrm{ran}}$. In the second case, we push the maximum entropy solution towards the original, randomly generated weights. Only in this case, we can predict the location of the global solution analytically and test our implementation rigorously. For ensuring fair conditions we set the initial weights to $w_{i,\mathrm{ini}} = 1$ in both cases when we start the minimization. An efficient optimization algorithm should be able to find two equivalent degenerate solutions, one for case (i) and a different one for case (ii). The true orbital weights of the RANDOM model should be recovered (only) in the latter case.

SMART is indeed able to fit the input data for both cases very well. We stopped the minimization at $\bar\chi^2 = 2 \times 10^{-9}$ for $\omega_i = 1$ and $\bar\chi^2 = 5 \times 10^{-9}$ for $\omega_i = \exp(1) \cdot w_{i,\mathrm{ran}}$. Fig. D1 shows the comparison between the true orbital weights of the RANDOM model and the recovered weights when using $\omega_i = 1$ (case (i) above). As expected, these weights *differ* from the RANDOM weights, since the

χ^2 minimization and, hence, the recovery of the entire phase-space distribution function, is non-unique. Orbits that contribute to a larger number of LOVSD data points and, in turn, are better constrained by the data have fitted weights that tend to be closer to the true ones. Fig. D2 shows the orbital weights of the input model and the modelled fit using $\omega_i = \exp(1) \cdot w_{i,\mathrm{ran}}$. As explained above, in this case we expect the recovered solution to exactly match with the RANDOM model. Fig. D2 demonstrates the high quality of our solver algorithm since the fitted weights indeed match exactly with the RANDOM weights ($\Delta\bar w = 4 \times 10^{-9}$).

The two different fits presented in Figs D1 and D2 illustrate how the maximum entropy technique with variable ω_i can be used to sample different solutions that are equivalent with respect to the χ^2 minimization.

In Fig. D3, we compare the 'macroscopic' internal velocity structure of these two fits. Even though the detailed population of the orbits (i.e. the exact phase-space distribution function) of both models differ, they both reproduce the internal moments of the RANDOM model very well ($\mathrm{rms}_\sigma = 5 \times 10^{-3}$ for $\omega_i = 1$ and $\mathrm{rms}_\sigma = 3 \times 10^{-5}$ for $\omega_i = \exp(1) \cdot w_{i,\mathrm{ran}}$). As further discussed in Section 5, this suggests that *when fitting the full LOSVDs* the remaining degeneracies in the recovery of the distribution function of a triaxial galaxy (with known normalized densities) show only little effect on the 'macroscopic' galaxy parameters of interest.

APPENDIX E: ORBIT FRACTION RECOVERY WHEN TESTING THE UNIQUENESS OF THE ANISOTROPY RECOVERY

We here show the remaining orbit fraction recovery plots for the analysis described in Section 5.2. The recovery of the z-loops was already shown in Fig. 14 of that section.

Here, we plot the recoveries of the fraction of orbits classified as x-loops (see Fig. E1), box/chaotic orbits (see Fig. E2) as well as spherical/Kepler orbits (see Fig. E3). Independent of the line of sight (different rows) or chosen entropy method (black lines), the orbit class fractions of the individual input toy-models (different rows) are well recovered.
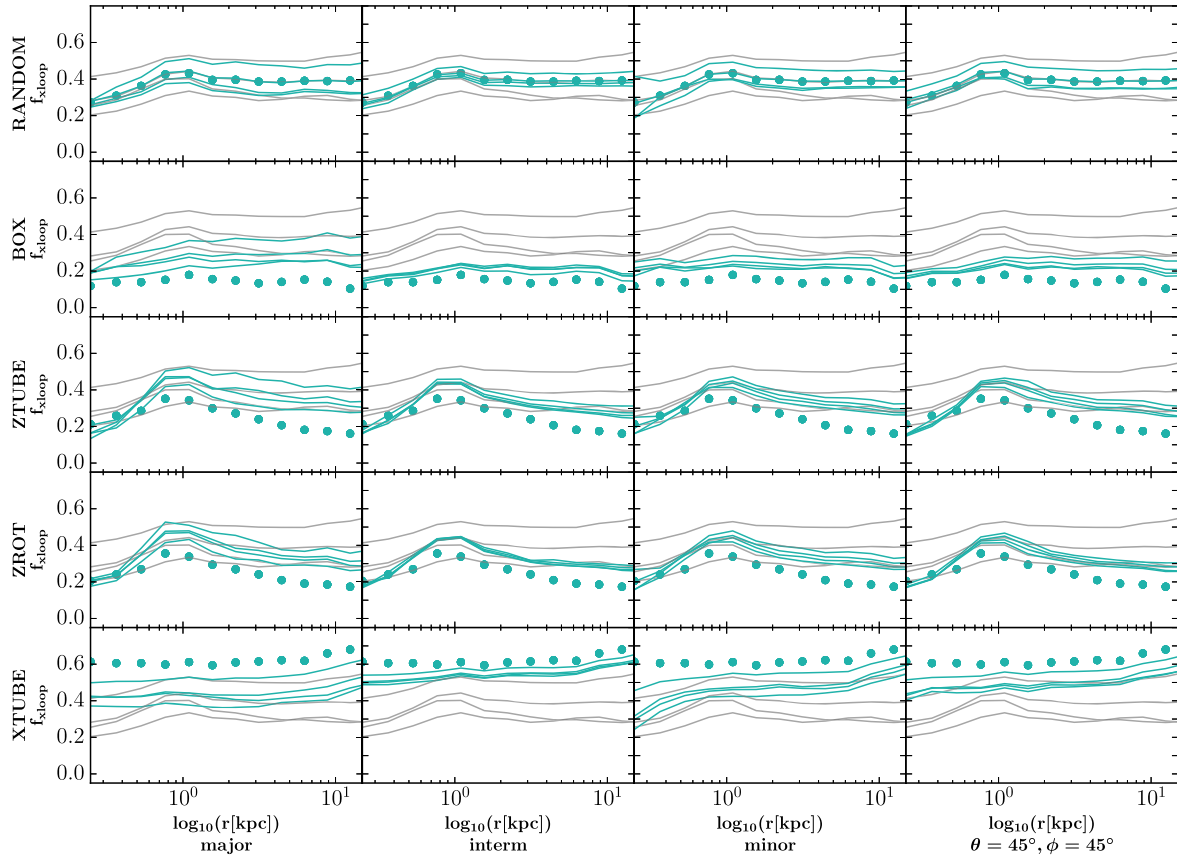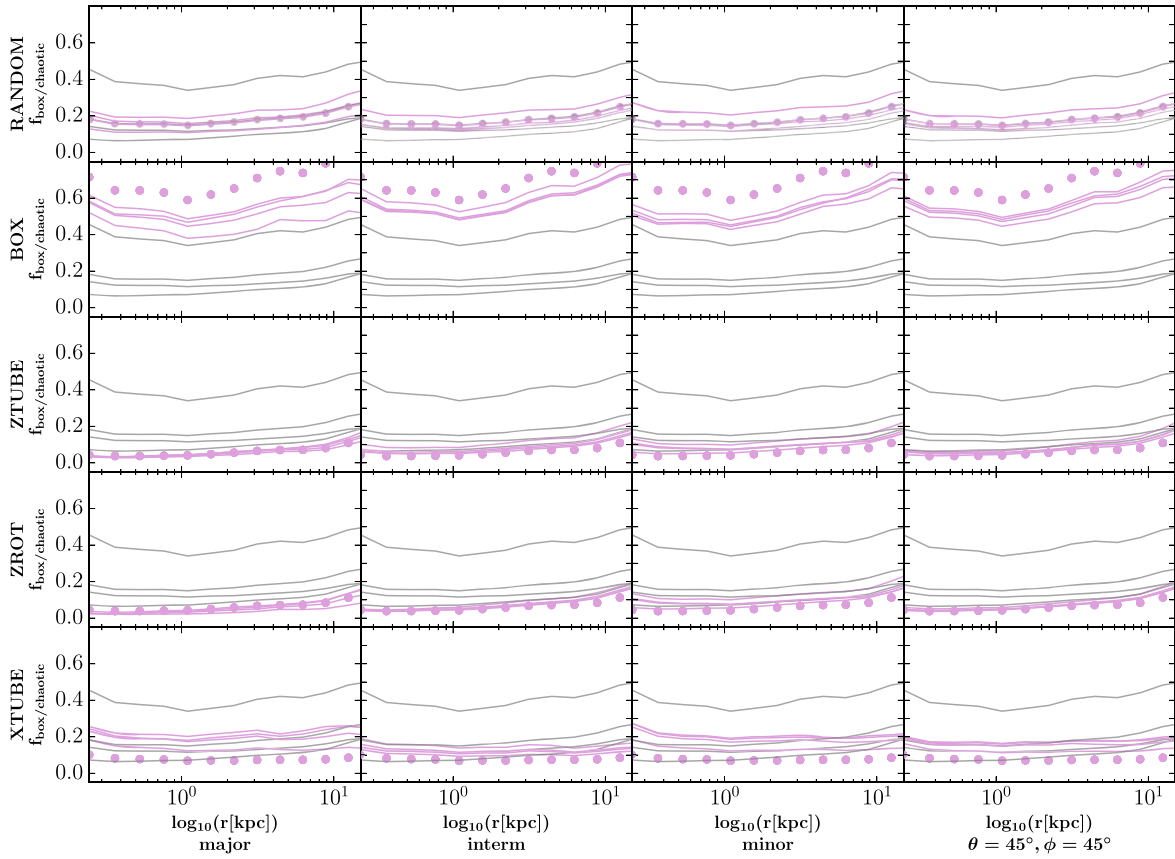
Figure E1. Recovery of the *x*-loop orbit fractions of different input toy models by models with different entropy methods. We here show the same analysis as in Figs 13 and 14 but now for the reconstruction of the fraction of orbits classified as *x*-tubes. Independent of the tested projection, the *x*-loop fractions of the individual input toy models are well recovered by the models using different entropy methods.
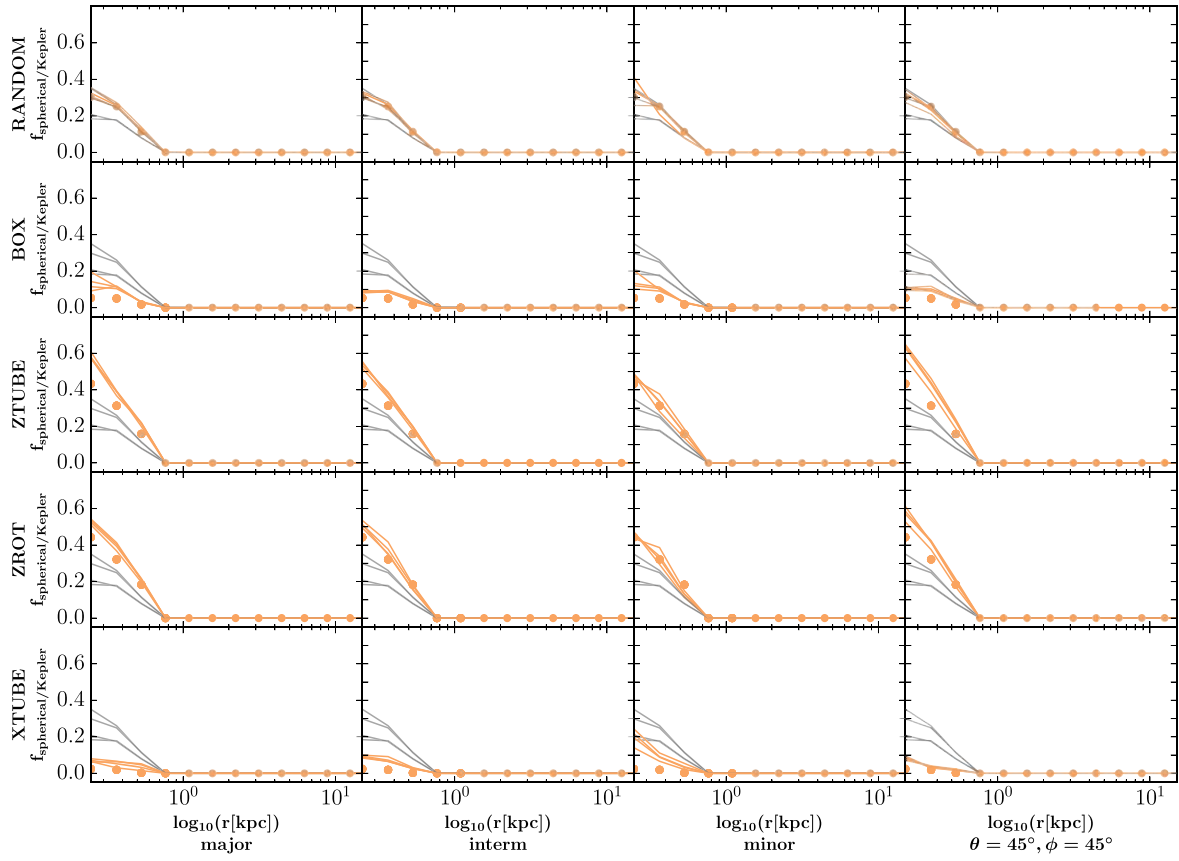
Figure E2. Recovery of the box/chaotic orbit fractions of different input toy models by models with different entropy methods. For a more detailed caption description see Figs 13 and E1.

Figure E3. Recovery of the spherical/Kepler orbit fractions of different input toy models by models with different entropy methods. For a more detailed caption description see Figs 13 and E1.

This paper has been typeset from a TEX/LATEX file prepared by the author.

Chapter 3

Accuracy and precision of triaxial orbit models I: SMBH mass, stellar mass and dark-matter halo

Bibliographic information

Author's contribution

For this paper, I dynamically modeled three of the five discussed projections of the N-body merger simulation. The dynamical models for the remaining two projections and the deprojections were performed by S. de Nicola. I evaluated all relevant input data for the dynamical modeling and deprojection routines from the used N-body simulation. The N-body simulation itself was kindly made available by A. Rantala. As the first author of

this paper, I performed the main part of the discussed analyses, created the majority of the shown plots and wrote the main body of the text. The implementation of the model selection approach into SMART and the corresponding discussion about the importance of the model selection shown in the paper was made by J. Thomas. J. Thomas furthermore supported the project with help, ideas and text corrections. R. Saglia and R. Bender contributed to the paper with valuable discussions and text corrections.

Copyright notice

Accuracy and precision of triaxial orbit models I: SMBH mass, stellar mass, and dark-matter halo

B. Neureiter [1,2]★ S. de Nicola [1,2] J. Thomas [1,2] R. Saglia,[1,2] R. Bender[1,2] and A. Rantala [3]

[1]*Max-Planck-Institut für Extraterrestriche Physik, Giessenbach-Str. 1, D-85748 Garching, Germany*
[2]*Universitäts-Sternwarte München, Scheinerstrasse 1, D-81679 München, Germany*
[3]*Max-Planck-Institut für Astrophysik, Karl-Schwarzschild-Str. 1, D-85748 Garching, Germany*

ABSTRACT
We investigate the accuracy and precision of triaxial dynamical orbit models by fitting 2D mock observations of a realistic *N*-body merger simulation resembling a massive early-type galaxy with a supermassive black hole. We show that we can reproduce the triaxial *N*-body merger remnant's correct black hole mass, stellar mass-to-light ratio and total enclosed mass (inside the half-light radius) for several different tested orientations with an unprecedented accuracy of 5–10 per cent. Our dynamical models use the entire non-parametric line-of-sight velocity distribution (LOSVD) rather than parametric LOSVDs or velocity moments as constraints. Our results strongly suggest that state-of-the-art integral-field projected kinematic data contain only minor degeneracies with respect to the mass and anisotropy recovery. Moreover, this also demonstrates the strength of the Schwarzschild method in general. We achieve the proven high recovery accuracy and precision with our newly developed modelling machinery by combining several advancements: (i) our new semiparametric deprojection code probes degeneracies and allows us to constrain the viewing angles of a triaxial galaxy; (ii) our new orbit modelling code SMART uses a 5-dim orbital starting space to representatively sample in particular near-Keplerian orbits in galaxy centres; (iii) we use a generalized information criterion AIC_p to optimize the smoothing and to compare different mass models to avoid biases that occur in χ^2-based models with varying model flexibilities.

Key words: methods: numerical – galaxies: elliptical and lenticular, cD – galaxies: kinematics and dynamics – galaxies: structure.

1 INTRODUCTION

Early-type galaxies (ETGs) at the high-mass end (absolute magnitude $M_B < -20.5$ mag) bring along particular interesting aspects. They provide information about advanced stages of galaxy evolution, they host the most massive black holes (BHs) observed so far (Mehrgan et al. 2019), form in mergers, and typically show a central flat core with a tangentially anisotropic orbit distribution (Bender 1988a; Bender et al. 1989; Faber et al. 1997; Gebhardt et al. 2003; Kormendy & Bender 2009; Gebhardt et al. 2011; Kormendy & Ho 2013; Thomas et al. 2014). The most massive ETGs also reveal particularities concerning supermassive black hole scaling relations and stellar population analysis. Growth models for supermassive black holes (SMBHs) present different predictions for the level of scatter at the high-mass end of SMBH scaling relations (Peng 2007; Hirschmann et al. 2010; Somerville & Davé 2015; Naab & Ostriker 2017). Moreover, it is highly debated whether the stellar initial mass function (IMF) is universal across galaxies or not. Massive ETGs may show the highest fraction of low-mass dwarf stars compared to the Milky Way-like Kroupa- (Kroupa 2001) or Chabrier- (Chabrier 2003) IMF (Treu et al. 2010; van Dokkum & Conroy 2010; Thomas et al. 2011; Cappellari et al. 2012; Spiniello et al. 2012; Ferreras

et al. 2013; La Barbera et al. 2013; Smith, Lucey & Conroy 2015; Vazdekis et al. 2015; Lyubenova et al. 2016; Parikh et al. 2018).

Studying these internal structure and mass composition properties of ETGs is indispensable for understanding massive galaxy formation and evolution. This emphasizes the importance of accurate dynamical modelling routines being able to provide precise information about the intrinsic dynamical structure of ETGs.

Modelling massive ETGs, however, poses challenges, since specific observational phenomena of massive ETGs, e.g. isophotal twists (Binney 1978; Bertola & Galletta 1979; Williams & Schwarzschild 1979), minor axis rotation (Contopoulos 1956; Schechter & Gunn 1978; Binney 1985) and kinematically decoupled components (Bender 1988b; Franx & Illingworth 1988; Statler 1991; Ene et al. 2018) point to a triaxial intrinsic shape of ETGs. Within the SDSS Data Release 3, the bright and massive elliptical galaxies with a de Vaucouleurs profile (de Vaucouleurs 1948) were reported to have a general distribution of the triaxiality parameter[1]Franx, Illingworth & de Zeeuw (1991) of $0.4 < T < 0.8$ (Vincent & Ryden 2005). Recently, de Nicola et al. (2022b) used a newly developed semiparametric triaxial deprojection code (de Nicola et al. 2020)

★ E-mail: bneu@mpe.mpg.de

---

[1]The triaxiality parameter is defined as $T = \frac{1-p^2}{1-q^2}$ with $q = \frac{c}{a}$ and $p = \frac{b}{a}$, where a, b, and c are the semimajor, intermediate, and minor axes of the galaxy.

to measure radially resolved shape profiles of individual brightest cluster galaxies. These galaxies are almost maximally triaxial at all radii, however tend to be rounder at their centres compared to their outskirts.

Besides the triaxial nature of the stellar components of massive ETGs, most cosmological simulations with collision-less dark matter (DM) haloes also predict triaxial DM halo shapes (e.g. Jing & Suto 2002; Bailin & Steinmetz 2005; Allgood et al. 2006; Bett et al. 2007; Hayashi, Navarro & Springel 2007; Schneider, Frenk & Cole 2012; Despali, Tormen & Sheth 2013; Vega-Ferrero, Yepes & Gottlöber 2017).

The given 3D shape of ETGs complicates the extraction of information about their intrinsic properties, since observations only provide a 2D projection onto the plane of the sky. The state-of-the-art method to tackle this problem is a dynamical modelling method based on Schwarzschild's orbit superposition technique (Schwarzschild 1979). However, it is still unclear how accurate dynamical models in general – and Schwarzschild models in particular – can get. The literature about dynamical models addresses a large variety of possible degeneracy issues. For example, Gerhard & Binney (1996) proved that even in the axisymmetric limit, the deprojection of density distributions is not unique. Dynamical models are moreover affected by the well-known mass-anisotropy degeneracy (e.g. Gerhard 1993), where missing mass in the outer parts, for example, can be hidden by a more tangential orbit distribution. In the axisymmetric limit, the determination of the correct viewing angles with dynamical modelling routines holds repeatedly stated degeneracies (e.g. Krajnović et al. 2005; Cappellari et al. 2006; Onken et al. 2007; Thomas et al. 2007). Such problems generally increase when going from 2D to 3D systems and the recovery of the orientation and shape of triaxial galaxies has also been reported to be difficult (van den Bosch et al. 2008). Moreover, Jin et al. (2019) report large possible stellar and dark-matter mass uncertainties due to the potential degeneracy between them, when analysing galaxies from the Illustris (Vogelsberger et al. 2014) simulation with a triaxial Schwarzschild modelling routine (van den Bosch et al. 2008).

Nevertheless, the discussion of scientifically interesting issues, like the previously mentioned questions concerning the stellar IMF and SMBH growth models *demand* correct and accurate black hole mass and stellar mass-to-light ratio recoveries. Fortunately, the last years have provided a lot of progress in various aspects of dynamical modelling such that it is worth to readdress the above degeneracy issues. For example, in the early days of Schwarzschild modelling it was standard to parametrize line-of-sight velocity distributions with Gauss-Hermite moments. Today, it is possible to routinely use the entire, non-parametric line-of-sight velocity distribution (Mehrgan et al. 2019; Falcón-Barroso & Martig 2021). The so increased amount of information available certainly helps us to overcome some of the degeneracies in earlier models.

Also, until recently, the most common method for determining the best-fitting parameters of dynamical models was a minimization of the observed and modelled discrepancies in a least-squares sense (e.g. Richstone & Tremaine 1984; Rix et al. 1997; Cretton et al. 1999; Gebhardt et al. 2000; Häfner et al. 2000; Siopis & Kandrup 2000; Thomas et al. 2004; Valluri, Merritt & Emsellem 2004; van den Bosch et al. 2008; Vasiliev & Valluri 2020; Neureiter et al. 2021). However, Lipka & Thomas (2021) showed that the quality of fit between different models cannot be compared with each other without considering the individual model's degrees of freedom. Minimizing a χ^2 across models with varying degrees of freedom leads to biased results. Thomas & Lipka (2022) derived a

generalization of the classical Akaike Information Criterion (AIC) which can be applied to penalized maximum-likelihood models such as most implementations of the Schwarzschild method are. This generalized AIC_p allows us to rigorously include the varying model flexibilities in the comparison of different mass models. Moreover, it allows a data-driven optimization of the regularization for each individual trial model (Thomas & Lipka 2022).

As another improvement, in our newly developed 3D triaxial Schwarzschild Modelling code called SMART (Neureiter et al. 2021), we use a 5D starting space for orbits to guarantee that all the different orbit types, in particular near the central black hole, are included in the model.

Finally, the new semiparametric deprojection method SHAPE3D introduced by de Nicola et al. (2020) has shown that the goodness-of-fit strongly depends on the chosen viewing angles, thus allowing us to select the light densities yielding the best rms (cf. de Nicola et al. 2022b).

All these advancements can potentially reduce the amount of degeneracy in dynamical modelling, and in Schwarzschild modelling in particular.

In order to test the combined power and precision of the new semiparametric deprojection code SHAPE3D by de Nicola et al. (2020), the dynamical modelling routine SMART by Neureiter et al. (2021) and the advanced model selection tools developed by Lipka & Thomas (2021) and Thomas & Lipka (2022), we apply them to high-resolution *N*-body simulations including SMBHs by Rantala et al. (2018). This provides us with the knowledge of the intrinsic scatter and remaining degeneracy uncertainties that one has to deal with when applying triaxial deprojection and dynamical modelling routines to future observational data. In this paper we focus on the mass reconstruction while in a companion paper by de Nicola et al. (2022a), hereafter called PAPER II, we discuss the shape and anisotropy recovery.

This paper will be structured as follows: Section 2 and 3 briefly summarize the used deprojection and dynamical modelling codes. In Section 4 we describe the used *N*-body simulation and our methodology to process its data and model it. In Section 5 we present our results, which are then discussed in Sections 6 and summarized in Section 7.

2 TRIAXIAL DEPROJECTION

de Nicola et al. (2020) presented a new semiparametric deprojection code called SHAPE3D as triaxial extension of the non-parametric axisymmetric algorithm by Magorrian (1999). Triaxial deprojections are highly degenerate. Therefore, one aims for a deprojection method being able to consider all possible density distributions leading to the same projected surface brightness and afterwards evaluate their individual likelihood. Parametric methods like the well known and widely used Multi-Gaussian Expansion Method (MGE, introduced by Monnet, Bacon & Emsellem (1992)) are fast, however fail to suggest more than one out of many possible solutions per viewing angle and to select the best light densities using an rms-cutoff.

SHAPE3D is, in contrast, able to deal with the degeneracy issue and allows us to search for a range of possible deprojections per viewing angle. It is a semiparametric constrained-shape approach in the sense that it searches for best-fitting light densities assuming that the contours of the luminosity density can be described as ellipsoids with possible boxy or discy deformations as well as radially varying axis ratios. Under this assumption the galaxy's 3D density function $\rho(x, y, z)$ can at every point be described by an ellipsoid whose radius

is given as

$$m^{2-\xi(x)} = x^{2-\xi(x)} + \left[\frac{y}{p(x)}\right]^{2-\xi(x)} + \left[\frac{z}{q(x)}\right]^{2-\xi(x)}. \quad (1)$$

The four 1D functions $\rho(x)$, $p(x)$, $q(x)$, and $\xi(x)$ describe the density, axis ratios $p \equiv y/x$, and $q \equiv z/x$ and the discy- ($\xi > 0$) or boxiness ($\xi < 0$) along the major axis. The code utilizes a grid-based approach, where the observed surface brightness and density are evaluated on elliptical and ellipsoidal polar grids, respectively. Due to the used semiparametric method, a regularizing penalty function P is necessary to discard unsmooth, non-physical solutions. In total, the code minimizes $L = -\frac{\chi^2}{2} + P$, where χ^2 describes the difference between the observed and modelled SB. de Nicola et al. (2020) proved that their code is able to recover the triaxial intrinsic density of an *N*-body simulation (Rantala et al. 2018) with high precision when the viewing angles are known.

Very important for the dynamical modelling is the fact that in the observationally realistic case of unknown viewing directions the assumption of a pseudo-ellipsoidal density structure constrains the range of possible orientations quite strongly (de Nicola et al. 2020). Moreover, the code filters out deprojections leading to unrealistic *p*- and *q*-profiles, i.e. deprojections which are either not smooth, or are outside the observed shape distribution of massive ellipticals. Furthermore, the code identifies deprojections where the order of the principal axes (short, intermediate, long) changes with radius. Finally, the range of possible viewing directions is narrowed down even more by re-projecting the remaining densities and by evaluating the likelihood of the corresponding isophotal shapes in comparison with the distribution of observed isophotal shapes of ETGs in general (see also Thomas et al. 2005).

3 TRIAXIAL SCHWARZSCHILD CODE SMART

SMART is the abbreviation for 'Structure and MAss Recovery of Triaxial galaxies' and is a 3D implementation of Schwarzschild's Orbit Superposition Technique based on its axisymmetric predecessor by Thomas et al. (2004). We refer to our paper by Neureiter et al. (2021) for a detailed description and will only briefly summarize the most important aspects here.

(i) SMART assembles the total gravitational potential

$$\Phi = \Phi_* + \Phi_{DM} + \Phi_{SMBH} \quad (2)$$

out of its three relevant contributions. Φ_* and Φ_{DM} are the potentials of stars and dark matter (DM). They are computed from the stellar and DM densities (see Section 4.3) via expansion into spherical harmonics. This enables the capability to deal with non-parametric densities. Φ_{SMBH} corresponds to the point-like potential from the central supermassive black hole.

(ii) SMART launches thousands of orbits from a 5D starting space and integrates their trajectories for 100 surfaces of section crossings. The 5D starting space enables us to deal with radially changing structures in the integrals-of-motion-space and therefore allows an automatic adaption to changes in the gravitational potential including a more spherical shape of the potential in the close vicinity of the SMBH giving rise to nearly Keplerian or rosette orbits (e.g. Frigo et al. 2021; Neureiter et al. 2021).

(iii) SMART fits the kinematic data by computing

$$\chi^2 = \sum_j^{N_{losvd}} \sum_k^{N_{vlos}} \left(\frac{\mathcal{L}_{data}^{jk} - \mathcal{L}_{mod}^{jk}}{\Delta\mathcal{L}_{data}^{jk}}\right)^2 \quad (3)$$

as the discrepancy between the non-parametric, full LOSVD of the model $\mathcal{L}_{mod}$ and the data $\mathcal{L}_{data}$ summed over all spatial bins j and velocity bins k. $\mathcal{L}_{mod}$ is the sum over of the individual orbital LOSVDs weighted by the orbits' occupation numbers, hereafter called orbital weights w_i. Since the number of orbital weights as free parameters in general is larger than the total number of observed data consisting as the number of kinematic bins N_{vlos} times the number of spatial bins N_{losvd}, solving for the orbital weights is underconstrained and the solution ambiguous. This issue asks for the inclusion of a penalty function.

(iv) SMART therefore conducts the orbit superposition by maximizing and entropy-like quantity

$$\hat{S} \equiv S - \alpha\,\chi^2, \quad (4)$$

where α is a regularization parameter and

$$S = -\sum_i w_i \ln\left(\frac{w_i}{\omega_i}\right). \quad (5)$$

The parameters ω_i can be interpreted as weights of the orbital weights w_i. The orbital weights w_i are constrained to reproduce the observed photometry as a boundary condition and the specific choice of ω_i defines the chosen entropy term which gets maximized. In our fiducial set-up, we use $\omega_i = $ const. so that S is linked to the Shannon entropy. By picking a specific set of ω_i the solution for the orbital weights becomes unique and SMART recovers this solution in the extremely high-dimensional space of the orbital weights with very high precision (Neureiter et al. 2021). Different sets of ω_i lead to formally different solutions. We showed in Neureiter et al. (2021) that varying the ω_i allows us to probe the entire space of possible solutions. However, in the same paper we showed that this modelling freedom does not significantly affect the macroscopic properties of interest such as the mass or anisotropy recovery. Hence, we do not need to explore this additional model space and only use the set $\omega_i = $ const. as described above.

(v) In contrast to the orbital weights, the specific choice of the regularization parameter α however does show a notable impact on the model results and achieved precision. It has been shown for axisymmetric models by Lipka & Thomas (2021) that using the optimal smoothing is important to obtain unbiased results. To optimize the smoothing in each individual mass model we compute models for a range of different smoothing values[2] and select the best one using the generalized information criterion

$$AIC_p = \chi^2 + 2m_{eff} \quad (6)$$

for penalized maximum-likelihood models (Thomas & Lipka 2022). In AIC_p the model flexibility – which decreases with increasing smoothing strength (i.e. $\alpha \to 0$) – is represented by the number of effective free parameters m_{eff} (Lipka & Thomas 2021). As discussed in more detail in this paper, m_{eff} is computed by creating N_b bootstrap iterations for the LOSVDs, hereafter called $\mathcal{L}_{bdata}$, by adding random Gaussian noise based on the observational error $\Delta\mathcal{L}_{data}$ to the original modelled fit $\mathcal{L}_{mod}$. The number of free parameters is then given as:

$$m_{eff} = \frac{1}{N_b} \sum_b^{N_b} \sum_n^{N_{data}} \frac{1}{\Delta\mathcal{L}_{data}^2{}^n} \left(\mathcal{L}_{bfit}^{bn} - \mathcal{L}_{mod}^n\right)\left(\mathcal{L}_{bdata}^{bn} - \mathcal{L}_{mod}^n\right), \quad (7)$$

where $N_{data} = N_{losvd} \times N_{vlos}$ is the total number of data points and $\mathcal{L}_{bfit}$ is the new modelled fit to the bootstrap data set $\mathcal{L}_{bdata}$. It was shown

---

[2]We typically use $N_\alpha = 30$ trial smoothing values distributed homogeneously between $\log\alpha = -6$ and $\log\alpha = 1$.

in Thomas & Lipka (2022) that the optimal smoothing is achieved at the minimum of AIC$_p$. As discussed in detail in the same paper, the smoothing optimization can be done with a very low number of bootstrap iterations for m_{eff}. We use $N_b = 1$. We note that the optimal smoothing strength usually varies from model to model. In our case, the closer the assumed mass distribution and orientation are to the true properties of the *N*-body projection, the stronger the optimal smoothing becomes.

(vi) When evaluating different mass models (or orientations) against each other, the intrinsic model flexibilities vary as described above. The fit qualities cannot be compared to each other in an un-biased manner without taking into account the individual number of the models' degrees of freedom (Lipka & Thomas 2021). Again, we select the best model based on AIC$_p$. However, here the correlations between different models are weaker than in the case of the smoothing optimization. As a result, one is often faced with jagged χ^2 curves and also with an increased scatter in m_{eff} (cf. the extended discussion in Thomas & Lipka 2022). When comparing models obtained with different orbit libraries (i.e. models with different mass distributions and/or with different assumed orientations/shapes), we therefore use $N_b = 15$ bootstrap iterations to calculate an improved estimate of m_{eff} at the optimal value of the regularization parameter α of the individual mass model. As we will show below, with this newly integrated approach we avoid any bias and achieve significantly improved constraints when searching for our best-fitting parameters.

4 THE *N*-BODY SIMULATION

We apply our deprojection routine and SMART to the high-resolution *N*-body simulation by Rantala et al. (2018). The simulation is in particular suitable for our application under study since it represents a realistic triaxial remnant of a single generation binary galaxy merger with a structure and shape resembling the core galaxy NGC1600 (e.g. Thomas et al. 2009; Rantala et al. 2019). It has a final SMBH of $1.7 \times 10^{10} M_\odot$, a sphere of influence[3] of $r_{SOI} \sim 1$ kpc and an effective radius of $r_e \sim 14$ kpc. The simulation was chosen on purpose for our requested analysis because of its ability to accurately compute the dynamics close to the SMBH due to an algorithmic chain regularization routine AR-CHAIN (Mikkola & Merritt 2006, 2008) included in the Gadget-3 (Springel 2005) based KETJU simulation code (Rantala et al. 2017). The used snapshot, which is about 1 Gyr after the merger has happened, shows a large core and a prolate shape in the outskirts with a more spherical shape towards the centre. The stellar component of the merger remnant is maximally triaxial (i.e. $T = 0.5$) at ~ 3 kpc.

4.1 Tested viewing directions

We analyse four different projections of this *N*-body simulation: two principal axes of the chosen snapshot as lines of sight ('interm', 'minor') as well as one projection exactly in between the principal axes ('middle') and one projection with randomly sampled viewing angles ('rand'). The specific projections and their corresponding viewing angles can be read from Table 1. The viewing angles θ and ϕ determine the projection to the plane on the sky and ψ determines the rotation in the plane of the sky. The viewing angles transform the intrinsic coordinates (x, y, z), which are adapted to the symmetry

---

[3]We here define the sphere of influence as the radius within which the total stellar mass equals the black hole mass.

Table 1. Tested projections with corresponding viewing angles. In order to deproject and model different sets of input data we evaluate the SB and kinematic data of the *N*-body simulation along four different lines of sight. The tested projections include two principal axes, i.e. the intermediate (hereafter called 'interm') and 'minor' axes of the triaxial merger remnant, as lines of sight. We test another projection exactly in between the principal axes, which we hereafter call 'middle', and one more projection (hereafter called 'rand') with randomly drawn viewing angles.

projection:	(θ, ϕ, ψ)
interm	$(90, 90, 90)°$
minor	$(0, 90, 90)°$
middle	$(45, 45, 45)°$
rand	$(60.4, 162.3, 7.5)°$

of the object, to the sky-projected coordinates (x', y', z') via the two matrices *P* and *R*:

$$\left(x' y' z'\right) = R \cdot P \cdot \left(xyz\right), \tag{8}$$

with

$$R = \left(\sin \psi \ -\cos \psi \ 0 \cos \psi \ \sin \psi \ 0 0 \ 0 \ 1\right) \tag{9}$$

and

$$P = \begin{pmatrix} -\sin \phi & \cos \phi & 0 \\ -\cos \theta \cos \phi & -\cos \theta \sin \phi & \sin \theta \\ \sin \theta \cos \phi & \sin \theta \sin \phi & \cos \theta \end{pmatrix}. \tag{10}$$

4.2 Processing the simulation data

We align the coordinate system of the remnant galaxy to the centre-of-mass and principle axes of the reduced inertia tensor for stars and dark matter within 30 kpc.

Afterwards, we individually compute the surface brightness (SB) and kinematics for the four different projections under study (see Table 1). We assume the galaxy to be in a distance of 20 Mpc.

The SB in units of stellar simulation particles is computed with a resolution of 0.1 arcsec within an FOV of (40×40) arcsec and a resolution of 0.5 arcsec within $(10\,300 \times 10\,300)$ arcsec (spanning about 30 times the effective radius).

The kinematic data are computed by using the Voronoi tessellation method of Cappellari & Copin (2003). Our chosen field of view of ~ 15 kpc spans about the effective radius. The central Voronoi tessellation within the sphere of influence samples a higher resolution than the tessellation scheme in the outskirts. We compute the Voronoi tessellation grid individually for every projection to guarantee a constant number of stellar simulation particles N_* in each bin. The size of the Voronoi bins is chosen so that the signal-to-noise ratio is

$$\frac{signal}{noise} = \sqrt{signal} = \sqrt{N_*} = \begin{cases} 70 & \text{for } r < r_{SOI}, \\ 150 & \text{for } r_{SOI} < r < 15 \text{ kpc}. \end{cases} \tag{11}$$

Averaged over the four tested projections, our kinematic data exhibit $N_{voronoi} = 220$ Voronoi bins within the whole FOV and $N_{voronoi} = 51$ Voronoi bins within r_{SOI}. The innermost Voronoi bin spans an average radius of 0.58 arcsec. With this, our chosen resolution matches realistic observational data.

For each Voronoi bin we compute the simulation's LOSVDs for $N_{vlos} = 15$ spanning $v_{min}^{max} = \pm 1669$ km s^{-1}.

To provide realistic conditions, which are comparable to future ob-servational data, we add Gaussian noise to the intrinsically noiseless kinematic data of the simulation. We set the standard deviation for the Gaussian scattering as 3 per cent of the maximum of each LOSVD.

With this, the velocity dispersion of the noisy kinematic simulation data results in an observationally realistic error of ~ 2 per cent.

We have chosen this simulation and mock data setup on purpose, since its high resolution meets the requirements of our study. Our goal is to demonstrate the accuracy and precision that can be achieved with advanced dynamical models and the best current observational data. The actual precision in any specific measurement will depend on the circumstances, e.g. signal-to-noise ratio in the spectral observations, spatial resolution, distance, and many other factors. It is not an intrinsic property of the modelling process. However, better data do not necessarily guarantee better results. In particular for dynamical modelling, the existence of intrinsic degeneracies (e.g. between mass and anisotropy) may eventually limit the achievable precision regardless of the quality of the data. However, while often discussed, the effect of such degeneracies has rarely been quantified. Our goal here is to show that they do not hamper highly accurate dynamical measurements on a 10 per cent level.

4.3 Modelling the *N*-body simulation

We first apply the deprojection routine to the different tested projections of the *N*-body simulation as if dealing with an observed galaxy. For each tested projection, the original grid of 1800 trial viewing angles is reduced by the deprojection code to a few dozen candidate orientations or shapes, respectively (see also PAPER II).

Similar to when modelling real observational data, we model a multidimensional parameter space and do not provide any a priori knowledge about the analysed *N*-body merger. Besides the viewing angles θ, ϕ, and ψ, we vary the black hole mass $M_{\rm BH}$, the stellar mass-to-light ratio Υ as well as five dark matter halo parameters. The DM halo profile is parametrized similar to a generalized NFW model with a scale radius r_s, density normalization ρ_0, axis ratios $p_{\rm DM}$, and $q_{\rm DM}$ and a variable inner logarithmic density slope $\gamma_{\rm in}$. However, because the original haloes of the *N*-body progenitor galaxies were based on a Hernquist profile, we set the outer logarithmic density slope equal to $\gamma_{\rm out} = -4.5$ (measured value for the remnant of our merger simulation) rather than the canonical NFW value of $\gamma_{\rm out} = -3.0$.

The individual parameters of our 10D parameter space are each sampled on a grid and the best-fitting parameters are determined by looking for the minimum in AIC$_p$ (see equation 6 in Section 3). We do this individually for each tested projection. The results for the best-fitting viewing angles are detailed in PAPER II. There, it is shown that the viewing angles are recovered with an average deviation of $\sim 20°$.

In this paper we focus on the detailed recovery of the stellar mass-to-light ratio and black hole mass. The sampled grid for the stellar mass-to-light ratio covers 10 values within $\Upsilon \in [0.6, 1.4]$. The corresponding grid size is $\Delta \Upsilon = 0.09$, which equals 9 per cent of the true value $\Upsilon_{\rm sim} = 1$ of the simulation. The grid for the black hole mass covers 10 values within $M_{\rm BH} \in [1.0, 3.0] \times 10^{10} M_\odot$ ($\Delta M_{\rm BH} = 0.22 \times 10^{10} M_\odot$, i.e. 13 per cent of the true black hole mass $M_{\rm BH, sim} = 1.7 \times 10^{10} M_\odot$).

The model results presented in this paper are attained by modelling each projection twice: by taking advantage of the triaxial symmetry of the simulation we can split the kinematic data of each projection along, e.g. the apparent minor axis (determined by averaging over the projected isophotes). One data set shows only positive values for the sky-projected coordinates $x' > 0$ (hereafter called 'right side' of the galaxy) and the other data set shows only negative values for the long axis of the sky-projection coordinates, i.e. $x' < 0$ (hereafter called 'left side' of the galaxy). This provides us

with two independent kinematic data sets for each tested projection, allowing us to determine the scatter of our modelling results. While it is actually common practice in Schwarzschild models to derive parameter uncertainties from a $\Delta\chi^2$ criterion, we specifically chose to use a different method. Since Lipka & Thomas (2021) showed that the effective number of parameters in the models varies with mass, viewing angles, etc. and that the Schwarzschild fitting is a model selection process rather than a parameter optimization, a $\Delta\chi^2$-criterion is statistically meaningless. An easy and unbiased way to determine errors in such a situation is to use the actual scatter 'measured' over fits to several data sets (see Lipka & Thomas 2021).

As our results in Section 5 will demonstrate, this method results in robust estimates of the actual scatter in the best-fitting parameters.

For every kinematic data set we ran on average 3000 models to sample our 10D parameter space. We use the software NOMAD (Nonlinear Optimization by Mesh Adaptive Direct search; Audet & Dennis et al. 2006; Le Digabel 2011) to optimize the search. NOMAD is designed for time-consuming constrained for the so-called black-box optimization problems.
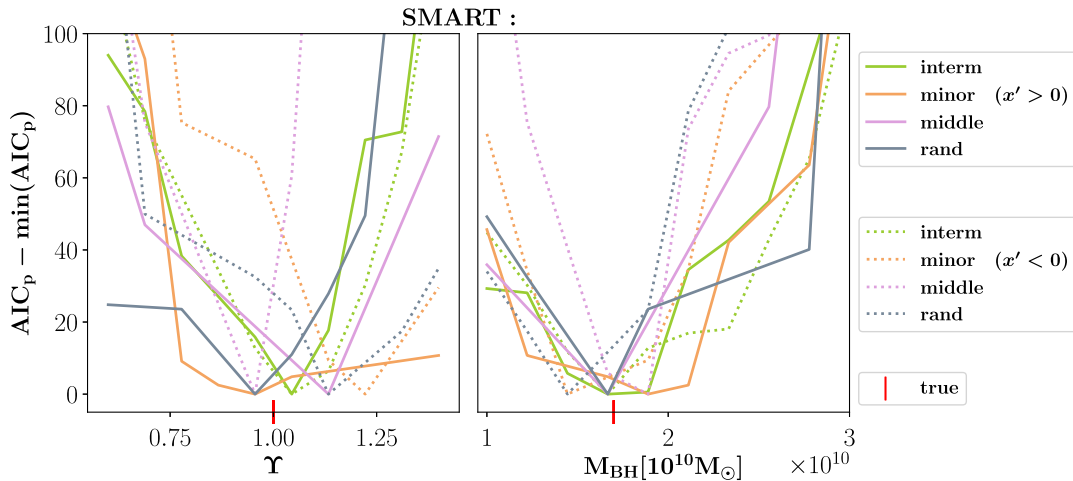
5 RESULTS

In PAPER II, we discuss the recovery of the intrinsic shape, including the recovery of the viewing angles θ, ϕ, ψ, axis ratios p, q and triaxiality parameter T, as well as anisotropy β of the *N*-body simulation, while we here focus on the question how well we can recover the mass distribution.

SMART fits the kinematic input data very well, independent of the chosen projection. The average goodness-of-fit is $\Delta\chi^2/N_{\rm data} = 0.69$, where $N_{\rm data} = N_{\rm vlos} \times N_{\rm voronoi}$ consists of the number of velocity bins $N_{\rm vlos}$ times the number of Voronoi bins $N_{\rm voronoi}$ of the individual projection and respective modelled side. Fig. 1 shows maps of the velocity, velocity dispersion, as well as the Gauss–Hermite parameters h_3 and h_4 (Gerhard 1993; van der Marel & Franx 1993; Bender, Saglia & Gerhard 1994). The Figure shows both the input data and the model fit and we have chosen the intermediate-axis projection as an example. The velocity maps for the minor, middle, and rand projections are plotted in Apendix B. As one can see, the modelled maps match the input kinematic data homogeneously well over the whole field of view. In particular, SMART is able to reproduce the negative h_4-parameter in the centre, which corresponds to a tangentially anisotropic orbit distribution produced during the core formation process. Note, that we do not fit the Gauss–Hermite moments but instead fit the entire non-parametric LOSVDs at $N_{\rm vlos}$ line-of-sight velocities $v_{\rm los}$ in each Voronoi bin. We show the Gauss–Hermite maps only to illustrate the fit quality. However, the Figure also shows the goodness-of-fit $\Delta\chi^2/N_{\rm vlos}$ achieved over the entire non-parametric LOSVD in each individual Voronoi bin.

Fig. 2 shows the curves of AIC$_p$ versus the tested stellar mass-to-light ratios and black hole masses for the different projections and sides. For these curves we first search at each Υ (or $M_{\rm BH}$, respectively) the minimum AIC$_p$ over all other parameters and then connect these values. As already mentioned in Section 4.3, the final best-fitting model is determined as the global minimum of all AIC$_p$ values over all parameters, hereafter called min(AIC$_p$). The absolute AIC$_p$ values of the various projections/sides are not important. They cannot be compared to each other, because every data set has a different number of kinematic input data (see section 4.2). We therefore subtract the individual min(AIC$_p$) from the respective AIC$_p$ values of the same data set. Each AIC$_p$ curve represents the results
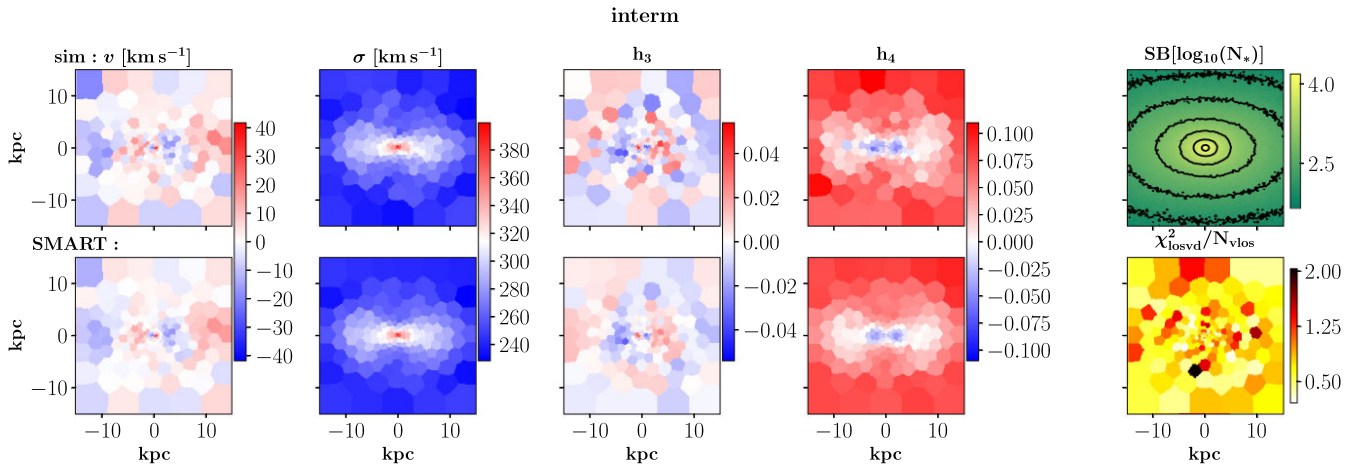
Figure 1. Velocity (first column), velocity dispersion (second column), h_3 (third column), and h_4 (fourth column) map of the simulation (first row) and the best-fitting model (second row) for the intermediate axis projection ('right' data set). The true viewing angles are $\theta = \phi = \psi = 90°$ in this case, the recovered ones are $\theta = 60°$, $\phi = 90°$, $\psi = 90°$ (see PAPER II). SMART is able to accurately fit the kinematic input data with $\chi^2/N_{data} = 0.62$. The χ^2/N_{vlos}-map (bottom right-hand panel) shows that the fit can be produced homogeneously well over the whole field of view. The top right-hand panel shows the surface brightness map in logarithmic units of stellar particle numbers N_* of the simulation.

Figure 2. Mass recovery results of Υ (left-hand panel) and M_{BH} (right-hand panel) for the four tested projections (different colours) and their respective modelled sides (solid lines for the right-hand sides and dotted lines for the left-hand sides). The minima of the AIC$_p$-curves point at the best-fitting stellar mass-to-light ratio (left-hand panel) and black hole mass (right-hand panel) of the individual models, which cover a multidimensional parameter space. The true mass values from the simulation ($\Upsilon_{sim} = 1$ and $M_{BH,\,sim} = 1.7 \times 10^{10} M_\odot$) are marked with red lines. For each modelled projection, the best-fitting values consistently scatter within 10 per cent of the true values (see Table 2). With this, we are able to reproduce the correct mass parameters with an unprecedented accuracy. This achieved precision indicates that, in general, projected kinematic data of a triaxial galaxy contain only minor degeneracies.

of ~3000 models in the 10D space of the mass and orientation parameters.

As one can see, all best-fitting stellar mass-to-light ratios and black hole masses scatter within a small variation range around the true values of the simulation (red lines). For future studies it is interesting to investigate the accuracy and precision of individual measurements for observational data with similar resolution and coverage as assumed in this study. For this we analyse the mean black hole masses and stellar mass-to-light ratios and their corresponding standard deviations for the two sides of each individual projections (as in detail explained in Section 4.3). The results for the individual measurements are summarized in Table 2. Within the individual standard deviations, the black hole mass as well as the stellar mass-to-light ratio were correctly recovered on the 10 per cent accuracy level. As one can see, with our choice of averaging over two independent

data sets, we yield representative scatter measurements, which are in the same order of magnitude for each tested projection.

In addition to the precision of individual measurements it is also important to study the statistical accuracy, which can in principle be achieved with an accurate triaxial dynamical modelling machinery. Due to the fact that we analyse several mock samples by modelling different projections, we can determine an average accuracy of the method. Averaged over the results of the interm, minor, middle, and rand projection, we achieve $\Upsilon = 1.06 \pm 0.09$ and $M_{BH} = (1.67 \pm 0.16) \times 10^{10} M_\odot$. With this, the mean stellar mass-to-light ratio is recovered within $\Delta\Upsilon = 6$ per cent and the mean black hole mass is recovered within $\Delta M_{BH} = 2$ per cent in comparison to the true values ($\Upsilon_{sim} = 1$, $M_{BH,\,sim} = 1.7 \times 10^{10} M_\odot$) of the simulation. The true values lie within the standard deviation of our tested models. This accuracy is slightly below our considered grid step sizes of

Table 2. Recovery precision of Υ and M_{BH} for individual measurements. In order to estimate the precision level one can expect when analysing future observational data with a resolution similar to the one from the N-body simulation in the current analysis, we here individually list the results of the black hole mass and stellar mass-to-light ratio of the four tested projections and compare them to the true values from the simulation. Within the standard deviations, which are given by modelling the two sides of each projection, every tested data set correctly recovers the true values from the simulation with a minor deviation on the $\sim 5-10$ per cent level.

	Υ	M_{BH}
interm	1.04 ± 0.05	$(1.67 \pm 0.07) \times 10^{10} M_\odot$
minor	1.09 ± 0.13	$(1.67 \pm 0.22) \times 10^{10} M_\odot$
middle	1.05 ± 0.08	$(1.78 \pm 0.11) \times 10^{10} M_\odot$
rand	1.05 ± 0.08	$(1.56 \pm 0.11) \times 10^{10} M_\odot$
true	$\Upsilon_{sim} = 1$	$M_{BH, sim} = 1.7 \times 10^{10} M_\odot$

$\Delta_{grid}\Upsilon = \pm 9$ per cent and $\Delta_{grid}M_{BH} = \pm 13$ per cent. We therefore estimate conservatively that the accuracy is at least the grid step size, i.e. of the order of 10 per cent, though it is probably even better.

In order to provide a complete test in our analysis along all principal axes of a triaxial galaxy, we also performed models along the long axis of the analysed N-body galaxy and found that the discussed results change for this particular line of sight. For our fiducial 10D parameter space setup, the best-fitting black hole masses derived from the major-axis projection of the N-body are off by more than 70 per cent. In Appendix A we show that these offsets vanish when we assume the right orientation and radial shape of the DM halo profile, i.e. when we provide the normalized stellar and DM halo density profiles of the simulation and/or when we increase the input data resolution. Hence, these offsets are not related to SMART, but instead indicate that the dynamical modelling and in particular the recovery of the exact black hole mass of a triaxial galaxy gets more difficult when a galaxy happens to be observed along its intrinsic long axis. This would not be entirely surprising since we know that even the pseudo-ellipsoidal deprojections become degenerate when an object happens to be observed along one of its principal axes. Kinematic degeneracies are likely largest for viewing angles along the principal axes as well. However, such viewing angles – in particular if only the major axis is concerned – are rare and an increased uncertainty along this direction will not severely affect the results of triaxial models for randomly selected galaxies. Nevertheless, we plan a more in-depth analysis of this particular case and its implications in a future paper.

Fig. 3 shows the recovery of the enclosed stellar (left-hand panel) and total mass (right-hand panel) profiles for the interm, minor, middle, and rand projection. The total mass consists of the sum of the black hole, stellar, and DM mass. Within $r_{SOI} < r < r_e$ the stellar part dominates over the BH and dark matter. At a distance of $r \sim r_e$, the enclosed DM mass equals the enclosed stellar mass of the simulation. Therefore, for radii $r > r_e$ the DM mass is the main contribution to the enclosed total mass, whereas the BH mass dominates the mass contribution within the sphere of influence. As one can see, the stellar enclosed mass profiles of all best-fitting models (different colours) follow the real one from the simulation (red) over all radii, in particular within the relevant radial region between $r_{SOI} < r < r_e$, and even down to a radius, where the stellar mass is less than 10 per cent of M_{BH}. At an intermediate radius of 7 kpc the mean deviation from the stellar enclosed mass between the best-fitting models and the simulation is only $\Delta M_*(7\,kpc) = 5.9$ per cent. Also the total enclosed mass profiles of all best-fitting models follow the real one from the simulation over all radii. It follows that also the enclosed DM profile is well reproduced. Averaged over the four different projections, the relative deviation from the total enclosed mass is $\Delta M_{tot}(r_{SOI}) = 5.9$ per cent at the sphere of influence and $\Delta M_{tot}(r_e) = 4.5$ per cent at the effective radius.

Besides the accurate recovery of the total enclosed mass, SMART is furthermore able to determine the correct, non-spherical shape of the DM halo. Averaged over our tested projections and sides, the axis ratios $p_{DM} = 0.79 \pm 0.06$ and $q_{DM} = 0.91 \pm 0.06$ show a maximum deviation of the true values $p_{DM, sim} = q_{DM, sim} = 0.93$ of only 0.14. The principal axis ratios $p_{DM, sim}, q_{DM, sim}$ are thereby computed via the eigenvalues from the reduced inertia tensor of the simulated DM particles within 100 kpc. Our findings show that our triaxial deprojection and orbit modelling codes prove to produce reliable mass recovery results for the SMBH, stellar, and DM components with an accuracy on the $\sim 5-10$ per cent level.

Of course the precision of individual measurements depends on specific circumstances like the signal-to-noise ratio of the data, their spatial resolution etc. Hence the above numbers do not imply that every measurement will have this precision. However, our tests
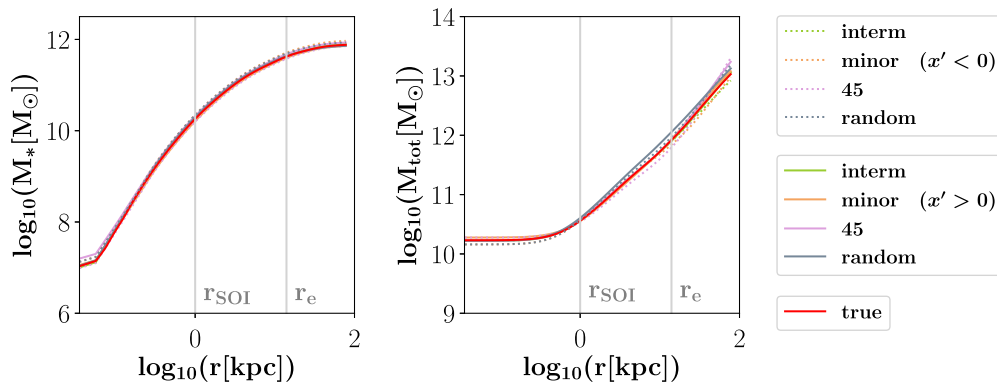
Figure 3. Mass recovery results of the enclosed stellar (left-hand panel) and total mass (right-hand panel) profiles. The simulation's sphere of influence and effective radius are marked with grey lines. For $r < r_{SOI}$ the black hole is the dominant mass contributor. The stellar mass dominates within $r_{SOI} < r < r_e$ and the DM mass dominates for $r > r_e$. The stellar and total enclosed mass profiles from the different projections and modelled sides (different colours) follow the real one from the simulation (red line) over all radii. The average deviation of the stellar mass is only $\Delta M_*(7kpc) = 5.9$ per cent at an intermediate radius of 7 kpc and the average deviation of the total enclosed mass is $\Delta M_{tot}(r_{SOI}) = 5.9$ per cent at the sphere of influence and $\Delta M_{tot}(r_e) = 4.5$ per cent at the effective radius.

demonstrate that a $5 - 10$ per cent level of precision is possible with appropriate data and advanced Schwarzschild models.

In PAPER II we show that a similar level of accuracy is achieved for the orbital anisotropy. This provides a rigorous test for our modelling machinery.

All these results together strongly suggest that, in principle, the intrinsic degeneracies contained in the photometric data and in particular in state-of-the-art integral field kinematic data are small enough so that macroscopic parameters of interest like the mass of the central SMBH, the stellar mass-to-light ratio, and also the anisotropy profile (cf. PAPER II) of a triaxial galaxy can be determined with better than 10 per cent precision. In this sense, this sets a reference for the astonishing small *intrinsic scatter* of triaxial dynamical modelling routines, which can be expected and achieved for precise kinematic data comparable to the *N*-body's resolution.

Special caution must be paid, when a triaxial galaxy is observed along its long axis (Appendix A).

6 DISCUSSION

The results presented in the previous Section 5 suggest that the accuracy and precision that can be achieved with (triaxial) dynamical orbit models is much better than previously anticipated.

6.1 Importance of model selection

We used the same triaxial *N*-body simulation already in Neureiter et al. (2021) to show that the central SMBH mass, the stellar mass-to-light ratio, and β-profile can be recovered to better than a few per cent accuracy with our dynamical models. In that paper, we assumed the angles and the stellar and DM density shape to be known and focused on testing our orbit modelling code SMART, i.e. did not go through all the analysis steps of a real galaxy. Here we go one step further. We simulate the entire modelling process of an observed galaxy. The difference to Neureiter et al. (2021) is not only that we here use *noisy* input data but we also simulate the realistic situation where we do not know the galaxy's orientation and intrinsic shape because we only have its projected image on the sky. Still, the mass and anisotropy recovery results of our current studies (see also PAPER II) reach a similar precision ($\sim 5 - 10$ per cent) as in the idealized case studied in Neureiter et al. (2021). On the one side, this reaffirms our previous tests and suggests that even in the realistic case where one has to deal with (i) noisy data and (ii) a situation where the intrinsic shape and orientation are unknown, an almost unique solution for the macroscopic parameters of interest of a triaxial galaxy can be found. However, on the other side it is surprising that even though the number of unknowns in the modelling process has increased so much, we still reach a comparable precision as in Neureiter et al. (2021). A substantial difference between this work and the work presented in Neureiter et al. (2021) is the way in which we choose our best-fitting model. The results presented in Neureiter et al. (2021) were evaluated at values of α, for which the internal velocity dispersions of the *N*-body simulation were best recovered by the model. This information is of course not available for real observational data.

Therefore, in this paper we use the approach explained in Section 3: We optimize the smoothing for each individual orbit library using a purely data-driven method. This allows the smoothing to adapt to the particular data set at hand and varies from one mass model to the other.

To illustrate how important this smoothing optimization and the AIC$_p$ comparison (cf. Section 3) of different models is, we remodelled ten different mock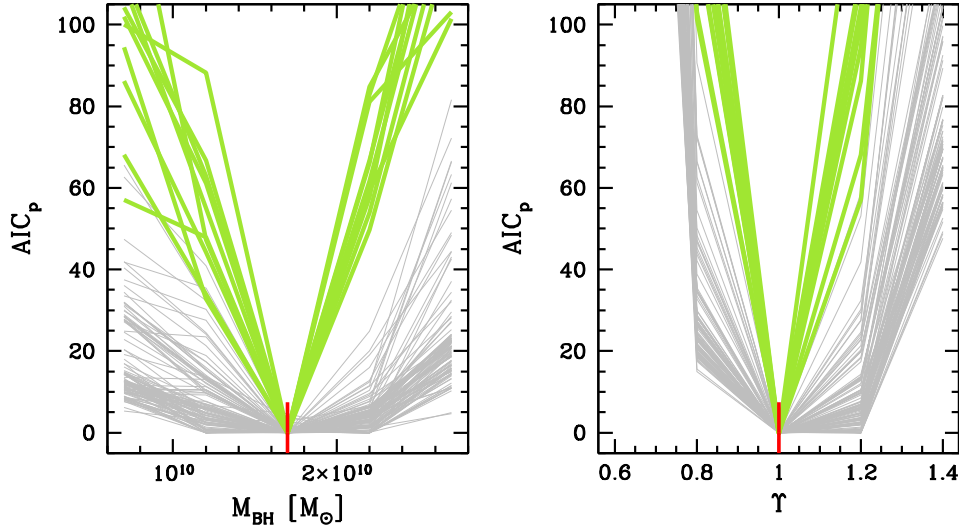 realizations of the interm projection of the *N*-body simulation using a very idealized model setup: we assumed the DM halo to be known, the 3D stellar light profile to be known and the viewing angles to be known. Only M_{BH} and Υ were treated as free parameters. In classical Schwarzschild applications the χ^2 (see equation 3) would be minimized for some constant value of the smoothing value α. In Fig. 4 we illustrate this case by the grey lines. Each line shows the modelling results of a classical χ^2 minimization for some constant value of α. We consider only smoothing values for which the minimum obtained $\chi^2 < N_{\mathrm{data}} -$ i.e. only smoothing values that lead us to acceptable best-fitting models. As the figure shows, even in this highly idealized case, where almost all properties are known to the model, the optimization of the remaining two parameters M_{BH} and Υ leads to results with unsatisfyingly large uncertainties ($\sim$30 per cent for M_{BH}). Moreover, the values for Υ tend to be biased high by up to 20 per cent. In comparison, the model selection using AIC$_p$ and adaptive optimized smoothing is much more accurate and precise (see green lines in Fig. 4). The fact that the χ^2 minimization in this case, where almost every property of the model is assumed to be known, results in uncertainties/biases much larger than for our fiducial full modelling shows how important the correct model selection is to reach the accuracy and precision that we reported above.

Another possible way to calibrate the relative strength of goodness-of-fit – measured by the χ^2 – and the strength of the smoothing would be through Monte-Carlo simulations. Based on a toy model with known properties one tests different smoothing strengths and checks which one allows for the best recovery. This (constant) smoothing strength is then used for the analysis of observed galaxies. This method is expensive since in principle it should be repeated for each individual data set with its characteristic individual error distributions, spatial coverage etc. and for each galaxy with its characteristic individual orbital structure, shape etc. It is also uncertain since there is no guarantee that the toy model used for calibration has the same structure as the galaxy to be analysed. In this context, we want to stress here, that the optimal smoothing in our case even depends on which projection of the *N*-body we analyse – even though it is always the *same N*-body simulation that we fit.

Since all Schwarzschild codes use some sort of regularization in order to avoid overfitting (e.g. Richstone & Tremaine 1988; Merritt 1993; Verolme & de Zeeuw 2002; Thomas et al. 2004; Valluri et al. 2004; van den Bosch et al. 2008; Vasiliev & Valluri 2020; Neureiter et al. 2021), the question of how to choose an optimized regularization becomes crucial when it comes to the level of high accuracy and precision that we could achieve with SMART.

6.2 Comparison to other triaxial Schwarzschild models

van den Bosch & van de Ven (2009) modelled 13 simulated photometric and kinematic data resembling SAURON (e.g. Emsellem et al. 2004) observations from possible oblate fast rotators to triaxial slow rotators. They skipped any recovery of black hole masses and concentrated on recovering the intrinsic shape and stellar mass-to-light ratio. They correctly recovered Υ within 10 per cent for the cases with well recovered intrinsic shape and within 20 per cent for the cases with less constrained intrinsic shapes. Using the same code, Jin et al. (2019) modelled nine triaxial early-type galaxies from the high resolution Illustris simulation. They were able to recover the total enclosed mass within the effective radius with 15 per cent accuracy and an underestimation of the stellar mass of ~ 24 per cent. Again, no recovery of black holes was included in the study. A direct comparison remains difficult because different studies assume different input data. Nevertheless, the unprecedented

Figure 4. Constraints on the black-hole mass M_{BH} (left-hand panel) and the stellar mass-to-light ratio Υ (right-hand panel) in idealized model fits. As input data we use ten different mock realizations of the interm projection. For the model fits we assume the true DM halo, the true viewing angles and the true 3D stellar light profile – only M_{BH} and the normalization of the stellar mass are assumed to be unknown. The grey lines show χ^2 curves derived using a constant regularization parameter α. We only show results for α values that lead to acceptable fits ($\chi^2 < N_{data}$). This does not uniquely determine α. Typically, all models for $\alpha > \sim 10^{-3}$ provide such acceptable fits. We show for all ten mocks all of the χ^2 curves resulting from these different assumed plausible smoothings. The green lines show the AIC$_p$ curves derived as described in Section 3. The red vertical lines mark the true values of the *N*-body simulation. The figure shows that even under the idealized conditions assumed here (halo, orientation, and stellar light profile known), the χ^2 minimization allows for a wide range of different solutions and that the best-fitting Υ-values are often strongly biased ($\Upsilon \approx 1.0 - 1.2$). The fact that χ^2-based mass derivations can be biased high was already discussed in Lipka & Thomas (2021) for axisymmetric models. This bias disappears and the constraints *improve significantly* when the model selection via AIC$_p$ is applied – for both the optimization of the smoothing and the comparison of different mass models.

precision that we achieved in our tests highlights the importance of extensive methodology verifications, e.g. by application to high resolution *N*-body simulations. The application of triaxial dynamical models with an unexpected high precision as demonstrated here for our code to future observational data promises interesting new results from stellar dynamics.

7 SUMMARY AND CONCLUSION

We have presented the updated version of our modelling machinery and its efficiency by application to an *N*-body merger simulation resembling a realistic massive early-type galaxy hosting a supermassive black hole. In order to create realistic conditions we compute the triaxial merger remnant's kinematic 2D data on a Voronoi binning with a spatial resolution comparable to today's telescopes' resolution. We furthermore add a plausible amount of Gaussian noise and evaluate the kinematic data with a velocity resolution similar to future observational data. Our modelling machinery implements several features:

(i) To provide our dynamical modelling code SMART with a predecision on possible deprojections and viewing angles, we use the flexible new semiparametric triaxial deprojection code SHAPE3D (cf. de Nicola et al. 2020).

(ii) SMART reconstructs the stellar orbit distribution by integrating thousands of orbits, which are launched from a 5D starting space to cover all orbital shapes in particular near the central black hole (cf. Neureiter et al. 2021).

(iii) SMART exploits the full non-parametrically sampled LOSVDs rather than using velocity moments as constraints (cf. Neureiter et al. 2021).

(iv) SMART uses an adaptive smoothing scheme to optimize the regularization in each trial mass model (cf. Thomas & Lipka 2022).

(v) SMART uses a generalized information criterion for penalized models to select the best-fitting orbit model, avoiding potential biases in χ^2-based approaches (cf. Lipka & Thomas 2021; Thomas & Lipka 2022).

Similar to the case of observed galaxies, we model a multidimensional parameter space, including the a priori unknown viewing angles as well as the mass parameters for the stellar and DM components of the galaxy's potential. In order to test multiple mock samples, we apply our triaxial deprojection code SHAPE3D and modelling code SMART to four different projections from the *N*-body simulation.

SMART is able to fit the kinematic input data homogeneously well over the whole field of view with a mean accuracy of $\Delta\chi^2/N_{data} = 0.69$.

For each modelled projection, we are able to reconstruct the true stellar mass-to-light ratio $\Upsilon_{sim} = 1$ and black hole mass $M_{BH, sim} = 1.7 \times 10^{10} M_\odot$ of the simulation with an accuracy on the $\sim 5 - 10$ per cent level.

Also the enclosed total mass profile was correctly recovered by SMART over all radii. The average deviation of the total enclosed mass, consisting of the black hole, stellar, and DM mass contributions, is only $\Delta M_{tot}(r_{SOI}) = 5.9$ per cent at the sphere of influence and $\Delta M_{tot}(r_e) = 4.5$ per cent at the effective radius.

We are furthermore able to recover the correct, non-spherical shape of the simulation's DM halo by recovering the true axis ratios p_{DM} and q_{DM} with a maximum deviation of only 0.14.

As more extensively presented in our companion PAPER II by de Nicola et al. (2022a), we are also able to reconstruct the simulation's shape and anisotropy with similar accuracy. We refer to this paper for an extensive discussion of the recovery results for the viewing angles θ, ϕ, ψ, axis ratios p, q, and orbital anisotropy.

The surprisingly high accuracy and precision as well as low degree of degeneracy that we find in our models reaffirm our earlier results presented in Neureiter et al. (2021). There, in an idealized setting with known viewing angles and known deprojection we found that macroscopic parameters of a triaxial galaxy, like the anisotropy and mass composition, are not severely influenced by any degeneracy remaining in the reconstruction of the orbit distribution function. We can now go one step further. Our results strongly suggest that in general, the projected kinematic data of a triaxial galaxy hold only minor degeneracies, which enables an unentangled recovery of the intrinsic structure and mass composition.

With this analysis we were able to show that the intrinsic scatter of accurate triaxial dynamical modelling routines, which are applied to precise kinematic data, is small enough to target scientific questions concerning the scatter of SMBH scaling relations and the well known IMF issue.

Our study points to a possible change of this statement for the analysis of a triaxial galaxy observed along its long axis, which will be more extensively studied in a future paper.

Another study covered by a future paper will be the axisymmetric analysis of a triaxial galaxy.

ACKNOWLEDGEMENTS

DATA AVAILABILITY STATEMENT

The data underlying this article will be shared on reasonable request to the corresponding author.

REFERENCES

Allgood B., Flores R. A., Primack J. R., Kravtsov A. V., Wechsler R. H., Faltenbacher A., Bullock J. S., 2006, MNRAS, 367, 1781
Audet C., Dennis J. Jr, 2006, SIAM J. Optim., 17, 188
Bailin J., Steinmetz M., 2005, ApJ, 627, 647
Bender R., 1988a, A&A, 193, L7
Bender R., 1988b, A&A, 202, L5
Bender R., Surma P., Doebereiner S., Moellenhoff C., Madejsky R., 1989, A&A, 217, 35
Bender R., Saglia R. P., Gerhard O. E., 1994, MNRAS, 269, 785
Bertola F., Galletta G., 1979, A&A, 77, 363
Bett P., Eke V., Frenk C. S., Jenkins A., Helly J., Navarro J., 2007, MNRAS, 376, 215
Binney J., 1978, Comments Astrophys., 8, 27
Binney J., 1985, MNRAS, 212, 767
Cappellari M. et al., 2006, MNRAS, 366, 1126
Cappellari M. et al., 2012, Nature, 484, 485
Cappellari M., Copin Y., 2003, MNRAS, 342, 345
Chabrier G., 2003, PASP, 115, 763
Contopoulos G., 1956, Z. Astrophys., 39, 126
Cretton N., de Zeeuw P. T., van der Marel R. P., Rix H.-W., 1999, ApJS, 124, 383
de Nicola S., Saglia R. P., Thomas J., Dehnen W., Bender R., 2020, MNRAS, 496, 3076
de Nicola S., Neureiter B., Thomas J., Saglia R. P., Bender R., 2022a, MNRAS, 517, 3445 (Paper II)
de Nicola S., Saglia R. P., Thomas J., Pulsoni C., Kluge M., Bender R., Valenzuela L. M., Remus R.-S., 2022b, ApJ, 933, 215
de Vaucouleurs G., 1948, Ann. Astrophys., 11, 247
Despali G., Tormen G., Sheth R. K., 2013, MNRAS, 431, 1143
Emsellem E. et al., 2004, MNRAS, 352, 721
Ene I. et al., 2018, MNRAS, 479, 2810
Faber S. M. et al., 1997, AJ, 114, 1771
Falcón-Barroso J., Martig M., 2021, A&A, 646, A31
Ferreras I., La Barbera F., de La Rosa I. G., Vazdekis A., de Carvalho R. R., Falcon-Barroso J., Ricciardelli E., 2013, MNRAS, 429, L15
Franx M., Illingworth G. D., 1988, ApJ, 327, L55
Franx M., Illingworth G., de Zeeuw T., 1991, ApJ, 383, 112
Frigo M., Naab T., Rantala A., Johansson P. H., Neureiter B., Thomas J., Rizzuto F., 2021, MNRAS, 508, 4610
Gebhardt K. et al., 2000, AJ, 119, 1157
Gebhardt K. et al., 2003, ApJ, 583, 92
Gebhardt K., Adams J., Richstone D., Lauer T. R., Faber S. M., Gültekin K., Murphy J., Tremaine S., 2011, ApJ, 729, 119
Gerhard O. E., 1993, MNRAS, 265, 213
Gerhard O. E., Binney J. J., 1996, MNRAS, 279, 993
Häfner R., Evans N. W., Dehnen W., Binney J., 2000, MNRAS, 314, 433
Hayashi E., Navarro J. F., Springel V., 2007, MNRAS, 377, 50
Hirschmann M., Khochfar S., Burkert A., Naab T., Genel S., Somerville R. S., 2010, MNRAS, 407, 1016
Jin Y., Zhu L., Long R. J., Mao S., Xu D., Li H., van de Ven G., 2019, MNRAS, 486, 4753
Jing Y. P., Suto Y., 2002, ApJ, 574, 538
Kormendy J., Bender R., 2009, ApJ, 691, L142
Kormendy J., Ho L. C., 2013, ARA&A, 51, 511
Krajnović D., Cappellari M., Emsellem E., McDermid R. M., de Zeeuw P. T., 2005, MNRAS, 357, 1113
Kroupa P., 2001, MNRAS, 322, 231
La Barbera F., Ferreras I., Vazdekis A., de la Rosa I. G., de Carvalho R. R., Trevisan M., Falcón-Barroso J., Ricciardelli E., 2013, MNRAS, 433, 3017
Le Digabel S., 2011, ACM Trans. Math. Softw., 37, 1
Lipka M., Thomas J., 2021, MNRAS, 504, 4599
Lyubenova M. et al., 2016, MNRAS, 463, 3220
Magorrian J., 1999, MNRAS, 302, 530
Mehrgan K., Thomas J., Saglia R., Mazzalay X., Erwin P., Bender R., Kluge M., Fabricius M., 2019, ApJ, 887, 195
Merritt D., 1993, ApJ, 413, 79
Mikkola S., Merritt D., 2006, MNRAS, 372, 219
Mikkola S., Merritt D., 2008, AJ, 135, 2398
Monnet G., Bacon R., Emsellem E., 1992, A&A, 253, 366
Naab T., Ostriker J. P., 2017, ARA&A, 55, 59
Neureiter B. et al., 2021, MNRAS, 500, 1437
Onken C. A. et al., 2007, ApJ, 670, 105
Parikh T. et al., 2018, MNRAS, 477, 3954
Peng C. Y., 2007, ApJ, 671, 1098
Rantala A., Pihajoki P., Johansson P. H., Naab T., Lahén N., Sawala T., 2017, ApJ, 840, 53
Rantala A., Johansson P. H., Naab T., Thomas J., Frigo M., 2018, ApJ, 864, 113
Rantala A., Johansson P. H., Naab T., Thomas J., Frigo M., 2019, ApJ, 872, L17
Richstone D. O., Tremaine S., 1984, ApJ, 286, 27
Richstone D. O., Tremaine S., 1988, ApJ, 327, 82
Rix H.-W., de Zeeuw P. T., Cretton N., van der Marel R. P., Carollo C. M., 1997, ApJ, 488, 702
Schechter P. L., Gunn J. E., 1978, AJ, 83, 1360
Schneider M. D., Frenk C. S., Cole S., 2012, J. Cosmol. Astropart. Phys., 2012, 030
Schwarzschild M., 1979, ApJ, 232, 236
Siopis C., Kandrup H. E., 2000, MNRAS, 319, 43
Smith R. J., Lucey J. R., Conroy C., 2015, MNRAS, 449, 3441
Somerville R. S., Davé R., 2015, ARA&A, 53, 51

Spiniello C., Trager S. C., Koopmans L. V. E., Chen Y. P., 2012, ApJ, 753, L32

Springel V., 2005, MNRAS, 364, 1105

Statler T. S., 1991, AJ, 102, 882

Thomas J., Lipka M., 2022, MNRAS, 514, 6203

Thomas J., Saglia R. P., Bender R., Thomas D., Gebhardt K., Magorrian J., Richstone D., 2004, MNRAS, 353, 391

Thomas J., Saglia R. P., Bender R., Thomas D., Gebhardt K., Magorrian J., Corsini E. M., Wegner G., 2005, MNRAS, 360, 1355

Thomas J., Saglia R. P., Bender R., Thomas D., Gebhardt K., Magorrian J., Corsini E. M., Wegner G., 2007, MNRAS, 382, 657

Thomas J. et al., 2009, MNRAS, 393, 641

Thomas J. et al., 2011, MNRAS, 415, 545

Thomas J., Saglia R. P., Bender R., Erwin P., Fabricius M., 2014, ApJ, 782, 39

Treu T., Auger M. W., Koopmans L. V. E., Gavazzi R., Marshall P. J., Bolton A. S., 2010, ApJ, 709, 1195

Valluri M., Merritt D., Emsellem E., 2004, ApJ, 602, 66

van den Bosch R. C. E., van de Ven G., Verolme E. K., Cappellari M., de Zeeuw P. T., 2008, MNRAS, 385, 647

van den Bosch R. C. E., van de Ven G., 2009, MNRAS, 398, 1117

van der Marel R. P., Franx M., 1993, ApJ, 407, 525

van Dokkum P. G., Conroy C., 2010, Nature, 468, 940

Vasiliev E., Valluri M., 2020, ApJ, 889, 39

Vazdekis A. et al., 2015, MNRAS, 449, 1177

Vega-Ferrero J., Yepes G., Gottlöber S., 2017, MNRAS, 467, 3226

Verolme E. K., de Zeeuw P. T., 2002, MNRAS, 331, 959

Vincent R. A., Ryden B. S., 2005, ApJ, 623, 137

Vogelsberger M. et al., 2014, MNRAS, 444, 1518

Williams T. B., Schwarzschild M., 1979, ApJS, 41, 209

APPENDIX A: MAJOR AXIS ANALYSIS

When modelling the 10D parameter space of the *N*-body simulation projected along its major axis, we find different results in comparison to the other tested projections (cf. Section 5). Along this specific line of sight, the stellar mass-to-light ratio is reproduced with a maximum uncertainty of only 20 per cent (best-fitting stellar mass-

to-light ratio for the right-hand side of the major axis projection is $\Upsilon(x' > 0) = 1.04$ and $\Upsilon(x' < 0) = 1.22$ for the left-hand side), however, the best-fitting black hole mass is more than 70 per cent underestimated.

In order to check that the black hole mass uncertainty along the major axis projection is not caused by an intrinsic bug of SMART along this axis, we remodelled a 3D mass parameter grid for the right-hand side of the kinematic data for this axis. To minimize modelling uncertainties that originate from incomplete sampling in the 10D parameter space or from uncertainties in the deprojection, we make the following simplifications: We do not provide SMART with plausible deprojections determined by the triaxial deprojection routine from de Nicola et al. (2020), but we forward the true normalized stellar density from the simulation to SMART. Also, instead of modelling a gNFW halo with five unknown parameters, as used for the analysis in Section 5, we here model the DM halo by providing SMART with the correct normalized DM density of the simulation with an unknown scaling parameter s_{DM}. This is the same Ansatz as used in Neureiter et al. (2021). The remaining three parameters for this analysis to be determined by SMART are Υ, M_{BH} and s_{DM}.

We also increase the resolution of the kinematic input data from $N_{vlos} = 15$ (see Section 4.2) to $N_{vlos} = 45$. This allows us to fit the kinematic input data with a velocity resolution of $\Delta v_{vlos} = 71.1$ km s^{-1} instead of the lower velocity resolution of $\Delta v_{vlos} = 223.5$ km s^{-1} used for the more time-consuming analysis of Section 5.

For this adapted set-up, we evaluate 343 models with different Υ-, M_{BH}- and s_{DM}-input-masses. The tested mass grid covers a grid size of 5 per cent around the correct mass parameters.

Fig. A1 shows the outcome of this analysis, where we plot the AIC$_p$ curves of the models with different s_{DM}-input-masses (different colours) against the tested Υ- (left-hand panel) and M_{BH}- values (right-hand panel). Since all models are provided with the same number of kinematic input data N_{data}, their absolute AIC$_p$ values can be compared with each other and their total minimum provides
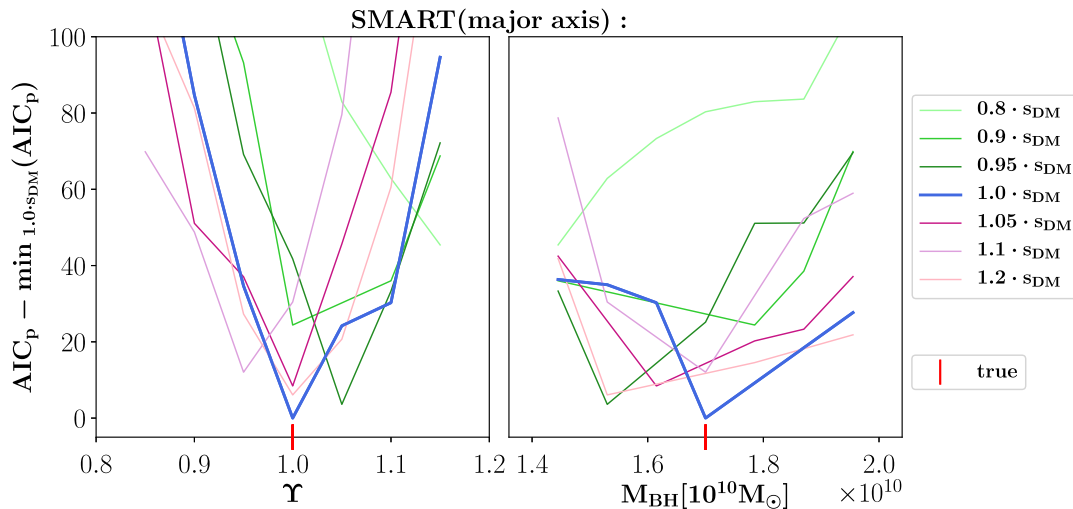
Figure A1. Mass recovery results of Υ (left-hand panel), M_{BH} (right-hand panel), and dark matter scaling factor s_{DM} (different colours) for the major-axis projection. In this analysis we remodel a higher resolved kinematic input data of the right-hand side of the major axis by providing SMART with the true normalized stellar and DM density of the simulation. For a better comparison we subtract the minimum AIC$_p$-value of the models with the correct s_{DM}-parameter, i.e. min$_{1.0 s_{DM}}$(AIC$_p$) (blue line), from all AIC$_p$ curves. The individual minima for the different coloured AIC$_p$-curves provide the respective best-fitting Υ- and M_{BH}-values for the models with different s_{DM}-input values. It turns out, that the best-fitting model of all tested 343 models covering this 3D parameter space, is the one with the true Υ_{sim}- and $M_{BH, sim}$-values from the simulation (red) as well as the correct s_{DM}-parameter (minimum of all curves). This indicates that SMART shows no intrinsic bug when modelling kinematic data with high enough resolution projected along the major axis of a triaxial galaxy.

the best-fitting model. SMART is able to determine the true stellar mass-to-light ratio, black hole mass as well as DM scaling parameter.

This test enables us to show that SMART is in principle able to recover the correct mass parameters for kinematic data projected along the long axis of a triaxial galaxy.

The uncertainty of the black hole mass recovery of 70 per cent, which was achieved within our fiducial 10D parameter space setup with unknown stellar and DM shape, therefore appears to origin from uncertainties caused by the deprojection and/or the multidimensional DM halo modelling and/or the lower resolution of the tested parameter grid size as well as of the kinematic input data, which was used for reasons of computational time.

Of course, a non-negligible intrinsic physical degeneracy along this axis cannot be excluded. A more detailed study of this apparent major-axis abnormality will be performed in the future.

APPENDIX B: VELOCITY-, SURFACE BRIGHTNESS-, AND χ^2-MAPS

Fig. B2 shows the velocity v, velocity dispersion σ, h_3 and h_4 maps of the simulation and kinematic fit for the minor, middle, and rand axis as line of sight. In addition, the surface brightness of the simulation is plotted in logarithmic units of stellar simulation particles. The χ^2-map shows the deviation between the kinematic input data and the best-fitting model evaluated by SMART. As already stated in Section 5, SMART fits the kinematic input data well for all tested axes over the whole field of view with an average deviation between the input and modelled LOSVDs of $\Delta \chi^2 / N_{data} = 0.69$. The maps of the Gauss–Hermite parameters in Fig. B2 are only to illustrate the fit quality. SMART actually fits the entire LOSVDs. To demonstrate the fit of the true LOSVD data, Fig. B1 shows two input LOSVDs (red lines) and two fitted LOSVDs (green lines) for a central Voronoi bin and an outer Voronoi bin projected along two different lines-of-sight.
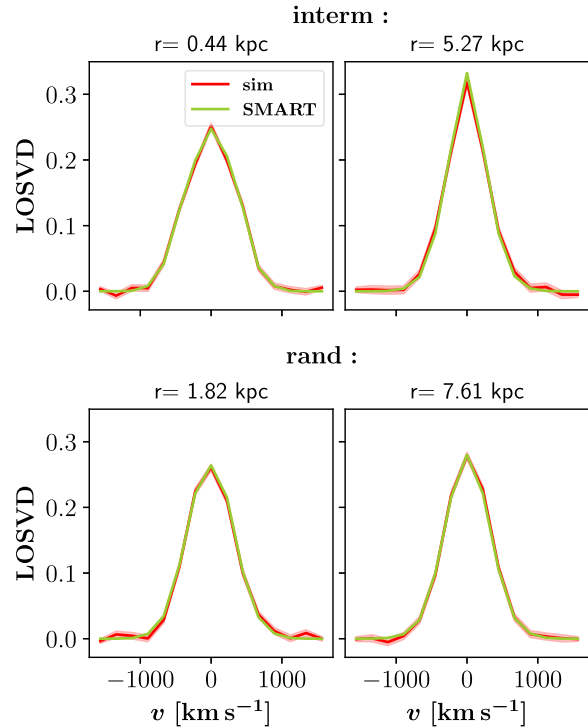
Figure B1. Exemplary demonstration of the achieved LOSVD fit (green lines) in comparison to the input LOSVDs (red lines) for the interm projection (top panels) and for the rand projection (bottom panels) at two different radii, respectively.
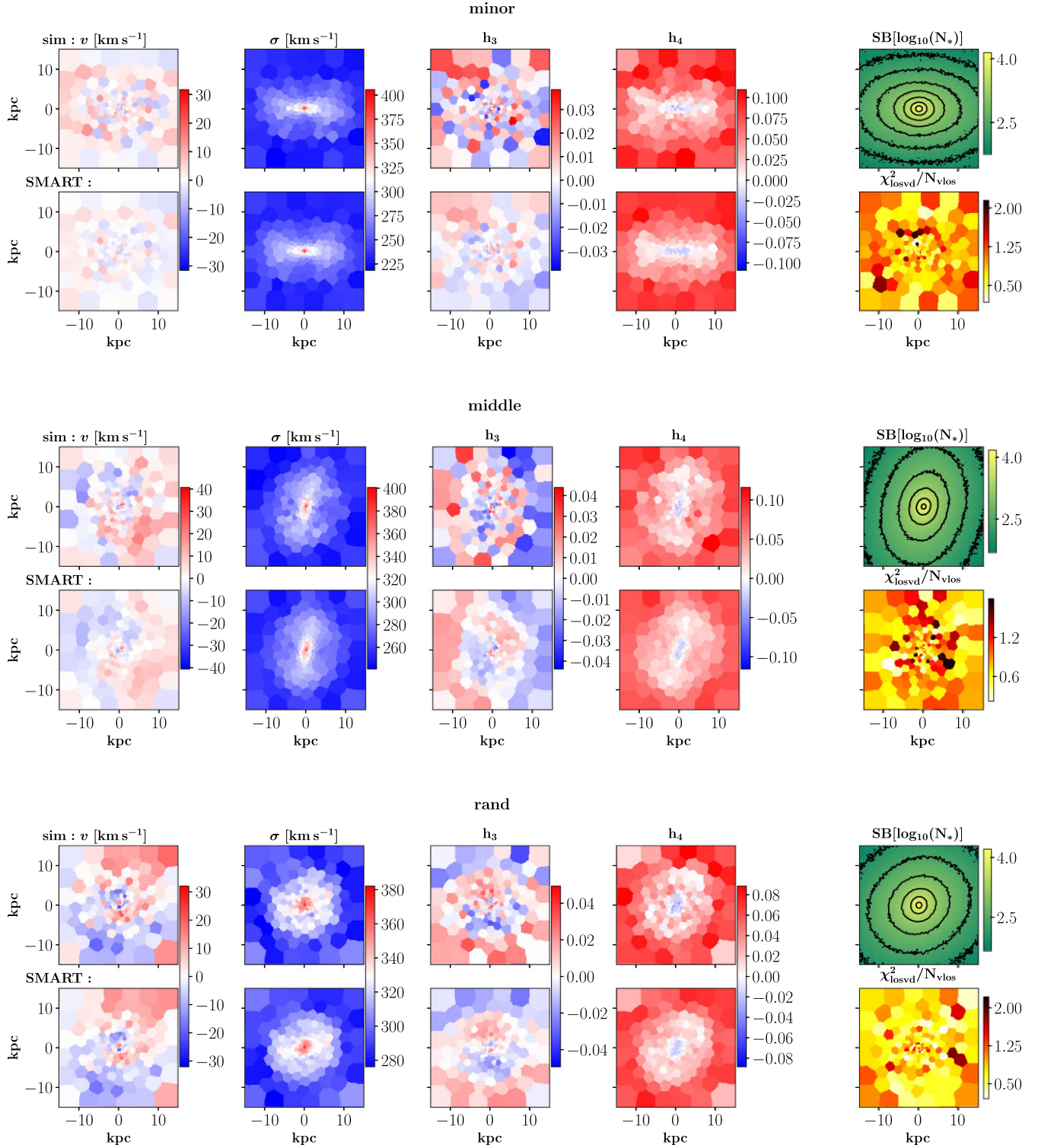
Figure B2. Velocity, velocity dispersion, h_3, h_4 and surface brightness maps of the simulation (top row) as well as velocity maps of the best-fitting model and corresponding χ^2-map (bottom row) for different projections. The individual line of sight for the different projections can be read from the title. The velocity maps for the intermediate axis were already shown in Fig. 1. Overall, SMART is able to well fit the kinematic input data independent of the individual viewing angles. The average deviation from the kinematic input data with the modelled fit is $\Delta\chi^2/N_{data} = 0.69$. The χ^2-maps indicate SMART's ability to fit the kinematic input data homogeneously well over the whole field of view.

This paper has been typeset from a TEX/LATEX file prepared by the author.

Chapter 4

The isotropic center of NGC 5419 - A core in formation?

Bibliographic information

Author's contribution

As the first author of this paper, I deprojected the surface brightness data and afterwards dynamically modeled the kinematic data of NGC 5419. I performed all analyses, created all plots and wrote the text for this paper. I was supported by J. Thomas with ideas and help. The project was done in close collaboration with A. Rantala and T. Naab, who participated in the analysis with discussions and N-body simulation data. R. Saglia and R. Bender contributed with discussions and text corrections. The kinematics from the new MUSE observations were derived by K. Mehrgan. S. de Nicola helped with explanations concerning the deprojection code.

Copyright notice

CrossMark

The Isotropic Center of NGC 5419—A Core in Formation?

Bianca Neureiter[1,2] ⓘ, Jens Thomas[1,2] ⓘ, Antti Rantala[3] ⓘ, Thorsten Naab[3] ⓘ, Kianusch Mehrgan[1,2] ⓘ, Roberto Saglia[1,2] ⓘ, Stefano de Nicola[1,2] ⓘ, and Ralf Bender[1,2] ⓘ
[1] Max-Planck-Institut für extraterrestrische Physik, Giessenbachstrasse 1, D-85748 Garching, Germany; bneu@mpe.mpg.de
[2] Universitäts-Sternwarte München, Scheinerstrasse 1, D-81679 München, Germany
[3] Max-Planck-Institut für Astrophysik, Karl-Schwarzschild-Str. 1, D-85748 Garching, Germany
Received 2022 November 8; revised 2023 April 21; accepted 2023 April 22; published 2023 June 7

Abstract

With its cored surface brightness profile, the elliptical galaxy NGC 5419 appears as a typical high-mass early-type galaxy (ETG). However, the galaxy hosts two distinct nuclei in its center. We use high-signal MUSE (Multi-unit Spectroscopic Explorer (Based on observations collected at the European Organisation for Astronomical Research in the Southern Hemisphere under ESO program 099.B-0193(A).)) spectral observations and novel triaxial dynamical orbit models to reveal a surprisingly isotropic central orbit distribution in NGC 5419. Recent collisionless simulations of merging massive ETGs suggest a two-phase core formation model, in which the low-density stellar core forms rapidly by supermassive black holes (SMBHs) sinking into the center due to dynamical friction. Only afterwards do the SMBHs form a hard binary, and the black hole scouring process slowly changes the central orbit distribution from isotropic to tangential. The observed cored density profile, the double nucleus, and the isotropic center of NGC 5419 together thus point to an intermediate evolutionary state where the first phase of core formation has taken place, yet the scouring process is only beginning. This implies that the double nucleus is an SMBH binary. Our triaxial dynamical models indicate a total mass of the two SMBHs in the center of NGC 5419 of $M_{BH} = (1.0 \pm 0.08) \times 10^{10} M_\odot$. Moreover, we find that NGC 5419's complex kinematically distinct core can be explained by a coherent flip of the direction of orbital rotation of stars on tube orbits at ~3 kpc distance from the galaxy center together with projection effects. This is also in agreement with merger simulations hosting SMBHs in the same mass regime.

Unified Astronomy Thesaurus concepts: Supermassive black holes (1663); Stellar dynamics (1596); Early-type galaxies (429); Elliptical galaxies (456); Galaxy structure (622); Galaxy nuclei (609); Galaxy spheroids (2032)

1. Introduction

NGC 5419 is the dominant galaxy of the poor cluster Abell S753 observable in the Centaurus constellation. With a brightness of $M_V = -23.1$, NGC 5419 belongs to the class of massive early-type galaxies (ETGs), which are thought to undergo gas-poor galaxy merging processes at least in late evolutionary phases (see, e.g., Bender 1988; Bender et al. 1992; Kormendy & Bender 1996; Moster et al. 2018). As a result of this, ETGs at the high-mass end characteristically show a central cored surface brightness (SB) profile (Nieto et al. 1991a, 1991b; Faber et al. 1997; Lauer et al. 2005, 2007) that indicates a light-deficit (Kormendy & Bender 2009; Kormendy & Ho 2013). Such cores naturally form in gas-poor mergers with supermassive black holes (SMBHs) (e.g., Begelman et al. 1980; Hills & Fullerton 1980; Ebisuzaki et al. 1991; Milosavljević & Merritt 2001; Merritt 2006; Rantala et al. 2018; Nasim et al. 2021). By using high-resolution simulations of galaxy mergers with SMBHs Rantala et al. (2018) and Frigo et al. (2021) recently revealed that the core formation actually happens in two phases: First, dynamical friction causes the two SMBHs of the progenitor galaxies to sink to the center of the merger remnant. This causes the surrounding stars to move to larger radii, happens rapidly (some tens of millions of years), and is the main driver of the formation of the shallow central stellar density core. At the time when the two SMBHs form a tightly bound (hard) binary, most of the stellar

density core structure is already in place. Afterwards, in a second and slower phase, slingshot interactions with the formed SMBH binary kick out stars, which are predominantly on radial orbits and get close enough to the binary. The result is a characteristic tangentially biased central orbit structure. This second, slower evolutionary phase (several hundred million years to up to 1 Gyr) flattens the SB profile only slightly. Inner tangential anisotropy is common in ETGs (e.g., Gebhardt et al. 2003; McConnell et al. 2012). The most massive ETGs, in particular, have a very uniform anisotropy structure near their cores that matches very well with the predictions of the SMBH binary model (Thomas et al. 2014; Rantala et al. 2018; Mehrgan et al. 2019).

While NGC 5419 with its central SB core appears as a typical ETG at first glance, this galaxy is clearly distinct from other elliptical core galaxies because Hubble Space Telescope (HST) as well as SINFONI observations reveal a double nucleus in its center (Capetti et al. 2005; Lauer et al. 2005; Lena et al. 2014; Mazzalay et al. 2016). Besides a low-luminosity active galactic nucleus (AGN) at the center of the galaxy (Goss et al. 1987; Subrahmanyan et al. 2003; Balmaverde et al. 2006), NGC 5419 hosts a second nucleus about ~0″25 away from the AGN (Capetti et al. 2005; Lauer et al. 2005; Lena et al. 2014; Mazzalay et al. 2016). Assuming a distance of 56.2 Mpc for NGC 5419 (Mazzalay et al. 2016), this corresponds to a separation of ~70 pc. High-resolution SINFONI spectra reveal a high stellar velocity dispersion around both nuclei and between them, suggesting that each nucleus contains an SMBH and their masses are almost equal (Mazzalay et al. 2016). Axisymmetric dynamical models indicate a combined SMBH mass of $M_{BH} = 7.2^{+2.7}_{-1.9} \times 10^9 M_\odot$ (Mazzalay et al. 2016). Together with the observed radial
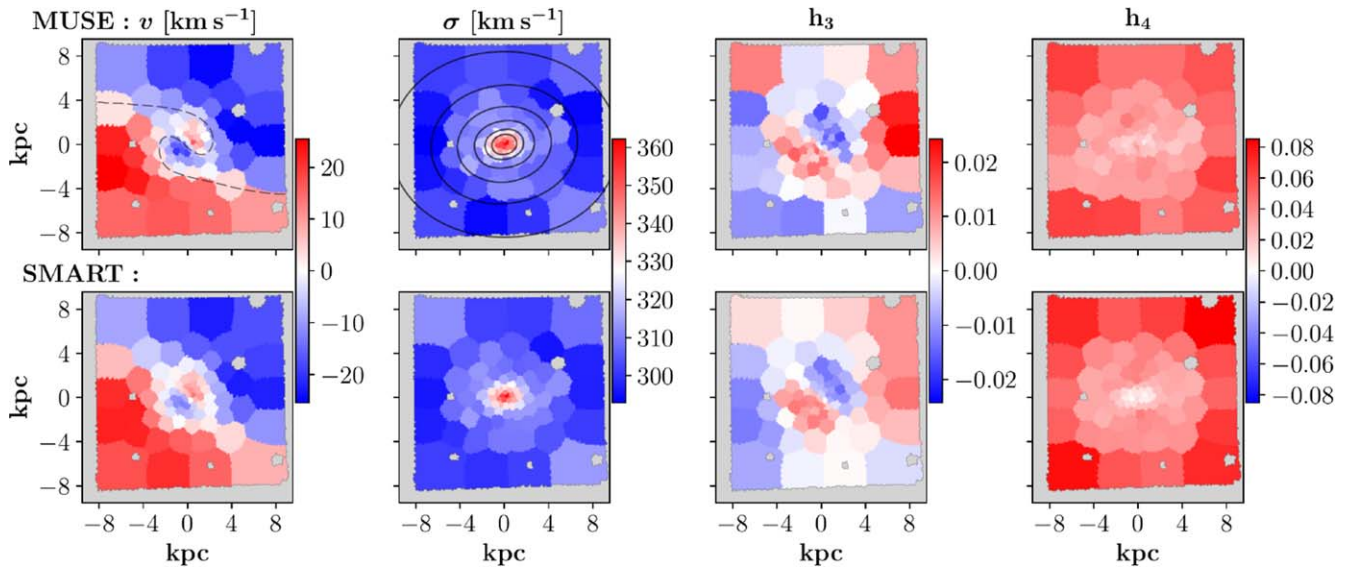
Figure 1. Maps of the velocity v, velocity dispersion σ, and Gauss–Hermite moments h_3 and h_4 of the MUSE data (top row) and accurately matching modeling fit by SMART (bottom row). The observed velocity panel (top left) shows a prominent kinematically distinct core. The counter-rotating core is misaligned by $\sim 120°$ in comparison to the outermost velocity structure. The inner velocity pattern is not abruptly separated from the outer one but the kinematic axis rotates continuously (see also Figure 3). This connection makes the overall velocity pattern resemble a "yin–yang" symbol (illustratively sketched in the top left panel by the dashed curve). For comparison, NGC 5419's isophotes are shown in black in the map of model velocity dispersion (top second panel). The MUSE kinematics are aligned along the position angle PA = 78° in agreement with the photometric major axis, i.e., north is at the top and east is to the left (see Mazzalay et al. 2016; Mehrgan et al. 2023).

separation of the two nuclei this implies that if the double nucleus is indeed an SMBH binary, then it is just about to become a hard binary.

With this, NGC 5419 could be the first ETG observed just at the transition between the two core formation phases described above. The rapid formation of the shallow density core through dynamical friction appears to have already taken place. However, the observed double nucleus suggests that the slower BH scouring process causing the characteristic tangentially biased central orbit distribution might have just begun.

The key to reveal the evolutionary stage of NGC 5419 is therefore to get precise measurements of NGC 5419's anisotropy profile. In this paper, we provide a new dynamical analysis of NGC 5419 that extends the previous models by Mazzalay et al. (2016) in several respects: we use additional 2D stellar kinematics based on MUSE observations (Mehrgan et al. 2019). We use nonparametric line-of-sight velocity distributions (LOSVDs) derived with a novel nonparametric spectral fitting code called WINGFIT (J. Thomas et al. 2023, in preparation). Our new dynamical models are triaxial rather than axisymmetric. They are based on the newly developed nonparametric deprojection routine SHAPE3D (de Nicola et al. 2020) and the new triaxial Schwarzschild code SMART (Neureiter et al. 2021). The current version of SMART uses a recently developed model selection framework (Lipka & Thomas 2021; Thomas & Lipka 2022) that avoids potential biases in χ^2-based models.

This paper is organized as follows. In Section 2 we briefly present the observations. In Section 3 we explain the triaxial deprojection and dynamical modeling machinery we use. In Section 4 we present our findings and results, which we discuss and summarize in Sections 5 and 6.

2. Observations

2.1. Surface Brightness

For our current study we use the SB data and analysis as described in Mazzalay et al. (2016), which is based on archived

HST/WFPC2 F555W and 3.6 μm Spitzer IRAC1 images. After masking the two central nuclei and matching the HST and Spitzer data (for a more detailed description we refer to Mazzalay et al. 2016), the elliptical isophotes were determined by using the IRAF task ELLIPSE (Jedrzejewski 1987). The corresponding profiles of surface brightness, ellipticity, and position angle are discussed in more detail in Section 4.2.

2.2. Nonparametric Stellar Kinematics

The stellar kinematical data for the dynamical modeling are based on spectroscopic observations for NGC 5419 using MUSE at the Very Large Telescope (VLT). NGC 5419 is part of a larger sample[4] of massive ETGs for which we obtained MUSE spectra with high signal-to-noise ratio (S/N). The data analysis and stellar kinematical measurements for the whole program are described in detail in Mehrgan et al. (2023). Our kinematic analysis is identical to what is explained in that paper except that we bin for an S/N that is roughly twice as high (to reduce the number of kinematic bins by a factor of two). The resulting spatial resolution is sufficiently high to produce robust and reliable results (see Sections 4.3 and 4.4) and it allows for an optimized usage of computational resources. To extract nonparametric LOSVDs for the dynamical models we use the nonparametric modeling code WINGFIT. For illustration, we show maps of the velocity, dispersion, and Gauss–Hermite coefficients (Gerhard 1993; Van der Marel & Franx 1993) derived from the nonparametric LOSVDs of NGC 5419 in Figure 1. More details about the kinematics and plots with the entire LOSVDs can be found in Mehrgan et al. (2023).

To test higher spatial resolution in the center, we performed an additional modeling analysis of a combined data set of the MUSE kinematics together with central adaptive-optics (AO)-assisted near-infrared observations from the SINFONI integral field spectrograph at the VLT. We use the nonparametric

---

LOSVDs derived from the SINFONI data by Mazzalay et al. (2016). The field of view (FOV) of these data covers $\sim(3 \times 3)$ arcsec and the AO operation enabled a spatial resolution of $\sim 0.''2$. Similar to the study in Mazzalay et al. (2016) we exclude the innermost Voronoi bins with $r < 0.''35$, where the galaxy hosts its double nucleus.

3. Triaxial Dynamical Modeling

NGC 5419 is the first galaxy that we analyze with our new triaxial codes SHAPE3D for the deprojection and SMART for the Schwarzschild orbit models. The two codes are described in detail in de Nicola et al. (2020) and Neureiter et al. (2021). The Schwarzschild models (Schwarzschild 1979) employ a new model selection framework extension, in which a generalized information criterion $AIC_p = \chi^2 + 2m_{eff}$ rather than the usual χ^2 gets minimized (Lipka & Thomas 2021; Thomas & Lipka 2022). By taking the individual model's degrees of freedom m_{eff} into account, bias in the evaluation of different mass models gets avoided. In Neureiter et al. (2023) and de Nicola et al. (2022a) we show that our triaxial models are able to recover the correct dynamical structure and mass composition of a realistic simulated ETG merger remnant with an accuracy at the 5%–10% level. SMART uses the density output from SHAPE3D to compute the corresponding stellar part of the gravitational potential by expansion into spherical harmonics. SMART launches stellar orbits, including near-Keplerian orbits in the center, from a five-dimensional orbit starting space. It can use the entire information contained in the nonparametric LOSVDs.

When modeling NGC 5419 with SMART we focus on recovering its stellar orbit distribution, in particular its anisotropy distribution. We furthermore want to obtain updated measurements of the stellar mass-to-light ratio Υ and black hole mass M_{BH} of NGC 5419.

For the modeling we assume that the central region of NGC 5419 can be described by the potential of a single BH. We furthermore assume a constant mass-to-light ratio in our dynamical models and ignore possible initial mass function gradients.

We set up a parameter grid covering 10 values of stellar mass-to-light ratio within $\Upsilon \in [4.0, 8.0]$ with a corresponding grid size of $\Delta\Upsilon = 0.44$ and 10 tested values of black hole mass within $M_{BH} \in [0.5, 2.0] \times 10^{10}\, M_\odot$ with $\Delta M_{BH} = 0.17 \times 10^{10}\, M_\odot$. We furthermore vary the viewing angles θ, ϕ, and ψ in our models in correspondence with the SB density candidates, which are provided by SHAPE3D.

SHAPE3D is able to constrain the range of possible orientations of a triaxial galaxy based on photometric information alone by discarding deprojections where the radial profiles of the flattenings $p = b/a$ and $q = c/a$ (with a being the semimajor, b the semi-intermediate, and c the semiminor axes of a triaxial galaxy) are not smooth (de Nicola et al. 2020, 2022b). When deprojecting the observed SB of NGC 5419 we apply an rms cutoff rms$= \sqrt{\langle(\ln(I_{obs}/I_{fit}))^2\rangle} \leqslant 0.013$ for the maximum discrepancy between the observed and modeled surface brightnesses. We furthermore discard all deprojections where p and q deviate by more than 0.1 from their expected values due to radial changes in the order of the principal axes. With this, SHAPE3D provides 25 candidate orientations and respective luminosity profiles, which we probe with the dynamical models.

We assume a Dark Matter (DM) profile similar to a spherical Navarro–Frenk–White (NFW) halo (Navarro et al. 1996), yet with an inner density slope $\gamma = 0$. We vary the density normalization $\rho_0 \in [10^{7.6}, 10^{8.1}]\, M_\odot\, kpc^{-3}$ at $r = 10\, kpc$ $(\Delta \log_{10}(\rho_0[M_\odot\, kpc^{-3}]) = 0.08)$ and use a fixed scale radius $r_s = 40\, kpc$.

Following triaxial symmetry we can separate the kinematic input data of NGC 5419 along the galaxy's apparent minor axis (see Figure 1) in order to model two equivalent data sets without loss of information. This provides us with an estimate of the statistical error of our modeling results (see Neureiter et al. 2023).

4. Results

4.1. Kinematic Recovery

Figure 1 shows the MUSE kinematic maps in the top row and the best-fit model by SMART in the bottom row. The kinematic structure of NGC 5419 can be well explained by the triaxial models (averaged over both sides we get $\chi^2/N_{data} = 0.45$). As already visible in the SALT stellar kinematics (Mazzalay et al. 2016) but much more clearly revealed by the MUSE observations (Mehrgan et al. 2023), the velocity map of NGC 5419 points to a kinematically distinct core (KDC). We will come back to the KDC in Section 4.5.

Figure 2 shows the quality of the triaxial dynamical modeling fit illustrated by a comparison between the Gauss–Hermite parameterizations of the observed MUSE data (black data points) and modeled fit (red data points). We note that all the main features of NGC 5419, in particular its specific velocity pattern including the KDC, can be explained in our equilibrium triaxial model. This suggests that the galaxy is observed at an evolutionary state that is relaxed enough that the dynamical modeling results are robust.

4.2. Shape Recovery

Figure 3 shows profiles of the observed SB, ellipticity (ϵ), and position angle (PA) (colored black) as well as the best-fit deprojection (colored red). The red shaded line is bounded by the two best-fit deprojections from modeling the two sides of the kinematic observational data (see Section 3) and we also show their mean (red solid line). The data suggest that the line of sight is between the galaxy's long and short axes with best-fit viewing angles[5] of $\theta = (65 \pm 10)°$, $\phi = (30 \pm 10)°$, and $\psi = (100 \pm 10)°$. At this orientation both the SB profile and the kinematics of the triaxial model match very well with the observations at all radii. The observed position angle shows a twist of $\sim 20°$, such that the galaxy cannot be axisymmetric. The relatively large PA twist and the observed ellipticity, which shows bumps of the order of $\Delta\epsilon \sim 0.05$, are consistent with the findings described in the subsequent Sections 4.4, 4.5, and 5.2, pointing to a late but presumably not *fully* completed merging phase of the galaxy. The deprojected profiles of ϵ and PA match the observed ones particularly well outside the sphere of influence, r_{SOI} (gray vertical line, see Section 4.3).

The radii where the ellipticity profile features bumps appear to match with the radii at which the rotation velocity along the galaxy's photometric major axis (aligned along PA = 78°, see Figure 1) changes direction (see lower right panel in Figure 3 with the eastern side of the kinematic data colored brown and

---

[5] For a detailed explanation of the viewing angles, see Neureiter et al. (2021).
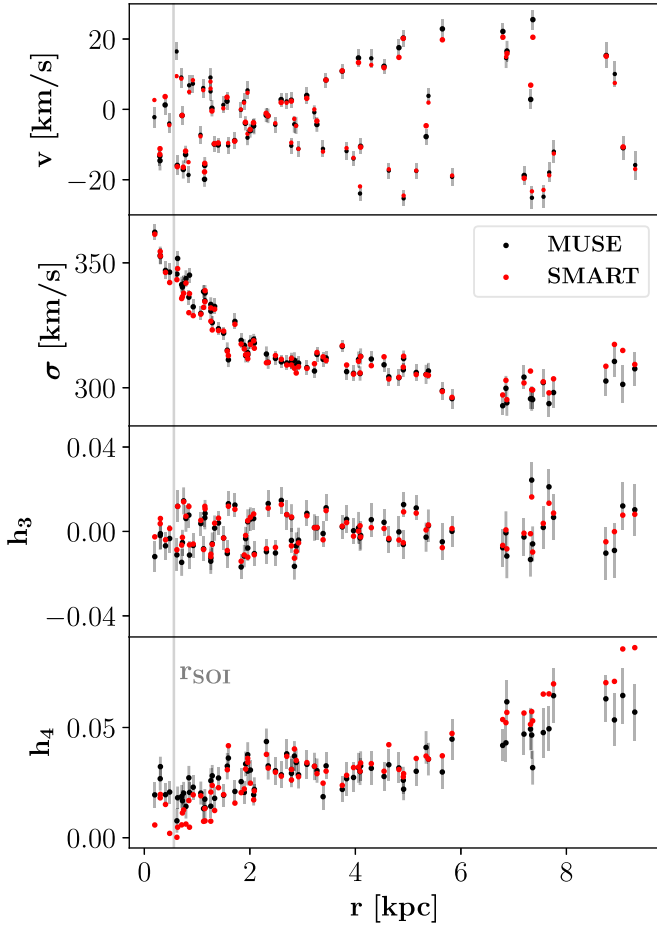
Figure 2. Comparison of Gauss–Hermite parameters of the observed MUSE data (black points with error bars) and best-fit model (red points). This plot shows all data and model points as a function of radius computed for all Voronoi bins. The sphere of influence, r_{SOI} (= 0.57 kpc; defined as $M_*(r < r_{SOI}) = M_{BH}$; see also Section 4.3), is marked as a gray vertical line. While our triaxial model fits the full nonparametric LOSVDs, we here illustrate the quality of the fit in terms of Gauss–Hermite parameters that were determined a posteriori. The agreement between model and data is very good.

the western side colored gray). These radial changes in the rotation direction can also be seen in the velocity map in Figure 1 and their origin will be explained in Section 4.5.

The bottom left panel in Figure 3 shows the profiles of p and q of the best-fit deprojections of NGC 5419, where one can see that this galaxy becomes oblate in both its center and its outskirts while it is triaxial at intermediate radii.

The bottom right panel quantifies the variation of NGC 5419's kinematic position angle (determined with the Kinemetry Code of Krajnović et al. 2006). The total amplitude of the variation is ∼120°, in accordance with the visual impression that the center of the galaxy "almost" counter-rotates with respect to the outer parts (Figure 1).

Altogether, the photometric twist, the variation in ϵ, and the change in the kinematic PA are typical for a triaxial galaxy.

4.3. Mass Recovery

Figure 4 shows the minimum-subtracted AIC_p curves (see Section 3) plotted against the stellar mass-to-light ratio Υ (left panel) and black hole mass M_{BH} (right panel). The solid line corresponds to the models covering the eastern side and the
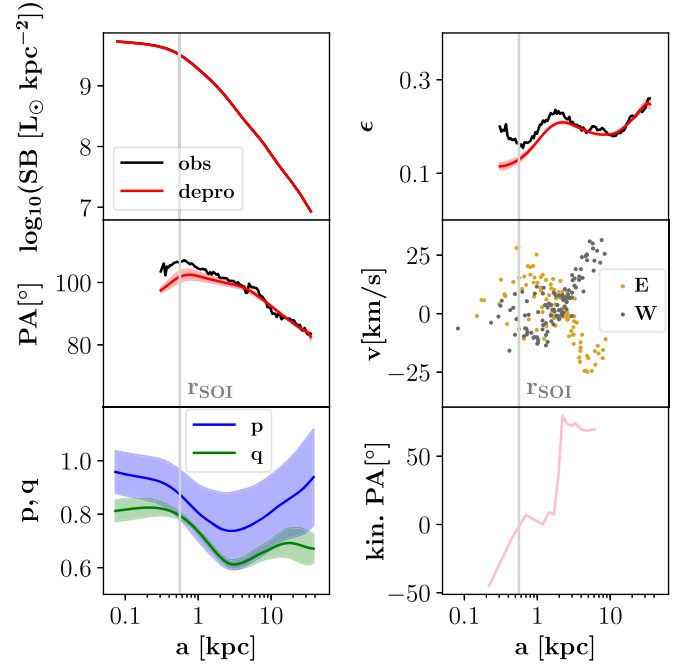

Figure 3. Surface brightness SB, ellipticity ϵ, photometric position angle PA, velocity v along the galaxy's photometric major axis, profiles of axis ratios p and q, and kinematic PA as functions of the elliptical isophotes' semimajor axis length a. The red solid line shows the mean and the shaded region shows the standard deviation of the best-fit deprojections of the modeled two sides of the galaxy. The deprojection follows the observed profile (black line) within the relevant region of $r > r_{SOI}$ (marked as a gray vertical line). The bumps in the ellipticity profile match with the changes in rotation sign in the velocity signal of the MUSE data along the galaxy's major axis (second right panel). The p and q profiles reveal a nearly oblate shape of the center and the outskirts of NGC 5419. The variation in the kinematic PA corresponds to the observed KDC.

dashed line corresponds to the models covering the western side of the kinematic MUSE data. The vertical lines mark the mass parameters of the best-fit model, which is determined as the one with the minimum of all AIC_p values.

As Figure 4 shows, we obtain well-determined best-fit mass parameters. Averaged over the two sides we measure $\Upsilon = 5.56 \pm 0.22$ and $M_{BH} = (1.0 \pm 0.08) \times 10^{10}\ M_\odot$. With these, we determine a sphere of influence[6] of $r_{SOI} = (0.57 \pm 0.02)$ kpc, i.e., $2\farcs09 \pm 0\farcs07$, for NGC 5419. We find that our best-fit BH mass fits well into the M_{BH}–r_b correlation found by Rusli et al. (2013) based on 20 analyzed core galaxies with dynamical M_{BH} measurements, confirming our results (here we use the core radius measurement $r_b = 1\farcs58$ from Mazzalay et al. 2016; also the similar core radius measurement of $r_b = 1\farcs43$ from Dullo & Graham 2014 aligns with the M_{BH}–r_b correlation by Rusli et al. 2013 within its uncertainties). The DM density normalization is recovered as $\log_{10}(\rho_0[M_\odot\ \mathrm{kpc}^{-3}]) = 7.93 \pm 0.08$.

With a point spread function radius of ∼0$\farcs$78 for the MUSE data alone the sphere of influence of ∼2$\farcs$09 is marginally resolved. The constraints on M_{BH} are significant (the difference between the two modeled sides is very small), probably due to the high S/N ($\gtrsim$200 per spectral bin in the optical region in each of about 220 Voronoi bins distributed over the whole FOV) in the MUSE data, which allows us to extract LOSVDs with a high level of detail.

---

[6] We use the definition of the sphere of influence as the radius within which the total stellar mass equals the black hole mass.
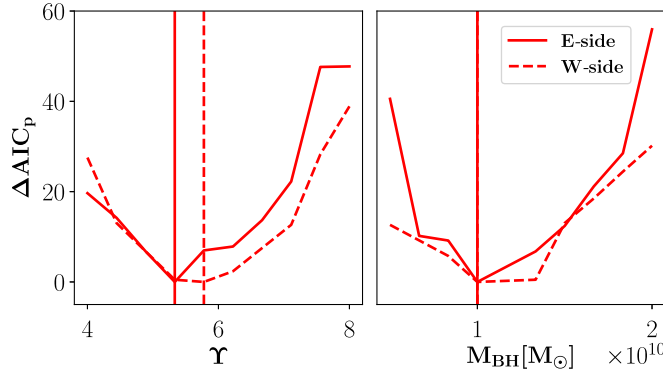
Figure 4. Minimum-subtracted $AIC_p = \chi^2 + 2m_{eff}$ curves for Υ (left panel) and M_{BH} (right panel) when modeling the eastern (solid line) and western (dashed line) sides of the MUSE data with SMART. Instead of minimizing only χ^2, our advanced dynamical modeling machinery takes the degrees of freedom m_{eff} of the individual models into account to avoid any bias when determining the best-fit parameters. The vertical lines show the best-fit mass parameters ($\Upsilon = 5.56 \pm 0.22$ and $M_{BH} = (1.0 \pm 0.08) \times 10^{10} \, M_{\odot}$).

To test the robustness of our measurement, we performed an additional modeling analysis including the central AO-assisted SINFONI data. While the focus of this cross-check is the recovery of NGC 5419's central orbit distribution, which is of particular interest for our current study (see Sections 4.4 and 5.2), we also try to again recover Υ and M_{BH} using this combined data set. Assuming that the SINFONI FOV coverage is too small to significantly affect the DM halo recovery, we remodelled a 2D grid with variations of the black hole mass and stellar mass-to-light ratio and set the generalized NFW (gNFW) parameters to the best-fit DM halo parameters from modeling the MUSE kinematics only. With this simplified analysis, SMART finds a best-fit stellar mass-to-light ratio of $\Upsilon = 6.1 \pm 0.1$ and black hole mass of $M_{BH} = (7.2 \pm 0.5) \times 10^9 \, M_{\odot}$ with an average kinematic deviation of only $\chi^2/N_{data} = 0.49$. With this, the BH mass found in this way deviates by 28% and the stellar mass-to-light ratio slightly deviates by 10% in comparison to the modeling results based on the MUSE data alone. More crucial, however, is the fact that the anisotropy profile remains unaffected by the data set used and the corresponding best-fit mass parameters (see Section 4.4).

4.4. Anisotropy Recovery

Figure 5 shows the mean anisotropy profile of the best-fit models of the two sides when modeling the MUSE data with SMART, plotted against the radius scaled by the core radius $r_b = 1.''58$ (Mazzalay et al. 2016). The red shaded region is bounded by the two respective best-fit models. The anisotropy parameter $\beta = 1 - (\sigma_\theta^2 + \sigma_\phi^2)/2\sigma_r^2$ (e.g., Binney & Tremaine 2008) consists of the velocity dispersions along the radial (σ_r) and tangential (σ_θ, σ_ϕ) directions and describes whether a galaxy's orbit distribution is radially anisotropic for $\beta > 0$ or tangentially anisotropic for $\beta < 0$. Our triaxial models reveal an isotropic, i.e., $\beta \sim 0$, central orbit distribution for NGC 5419. Such an isotropic central β profile is highly unusual for cored ETGs and we will discuss its implication further in Section 5.2.

The central isotropy remains when we model the combined data set MUSE+SINFONI (even though the best-fit models for this run are weakly tangential in the very center; see the blue line in Figure 5). As another robustness check we modified the smoothing parameter of the central deprojection. As is visible in Figure 3, our best-fit deprojections used for the dynamical models show minor deviations in the ϵ and PA profiles within r_{SOI}. By reducing the smoothing in SHAPE3D (for a detailed
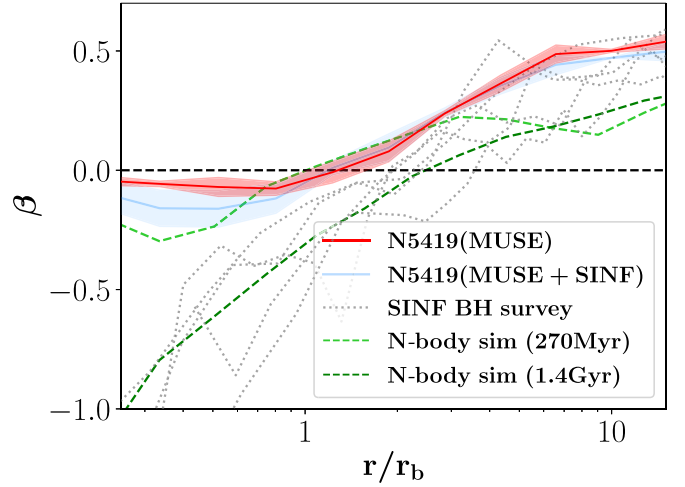

Figure 5. Anisotropy profile as a function of the radius scaled by r_b. The red shaded region is bounded by the β profiles when modeling the two sides of the MUSE data and we also show the mean of the two models in between (red solid line). In contrast to the dark green and gray dashed lines, which correspond to the β profiles of a numerical simulation of a gas-free major merger with cuspy progenitor galaxies (observed ∼1.4 Gyr after the merger has happened) and a sample of SINFONI-observed core ETGs, NGC 5419 shows an isotropic central orbit distribution. This behavior is data-independent and does not change when modeling the MUSE kinematics combined with central high-resolution SINFONI data (blue line). The light green dashed line corresponds to the ETG merger simulation observed at an earlier stage (∼270 Myr after the merger), which will be explained and discussed in Section 5.2.

description see de Nicola et al. 2020), we obtained additional deprojections that better fit the central changes in ϵ and PA. As expected, however, remodelling the galaxy with these deprojections (in our best-fit MUSE mass distribution) had no impact on the central anisotropy structure.

4.5. Origin of the Kinematically Distinct Core

As already shown in Figure 1 and briefly described in Section 4.1, NGC 5419 shows a KDC. In general, KDCs together with isophote twists are frequently observed in massive ellipticals with depleted stellar cores such as NGC 5419 (e.g., Efstathiou et al. 1982; Bender 1988; Franx & Illingworth 1988; Emsellem et al. 2004; Hau & Forbes 2006; McDermid et al. 2006; Krajnović et al. 2011; Ene et al. 2018).
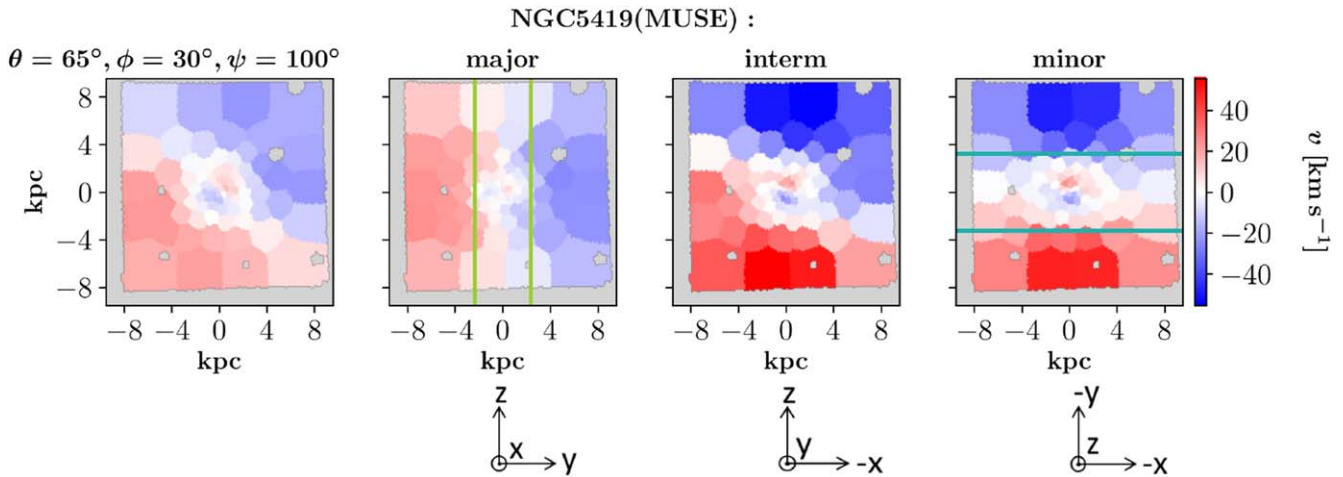
Figure 6. Velocity maps of the best-fit model of NGC 5419 projected along different lines of sight: at the viewing angles assumed in the fit (left panel) as well as along the model's principal axes (second to fourth panels). The indicated coordinate systems demonstrate the orientation of the principal axes. The observed KDC and "yin–yang" velocity pattern of NGC 5419 appear to result from a projection effect caused by the overlay of z-tubes and x-tubes. The major (minor) axis projection singles out the rotation pattern of the z-tubes (x-tubes). The stronger velocity signal is in the x-tubes while the velocity signal from the z-tubes is weaker, but both show a velocity flip. Inside the flip radius marked by green vertical lines, the z-tubes rotate in the opposite direction to in the outskirts, and inside the blue horizontal lines, the x-tubes rotate in the opposite direction to outside.

The early standard model for KDCs in ETGs was early merging with dissipative formation of the KDC (see, e.g., Bender 1996; Davies et al. 2001). This is a still valid formation scenario for some ellipticals, such as NGC 5322 (Bender 1988; Dullo et al. 2018) or IC 1459 (Franx & Illingworth 1988; Cappellari et al. 2002), which show a fast rotating core with stars that counter-rotate in a disk on orbits that are close to circular and slow outer parts rotating in the opposite direction.

Several observations suggest that the stellar populations of KDCs in some slowly rotating ETGs show little or no difference to the stellar populations of the surrounding host galaxies (Davies et al. 2001; McDermid et al. 2006; Nedelchev et al. 2019; Kuntschner et al. 2010). Recent high-resolution numerical simulations of gas-free mergers hosting SMBHs (Rantala et al. 2019; Frigo et al. 2021) provide another possible explanation for the origin of kinematically distinct velocity structures in such ETGs.

These simulations consist of collisionless dark matter halos, collisionless stellar components, and SMBHs and they accurately compute the collisional interactions of the stars with the SMBHs with a regularized integration scheme (Rantala et al. 2017, 2018). In these simulations, the formation of counter-rotating cores is explained by the infall of the SMBHs with the bound stellar nuclei, which experience angular momentum reversals of their orbits after pericenter passages. The gravitational torque effects resulting in the reversals can be caused by deflections between the bulge and the halo due to the merger process (Barnes 2016) or "dynamical self-friction," in which tidally expelled material exerts a force on the merger subhalo (Van den Bosch & Ogiya 2018). The specific velocity pattern of NGC 5419 visible in Figure 1, however, not only shows a counter-rotating core but, more generally, a kinematically misaligned core in the sense that the inner velocity structure shows a slight misalignment in comparison to the direction of the outermost velocity structure. Moreover, the 2D velocity pattern resembles a kind of "yin–yang symbol" on the sky caused by an apparent connection between the velocity pattern of the KDC and its surrounding large-scale velocity field. The connections

between the red and blue inner and outer velocity structures, which cause the similarity to a yin–yang symbol, become even more apparent with the finer bins of Mehrgan et al. (2023).

Figure 6 shows rotation maps of the best-fit model of the MUSE kinematics (when modeling all the kinematic data with the best-fit parameters from the models for the eastern side) projected along different lines of sight: along the best-fit orientation of the galaxy (left panel) as well as along its three principal axes (labeled major, interm, and minor). Our projected velocity maps reveal that the origin of such complex and misaligned KDCs as in NGC 5419 can be simply explained by an overlay of orbits rotating around two different axes in an equilibrium triaxial model. These orbits are z-tubes, e.g., visible in the major axis projection, and x-tubes, e.g., visible in the minor axis projection (see Figure 6, second and fourth panels). As one can see in Figure 6, the z-tubes within $r < 2.4$ kpc (marked by green vertical lines) and the x-tubes within $r < 3.3$ kpc (marked as blue horizontal lines) rotate in the opposite direction to their respective counterparts at large radii. The left panel in Figure 7 demonstrates this behavior in another way by showing the radial mass difference $\Delta(M_{pro} - M_{retro})$ between prograde and retrograde z- and x-tube orbits, which is computed within radial shells. The orbit classification in our triaxial dynamical models is thereby done by checking the sign conservation of the angular momentum components along the three principal axes during the surfaces-of-section crossings (for a more detailed explanation see Neureiter et al. 2021). Outside the flip radius $r = 3.3$ kpc of the x-tubes, the prograde component dominates, and inside this radius the retrograde component dominates (we here define prograde orbits as those with $L_x > 0$ and retrograde orbits as those with $L_x < 0$ according to the coordinate systems shown in Figure 6). This is in agreement with the prominent central counter-rotation signal of the x-tubes visible in the minor-axis projection of our model of NGC 5419 (see Figure 6, fourth panel). Outside $r = 2.4$ kpc, the prograde component of the z-tubes dominates clearly over the retrograde component, and within $r < 2.4$ kpc, the components are almost equal with a slight overabundance of retrograde z-tubes. This corresponds to the weak central
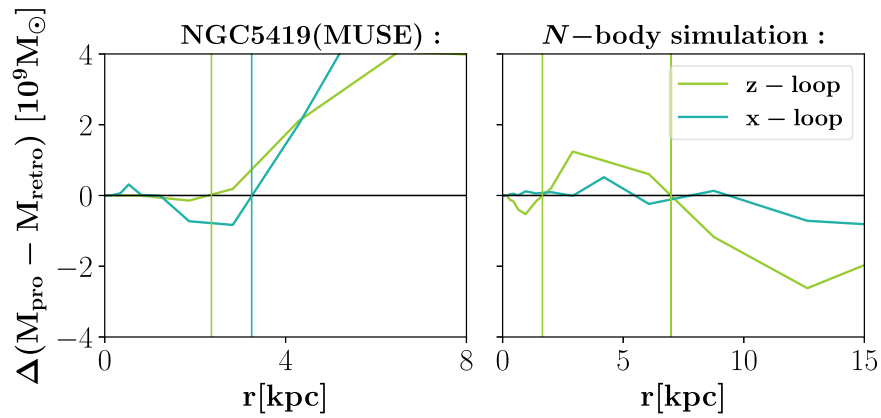
Figure 7. Left: mass excess of prograde and retrograde z-tube (green) and x-tube (blue) orbits in NGC 5419. The radial regions of KDCs can be determined as "flip radii" (vertical lines) at which the net rotation direction of a certain orbit family (z- and/or x-tubes) switches sign. The net rotation results from the prograde orbits carrying more stars than the retrograde ones or vice versa. Right: same for a merger simulation. While the profile of $\Delta(M_{\mathrm{pro}} - M_{\mathrm{retro}})$ of the numerical merger simulation shows two flip radii, resulting in an inner KDC and an outer one, NGC 5419 shows a single flip radius. Nevertheless, the KDC in the simulation is—similar to NGC 5419—caused by the excess of tube orbits rotating around a preferred direction, and the N-body simulation's outer flip radius is qualitatively similar to that of NGC 5419. This hints at a similar formation process.

counter-rotation signal of the z-tubes visible in the major-axis projection of our model of NGC 5419 (see Figure 6, second panel).

In order to understand whether the properties of NGC 5419's KDC can be explained by the black hole spin-flip scenario outlined above, we now compare it to the numerical N-body simulation by Rantala et al. (2019) for which the counter-rotating core was shown to result from the rotation flips. This simulation of an ETG major merger includes two equal-mass SMBHs with a total black hole mass of $1.7 \times 10^{10} \, M_\odot$, and the two progenitor galaxies are set up by using a spherically symmetric Dehnen density potential (Dehnen 1993) with an initial inner stellar density slope of $\rho \propto r^{-3/2}$. In a series of recent papers (Neureiter et al. 2021, 2023; de Nicola et al. 2022a) we have modeled this simulation in great detail in order to test our triaxial modeling code. This N-body simulation was designed to explain another core galaxy (NGC 1600), which is only slightly different from NGC 5419 in terms of its stellar mass and black hole mass. As shown in Rantala et al. (2019), the velocity amplitude of the KDC signal is qualitatively similar to the one observed in NGC 5419. Different to NGC 5419, this simulation has undergone a second reversal of the SMBH angular momentum. As one can see in the right panel of Figure 7, the rotation flip in the simulation is mainly caused by an overpopulation of retrograde z-loops within $r < r_1 = 1.65$ kpc, an overpopulation of prograde z-loops within $r_1 < r < r_2 = 7.0$ kpc and an overpopulation of retrograde z-loops in the outskirts $r > r_2$. The N-body simulation's outer flip radius $r_2 = 7.0$ kpc thereby is qualitatively similar to NGC 5419's single flip radius.

With this, we find that in both cases—in NGC 5419 as well as in the N-body simulation—the KDC can be explained by the mass excess of counter-/corotating tube orbits inside/outside the respective flip radii. While the number of rotation flips and the type of affected tube orbits can be expected to depend on the merger's specific initial conditions, such as the orbit geometry and impact parameter, the spatial scale and velocity amplitude of NGC 5419's KDC are notably similar to what can be found in the numerical simulation of a gas-free merger.

Altogether this strongly suggests that the KDC in NGC 5419 formed as a result of orbital angular momentum flips of the BHs during a merging process.

5. Discussion

5.1. Comparison to Other KDC Studies

Other studies from the literature that analyzed KDCs with Schwarzschild models (Cappellari et al. 2002; Van den Bosch et al. 2008; Krajnović et al. 2015; den Brok et al. 2021) suggested that their examined KDCs are not actually *decoupled* in the sense that counter-rotating orbits are not exclusively localized in the central region but present everywhere. This is in agreement with our analysis from Section 4.5, where we show that NGC 5419's KDC results from an excess of tube orbits rotating in the contrary direction compared to the outskirts. A smooth excess mass profile as shown in Figure 7 is less likely for dissipationally formed KDCs in massive ETGs, such as in the already mentioned examples of NGC 5322 and IC 1459 (see Section 4.5), where the counter-rotating stars on a central disk have a more prominent separation in phase space. In this respect, the slow inner KDCs of some of the most massive galaxies might also be different from those in less massive galaxies, which are faster and probably also have a dissipative origin (McDermid et al. 2006). The stellar populations in KDCs of less massive galaxies are often distinct from the rest of the galaxy (Hau et al. 1999; McDermid et al. 2006; Nedelchev et al. 2019). The term kinematically *decoupled* core might be misleading when used for both cases. For most massive galaxies, the term kinematically *decoupled* core infers neither an abrupt depletion of corotating orbits inside the KDC nor a distinct stellar population in the KDC. Nevertheless, the orbital properties inside the KDC are in some sense "distinct" from those in the rest of the galaxy. The specific properties of the KDC likely depend on the specific dynamics that take place in the center of a merger remnant and are somewhat local and detached from the global properties of the remnant. A probably more intuitive description of a "KDC" in slowly rotating ETGs, as it is described in this study, might be a kinematically *distinct* or *misaligned* core (where a

counter-rotating core would be a particular form of kinematical misalignment observed under certain viewing angles).

5.2. A Core in Formation?

NGC 5419's isotropic central orbit distribution (Figure 5 and Section 4.4) differs significantly from the strong tangential anisotropy observed in other core galaxies with high-resolution SINFONI data (Thomas et al. 2014; gray lines in Figure 5). The orbital structure of these other core galaxies and in particular their central tangential anisotropy, however, are remarkably similar to the orbital structure in ETG merger simulations. The dark green dashed line plotted in Figure 5 shows the β profile of the N-body simulation by Rantala et al. (2018), which is observed ~1.4 Gyr after the merger has happened (we use $r_b(1.4\,\mathrm{Gyr}) = 0.49$ kpc; Rantala et al. 2019).

Why is the core of NGC 5419 isotropic? As already explained in the Introduction, the core forms in two phases: First, a shallow central stellar density profile forms very rapidly within a timescale of some 10 million years around the first passage of the two galaxies. This is followed by the much slower BH slingshot process that changes the central orbital structure from being isotropic to becoming tangential on a timescale of some 100 million years up to 1 Gyr. According to this, the snapshot of the ETG merger simulation 1.4 Gyr after the merger represents a galaxy where both formation phases have completed and the core region is strongly tangential. The cored ETGs in the sample of Thomas et al. (2014) are all consistent with being ETGs where both core phases have already taken place.

A simple explanation for the fact that NGC 5419 already has a flattened density profile but is still isotropic in its center would be that the galaxy is just between the two phases: the rapid formation of the shallow density core driven by dynamical friction has already passed yet the scouring process is yet to begin. In fact, we analyzed the same merger simulation (Rantala et al. 2018) at an earlier stage, ~270 Myr after the merger has happened, which is about the time when the BHs form a hard binary (Frigo et al. 2021; light green dashed line in Figure 5; we use $r_b(270\,\mathrm{Myr}) = r_b(1.4\,\mathrm{Gyr})$). As one can see, at this earlier evolutionary stage, the center of the ETG merger simulation is indeed still isotropic (as already described in Rantala et al. 2018 and Frigo et al. 2021). The similarity between the orbital structure of NGC 5419 and the early snapshot of the ETG merger simulation supports the idea that core scouring is just beginning in NGC 5419.

In principle, repeated minor mergers can also lead to a weaker central tangential anisotropy than a single major merger (Rantala et al. 2019), which can stay almost isotropic over time. However, the KDC in NGC 5419 is characteristic of the orbital reversals of the progenitor SMBHs that only happen in major mergers with massive SMBHs (Rantala et al. 2019). Another scenario presented in Rantala et al. (2019), which results in an only mildly tangentially biased central orbit distribution and a velocity structure similar to NGC 5419, would be a major merger of two core galaxies. Here, violent relaxation processes and the infall of SMBHs can weaken the tangential anisotropy of the progenitor galaxies in the remnant. While in such a scenario the central orbit distribution can remain almost isotropic even after the BHs have merged (Rantala et al. 2019), a *fully evolved* core–core merger scenario does not provide a direct explanation for the observed double nucleus.

In conclusion, the most plausible scenario is that while the galaxy merger that forms NGC 5419 is almost completed, the core formation process is at an *earlier* stage. This approach is able to simultaneously explain all observed and measured features:

1. the central isotropic orbit distribution,
2. the double nucleus visible in the HST image surrounded by a region of enhanced stellar velocity dispersion,
3. the already evolved cored SB profile, and
4. the galaxy's KDC, which probably reflects orbital reversals of the progenitor SMBHs that only happen in major mergers with massive SMBHs.

Finally, we note that the observed wiggles in the galaxy's ellipticity profile and their correlation with the flips in the rotation direction of the stars may further indicate that the galaxy is in an earlier phase of core formation. Nevertheless, the evolutionary state of NGC 5419 appears to already be relaxed enough for us to obtain robust dynamical equilibrium models. This is supported by the plausible mass results and anisotropy profiles, which are similar for both modeled data sets (eastern and western sides of the kinematics), as well as by the fact that all specific velocity features can be well fitted with an averaged deviation of only $\chi^2/N_{\mathrm{data}} = 0.45$.

5.3. Comparison of Mass Recovery with Other Studies

By modeling SINFONI data and optical long-slit SALT spectra assuming axisymmetry, Mazzalay et al. (2016) determined a best-fit stellar mass-to-light ratio of $\Upsilon = 5.37^{+1.86}_{-1.42}$ and black hole mass of $M_{\mathrm{BH}} = 7.24^{+2.74}_{-1.91} \times 10^9\,M_\odot$. Within the error bars, their determined mass parameters agree with our best-fit values determined when modeling the MUSE data alone as well as with our best-fit parameters when modeling the combined MUSE and SINFONI kinematics (see Section 4.3).

6. Conclusion

We present new triaxial dynamical models based on new spectroscopic MUSE data on the massive elliptical core galaxy NGC 5419, which hosts a double nucleus. We focused on a precise recovery of the galaxy's orbital structure. Our best-fit model shows a surprisingly isotropic central orbit distribution, which is in contrast to other core ETGs, which typically show a tangentially biased central orbit distribution. The observed double nucleus together with the isotropic central orbit distribution most likely suggest that NGC 5419 has undergone only the first phase of core formation so far: the dynamical friction associated with the sinking SMBHs in a gas-free merger causes a flattening of the central density profile. Such a depleted stellar density core is definitely in place in NGC 5419. However, the subsequent SMBH scouring process, which kicks out stars on radial orbits and slowly produces a tangentially biased orbit distribution, has probably just begun. This supports the idea that the double nucleus at the center of the galaxy is in fact an SMBH binary (Mazzalay et al. 2016).

We find a best-fit stellar mass-to-light ratio of $\Upsilon = 5.56 \pm 0.22$ and best-fit black hole mass of $M_{\mathrm{BH}} = (1.0 \pm 0.08) \times 10^{10}\,M_\odot$ for the MUSE data set. We find a slightly smaller best-fit BH mass when adding high-resolution AO-assisted SINFONI data. The recovery of the anisotropy profile, however, is unaffected by this, and in particular the central orbit distribution remains isotropic independent of which data are fitted.

NGC 5419 has a prominent yin–yang-like KDC and is a particularly interesting case in which to study the formation of kinematic misalignments. When projecting our best-fit triaxial model along the galaxy's principal axes, we find rotation flips in the tube orbits around $r \sim 3$ kpc. These flips together with projection effects are sufficient to produce the observed complex rotation field. Recent ETG merger simulations have shown that during gas-free major mergers, SMBHs (in the mass range implied by our models for NGC 5419) and the bound stellar nuclei can experience one or more reversals of their orbits (Rantala et al. 2019). Similar to what can be found in our models of NGC 5419, the traces of these orbital reversals in the N-body simulations appear as an excess mass of counter-/corotating tube orbits inside/outside the effective flip radii. The fact that the spatial scale and velocity amplitude of NGC 5419's KDC are qualitatively similar to what can be found in the N-body simulation hints at a similar formation process of the KDC.

ORCID iDs

Bianca Neureiter ⓘ https://orcid.org/0000-0001-6564-9693
Jens Thomas ⓘ https://orcid.org/0000-0003-2868-9244
Antti Rantala ⓘ https://orcid.org/0000-0001-8789-2571
Thorsten Naab ⓘ https://orcid.org/0000-0002-7314-2558
Kianusch Mehrgan ⓘ https://orcid.org/0000-0002-9821-3535
Roberto Saglia ⓘ https://orcid.org/0000-0003-0378-7032
Stefano de Nicola ⓘ https://orcid.org/0000-0001-6173-5404
Ralf Bender ⓘ https://orcid.org/0000-0001-7179-0626

References

Balmaverde, B., Capetti, A., & Grandi, P. 2006, A&A, 451, 35
Barnes, J. E. 2016, MNRAS, 455, 1957
Begelman, M. C., Blandford, R. D., & Rees, M. J. 1980, Natur, 287, 307
Bender, R. 1988, A&A, 202, L5
Bender, R. 1996, in IAU Symp. 171, New Light on Galaxy Evolution, ed. R. Bender (Dordrecht: Kluwer), 181
Bender, R., Burstein, D., & Faber, S. M. 1992, ApJ, 399, 462
Binney, J., & Tremaine, S. 2008, Galactic Dynamics (2nd ed.; Princeton, NJ: Princeton Univ. Press), 263
Capetti, A., Verdoes Kleijn, G., & Chiaberge, M. 2005, A&A, 439, 935
Cappellari, M., Verolme, E. K., van der Marel, R. P., et al. 2002, ApJ, 578, 787
Davies, R. L., Kuntschner, H., Emsellem, E., et al. 2001, ApJL, 548, L33
de Nicola, S., Neureiter, B., Thomas, J., Saglia, R. P., & Bender, R. 2022a, MNRAS, 517, 3445
de Nicola, S., Saglia, R. P., Thomas, J., et al. 2022b, ApJ, 933, 215
de Nicola, S., Saglia, R. P., Thomas, J., Dehnen, W., & Bender, R. 2020, MNRAS, 496, 3076

Dehnen, W. 1993, MNRAS, 265, 250
den Brok, M., Krajnović, D., Emsellem, E., Brinchmann, J., & Maseda, M. 2021, MNRAS, 508, 4786
Dullo, B. T., & Graham, A. W. 2014, MNRAS, 444, 2700
Dullo, B. T., Knapen, J. H., Williams, D. R. A., et al. 2018, MNRAS, 475, 4670
Ebisuzaki, T., Makino, J., & Okumura, S. K. 1991, Natur, 354, 212
Efstathiou, G., Ellis, R. S., & Carter, D. 1982, MNRAS, 201, 975
Emsellem, E., Cappellari, M., Peletier, R. F., et al. 2004, MNRAS, 352, 721
Ene, I., Ma, C.-P., Veale, M., et al. 2018, MNRAS, 479, 2810
Faber, S. M., Tremaine, S., Ajhar, E. A., et al. 1997, AJ, 114, 1771
Franx, M., & Illingworth, G. D. 1988, ApJL, 327, L55
Frigo, M., Naab, T., Rantala, A., et al. 2021, MNRAS, 508, 4610
Gebhardt, K., Richstone, D., Tremaine, S., et al. 2003, ApJ, 583, 92
Gerhard, O. E. 1993, MNRAS, 265, 213
Goss, W. M., McAdam, W. B., Wellington, K. J., & Ekers, R. D. 1987, MNRAS, 226, 979
Hau, G. K. T., Carter, D., & Balcells, M. 1999, MNRAS, 306, 437
Hau, G. K. T., & Forbes, D. A. 2006, MNRAS, 371, 633
Hills, J. G., & Fullerton, L. W. 1980, AJ, 85, 1281
Jedrzejewski, R. I. 1987, MNRAS, 226, 747
Kormendy, J., & Bender, R. 1996, ApJL, 464, L119
Kormendy, J., & Bender, R. 2009, ApJL, 691, L142
Kormendy, J., & Ho, L. C. 2013, ARA&A, 51, 511
Krajnović, D., Cappellari, M., de Zeeuw, P. T., & Copin, Y. 2006, MNRAS, 366, 787
Krajnović, D., Emsellem, E., Cappellari, M., et al. 2011, MNRAS, 414, 2923
Krajnović, D., Weilbacher, P. M., Urrutia, T., et al. 2015, MNRAS, 452, 2
Kuntschner, H., Emsellem, E., Bacon, R., et al. 2010, MNRAS, 408, 97
Lauer, T. R., Faber, S. M., Gebhardt, K., et al. 2005, AJ, 129, 2138
Lauer, T. R., Gebhardt, K., Faber, S. M., et al. 2007, ApJ, 664, 226
Lena, D., Robinson, A., Marconi, A., et al. 2014, ApJ, 795, 146
Lipka, M., & Thomas, J. 2021, MNRAS, 504, 4599
Mazzalay, X., Thomas, J., Saglia, R. P., et al. 2016, MNRAS, 462, 2847
McConnell, N. J., Ma, C.-P., Murphy, J. D., et al. 2012, ApJ, 756, 179
McDermid, R. M., Emsellem, E., Shapiro, K. L., et al. 2006, MNRAS, 373, 906
Mehrgan, K., Thomas, J., Saglia, R., et al. 2019, ApJ, 887, 195
Mehrgan, K., Thomas, J., Saglia, R., Parikh, T., & Bender, R. 2023, ApJ, 948, 79
Merritt, D. 2006, ApJ, 648, 976
Milosavljević, M., & Merritt, D. 2001, ApJ, 563, 34
Moster, B. P., Naab, T., & White, S. D. M. 2018, MNRAS, 477, 1822
Nasim, I. T., Gualandris, A., Read, J. I., et al. 2021, MNRAS, 502, 4794
Navarro, J. F., Frenk, C. S., & White, S. D. M. 1996, ApJ, 462, 563
Nedelchev, B., Coccato, L., Corsini, E. M., et al. 2019, A&A, 623, A87
Neureiter, B., de Nicola, S., Thomas, J., et al. 2023, MNRAS, 519, 2004
Neureiter, B., Thomas, J., Saglia, R., et al. 2021, MNRAS, 500, 1437
Nieto, J. L., Bender, R., Arnaud, J., & Surma, P. 1991a, A&A, 244, L25
Nieto, J.-L., Bender, R., & Surma, P. 1991b, A&A, 244, L37
Rantala, A., Johansson, P. H., Naab, T., Thomas, J., & Frigo, M. 2018, ApJ, 864, 113
Rantala, A., Johansson, P. H., Naab, T., Thomas, J., & Frigo, M. 2019, ApJL, 872, L17
Rantala, A., Pihajoki, P., Johansson, P. H., et al. 2017, ApJ, 840, 53
Rusli, S. P., Erwin, P., Saglia, R. P., et al. 2013, AJ, 146, 160
Schwarzschild, M. 1979, ApJ, 232, 236
Subrahmanyan, R., Beasley, A. J., Goss, W. M., Golap, K., & Hunstead, R. W. 2003, AJ, 125, 1095
Thomas, J., & Lipka, M. 2022, MNRAS, 514, 6203
Thomas, J., Saglia, R. P., Bender, R., Erwin, P., & Fabricius, M. 2014, ApJ, 782, 39
Van den Bosch, F. C., & Ogiya, G. 2018, MNRAS, 475, 4066
Van den Bosch, R. C. E., van de Ven, G., Verolme, E. K., Cappellari, M., & de Zeeuw, P. T. 2008, MNRAS, 385, 647
Van der Marel, R. P., & Franx, M. 1993, ApJ, 407, 525

Bibliography

Alton P. D., Smith R. J., Lucey J. R., 2017, MNRAS, 468, 1594

Alton P. D., Smith R. J., Lucey J. R., 2018, MNRAS, 478, 4464

Bacon R., et al., 2001, MNRAS, 326, 23

Baes M., Dejonghe H., Buyle P., 2005, A&A, 432, 411

Barden M., et al., 2005, apj, 635, 959

Begelman M. C., Blandford R. D., Rees M. J., 1980, Natur, 287, 307

Bender R., 1988a, A&A, 193, L7

Bender R., 1988b, A&A, 202, L5

Bender R., 1990, A&A, 229, 441

Bender R., 1996, in Bender R., Davies R. L., eds, Vol. 171, New Light on Galaxy Evolution. p. 181

Bender R., 1997, in Arnaboldi M., Da Costa G. S., Saha P., eds, Astronomical Society of the Pacific Conference Series Vol. 116, The Nature of Elliptical Galaxies; 2nd Stromlo Symposium. p. 11 (arXiv:astro-ph/9701204)

Bender R., Doebereiner S., Moellenhoff C., 1987, A&A, 177, L53

Bender R., Doebereiner S., Moellenhoff C., 1988, A&AS, 74, 385

Bender R., Surma P., Doebereiner S., Moellenhoff C., Madejsky R., 1989, A&A, 217, 35

Bender R., Saglia R. P., Gerhard O. E., 1994, MNRAS, 269, 785

Bender R., Saglia R. P., Ziegler B., Belloni P., Greggio L., Hopp U., Bruzual G., 1998, apj, 493, 529

Bernardi M., Domínguez Sánchez H., Brownstein J. R., Drory N., Sheth R. K., 2019, MNRAS, 489, 5633

Bertola F., Galletta G., 1979, A&A, 77, 363

Best P. N., 2007, , 51, 168

Binney J., 1978, Comments on Astrophysics, 8, 27

Binney J., 1985, MNRAS, 212, 767

Binney J., Mamon G. A., 1982, MNRAS, 200, 361

Binney J., Tremaine S., 2008, Galactic Dynamics: Second Edition

Binney J. J., Davies R. L., Illingworth G. D., 1990, apj, 361, 78

Bishop J. L., 1987, apj, 322, 618

Bissantz N., Debattista V. P., Gerhard O., 2004, APjL, 601, L155

Bower R. G., Lucey J. R., Ellis R. S., 1992, MNRAS, 254, 601

Buitrago F., Trujillo I., Conselice C. J., Häußler B., 2013, MNRAS, 428, 1460

Cappellari M., 2002, MNRAS, 333, 400

Cappellari M., 2008, MNRAS, 390, 71

Cappellari M., 2017, MNRAS, 466, 798

Cappellari M., et al., 2007, MNRAS, 379, 418

Cappellari M., et al., 2012, Natur, 484, 485

Cattaneo A., Dekel A., Devriendt J., Guiderdoni B., Blaizot J., 2006, MNRAS, 370, 1651

Cattaneo A., Dekel A., Faber S. M., Guiderdoni B., 2008, MNRAS, 389, 567

Chabrier G., 2003, PASP, 115, 763

Collier W. P., Smith R. J., Lucey J. R., 2018, MNRAS, 478, 1595

Conroy C., van Dokkum P. G., 2012, apj, 760, 71

Contopoulos G., 1956, , 39, 126

Contopoulos G., 1963, AJ, 68, 1

Cretton N., de Zeeuw P. T., van der Marel R. P., Rix H.-W., 1999, APjS, 124, 383

Curtis H. D., 1921, Bulletin of the National Research Council 2, 2, 194

Daddi E., et al., 2005, apj, 626, 680

Davies R. L., Efstathiou G., Fall S. M., Illingworth G., Schechter P. L., 1983, apj, 266, 41

Davies R. L., et al., 2001, APjL, 548, L33

Dehnen W., Gerhard O. E., 1993, MNRAS, 261, 311

Dejonghe H., 1984, A&A, 133, 225

Dejonghe H., 1986, , 133, 217

Dejonghe H., Merritt D., 1992, apj, 391, 531

Dekel A., Birnboim Y., 2006, MNRAS, 368, 2

Dekel A., Birnboim Y., 2008, MNRAS, 383, 119

Djorgovski S., Davis M., 1987, apj, 313, 59

Domínguez Sánchez H., Bernardi M., Brownstein J. R., Drory N., Sheth R. K., 2019, MNRAS, 489, 5612

Dressler A., 1980, apj, 236, 351

Dressler A., Lynden-Bell D., Burstein D., Davies R. L., Faber S. M., Terlevich R., Wegner G., 1987, apj, 313, 42

Eales S., et al., 2015, MNRAS, 452, 3489

Ebisuzaki T., Makino J., Okumura S. K., 1991, Natur, 354, 212

Emsellem E., et al., 2004, MNRAS, 352, 721

Emsellem E., et al., 2007, MNRAS, 379, 401

Ene I., et al., 2018, MNRAS, 479, 2810

Event Horizon Telescope Collaboration et al., 2019, APjL, 875, L1

Faber S. M., Jackson R. E., 1976, apj, 204, 668

Falcón-Barroso J., Martig M., 2021, A&A, 646, A31

Ferrarese L., Merritt D., 2000, APjL, 539, L9

Ferreras I., La Barbera F., de La Rosa I. G., Vazdekis A., de Carvalho R. R., Falcon-Barroso J., Ricciardelli E., 2013, MNRAS, 429, L15

Franx M., Illingworth G. D., 1988, APjL, 327, L55

Frigo M., Naab T., Rantala A., Johansson P. H., Neureiter B., Thomas J., Rizzuto F., 2021, MNRAS, 508, 4610

Gebhardt K., Thomas J., 2009, apj, 700, 1690

Gebhardt K., et al., 2000, AJ, 119, 1157

Gebhardt K., et al., 2003, apj, 583, 92

Gerhard O. E., 1991, MNRAS, 250, 812

Gerhard O. E., 1993, MNRAS, 265, 213

Gerhard O. E., Binney J. J., 1996, MNRAS, 279, 993

Gerhard O., Jeske G., Saglia R. P., Bender R., 1998, MNRAS, 295, 197

Goldstein H., Poole C., Safko J., Addison S. R., 2002, American Journal of Physics, 70, 782

Goullaud C. F., Jensen J. B., Blakeslee J. P., Ma C.-P., Greene J. E., Thomas J., 2018, apj, 856, 11

Hamabe M., Kormendy J., 1987, in de Zeeuw P. T., ed., Vol. 127, Structure and Dynamics of Elliptical Galaxies. p. 379, doi:10.1007/978-94-009-3971-4˙32

Hau G. K. T., Forbes D. A., 2006, MNRAS, 371, 633

Heiligman G., Schwarzschild M., 1979, apj, 233, 872

Herschel W., 1786, Philosophical Transactions of the Royal Society of London Series I, 76, 457

Hills J. G., Fullerton L. W., 1980, AJ, 85, 1281

Hilz M., Naab T., Ostriker J. P., 2013, MNRAS, 429, 2924

Hirschmann M., Khochfar S., Burkert A., Naab T., Genel S., Somerville R. S., 2010, MNRAS, 407, 1016

Hubble E. P., 1925, The Observatory, 48, 139

Hubble E. P., 1926, apj, 64, 321

Hunter C., de Zeeuw P. T., 1992, apj, 389, 79

Illingworth G., 1977, APjL, 218, L43

Jeans J. H., 1915, MNRAS, 76, 70

Jesseit R., Naab T., Peletier R. F., Burkert A., 2007, MNRAS, 376, 997

Jin Y., Zhu L., Long R. J., Mao S., Xu D., Li H., van de Ven G., 2019, MNRAS, 486, 4753

Johansson P. H., Naab T., Burkert A., 2009, apj, 690, 802

Johansson P. H., Naab T., Ostriker J. P., 2012, apj, 754, 115

Kereš D., Katz N., Weinberg D. H., Davé R., 2005, MNRAS, 363, 2

Kluge M., et al., 2020, APjS, 247, 43

Kormendy J., 1977, apj, 218, 333

Kormendy J., Bender R., 1996, APjL, 464, L119

Kormendy J., Bender R., 2009, APjL, 691, L142

Kormendy J., Bender R., 2013, APjL, 769, L5

Kormendy J., Gebhardt K., 2001, in Wheeler J. C., Martel H., eds, American Institute of Physics Conference Series Vol. 586, 20th Texas Symposium on relativistic astrophysics. pp 363–381 (`arXiv:astro-ph/0105230`), doi:10.1063/1.1419581

Kormendy J., Richstone D., 1995, ARAA, 33, 581

Kormendy J., Fisher D. B., Cornell M. E., Bender R., 2009, APjS, 182, 216

Krajnović D., et al., 2011, MNRAS, 414, 2923

Kroupa P., 2001, MNRAS, 322, 231

Kuntschner H., et al., 2010, MNRAS, 408, 97

La Barbera F., Ferreras I., Vazdekis A., de la Rosa I. G., de Carvalho R. R., Trevisan M., Falcón-Barroso J., Ricciardelli E., 2013, MNRAS, 433, 3017

La Barbera F., Vazdekis A., Ferreras I., Pasquali A., Cappellari M., Martín-Navarro I., Schönebeck F., Falcón-Barroso J., 2016, MNRAS, 457, 1468

Lauer T. R., 2012, apj, 759, 64

Lauer T. R., et al., 1995, AJ, 110, 2622

Lauer T. R., et al., 2007, apj, 664, 226

Leavitt H. S., 1908, Annals of Harvard College Observatory, 60, 109

Lipka M., Thomas J., 2021, MNRAS, 504, 4599

Łokas E. L., 2002, MNRAS, 333, 697

Longhetti M., et al., 2007, MNRAS, 374, 614

Lyubenova M., et al., 2016, MNRAS, 463, 3220

Magorrian J., 1995, MNRAS, 277, 1185

Magorrian J., 1999, MNRAS, 302, 530

Magorrian J., Binney J., 1994, MNRAS, 271, 949

Magorrian J., et al., 1998, AJ, 115, 2285

Martín-Navarro I., La Barbera F., Vazdekis A., Falcón-Barroso J., Ferreras I., 2015, MN-RAS, 447, 1033

McConnell N. J., Ma C.-P., 2013, apj, 764, 184

McConnell N. J., Ma C.-P., Gebhardt K., Wright S. A., Murphy J. D., Lauer T. R., Graham J. R., Richstone D. O., 2011a, Natur, 480, 215

McConnell N. J., Ma C.-P., Graham J. R., Gebhardt K., Lauer T. R., Wright S. A., Richstone D. O., 2011b, apj, 728, 100

McConnell N. J., Ma C.-P., Murphy J. D., Gebhardt K., Lauer T. R., Graham J. R., Wright S. A., Richstone D. O., 2012, apj, 756, 179

McDermid R. M., et al., 2006, MNRAS, 373, 906

Mehrgan K., Thomas J., Saglia R., Mazzalay X., Erwin P., Bender R., Kluge M., Fabricius M., 2019, apj, 887, 195

Merritt D., 2006, apj, 648, 976

Messier C., 1781, Catalogue des Nébuleuses et des Amas d'Étoiles (Catalog of Nebulae and Star Clusters), Connoissance des Temps ou des Mouvements Célestes, for 1784, p. 227-267

Milosavljević M., Merritt D., 2001, apj, 563, 34

Mo H., van den Bosch F. C., White S., 2010, Galaxy Formation and Evolution

Moster B. P., Naab T., White S. D. M., 2013, MNRAS, 428, 3121

Naab T., Ostriker J. P., 2017, ARAA, 55, 59

Naab T., Johansson P. H., Ostriker J. P., Efstathiou G., 2007, apj, 658, 710

Naab T., Johansson P. H., Ostriker J. P., 2009, APjL, 699, L178

Nasim I. T., Gualandris A., Read J. I., Antonini F., Dehnen W., Delorme M., 2021, MNRAS, 502, 4794

Nedelchev B., et al., 2019, A&A, 623, A87

Neureiter B., et al., 2021, MNRAS, 500, 1437

Neureiter B., de Nicola S., Thomas J., Saglia R., Bender R., Rantala A., 2023a, MNRAS, 519, 2004

Neureiter B., Thomas J., Rantala A., Naab T., Mehrgan K., Saglia R., de Nicola S., Bender R., 2023b, apj, 950, 15

Oser L., Ostriker J. P., Naab T., Johansson P. H., Burkert A., 2010, apj, 725, 2312

Parikh T., et al., 2018, MNRAS, 477, 3954

Peng C. Y., 2007, apj, 671, 1098

Quenneville M. E., Liepold C. M., Ma C.-P., 2022, apj, 926, 30

Quinlan G. D., Hernquist L., 1997, , 2, 533

Rantala A., Johansson P. H., Naab T., Thomas J., Frigo M., 2018, apj, 864, 113

Rantala A., Johansson P. H., Naab T., Thomas J., Frigo M., 2019, APjL, 872, L17

Rees M. J., Ostriker J. P., 1977, MNRAS, 179, 541

Renzini A., 2006, ARAA, 44, 141

Richstone D. O., Tremaine S., 1984, apj, 286, 27

Richstone D. O., Tremaine S., 1985, apj, 296, 370

Rix H.-W., de Zeeuw P. T., Cretton N., van der Marel R. P., Carollo C. M., 1997, apj, 488, 702

Rusli S. P., Thomas J., Erwin P., Saglia R. P., Nowak N., Bender R., 2011, MNRAS, 410, 1223

Rybicki G. B., 1987, in de Zeeuw P. T., ed., Vol. 127, Structure and Dynamics of Elliptical Galaxies. p. 397, doi:10.1007/978-94-009-3971-4_41

Saglia R. P., et al., 2016, apj, 818, 47

Salpeter E. E., 1955, apj, 121, 161

Saracco P., Longhetti M., Andreon S., 2009, MNRAS, 392, 718

Schechter P. L., Gunn J. E., 1978, AJ, 83, 1360

Schneider P., 2006, Extragalactic Astronomy and Cosmology

Schulze A., Gebhardt K., 2011, apj, 729, 21

Schwarzschild M., 1979, apj, 232, 236

Sérsic J. L., 1963, Boletin de la Asociacion Argentina de Astronomia La Plata Argentina, 6, 99

Shapley H., 1921, Bulletin of the National Research Council 2, 2, 171

Shen S., Mo H. J., White S. D. M., Blanton M. R., Kauffmann G., Voges W., Brinkmann J., Csabai I., 2003, MNRAS, 343, 978

Siopis C., et al., 2009, apj, 693, 946

Smith R. J., Lucey J. R., Conroy C., 2015, MNRAS, 449, 3441

Somerville R. S., Davé R., 2015, ARAA, 53, 51

Spiniello C., Trager S. C., Koopmans L. V. E., Chen Y. P., 2012, APjL, 753, L32

Spinrad H., 1962, apj, 135, 715

Springel V., 2005, MNRAS, 364, 1105

Statler T. S., 1987, apj, 321, 113

Syer D., Tremaine S., 1996, MNRAS, 282, 223

Thomas J., Lipka M., 2022, MNRAS,

Thomas D., Greggio L., Bender R., 1999, MNRAS, 302, 537

Thomas J., Saglia R. P., Bender R., Thomas D., Gebhardt K., Magorrian J., Richstone D., 2004, MNRAS, 353, 391

Thomas D., Maraston C., Bender R., Mendes de Oliveira C., 2005, apj, 621, 673

Thomas J., Jesseit R., Naab T., Saglia R. P., Burkert A., Bender R., 2007a, MNRAS, 381, 1672

Thomas J., Saglia R. P., Bender R., Thomas D., Gebhardt K., Magorrian J., Corsini E. M., Wegner G., 2007b, MNRAS, 382, 657

Thomas J., et al., 2011, MNRAS, 415, 545

Thomas J., Saglia R. P., Bender R., Erwin P., Fabricius M., 2014, apj, 782, 39

Thomas J., Ma C.-P., McConnell N. J., Greene J. E., Blakeslee J. P., Janish R., 2016, Natur, 532, 340

Toft S., et al., 2007, apj, 671, 285

Treu T., Auger M. W., Koopmans L. V. E., Gavazzi R., Marshall P. J., Bolton A. S., 2010, apj, 709, 1195

Trujillo I., Burkert A., Bell E. F., 2004, APjL, 600, L39

Trujillo I., Conselice C. J., Bundy K., Cooper M. C., Eisenhardt P., Ellis R. S., 2007, MNRAS, 382, 109

Tully R. B., Fisher J. R., 1977, A&A, 54, 661

Valluri M., Merritt D., Emsellem E., 2004, apj, 602, 66

Vasiliev E., Valluri M., 2020, apj, 889, 39

Vazdekis A., et al., 2015, MNRAS, 449, 1177

Veale M., et al., 2017, MNRAS, 464, 356

Veale M., Ma C.-P., Greene J. E., Thomas J., Blakeslee J. P., Walsh J. L., Ito J., 2018, MNRAS, 473, 5446

Vincent R. A., Ryden B. S., 2005, apj, 623, 137

Vogelsberger M., et al., 2014, MNRAS, 444, 1518

Williams T. B., Schwarzschild M., 1979, APjS, 41, 209

de Lorenzi F., Debattista V. P., Gerhard O., Sambhus N., 2007, MNRAS, 376, 71

de Nicola S., Saglia R. P., Thomas J., Dehnen W., Bender R., 2020, MNRAS, 496, 3076

de Vaucouleurs G., 1961, APjS, 5, 233

de Zeeuw P. T., et al., 2002, MNRAS, 329, 513

van Dokkum P. G., Conroy C., 2010, Natur, 468, 940

van Dokkum P. G., et al., 2008, APjL, 677, L5

van Dokkum P., Conroy C., Villaume A., Brodie J., Romanowsky A. J., 2017, apj, 841, 68

van den Bosch R. C. E., de Zeeuw P. T., 2010, MNRAS, 401, 1770

van den Bosch R. C. E., van de Ven G., Verolme E. K., Cappellari M., de Zeeuw P. T., 2008, MNRAS, 385, 647

van der Marel R. P., Cretton N., de Zeeuw P. T., Rix H.-W., 1998, apj, 493, 613

Acknowledgements

First and foremost, I would like to express my gratitude to Prof. Ralf Bender for his continuous support and the opportunity to write this PhD thesis under his caring supervision. Thank you for always providing me with the opportunity to delve into the research topics that inspire me the most and for your help whenever I needed guidance.

My greatest appreciation goes to Dr. Jens Thomas for the close collaboration. Thank you, Jens, for always being available to your students, for never leaving any of my questions unanswered thanks to your vast knowledge, and for making working together so enjoyable. I have learned an incredible amount from you during my PhD.

Furthermore, I would like to thank each of my co-authors for our great collaboration. Special thanks go to Roberto, Antti and Fabrizio, whose work contributed significantly to the basic idea of the three publications.

Another thank you goes to my dearest friends Vero, Michi and Fatos - thanks to you, studying physics was twice as much fun.

Last but not least, I would like to thank the people who build the center of my personal universe. Thank you to my parents Sonja and Franz - your unconditional support and love are the foundation of this work. Thank you to my sister Jenny, for always having an open hand for me and your fellow human beings. And thank you to my grandmothers Marianne and Anna - you are always there when I look up at the night sky.